

1      **Variability of the polar stratosphere**  
2      **and its influence on surface weather**  
3      **and climate**



5      William J. M. Seviour  
6      Linacre College  
7      University of Oxford

8      A thesis submitted for the degree of  
9      *Doctor of Philosophy*  
10     September 19, 2014



11 **Variability of the polar stratosphere and its influence on**  
12 **surface weather and climate**

13 William J. M. Seviour

14 Linacre College  
15 University of Oxford

16 *A thesis submitted for the degree of*  
17 *Doctor of Philosophy*

18 September 19, 2014

19 Research during the last two decades has established that variability of the win-  
20 ter polar stratospheric vortex can significantly influence the troposphere, affecting the  
21 likelihood of extreme weather events and the skill of long-range weather forecasts.  
22 This influence is particularly strong following the rapid breakdown of the vortex in  
23 events known as sudden stratospheric warmings (SSWs). This thesis addresses some  
24 outstanding issues in our understanding of the dynamics of stratospheric variability  
25 and its influence on the troposphere.

26 First, a geometrical method is developed to characterise two-dimensional polar vor-  
27 tex variability. This method is also able to identify types of SSW in which the vortex is  
28 displaced from the pole and those in which it is split in two; known as displaced and  
29 split vortex events. It shown to capture vortex variability at least as well as previous  
30 methods, but has the advantage of being easily applicable to climate model simula-  
31 tions. Such an application is desireable because of the relative lack of SSWs in the  
32 observational record.

33 This method is subsequently applied to 13 stratosphere-resolving climate models.  
34 Almost all models show split vortex events as barotropic and displaced vortex events  
35 as baroclinic; a difference also seen in observational reanalysis data. This supports the  
36 idea that split vortex events are caused by a resonant excitation of the barotropic mode.  
37 Models show consistent differences in the surface response to split and displaced vortex  
38 events which do not project stongly onto the annular mode. However, these differences  
39 are approximately co-located with lower stratospheric anomalies. This suggests that a  
40 local adjustment to stratospheric PV anomalies is the mechanism behind the different  
41 responses to split and displaced vortex events.

42 Finally, the predictability of the polar stratosphere and its influence on the tro-  
43 posphere is assessed in a stratosphere-resolving seasonal forecast system. Little skill is  
44 found in the prediction of the strength of the Northern Hemisphere vortex at lead times  
45 beyond one month. However, much greater skill is found for the Southern Hemisphere  
46 vortex during austral spring. This allows for forecasts of interannual changes in ozone  
47 depletion to be inferred at lead times much beyond previous forecasts. It is further  
48 demonstrated that this stratospheric skill descends with time and leads to an enhanced  
49 surface skill at lead times of more than three months.



---

50

## 51           Contents

52

---

53	<b>1 Introduction</b>	<b>11</b>
54	1.1 Overview and aims . . . . .	11
55	1.2 Relation to published work . . . . .	13
56	1.3 Thesis structure . . . . .	13
57	<b>2 Background</b>	<b>15</b>
58	2.1 Dynamics of the polar stratosphere . . . . .	16
59	2.1.1 Zonal-mean circulation . . . . .	16
60	2.1.2 Waves in the stratosphere . . . . .	18
61	2.1.2.1 Planetary waves . . . . .	18
62	2.1.2.2 Gravity waves . . . . .	23
63	2.1.3 Sudden stratospheric warmings . . . . .	24
64	2.2 Polar stratospheric ozone depletion . . . . .	27
65	2.3 Annular modes . . . . .	30
66	2.4 Stratosphere-troposphere coupling . . . . .	32
67	2.4.1 Observational evidence . . . . .	33
68	2.4.2 Modelling evidence . . . . .	38
69	2.4.3 Mechanisms . . . . .	42
70	<b>3 A geometrical description of vortex variability</b>	<b>47</b>
71	3.1 Introduction . . . . .	47
72	3.2 Vortex moment diagnostics . . . . .	51
73	3.3 Data and methods . . . . .	55
74	3.3.1 Reanalysis data . . . . .	55
75	3.3.2 Moment diagnostic calculation . . . . .	57
76	3.3.3 Event identification . . . . .	60
77	3.3.4 Comparison with CP07 and M13 . . . . .	66
78	3.4 Influence on the troposphere . . . . .	72
79	3.5 Conclusions . . . . .	79

80	3.A Comparison with zonal wave amplitudes . . . . .	81
81	<b>4 Representation of vortex variability in climate models</b>	<b>83</b>
82	4.1 Introduction . . . . .	83
83	4.1.1 CMIP5 model simulations . . . . .	86
84	4.2 Vortex mean state and variability . . . . .	86
85	4.2.1 Moment diagnostics . . . . .	86
86	4.2.2 Displaced and split vortex events . . . . .	90
87	4.2.3 Wave diagnostics . . . . .	96
88	4.3 Stratosphere-troposphere coupling . . . . .	99
89	4.3.1 Zonal-mean response to displaced and split vortex events . . . . .	99
90	4.3.2 Spatial response to displaced and split vortex events . . . . .	103
91	4.4 Discussion . . . . .	111
92	4.4.1 Effect of model resolution . . . . .	111
93	4.4.2 Measures of stratosphere-troposphere coupling . . . . .	114
94	4.4.3 Difference between split and displaced vortex events . . . . .	115
95	4.5 Conclusions . . . . .	117
96	<b>5 The role of the stratosphere in seasonal prediction</b>	<b>119</b>
97	5.1 Introduction . . . . .	119
98	5.2 Seasonal forecast system . . . . .	122
99	5.3 Northern Hemisphere results . . . . .	124
100	5.4 Southern Hemisphere results . . . . .	132
101	5.4.1 Stratospheric polar vortex . . . . .	132
102	5.4.2 Ozone depletion . . . . .	136
103	5.4.3 Southern Annular Mode . . . . .	138
104	5.4.4 Stratosphere-troposphere coupling . . . . .	140
105	5.5 Discussion . . . . .	144
106	5.5.1 Northern Hemisphere . . . . .	144
107	5.5.2 Southern Hemisphere . . . . .	145
108	5.5.2.1 Model limitations . . . . .	145
109	5.5.2.2 Statistical significance and ensemble size . . . . .	146
110	5.5.2.3 Application to other seasons . . . . .	148
111	5.6 Conclusions . . . . .	152
112	5.A Choice of time period for statistical forecast . . . . .	154
113	<b>6 Conclusions</b>	<b>157</b>
114	6.1 Summary of results . . . . .	157
115	6.2 Extensions of this work . . . . .	160
116	<b>Bibliography</b>	<b>165</b>

---

117

118 **List of Figures**

119

---

120      2.1	Zonal-mean zonal wind and temperature climatology. . . . .	17
121      2.2	Comparison of NH and SH polar vortex seasonal cycle. . . . .	17
122      2.3	Results from a Stewartson-Warn-Warn model of wave breaking. . . . .	22
123      2.4	Examples of a split and displaced vortex event from <i>Charlton and Polvani [2007]</i> . . . . .	26
124      2.6	Annular mode patterns from <i>Thompson and Wallace [2000]</i> . . . . .	32
125      2.7	NAM time series from <i>Baldwin and Dunkerton [2001]</i> . . . . .	34
126      2.8	NAM composite from <i>Mitchell et al. [2013]</i> . . . . .	36
127      2.9	Numerical simulation results from <i>Jung and Barkmeijer [2006]</i> . . . . .	39
128      2.10	Schematic from <i>Ambaum and Hoskins [2002]</i> . . . . .	45
130      3.1	Equivalent ellipse for a displaced vortex event. . . . .	54
131      3.2	Equivalent ellipse for a spit vortex event. . . . .	56
132      3.3	NH distributions of $Z_{10}$ and PV-based moment diagnostics. . . . .	59
133      3.4	SH distributions of $Z_{10}$ and PV-based moment diagnostics. . . . .	59
134      3.5	Clustering algorithms applied to the moment diagnostics. . . . .	61
135      3.6	Geopotential height at the peak of split vortex events. . . . .	67
136      3.7	Geopotential height at the peak of displaced vortex events. . . . .	68
137      3.8	Seasonal distribution of displaced and split vortex events. . . . .	70
138      3.9	PV composites for split and displaced vortex events. . . . .	71
139      3.10	NAM composites for split and displaced vortex events. . . . .	72
140      3.11	Significance of surface NAM difference following split and displaced vortex events. . . . .	74
141      3.12	Mean sea-level pressure composites for split and displaced vortex events. . . . .	75
142      3.13	Tropopause height composites for split and displaced vortex events. . . . .	77
143      3.14	Wave amplitude and moment diagnostic timeseries. . . . .	82
144      3.15	Comparison of vortex at maximum of moment diagnostics and wave amplitudes. . . . .	82
147      4.1	Distributions of moment diagnostics for the CMIP5 models. . . . .	87

148	4.2 Seasonal cycle of moment diagnostics in the CMIP5 models . . . . .	90
149	4.3 Frequency of split and displaced vortex events in the CMIP5 models . . .	91
150	4.4 Seasonal distribution of splits and displacements in the CMIP5 models .	93
151	4.5 Comparison of moment diagnostics and frequency of split and displaced vortex events. . . . .	95
152	4.6 Composites of 10 hPa Z at the onset date split and displaced vortex events in the CMIP5 models. . . . .	97
153	4.7 CMIP5 wave diagnostics . . . . .	98
154	4.8 NAM composites for splits and displacements in the CMIP5 models . . .	101
155	4.9 MSLP composites following splits and displacements in the CMIP5 models	104
156	4.10 NAM composites for splits and displacements in the CMIP5 models . . .	107
157	4.11 Difference of MSLP following split and displaced vortex events. . . . .	110
158	4.12 Vertical resolution and modal aspect ratio. . . . .	112
160		
161	5.1 Timeseries of $\bar{u}$ at 60°N, 10 hPa, for all GloSea5 ensemble members. . .	125
162	5.2 Timeseries of $\bar{u}$ at 60°S, 10 hPa, for all GloSea5 ensemble members. . .	126
163	5.3 NH comparison of GloSea5 and ERA-Interim zonal-mean zonal wind cli- matologies. . . . .	127
164	5.4 Moment diagnostics for GloSea5. . . . .	128
165	5.5 DJF $\bar{u}$ anomalies for GloSea5. . . . .	129
166	5.6 ROC curve for the prediction of SSWs. . . . .	130
167	5.7 ROC curves for the prediction of split and displaced vortex events. . . . .	131
168	5.8 Lag-height correlation of NH polar cap geopotential height. . . . .	132
169	5.9 Comparison of GloSea5 and ERA-Interim zonal-mean zonal wind clima- tologies. . . . .	133
170		
171	5.10 GloSea5 forecast skill for the stratospheric polar vortex strength and column ozone. . . . .	134
172		
173	5.11 Comparison of GloSea5 and observed SSWs. . . . .	136
174		
175	5.12 Relation between stratospheric polar vortex strenth and column ozone. .	137
176		
177	5.13 GloSea5 predictions of the SAM. . . . .	139
178		
179	5.14 Correlation of GloSea5 forecasts of sea-level pressure and temperature. .	140
180		
181	5.15 Lag-height correlation of GloSea5 polar cap geopotential height . . . . .	142
182		
183	5.16 Variation of GloSea5 forecast skill with ensemble size . . . . .	148
184		
185	5.17 GloSea5 predictions of the SAM. . . . .	149
	5.18 Lag-height correlation of Z' at 10 hPa and 1000 hPa. . . . .	151
	5.19 Correlation of the SOI with the SAM. . . . .	155
	5.20 Lag-height correlation of GloSea5 polar cap geopotential height . . . . .	155
184	6.1 Decadal variability of SSWs . . . . .	163
185	6.2 EMD timeseries . . . . .	164

186

---

187

## List of acronyms and abbreviations

188

---

- 189 **CCMVal-2** Second Chemistry–Climate Validation Activity  
190 **CFC** Chlorofluorocarbon  
191 **CMIP5** Coupled Model Intercomparison Project Phase 5  
192 **CP07** *Charlton and Polvani* [2007]  
193 **DJF** December to February (inclusive)  
194 **ECMWF** European Centre for Medium-Range Weather Forecasts  
195 **ENSO** El Niño–Southern Oscillation  
196 **EOF** Empirical orthogonal function  
197 **EP** Eliassen-Palm  
198 **ERA** ECMWF reanalysis  
199 **GCM** General circulation model  
200 **GEV** Generalised extreme value  
201 **M13** *Mitchell et al.* [2013]  
202 **MMM** Multi-model mean  
203 **MSLP** Mean sea-level pressure  
204 **NAM** Northern annular mode  
205 **NAO** North Atlantic oscillation  
206 **PNA** Pacific-North American (pattern)  
207 **PSC** Polar stratospheric cloud  
208 **PV** Potential vorticity  
209  $q_{850}$  PV on the 850 K potential temperature surface  
210 **QBO** Quasi-biennial oscillation  
211 **QG** Quasi-geostrophic  
212 **SAM** Southern Annular mode  
213 **SH** Southern Hemisphere  
214 **SON** September to November (inclusive)  
215 **SSW** Sudden stratospheric warming  
216 **TEM** Transformed Eulerian-mean  
217 **UTLS** Upper-troposphere/lower-stratosphere  
218  $Z_{10}$  10 hPa geopotential height

LIST OF FIGURES

219

# CHAPTER 1

220

---

221

## Introduction

222

---

### 223 1.1 Overview and aims

224 Traditionally the stratosphere was thought to respond passively to tropospheric forc-  
225 ing from below. However, modelling and observational evidence accrued over the last  
226 two decades has demonstrated that in some cases variability of the winter polar strato-  
227 sphere can cause consistent circulation anomalies at the Earth’s surface. This influ-  
228 ence has been shown to be particularly strong following the rapid breakdown of the  
229 usual westerly winter stratospheric polar vortex; events known as sudden stratospheric  
230 warmings (SSWs).

231 Despite these advances, important issues remain as to the dynamics of SSWs and  
232 the stratosphere’s influence on the troposphere. Most significantly:

- 233 i. The dynamics of SSWs are not fully understood, in particular whether different  
234 mechanisms may be responsible for different types of event.
- 235 ii. A mechanism for the stratosphere’s influence on the troposphere is not well de-  
236 veloped and it is not understood why some types of stratospheric event appear to  
237 have different impacts on the troposphere than others.

238 These are significant long-standing issues, and providing a comprehensive solution is  
 239 not possible here, but it is hoped that this thesis will go some way to addressing them.  
 240 A solution to these issues is not purely of theoretical interest, since it is necessary  
 241 to understand the dynamics of these phenomena in order to simulate them in weather  
 242 and climate prediction models; the ultimate aim being the development of more skillful  
 243 forecasts. With an eye on this application, this thesis also aims to assess the predictabil-  
 244 ity of the stratosphere and its connection to the troposphere.

245 The main original contributions of this thesis to the scientific literature are sum-  
 246 marised below:

247 1. In **Chapter 3** a new method to diagnose stratospheric polar vortex variability and  
 248 classify split and displaced vortex events is introduced and tested. This is the first  
 249 semi-Lagrangian (or vortex-centric) method that can be easily and robustly applied  
 250 to climate model simulations. Reanalysis data are then used to compare anomalies  
 251 at the tropopause and the surface following the split and displaced vortex events. Al-  
 252 though there may be some significant differences, the relatively short observational  
 253 record hinders the statistical significance of these results.

254 2. In **Chapter 4** this method is applied to carry out the first multi-model comparison of  
 255 split and displaced vortex events and their influence on the troposphere. It is found  
 256 that there is a wide range of biases in the representation of the stratospheric polar  
 257 vortex among models, at least some of which may be attributable to differences in  
 258 vertical resolution. It is also shown that there are consistent differences between  
 259 the tropospheric response to split and displaced vortex events among the models.  
 260 These differences, and the large number of events studied, allows some inference of  
 261 the mechanisms behind the different surface responses.

262 3. In **Chapter 5** the predictability of the stratospheric polar vortex is assessed in a  
 263 stratosphere-resolving seasonal prediction system. Little skill is found in the predic-  
 264 tion of the strength of the Northern Hemisphere stratospheric polar vortex or the

occurrence of split or displaced vortex events on seasonal timescales. However, significant skill is found in the case of the Southern Hemisphere vortex. This enables the skillful prediction of interannual variability in ozone depletion beyond the lead time of previous forecasts. Furthermore, it is demonstrated that the stratospheric skill significantly enhances the skill of tropospheric forecasts several months ahead.

## 1.2 Relation to published work

Chapter 3 is largely based on a paper written by myself, Daniel Mitchell and Lesley Gray published in *Geophysical Research Letters* [Seviour et al., 2013], although the analysis has been significantly extended and re-written. The part of Chapter 5 relating to the Southern Hemisphere is based on a paper written by myself, Steven Hardiman, Lesley Gray, Neal Butchart, Craig MacLachlan, and Adam Scaife published in *Journal of Climate* [Seviour et al., 2014]. Additionally, a paper based on Chapter 4 is in preparation and is expected to be submitted in the near future.

In both of the above papers, all the writing is my own and I carried out all the analysis and produced the figures. However, I am of course very grateful for the constructive comments of my coauthors in the preparation of these papers as well as my reviewers; Harry Hendon (from the Centre for Australian Weather and Climate Research), and three of whom are anonymous.

## 1.3 Thesis structure

The next chapter introduces the necessary background of the current understanding of the dynamics of the polar stratosphere, including the differences between the Northern and Southern Hemispheres and SSWs. It also reviews the role of dynamics in polar stratospheric ozone depletion, the atmospheric annular modes, and the observational, modelling, and theoretical evidence for the stratosphere's influence on the troposphere. The original results described above are presented in Chapters 3, 4, and 5. Conclusions and possible extensions to the work in this thesis are discussed in Chapter 6.



## CHAPTER 2

---

### Background

---

295 The stratosphere is the layer of the Earth's atmosphere which lies above the troposphere  
296 and is bounded by the tropopause below and the stratopause above. The height of  
297 the tropopause varies from about 15 km in altitude in the tropics to 7 km at high  
298 latitudes, while the stratopause lies at approximately 50 km. The defining feature  
299 of the stratosphere is a temperature gradient increasing with height (in contrast to  
300 the troposphere below), caused by the presence of ozone which absorbs ultraviolet  
301 radiation<sup>1</sup> and thereby heats the surrounding atmosphere. This temperature gradient  
302 makes the stratosphere stable against vertical convection and results in very different  
303 dynamical behaviour to the troposphere. In this chapter, our current understanding  
304 of the dynamics of the polar stratosphere are reviewed (Section 2.1), as well as the  
305 relationship between dynamics and polar stratospheric ozone depletion (Section 2.2),  
306 and stratosphere-troposphere coupling (Sections 2.3 and 2.4).

---

<sup>1</sup>For this reason, the region of the stratosphere with the highest ozone concentrations is often called the “ozone layer”.

## 307 2.1 Dynamics of the polar stratosphere

### 308 2.1.1 Zonal-mean circulation

Each winter the polar region descends into a polar night and the stratosphere cools by infrared radiation to space. This sets up a strong equator-to-pole temperature gradient which increases the vertical zonal wind shear in accordance with the thermal wind balance relation

$$\frac{\partial u_g}{\partial z} = -\frac{R}{fH} \frac{\partial T}{\partial y}, \quad (2.1)$$

309 where  $u_g$  is the geostrophic zonal velocity<sup>2</sup>,  $u_g = -f^{-1} \partial Z / \partial y$ ,  $Z$  is geopotential  
310 height,  $f$  is the Coriolis parameter,  $f = 2\Omega \sin \phi$ , and  $R$  is the specific gas constant.  
311 Here, a beta-plane geometry is used such that  $f = f_0 + \beta y$ , where  $f_0 = f(\phi_0)$  and  
312  $\beta = 2\Omega a^{-1} \cos \phi_0$ ,  $a$  is the Earth's radius and  $\phi_0$  is a reference latitude.  $H$  is the scale  
313 height given by  $H = RT_s/g$ , where  $T_s$  is a reference temperature and  $g$  is the accel-  
314 eration due to gravity. This equation relies on hydrostatic and geostrophic approxi-  
315 mations but is approximately satisfied on seasonal timescales. Hence, the meridional  
316 temperature gradient results in a region of westerly winds in the winter hemisphere,  
317 surrounding the pole; this is known as the *stratospheric polar vortex*.<sup>3</sup>

318 Figure 2.1 shows zonal-mean zonal wind and temperature averaged over the boreal  
319 winter (December-February; DJF) and austral winter (July-August; JJA) using data  
320 from 1979-2010 from the ERA-Interim reanalysis (details in Section 3.3.1). In both  
321 cases the westerly vortex in the winter hemisphere can be seen along with a local  
322 minimum in temperature at the winter pole in the lower stratosphere. Easterly winds  
323 are present in the summer hemisphere. The maximum strength of the polar vortex  
324 occurs at midlatitudes between 0.1-1 hPa in the mesosphere, and is stronger in the  
325 Southern Hemisphere (SH) with a maximum of  $90 \text{ ms}^{-1}$  than the Northern Hemisphere  
326 (NH) with a maximum of  $50 \text{ ms}^{-1}$ . The winter polar stratosphere is also approximately  
327 20 K colder in the SH than the NH.

---

<sup>2</sup>That is, the zonal wind balanced by pressure gradient forces.

<sup>3</sup>Alternative names for this which often appear in the literature are ‘polar night jet’ or ‘polar night vortex’. These names are not used here because the vortex persists outside of the polar night.

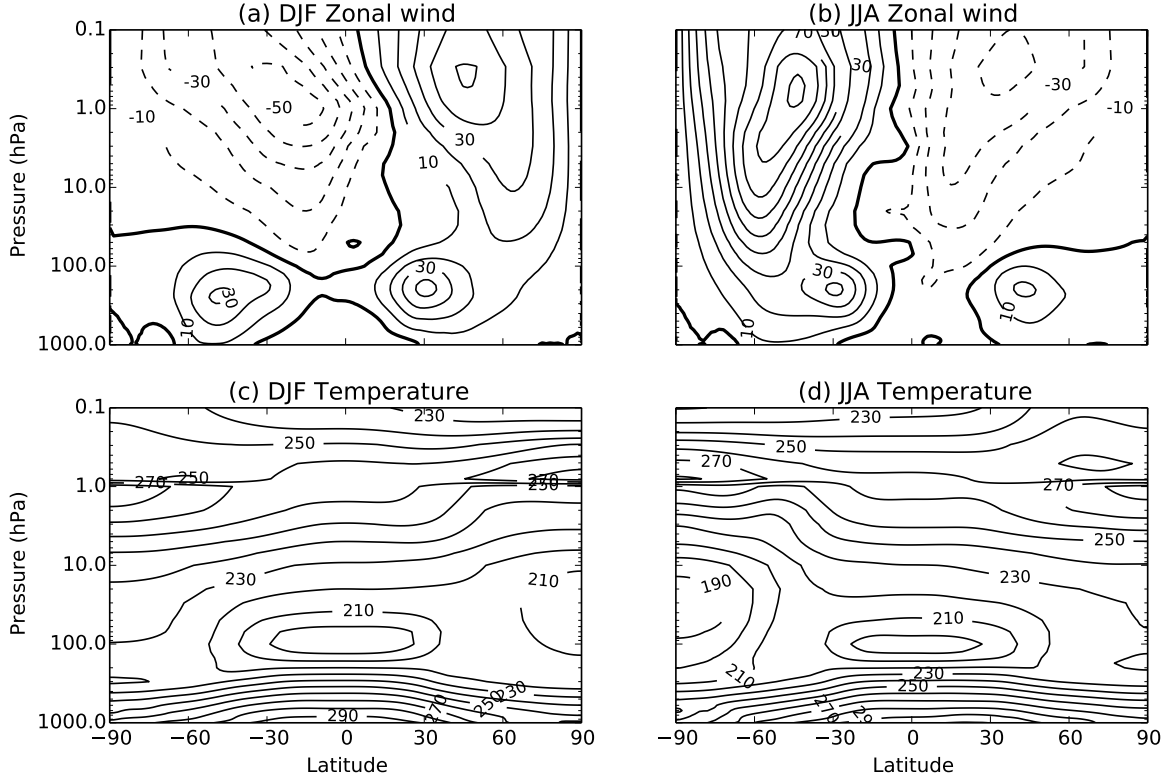


**Figure 2.1:** December-January (DJF) (a,c) and July-August (JJA) (b,d) averages of zonal-mean zonal wind ( $\text{m s}^{-1}$ ) (a,b) and temperature (K) (c,d). Dashed contours represent negative values. Data is from the ERA-Interim reanalysis (1979-2010).

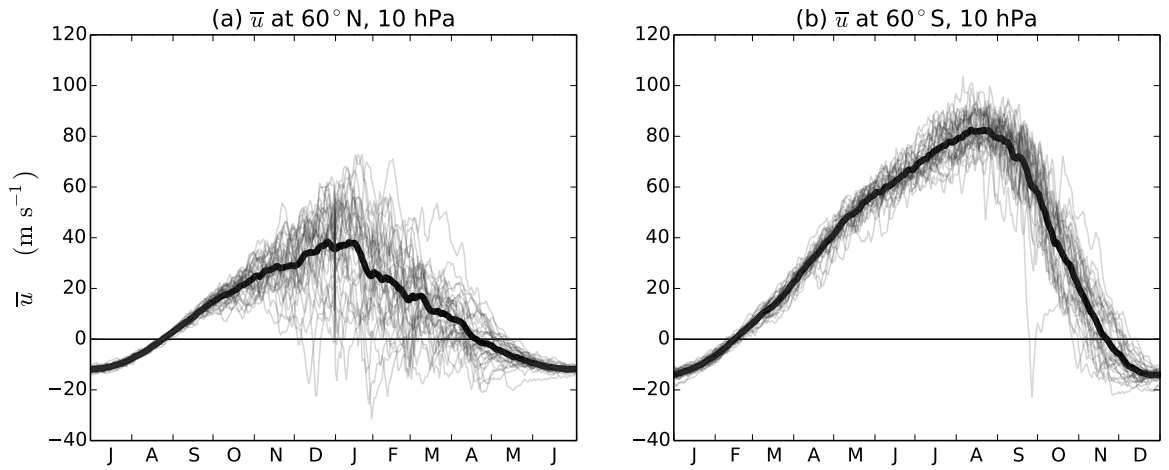


**Figure 2.2:** Seasonal cycle of NH (a) and SH (b) polar vortex strength, measured by  $\bar{u}$  at  $60^\circ\text{N/S}$ , 10 hPa. The annual mean is shown in a thick black line and individual years in thin grey lines. Both time series are centred on their respective winters. Data is from the ERA-Interim reanalysis (1979-2010).

328      The maximum strength of the vortex in the stratosphere occurs at approximately  
 329     $60^{\circ}\text{N/S}$  with little variation through the depth of the stratosphere. Figure 2.2 shows  
 330    the annual cycle and variability of zonal-mean zonal wind at 10 hPa  $60^{\circ}\text{N}$  and  $60^{\circ}\text{S}$ . As  
 331    well as being weaker on average than the SH, the winter NH stratospheric polar vortex  
 332    can also be seen to be significantly more variable than the SH. There are a number of  
 333    years in the NH for which  $\bar{u}$  becomes negative during the winter, but only one such year  
 334    in the SH (these events are discussed further in Section 2.1.3). A further clear feature  
 335    of both NH and SH is that variability during the summer is much less than that during  
 336    winter. Also, the transition to summer easterlies (known as the final warming) occurs  
 337    relatively earlier in the seasonal cycle in the NH than the SH. All these observations  
 338    are due almost entirely to the influence of wave phenomena in the stratosphere, as  
 339    described in the next section.

### 340    2.1.2 Waves in the stratosphere

#### 341    2.1.2.1 Planetary waves

Large-scale Rossby or planetary waves<sup>4</sup> play a vital role in the dynamics of the extratropical stratosphere. They mostly enter the stratosphere from the troposphere, where they are forced, for example, by air flow around topography, latent heat release, or non-linear evolution of tropospheric eddies [Scinocca and Haynes, 1998]. These large-scale waves approximately satisfy the quasi-geostrophic (QG) approximation of hydrostatically balanced incompressible flow with low Rossby number,  $\text{Ro} = U/f_0 L \ll 1$ , where  $U$  and  $L$  are characteristic velocity and length scales respectively [Andrews et al., 1987]. Under this approximation and in the absence of friction, the following relation, known as the *quasi-geostrophic potential vorticity equation*, holds:

$$D_g q_g = f_0 \rho_0 \frac{\partial}{\partial z} \frac{\rho_0 Q}{\partial \theta_0 / \partial z}. \quad (2.2)$$

Where

$$D_g \equiv \frac{\partial}{\partial t} + u_g \frac{\partial}{\partial x} + v_g \frac{\partial}{\partial y}, \quad (2.3)$$

---

<sup>4</sup>Here, as is common in the stratospheric literature, “wave” is taken to mean any deviation from the zonal-mean state.

and

$$q_g = f_0 + \beta y - \frac{\partial v_g}{\partial x} + \frac{\partial u_g}{\partial y} + \rho_0^{-1} \frac{\partial}{\partial z} \left( \rho_0 f_0 \frac{\theta_e}{\partial \theta_0 / \partial z} \right), \quad (2.4)$$

is the quasi-geostrophic potential vorticity. Here,  $v_g$  is the geostrophic meridional velocity,  $v_g = f^{-1} \partial Z / \partial x$ ,  $Q$  is the diabatic heating rate,  $\rho_0$  is a reference density and  $\theta_0$  is a reference potential temperature,  $\theta_0 = T_s(p_s/p)^\kappa$ , where  $p_s = 1000$  hPa, and  $\kappa = R/c_p \approx 2/7$ , where  $c_p$  is the specific heat capacity of air at constant pressure.  $\theta_e$  represents the departure from  $\theta_0$ , and is assumed to be small in the sense that  $|\partial \theta_e / \partial z| \ll |\partial \theta_0 / \partial z|$ . An important consequence of Equation 2.2 is that  $q_g$  is conserved following the geostrophic wind for adiabatic flow ( $Q = 0$ ), and therefore acts as a tracer.<sup>5</sup>

In the case of approximately zonal flow  $[\bar{u}(y, z), 0, 0]$ , Equation 2.2 can be linearised to give

$$\left( \frac{\partial}{\partial t} + \bar{u} \frac{\partial}{\partial x} \right) q'_g + v' \frac{\partial \bar{q}_g}{\partial y} = f_0 \rho_0 \frac{\partial}{\partial z} \frac{\rho_0 Q'}{\partial \theta_0 / \partial z}, \quad (2.5)$$

where primes represent deviations from the zonal mean (e.g.,  $q_g = \bar{q}_g + q'_g$ ). It can be shown that Equation 2.5 supports wave-like solutions, with vertical propagation dependent upon the condition:

$$0 < \bar{u} - c < \bar{u}_c \equiv \beta(k^2 + l^2 + \epsilon/4H^2)^{-1}, \quad (2.6)$$

which is known as the *Charney-Drazin criterion* after *Charney and Drazin* [1961]. Here,  $c$  is the wave's zonal phase speed,  $k$  and  $l$  are the zonal and meridional wavenumbers respectively, and  $\epsilon = f_0^2/N^2$ , where  $N^2 = H^{-1} Re^{-\kappa z/H} \partial \theta_0 / \partial z$  is the static stability. In

---

<sup>5</sup>Throughout most of this thesis, Ertel's potential vorticity,  $q$ , is used. This is defined by

$$q = \frac{1}{\rho} \zeta \cdot \nabla \theta,$$

where  $\zeta$  is the absolute vorticity. *Charney and Stern* [1962] showed that when the quasi-geostrophic approximation is valid

$$\left( \frac{\partial q}{\partial s} \right)_{\theta=\text{const.}} \approx \frac{1}{\rho_0} \frac{\partial \theta_0}{\partial z} \left( \frac{\partial q_g}{\partial s} \right)_{z=\text{const.}},$$

where  $s = t, x$  or  $y$ . Hence, a similar conservation law as for  $q_g$  applies to  $q$ , which is conserved on isentropic (e.g., constant  $\theta$ ) surfaces.

the case of waves whose phase is stationary with respect to the ground ( $c = 0$ ), this simplifies to

$$0 < \bar{u} < \bar{u}_c. \quad (2.7)$$

350 It is therefore apparent that in order for planetary waves to propagate vertically (such  
 351 as from the troposphere to the stratosphere), a westerly flow must be present that is not  
 352 too strong. Additionally, this maximum speed is dependent on wavenumber, such that  
 353 a lower wavenumber can propagate in a stronger westerly flow. While the assumptions  
 354 here are not representative of the real atmosphere (such as purely zonal flow, and  
 355 small deviations from the zonal mean), this criterion does capture the most important  
 356 features of the relation between zonal assymmetries and the zonal flow, and similar  
 357 relations can be found for more complex background states [Andrews *et al.*, 1987].

358 An important consequence of the Charney-Drazin criterion for stratospheric flow is  
 359 that the strength of the stratospheric polar vortices shown in Figures 2.1 and 2.2 is often  
 360 sufficient to exclude all but the lowest wavenumbers (typically zonal wavenumbers 1–  
 361 3; hereafter referred to as ‘wave- $n$ ’) from propagating upwards from the troposphere.  
 362 Hence the length-scale of typical stratospheric zonal asymmetries is much larger than  
 363 that of the troposphere.

364 When planetary waves reach a *critical surface*, where propagation is prohibited (for  
 365 instance, a region where  $\bar{u} = c$ ), the above linear analysis breaks down. In this sce-  
 366 nario waves can “break”, imparting momentum onto the zonal flow. There is therefore  
 367 a two-way interaction between the zonal flow and planetary waves; a phenomenon  
 368 known as *wave-mean flow interaction*. Wave breaking was studied in an idealised two-  
 369 dimensional model by Stewartson [1978] and Warn and Warn [1978]. They found  
 370 momentum to be absorbed in a narrow *critical layer* close to the critical surface, with  
 371 potential vorticity (PV) contours being irreversibly stretched and mixed in increasingly  
 372 fine scales; a process known as a ‘potential enstrophy cascade’ [e.g., Rhines and Hol-  
 373 land, 1979]. They also showed that the critical layer is initially absorbing, but be-  
 374 comes a reflecting surface after some time. Time varying results from a version of  
 375 the Stewartson-Warn-Warn model from Andrews *et al.* [1987] are shown in Figure 2.3.

<sup>376</sup> Similar wave breaking behaviour was first observed in the real stratosphere by *McIn-*  
<sup>377</sup> *tyre and Palmer* [1983] using isentropic maps of Ertel's potential vorticity, including  
<sup>378</sup> the irreversible deformation of PV contours of the kind shown in Figure 2.3.

A further effect of wave breaking is the induction of a *residual circulation*,  $[0, \bar{v}^*, \bar{w}^*]$ , where  $\bar{v}^*$  and  $\bar{w}^*$  are the transformed Eulerian-mean (TEM) meridional and vertical velocities given in spherical coordinates by

$$\bar{v}^* = \bar{v} - \frac{1}{\rho_0} \frac{\partial}{\partial z} \left( \frac{\rho_o \bar{v}' \theta'}{\partial \bar{\theta} / \partial z} \right), \quad (2.8)$$

$$\bar{w}^* = \bar{w} + \frac{1}{a \cos \phi} \frac{\partial}{\partial \phi} \left( \frac{\cos \phi \bar{v}' \theta'}{\partial \bar{\theta} / \partial z} \right), \quad (2.9)$$

which approximates the Lagrangian-mean circulation under time-averaged conditions [*Andrews and McIntyre*, 1976; *Dunkerton*, 1978; *Holton*, 1990]. Under the TEM formalism, the zonal momentum equation becomes

$$\frac{\partial \bar{u}}{\partial t} + \bar{v}^* \left( \frac{1}{a \cos \phi} \frac{\partial}{\partial \phi} (\bar{u} \cos \phi) - f \right) + \bar{w}^* \frac{\partial \bar{u}}{\partial z} = \frac{\nabla \cdot \mathbf{F}}{\rho_o a \cos \phi} + \bar{X} \equiv \bar{\mathcal{F}} \quad (2.10)$$

where  $\bar{X}$  represents frictional terms and  $\mathbf{F} = [0, F^\phi, F^z]$  is the Eliassen-Palm (EP) flux with components

$$F^\phi = \rho_0 a \cos \phi \left( \frac{\partial \bar{u}}{\partial z} \frac{\bar{v}' \theta'}{\partial \bar{\theta} / \partial z} - \bar{v}' u' \right), \quad (2.11)$$

$$F^z = \rho_0 a \cos \phi \left( \left[ f - \frac{1}{a \cos \phi} \frac{\partial}{\partial \phi} (\bar{u} \cos \phi) \right] \frac{\bar{v}' \theta'}{\partial \bar{\theta} / \partial z} - \bar{w}' u' \right). \quad (2.12)$$

<sup>379</sup>  $\mathbf{F}$  can be interpreted as the flux of wave activity [*Andrews et al.*, 1987], and there-  
<sup>380</sup> fore  $\nabla \cdot \mathbf{F} < 0$  (convergence) represents a dissipation of wave activity, as is the case  
<sup>381</sup> in wave breaking. It can be seen that for a steady zonal flow ( $\partial \bar{u} / \partial t = 0$ ) in the ab-  
<sup>382</sup> sence of wave driving ( $\nabla \cdot \mathbf{F} = 0$ ) or friction ( $\bar{X} = 0$ ), a solution of Equation 2.10 is  
<sup>383</sup>  $\bar{v}^* = 0, \bar{w}^* = 0$ . However, in the presence of these forcing terms, a non-zero residual  
<sup>384</sup> circulation will be induced. Climatologically, this circulation consists of wave-driven  
<sup>385</sup> poleward and downward motion in the extratropics which is balanced by upwelling in

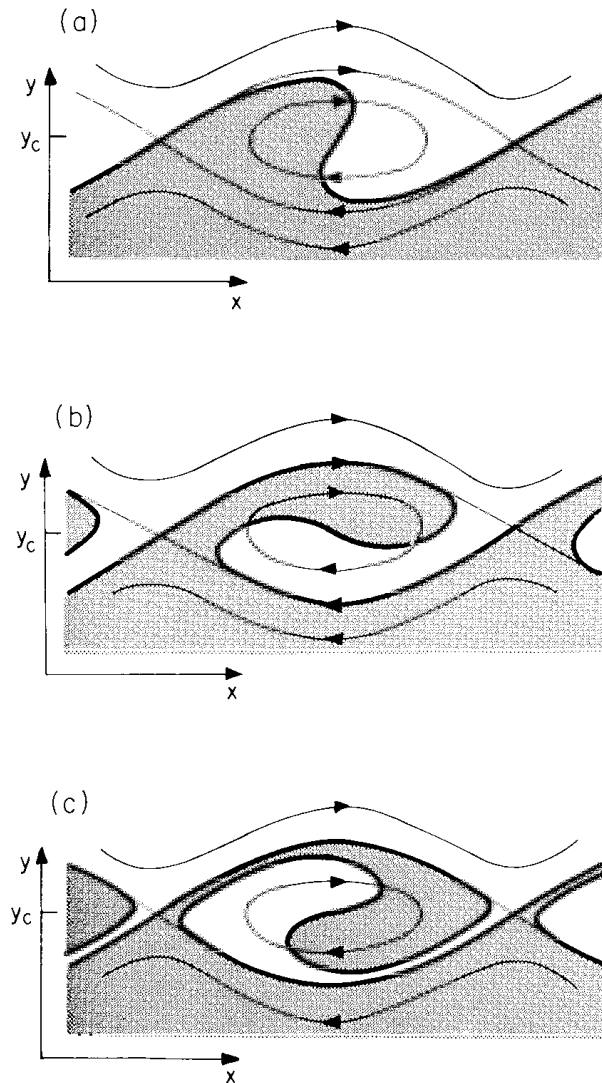


**Figure 2.3:** Stewartson-Warn-Warn time-dependent analytical solution of a Rossby wave non-linear critical layer (time advancing in even steps from (a)-(b)-(c)). The flow is periodic in  $x$  and the  $y$  scale is greatly exaggerated and the initial critical line was at  $y = y_c$ . The thin lines indicate streamlines and lens shaped regions of closed streamlines are known as “Kelvin’s cats’ eyes”. The thick line shows the position of the absolute vorticity contour  $\zeta = \zeta_c$ , that initially lay along  $y = y_c$  (in this barotropic model, the quasi-geostrophic potential vorticity,  $q_g$ , reduces to  $\zeta$ ). Hence,  $\zeta < \zeta_c$  in the stippled region and  $\zeta > \zeta_c$  in the unstippled region. In (a) it can be seen that  $v > 0$  for most of the stippled region, indicating partial absorption, whereas in (b) and (c)  $v \leq 0$  in the stippled region indicating reflection. Figure from [Andrews et al. \[1987\]](#).

## 2.1. DYNAMICS OF THE POLAR STRATOSPHERE

386 the tropics; a pattern which forms a significant part of the Brewer-Dobson circulation<sup>6</sup>.  
387 The downward motion near the poles can be easily seen from Equation 2.10 in the  
388 steady case; since  $\bar{v}^*$  must become small near the poles (by conservation of mass), and  
389  $\partial \bar{u} / \partial z > 0$  in the polar vortex, if  $\nabla \cdot \mathbf{F} < 0$ , then  $\bar{w}^* < 0$ . It is observed that this circu-  
390 lation is strongest in the winter hemisphere due to the fact that more planetary waves  
391 can propagate and break in the winter westerly flow than the summer easterly flow  
392 (due to the Charney-Drazin criterion). Furthermore, during periods of enhanced wave  
393 breaking the residual circulation accelerates and there is more descent and adiabatic  
394 heating at high latitudes. This is important in the physical understanding of sudden  
395 stratospheric warming events, described in Section 2.1.3.

### 396 2.1.2.2 Gravity waves

397 Gravity waves are another type of atmospheric wave important in the dynamics of the  
398 polar stratosphere. These waves owe their existence to buoyancy restoring forces and  
399 can be generated by a number of processes such as air flow over topography (oro-  
400 graphic gravity waves), convection or frontogenesis (non-orographic gravity waves).  
401 As with planetary waves, the differences in the land masses of the two hemispheres  
402 leads to orographic gravity wave activity being much greater in the NH. These waves  
403 make a net easterly contribution to the winter zonal flow [e.g., *Seviour et al., 2012*],  
404 and so act to enhance the residual circulation. Their typical length scales are much  
405 shorter than can be resolved in general circulation models or reanalyses, and so they  
406 are usually parametrised, appearing as the term  $\bar{X}$  in the zonal momentum equation  
407 (Equation 2.10).

408 Together, the Charney-Drazin criterion and the effects of planetary and gravity wave  
409 driving on the zonal flow can explain almost all hemispheric differences seen in Figures  
410 2.1 and 2.2: Greater topography results in more planetary and gravity wave generation  
411 in the NH, both of which cause a net deceleration of the westerly polar vortex, thereby  
412 causing the NH vortex to be weaker than the SH. This also explains why the NH vortex

---

<sup>6</sup>Strictly, the Brewer-Dobson circulation represents the meridional transport of tracers, and so also involves two-way mixing (i.e. transport without net transfer of mass) [*Hall and Plumb, 1994*].

413 is warmer than the SH, as the greater NH wave activity induces a stronger residual cir-  
 414 culation with enhanced descent and adiabatic warming at high latitudes. Additionally,  
 415 the strength of the SH vortex is such that it prohibits the vertical propagation of plane-  
 416 tary waves from the troposphere throughout much of the winter, meaning that the SH  
 417 vortex is less variable than the NH. Both hemispheres show very little variability in the  
 418 summer easterly flow because planetary wave propagation is prohibited in this regime.

### 419 2.1.3 Sudden stratospheric warmings

420 First observed by *Scherhag* [1952] in radiosonde measurements over Berlin, the ex-  
 421 tremere events visible in Figure 2.2 whereby the winter circulation temporarily becomes  
 422 easterly<sup>7</sup> are known as sudden stratospheric warmings<sup>8</sup> (SSWs). These events occur  
 423 approximately 5-7 times per decade in the NH, but only one such event has been ob-  
 424 served in the almost 60 year observational record in the SH (in 2002). They are called  
 425 “warmings” because associated with the circulation reversal is a dramatic increase in  
 426 temperature; as much as 50 K in the space of a few days in the mid-stratosphere.<sup>9</sup>

427 Initially these events were thought to result from either solar storms or baroclinic  
 428 instability of the stratospheric polar vortex. However, *Matsuno* [1970, 1971] proposed  
 429 a model of SSWs which relies on the influence of tropospherically forced planetary  
 430 waves. This model (or modifications thereof) remains the most widely accepted dy-  
 431 namical view of SSWs at present. The mechanism proceeds as follows:

- 432 i. A packet of enhanced planetary wave activity enters the stratosphere where it  
 433 reaches a critical surface and breaks. This decelerates the zonal flow over a broader  
 434 critical layer, and if strong enough causes it to reverse.

---

<sup>7</sup>For a discussion of more precise definitions of SSWs, see Section 3.1.

<sup>8</sup>Following *Butler et al.* [2014] it is suggested that the term “sudden stratospheric warming” is prefer-  
 able to the common alternative “stratospheric sudden warming”. This is because there are other varieties  
 of stratospheric warming (such as final warmings or Canadian warmings), but not other varieties of at-  
 mospheric sudden warming.

<sup>9</sup>A recent study [*Neef et al.*, 2014] has even suggested that SSWs have a sufficiently strong influence  
 on the Earth’s angular momentum that they have a detectable influence on the length of the day.

## 2.1. DYNAMICS OF THE POLAR STRATOSPHERE

- 435 ii. Hence a new critical surface is formed at a lower level (where  $\bar{u} = 0$ ), and wave  
436 breaking occurs at this level. The process continues as the critical layer descends  
437 to the lower stratosphere.
- 438 iii. At the same time, wave breaking induces an enhanced residual circulation with  
439 greater descent and adiabatic warming at high latitudes. If strong enough, this can  
440 act to reverse the meridional temperature gradient, further enhancing the easterly  
441 flow by thermal wind balance.
- 442 iv. When the critical surface is close to the tropopause, planetary wave activity is  
443 essentially prohibited from entering the polar stratosphere. Radiative cooling to  
444 space then acts to cool the polar stratosphere and the vortex reforms over a period  
445 of approximately 2-4 weeks.

446 This mechanism considers the effect of planetary waves on the zonal-mean flow.  
447 However, it has been observed that SSWs generally occur as either a split or dis-  
448 placement of the vortex, mostly depending (though not exclusively; see Section 3.1,  
449 [Waugh, 1997]) on whether wave-2 or wave-1 activity is dominant. An example of  
450 each of these events is shown in Figure 2.4. Charlton and Polvani [2007] and Matthew-  
451 man et al. [2009] studied the dynamics of these two types of events in reanalysis data  
452 and noted some differences. Most significantly, split vortex events were observed to  
453 occur near-barotropically, with two smaller vortices centred over Canada and Siberia  
454 throughout the depth of the stratosphere. On the other hand, displaced vortex events  
455 were observed to be more baroclinic, starting first in the upper stratosphere with a  
456 vortex centred over Canada, the centre of which rotates westward with height and is  
457 centred over Siberia in the lower stratosphere.

458 This different behaviour of split and displaced vortex events is not accounted for by  
459 the Matsuno [1970, 1971] model above, and so may suggest that other mechanisms  
460 are important in the generation of SSWs. For instance, O'Neill and Pope [1988] and  
461 Scott and Dritschel [2006] have suggested that SSWs can be generated by a cyclone-  
462 anticyclone interaction between the Aleutian high and the polar vortex. These studies

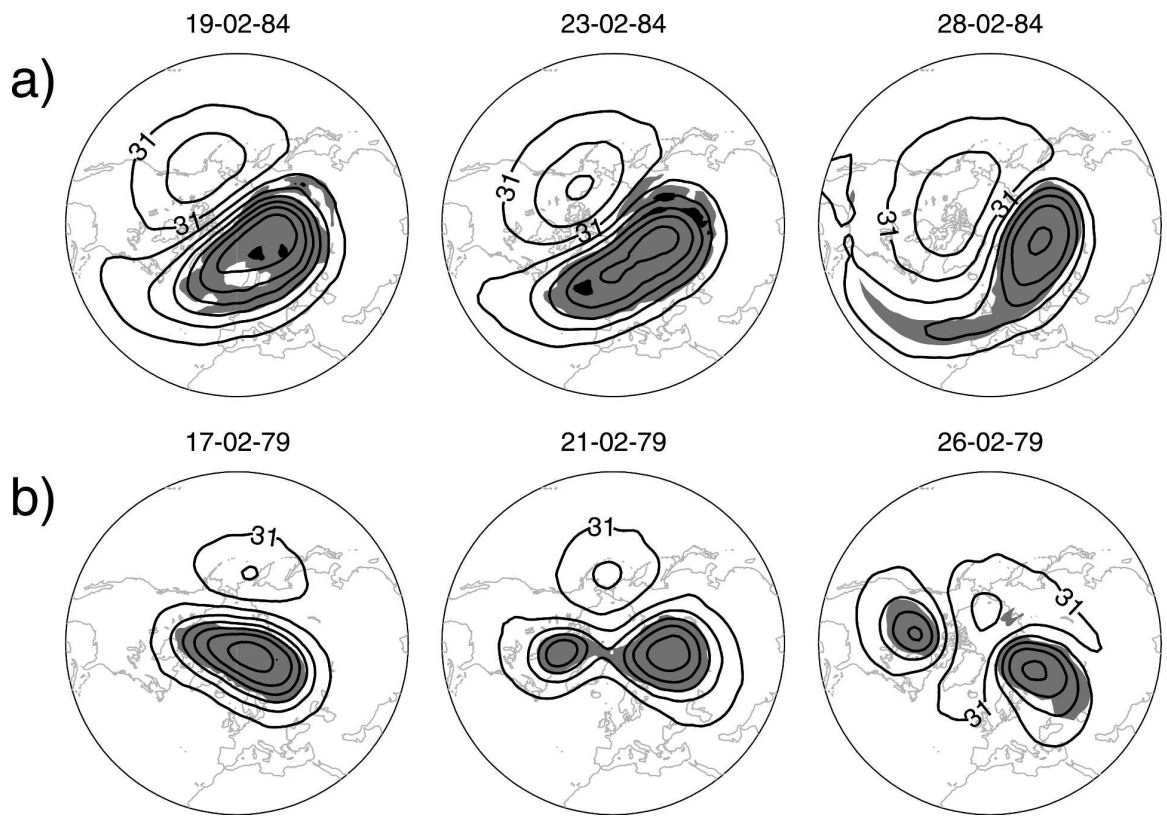


**Figure 2.4:** Polar stereographic plot of geopotential height (contours) on the 10 hPa pressure surface. Contour interval is 0.4 km, and shading shows potential vorticity greater than  $4.0 \times 10^{-6} \text{ K kg}^{-1} \text{ m}^2 \text{ s}^{-1}$ . (a) A vortex displacement type warming that occurred in February 1984. (b) A vortex splitting type warming that occurred in February 1979. Figure from [Charlton and Polvani \[2007\]](#).

## 2.2. POLAR STRATOSPHERIC OZONE DEPLETION

463 showed that a smaller anticyclone can act to significantly distort the polar vortex, al-  
464 though such interactions are greatest for circulation ratios higher than are typically  
465 found in the polar stratosphere. Other studies have suggested that SSWs can arise  
466 through the resonant excitation of normal modes of the stratosphere by planetary  
467 waves [Tung and Lindzen, 1979]. Significantly, Plumb [1981] found that the planetary  
468 wave forcing need not be at exactly the resonant frequency of the mode (an occur-  
469 rence which is probably unlikely), but that the two can be brought to resonance by a  
470 process known as nonlinear “self-tuning”. Smith [1989] found behaviour suggestive of  
471 this process in simulations of a SSW. More recently, Esler and Scott [2005] and Esler  
472 et al. [2006] suggested that a relevant mode in the case of split vortex events is the  
473 barotropic mode of the atmosphere, which may explain the more barotropic nature of  
474 split vortex events.

475 Further weight is given to these mechanisms which do not rely on strong transient  
476 tropospheric forcing by the occurrence of the 2002 SH SSW, since this forcing is much  
477 weaker in the SH (several studies of the dynamics of this event can be found in the  
478 March 2005 special issue of *Journal of Atmospheric Sciences*). Indeed, Esler et al. [2006]  
479 provided evidence that this event may have been influenced by resonant excitation of  
480 the barotropic mode.

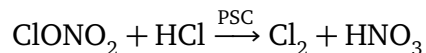
481 Overall, while significant advances in understanding the dynamics of SSWs have  
482 been made, several uncertainties remain. While tropospherically-driven wave activity  
483 is certainly an important factor, the roles (if any) of cyclone-anticyclone interactions or  
484 resonance are less certain. Moreover, it is not clear whether different mechanisms may  
485 be more or less important in driving split and displaced vortex events.

## 486 2.2 Polar stratospheric ozone depletion

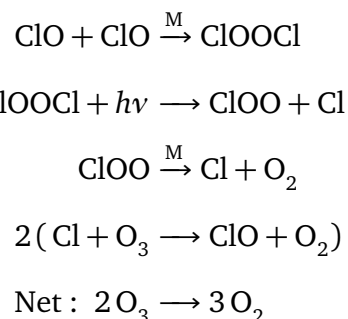
487 The Antarctic ozone hole is a large region of severely depleted ozone concentrations  
488 in the lower-mid stratosphere which occurs during the austral spring. During its for-  
489 mation ozone is often completely destroyed at some altitudes. A similar, but much

490 smaller depletion is observed in the NH [e.g., *Manney et al.*, 1997]. Following its dis-  
 491 covery by *Farman et al.* [1985], a chemical and dynamical theory of the ozone hole was  
 492 rapidly developed which largely attributes this rapid ozone depletion to the presence  
 493 of anthropogenic chlorofluorocarbon (CFC) compounds [*McElroy et al.*, 1986; *Solomon*  
 494 *et al.*, 1986]. This theory is summarised as follows:

- 495 i. The strong zonal winds of the stratospheric polar vortex act to confine air over  
 496 the polar regions, with little mixing with midlatitudes [*Schoeberl and Hartmann*,  
 497 1991]. This results in a region of very cold temperatures which allow the forma-  
 498 tion of polar stratospheric clouds (PSCs; these require temperatures below approx-  
 499 imately 195 K to form [*Newman*, 2010]).
- ii. Heterogeneous chemical reactions can take place on the surface of PSCs which act  
 to convert ‘reservoir’ chlorine species such as ClONO<sub>2</sub> and HCl into forms that can  
 accelerate ozone depletion, for instance [*Solomon et al.*, 1986]:



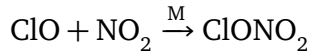
- iii. As sunlight returns to the vortex region in spring, Cl<sub>2</sub> is rapidly photolysed and  
 reacts with oxygen to form ClO. This can then catalytically destroy ozone through  
 a reaction sequence such as the following suggested by *Molina and Molina* [1987]:



500 where  $\nu$  is the frequency of light,  $h$  is Planck’s constant, and M a third body (nec-  
 501 essary for conservation of momentum). Several other reaction sequences are also  
 502 possible, for instance involving Bromine species.

## 2.2. POLAR STRATOSPHERIC OZONE DEPLETION

iv. A further effect of PSCs is that their particles fall out of the stratosphere and thereby remove nitrogen compounds ( $\text{NO}_x$ ) from the polar lower stratosphere [Toon *et al.*, 1986].  $\text{NO}_x$  compounds are important because they can react with ClO to form reservoir compounds. For instance the reaction



removes ClO from the ozone-depleting sequence above. Hence a reduction of  $\text{NO}_x$  due to PSCs leads to an increase in ozone depletion.

v. After some time, radiative heating of the stratosphere is sufficient to prevent the formation of PSCs, so ozone depletion halts. This heating is further accelerated by the increased wave breaking in the polar stratosphere which can take place as the vortex weakens (due to the Charney-Drazin criterion) and thereby induce an enhanced residual circulation. Following the final breakdown of the vortex and transition to summer easterlies (final warming), the ozone-depleted air is mixed to lower latitudes.

Importantly, the stratospheric dynamics described in Section 2.1, play an important role in ozone depletion. As discussed in Section 2.1.2.1, wave breaking in the stratosphere acts to drive a residual circulation, with descent and adiabatic warming over the pole. Enhanced descent and warming over the pole acts to inhibit the formation of PSCs which are necessary for the above heterogeneous chemical reactions which cause ozone depletion. A stronger meridional circulation also acts to transport more tropical ozone-rich air to the polar regions, further acting to increase ozone concentrations. Another mechanism in which wave breaking acts to inhibit ozone depletion is by actively stripping away filaments of ozone-depleted air from the polar vortex [Waugh *et al.*, 1994]. It is this greater wave activity in the NH then that explains why the extent of ozone depletion is much less in the NH than the SH.

In the extreme event of SSWs, the ozone hole can be severely disrupted. This can be seen in Figure 2.5, where a clear split of the ozone hole is visible during the 2002 SH SSW, which contrasts with the more zonally symmetric distributions seen at the same

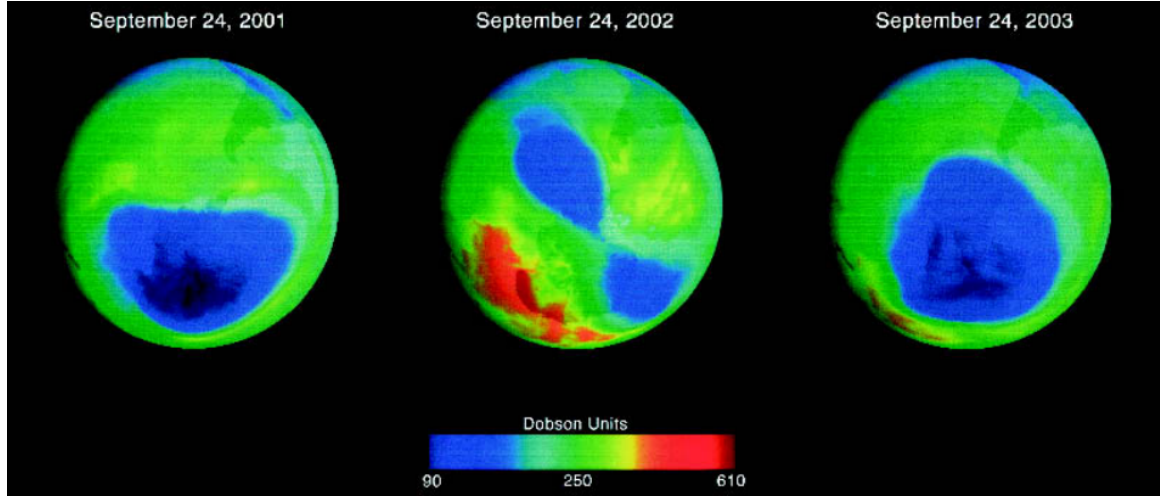


**Figure 2.5:** Comparison of the (middle) first split ozone hole on record (2002) and (left) the Antarctic ozone hole at the same time one year earlier (2001) and (right) one year later (2003). The hole is dark blue and magenta. In 2001, the ozone layer thinning over Antarctica reached  $26.5 \times 10^6 \text{ km}^2$ , larger than the size of the entire North American continent. Due to higher Antarctic winter temperatures, the 2002 “hole” seems to be about 40% smaller. In 2003, Antarctic winter temperatures returned to normal and the ozone hole returned to its usual state. Figure from *Shepherd et al.* [2005].

526 times in 2001 and 2003. The magnitude of the 2002 ozone hole can also be seen to  
 527 be reduced; a result of an enhanced residual circulation causing warmer stratospheric  
 528 temperatures. The importance of this link between dynamics and chemistry for pre-  
 529 dicting interannual variability in ozone depletion is discussed further in Sections 5.4.2  
 530 and 5.5.

### 531 2.3 Annular modes

532 Before discussing the influence of the stratosphere on the troposphere, it is necessary to  
 533 introduce the concept of the annular modes which are often analysed in studies on this  
 534 topic (as well as in this thesis). The northern and southern annular modes (NAM and  
 535 SAM) are the leading modes of large-scale variability in the two hemispheres [*Baldwin*  
 536 and *Dunkerton*, 1999; *Thompson and Wallace*, 2000; *Thompson et al.*, 2000; *Limpasuvan*  
 537 and *Hartmann*, 1999, 2000]. They are commonly defined to be the leading empirical

### 2.3. ANNULAR MODES

orthogonal function (EOF)<sup>10</sup> of extratropical monthly-mean geopotential height calculated at each pressure surface [e.g., *Baldwin and Dunkerton*, 1999], with an index of the respective principal component or the projection of daily data onto the EOF pattern. *Baldwin and Thompson* [2009] introduced an alternative using zonal-mean geopotential height, which is therefore less computationally expensive to calculate. The annular modes at the surface are also often calculated from mean sea-level pressure [e.g., *Gong and Wang*, 1999], where they may also be referred to as the Arctic and Antarctic oscillation (although in this thesis, the terms ‘surface NAM/SAM’ are used).

Figure 2.6 shows linear regressions of zonal-mean geostrophic winds and lower tropospheric geopotential height on the NAM and SAM indices as defined by *Thompson and Wallace* [2000]. It can be seen that the near-surface NAM structure is more zonally asymmetric than the SAM, with centres of action located over the Atlantic and Pacific oceans, and the SAM has a more clearly ‘annular’ structure. The vertical structure of the NAM and SAM appears near barotropic, although with a slight poleward tilt with height.<sup>11</sup> The magnitude of the zonal wind signature also increases with height, reaching a maximum in the upper troposphere/lower stratosphere in the SH, and the mid-stratosphere in the NH.

Despite this near-barotropic appearance, annular mode variability has quite different physical interpretations in the troposphere and stratosphere. Stratospheric variability is associated with approximately zonally symmetric strengthening and weakening of the stratospheric polar vortex, while tropospheric variability is more closely associated with meridional shifts in the eddy-driven jets [*Limpasuvan and Hartmann*, 1999]. Furthermore, stratospheric annular mode variability is largely confined to winter, while tropospheric variability has a much less pronounced seasonal cycle.

It can be seen from Figure 2.6(d) that the Atlantic centre of action of the NAM resembles the familiar North Atlantic Oscillation (NAO) pattern. Indeed, the surface NAM and NAO have been observed to be highly correlated [*Ambaum et al.*, 2001].

<sup>10</sup>EOFs are the eigenvectors of the spatially weighted covariance matrix of a variable. EOF analysis is also known as principal component analysis [*Wilks*, 2006].

<sup>11</sup>*Thompson and Woodworth* [2014] have recently argued that the barotropic and baroclinic aspects of the SAM can be viewed as two independent modes of variability.

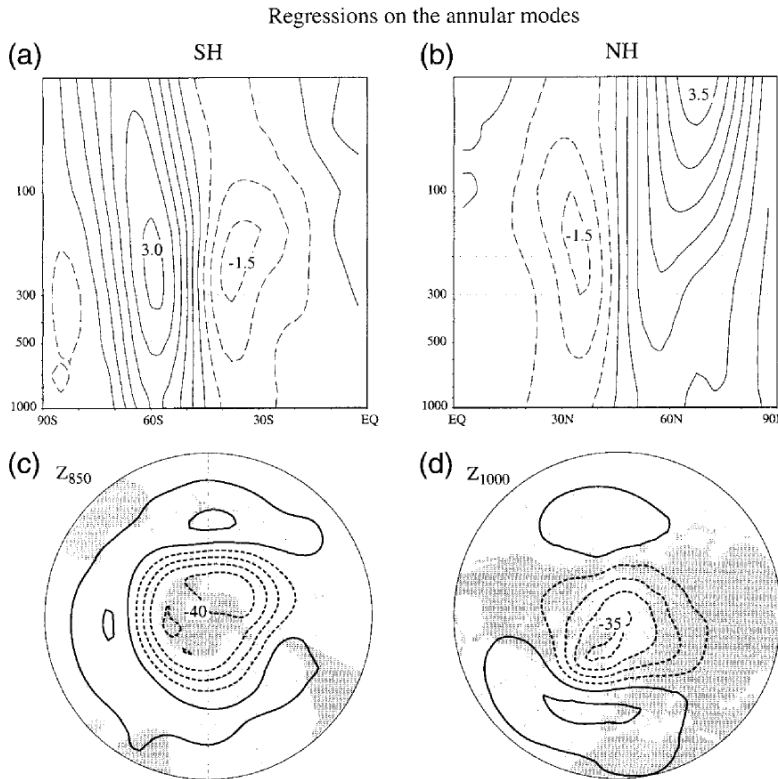


**Figure 2.6:** (top) Zonal-mean geostrophic wind and (bottom) lower-tropospheric geopotential height regressed on the standardised indices of the annular modes (the AO and its SH counterpart) based upon monthly data, Jan 1958–Dec 1997. Left panels are for the SH, right panels are for the NH. Units are  $\text{m s}^{-1}$  (top) and  $\text{m per std dev of the respective index time series}$  (bottom). Contour intervals are 10 m ( $-15, -5, 5, \dots$ ) for geopotential height and 0.5  $\text{m s}^{-1}$  ( $-0.75, -0.25, 0.25$ ) for zonal wind. Figure from *Thompson and Wallace [2000]*.

565 This has led to some debate as to whether the NAM represents a physical mode of  
 566 variability of which the NAO is just a regional manifestation, or whether the NAM  
 567 is simply a statistical artifact of more regional variability. This point is addressed in  
 568 Section 4.4.2.

## 569 2.4 Stratosphere-troposphere coupling

570 So far this chapter has dealt with the dynamics of the stratosphere as responding pas-  
 571 sively to tropospheric forcing from below. Indeed, this was the dominant view until  
 572 the last two decades [e.g., *Andrews et al., 1987*]. However observational evidence sup-  
 573 ported by modelling studies and some theoretical arguments, have now provided evi-

574 dence that variability of the polar stratosphere can significantly influence tropospheric  
 575 weather and climate. This section reviews this evidence.

### 576 2.4.1 Observational evidence

577 The accumulation of observational evidence for a two-way dynamical link between the  
 578 polar stratosphere and the troposphere began in the early 1990s. *Kodera et al.* [1990]  
 579 found that the strength of the NH upper stratospheric polar vortex during December  
 580 was correlated with the strength of the tropospheric eddy-driven jet in February. How-  
 581 ever, they did not investigate the mechanism for this relation, and suggested it may  
 582 be radiative. Further evidence was provided by *Nigam* [1990] who found barotropic  
 583 and baroclinic modes of the zonal-mean zonal wind which vary coherently in the tro-  
 584 posphere and stratosphere. This analysis was extended by *Baldwin et al.* [1994] who  
 585 found significant correlations between stratospheric and tropospheric EOFs of daily  
 586 NH geopotential height (patterns which would now be referred to as annular modes).  
 587 However, they found that the strongest correlations occurred with the troposphere  
 588 leading, and while suggesting that the stratosphere may exert some influence on the  
 589 troposphere, they concluded that the direction of causality was mostly upwards.

590 These studies were followed by several others which looked at the co-variability  
 591 of the stratospheric and tropospheric annular modes, and demonstrated links between  
 592 the strength of the polar vortex and surface temperature and sea level pressure pat-  
 593 terns [*Perlitz and Graf*, 1995; *Thompson and Wallace*, 1998; *Baldwin and Dunkerton*,  
 594 1999]. However, it was *Baldwin and Dunkerton* [2001] who first demonstrated that  
 595 the stratosphere-troposphere link is particularly strong following extreme weakenings  
 596 or strengthenings of the stratospheric polar vortex. Figure 2.7 shows a time series of the  
 597 NAM during the winter of 1998–1999, which includes two such weak vortex events (in  
 598 December and February), characterised by a negative stratospheric NAM (these events  
 599 are highly correlated with SSWs). It is apparent that the NAM signal appears to de-  
 600 scend in the case of the latter event (but not the former) and consistent anomalies  
 601 remain in the troposphere for approximately one month. This timescale is much longer  
 602 than the usual timescales of tropospheric NAM variability [e.g., *Simpson et al.*, 2011]

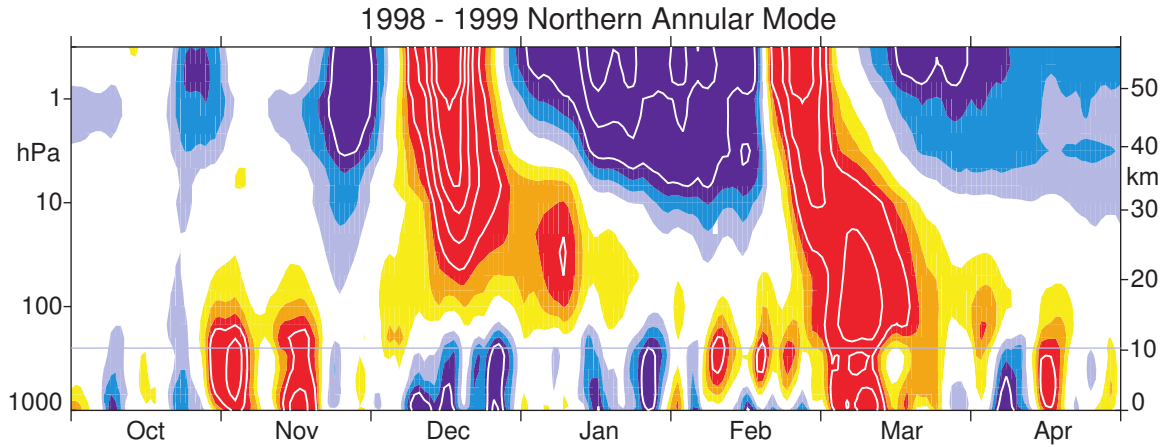


**Figure 2.7:** Time-height development of the northern annular mode during the winter of 1998–1999. The indices have daily resolution and are nondimensional. Blue corresponds to positive values (strong polar vortex), and red corresponds to negative values (weak polar vortex). The contour interval is 0.5, with values between –0.5 and 0.5 unshaded. The thin horizontal line indicates the approximate boundary between the troposphere and the stratosphere. Figure from *Baldwin and Dunkerton [2001]*.

603 but is more representative of the time taken for the stratosphere polar vortex to recover  
 604 following a SSW.

605 Most observational studies of stratosphere-troposphere coupling have focused on  
 606 the NH because of the greater stratospheric variability there. However, *Thompson and*  
*607 Solomon [2002]* argued that a long-term strengthening of the SH stratospheric po-  
 608 lar vortex resulting from ozone depletion may be causing trends in the tropospheric  
 609 SAM through a dynamical link. This was supported by *Thompson et al. [2005]*, who  
 610 performed an analysis similar to *Baldwin and Dunkerton [2001]*, finding long-lived tro-  
 611 pospheric SAM anomalies following strengthenings and weakenings of the SH strato-  
 612 spheric polar vortex (although these have a much smaller magnitude to the NH equiv-  
 613 alents). They also found a strong tropospheric SAM signal following the 2002 SH SSW.

614 More recent studies of tropospheric anomalies following stratospheric events have  
 615 focused on more localised extreme weather events in addition to the annular modes.  
 616 Several such studies have found associations between weakenings of the NH strato-  
 617 spheric polar vortex and an increased likelihood of extreme cold events over North  
 618 America, northern Europe and eastern Asia [*Thompson et al., 2002; Kolstad et al.,*

619 2010; *Tomassini et al.*, 2012]. These extreme cold events are often linked with per-  
 620 sistent ‘blocking’ weather patterns,<sup>12</sup> and a number of studies have investigated the  
 621 association between stratospheric variability and blocking. Although *Taguchi* [2008]  
 622 found no statistically significant change in blocking frequency during periods before  
 623 or after SSWs, several studies have asserted an upwards link, with blocking events  
 624 preceding a weakened polar vortex [*Quiroz*, 1986; *Andrews et al.*, 1987; *O’Neill et al.*,  
 625 1994]. More recent studies have further investigated whether blocking in particular  
 626 locations precedes split or displaced vortex events, although these have reached con-  
 627 flicting conclusions [*Martius et al.*, 2009; *Woollings et al.*, 2010; *Castanheira and Bar-*  
 628 *riopedro*, 2010]. A downwards link between stratospheric variability and the likelihood  
 629 of blocking events was suggested by *Kodera and Chiba* [1995]. *Woollings et al.* [2010]  
 630 and *Davini et al.* [2014] have recently found more evidence for this link, including  
 631 stratosphere-leading relationships between stratospheric variability and high-latitude  
 632 blocking which may be associated with the stratospheric impact on the tropospheric  
 633 NAM. Overall however, the nature of link between stratospheric variability and block-  
 634 ing remains uncertain and is a topic of active research.

635 It has been observed that some SSW events, while appearing to have similar magni-  
 636 tudes in the stratosphere, have very different signatures in the troposphere [e.g., *Bald-*  
 637 *win and Dunkerton*, 2001; *Tomassini et al.*, 2012] (See also the two events shown in  
 638 Figure 2.7). This issue was addressed by *Nakagawa and Yamazaki* [2006] and *Mitchell*  
 639 *et al.* [2013], who compared tropospheric anomalies following SSWs dominated by  
 640 wave-1/wave-2 activity and displaced/split vortex events respectively (these two clas-  
 641 sifications are related but not identical: e.g., *Waugh* [1997], Section 3.1). These studies  
 642 found stronger stratospheric anomalies following wave-2/split vortex SSWs than fol-  
 643 lowing wave-1/displaced vortex SSWs.<sup>13</sup> This result is illustrated in Figure 2.8, which

<sup>12</sup>These are characterised by a persistent anticyclonic anomaly that causes a reversal in the upper-tropospheric meridional gradient of a quantity such geopotential height [e.g., *Tibaldi and Molteni*, 1990].

<sup>13</sup>Using the method developed in Chapter 3, of the two weak vortex events illustrated in Figure 2.7, the first is identified as a displaced vortex event and the second as a split vortex event. Their tropospheric NAM may therefore be expected to be different, although no firm conclusions should be reached from the study of just two events.

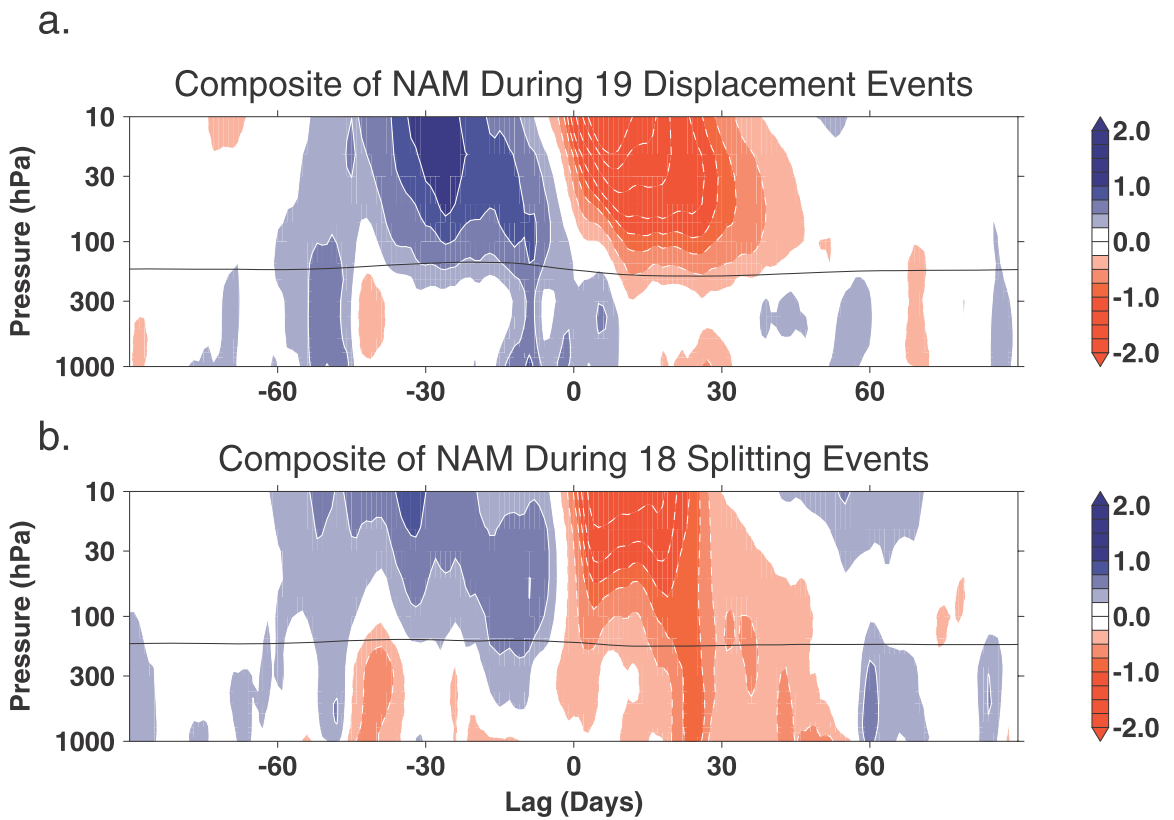


**Figure 2.8:** Composites of the time–height evolution of the NAM during (a) 19 vortex displacement events and (b) 18 splitting events. The horizontal line is a composite of the thermal tropopause level for the two types of event. Lag 0 shows the onset of an event as measured at 10 hPa. Contour intervals are 0.25 and the region between  $-0.25$  and  $0.25$  is unshaded. Figure from [Mitchell et al. \[2013\]](#).

## 2.4. STRATOSPHERE-TROPOSPHERE COUPLING

644 shows composites of the NAM following the split and displaced vortex events identi-  
645 fied by *Mitchell et al.* [2013]. It can be seen that tropospheric anomalies are stronger  
646 following split vortex events and persist for up to two months, while the NAM signal  
647 following displaced vortex events appears not to descend below the tropopause even  
648 though its stratospheric magnitude is greater. *Mitchell et al.* [2013] went on to link  
649 these different NAM signals to an increase in high-latitude blocking following split vor-  
650 tex events, and a weaker blocking signal following displaced vortex events. On the  
651 other hand *Charlton and Polvani* [2007], using a different classification method, found  
652 little difference in the tropospheric signals following split and displaced vortex events.  
653 This discrepancy between these studies highlights the importance of the classification  
654 method of split and displaced vortex events (or of tropospheric variability); an issue  
655 which is addressed in Chapter 3.

656 It is not only mid-winter stratospheric variability which has been suggested to influ-  
657 ence tropospheric weather. *Hardiman et al.* [2011] found differences in NH springtime  
658 sea-level pressure anomalies following two types of stratospheric final warming; more  
659 radiatively driven final warmings where the transition to easterlies happens first in the  
660 upper stratosphere and descends with time, and more dynamically driven final warm-  
661 ings where the transition to easterlies happens first in the midstratosphere.

662 A significant limitation of the above observational studies, which employ composite  
663 or correlation analysis, is that they cannot in themselves demonstrate *causality*. For  
664 example, there may be the possibility that a third factor (such as sea-surface temper-  
665 atures) affects both the troposphere and stratosphere separately. To address this, a  
666 number of modelling studies have been carried out which measure the tropospheric  
667 response to some imposed stratospheric perturbation. These are described in the next  
668 section.

### 669 2.4.2 Modelling evidence

670 Modelling investigations into a possible stratospheric influence on the troposphere pre-  
 671 date the observational evidence described above. In a general circulation model (GCM)  
 672 study, *Boville* [1984] showed that changes to upper tropospheric and lower strato-  
 673 spheric zonal mean zonal winds have a significant effect on mid-troposphere wave  
 674 fields, although the wind changes imposed in his model were larger than those in  
 675 reality. Using more realistic wind variations, *Jacqmin and Lindzen* [1985] found the  
 676 troposphere to be largely insensitive to changes in the state of the stratosphere. How-  
 677 ever, several more recent studies using models with a more realistic representation of  
 678 stratospheric dynamics, have found a consistent tropospheric response to an imposed  
 679 stratospheric torque [e.g., *Polvani and Kushner*, 2002; *Norton*, 2003; *Taguchi*, 2003].  
 680 This tropospheric response is found to resemble the negative phase of the NAO or NAM  
 681 following a weakening of the vortex, and as such is consistent with the observational  
 682 results discussed in the previous section.

683 Figure 2.9 shows the results from another such study by *Jung and Barkmeijer* [2006],  
 684 who imposed a weakening of the stratospheric polar vortex using an adjoint method.  
 685 Differences of zonal-mean zonal wind at four time periods following the imposition of  
 686 this forcing are shown for the composite of 60 forecasts. It can be seen that anomalies  
 687 are initially confined to the stratosphere but descend to the troposphere after approxi-  
 688 mately 20 days. *Jung and Barkmeijer* [2006] also found surface anomalies associated  
 689 with this forcing to resemble the negative phase of the NAO, though with the southern  
 690 node shifted slightly eastwards. Interestingly, they found an almost opposite surface  
 691 response when a strengthening of the stratospheric polar vortex was imposed. This in-  
 692 dicates that the surface response may be linear, potentially providing some information  
 693 about the mechanism responsible for the response, as discussed in the next section.

694 This tropospheric response to an imposed torque was shown to also operate on long  
 695 time scales by *Scaife et al.* [2005a]. They found that when a long-term acceleration of  
 696 the stratospheric polar vortex was imposed from the 1960s–1990s, in line with obser-  
 697 vations, their model more faithfully reproduced the long-term trend towards a more

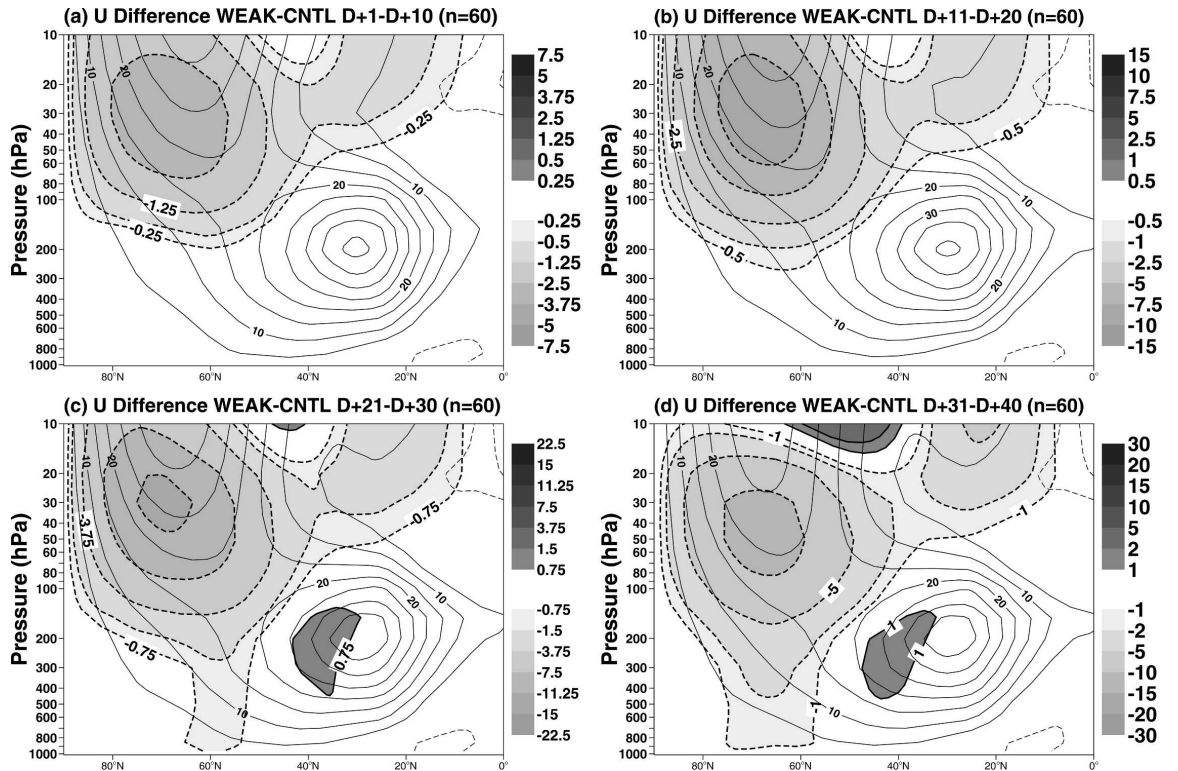


**Figure 2.9:** Difference of average zonal-mean zonal winds (shading in  $\text{m s}^{-1}$ ) between the weak polar vortex (WEAK) and the control experiment (CNTL) for 10-day averages: (a) D +1 to D +10, (b) D +11 to D +20, (c) D +21 to D +30, and (d) D + 31 to D +40. Shown is the average over 60 different cases (40-day integrations). Notice that the contour interval for the differences changes linearly with the forecast range. Also shown are zonal-mean zonal winds from the control integration (contour interval is  $5 \text{ m s}^{-1}$ ). Figure from [Jung and Barkmeijer \[2006\]](#).

698 positive phase of the NAO over this time. It is however, important to note that this does  
 699 not necessarily imply that stratospheric changes were driving the trend in reality.

700 In contrast to the studies above, which have calculated the tropospheric response  
 701 to an imposed stratospheric forcing, *Simpson et al.* [2011] removed the stratospheric  
 702 influence by damping the polar stratosphere to a climatological seasonal cycle. In  
 703 doing so, they found that the effect of the stratosphere is to lengthen SAM timescales<sup>14</sup>  
 704 during the austral late spring/early summer, and to lengthen NAM timescales during  
 705 the boreal winter-spring.

706 A criticism of studies with an imposed damping or torque is that they may not be  
 707 simulating a balanced, realistic, or physical state (for instance, the imposed torque  
 708 may not conserve angular momentum). As such, several studies have taken place us-  
 709 ing free-running GCMs. *Plumb and Semeniuk* [2003] found using a simple free-running  
 710 stratosphere-only model that descending annular mode-like signals of the kind shown  
 711 in Figure 2.7 can be simulated only by changing the forcing at the lower boundary.  
 712 They therefore conclude that observations of this kind do not necessarily indicate a  
 713 downwards influence from the stratosphere. However, *Gerber et al.* [2008] undertook  
 714 a similar study, comparing relatively simple GCM simulations with varying representa-  
 715 tions of the stratosphere. They altered the strength and variability of the stratospheric  
 716 polar vortex independently of the troposphere by varying the stratospheric lapse rate,  
 717 finding that simulations with a more variable polar vortex also had longer timescales  
 718 of the tropospheric NAM (a result similar to that of *Simpson et al.* [2011], although  
 719 using a free-running model). This lengthened timescale, in turn, was related to the  
 720 long-lived tropospheric anomalies following SSWs. Using the same model, *Gerber et al.*  
 721 [2009] performed a series of ensemble forecasts of model-simulated SSW events. They  
 722 compared events in which the initial tropospheric NAM was negative and positive,  
 723 finding a negative NAM to be much more likely following the SSW event in both cases.  
 724 Hence, they conclude that the stratosphere does indeed exert a significant downwards  
 725 influence on the troposphere in their model.

---

<sup>14</sup>The SAM/NAM timescale is defined as the lag (in days) for its autocorrelation to fall by  $1/e$ .

A further class of model investigation has been to compare models with a well-resolved stratosphere with models with a coarser stratospheric resolution; known as ‘high-top’ and ‘low-top’ models respectively [Huebener *et al.*, 2007; Sigmond *et al.*, 2008; Cagnazzo and Manzini, 2009; Sassi *et al.*, 2010; Scaife *et al.*, 2011a; Charlton-Perez *et al.*, 2013] (discussed in greater detail in Section 4.1). These have all indicated a more realistic representation of tropospheric variability and long-term trends is achieved with improved vertical resolution. Additionally, in a case study of the cold European winter 2005–2006, Scaife *et al.* [2008] found increased blocking activity in a model with greater stratospheric resolution. On the other hand, in a multi-model comparison of blocking, Anstey *et al.* [2013] found a stronger relationship between blocking frequency and upper-troposphere/lower-stratosphere vertical resolution than with model lid height. Overall, large biases remain in models’ representation of blocking. A difficulty of these studies is that there are often several differences between high- and low-top models besides their vertical resolution (such as their parametrisation schemes), so it is difficult to pin down any differences between the simulations to a stratospheric influence alone. Hardiman *et al.* [2012a] attempted to address this issue by comparing model simulations which differ only in their vertical resolution above 15 km. They found the climatology and trends of surface temperature to be largely insensitive to the increased vertical resolution, although stronger surface anomalies following SSWs and a more realistic trend in the NAO were found in the high-top model.

Several studies have investigated the influence of the stratosphere on the skill of medium-range forecasts (also discussed in Section 5.1). These have demonstrated improvements in the medium-range predictive skill of high-top relative to low-top models [Marshall and Scaife, 2010; Roff *et al.*, 2011], and enhanced predictability when forecasts are initialised at the time of anomalously negative stratospheric NAM or SSWs [Kuroda, 2008; Mukougawa *et al.*, 2009; Sigmond *et al.*, 2013]. These studies therefore further indicate a downwards influence of stratospheric variability on the troposphere.

### 754 2.4.3 Mechanisms

755 The results described in the previous two sections provide strong evidence that the  
 756 stratosphere does indeed exert a significant influence on tropospheric weather and  
 757 climate. Even so, many uncertainties about the exact nature of the influence remain;  
 758 observational studies are always open to the criticism that they do not demonstrate  
 759 causality, and modelling studies that they contain large model biases or are simulating  
 760 an unrealistic scenario. A coherent picture of stratosphere-troposphere coupling also  
 761 requires a physical understanding of the mechanism by which this takes place. Several  
 762 such mechanisms have been proposed, and are briefly described below:

- 763 • **Radiative effects:** It is well known that stratospheric (particularly lower-stratospheric)  
 764 temperature increases following SSWs lead to increasing downwelling longwave  
 765 radiation entering the troposphere. *Ramanathan* [1977] argued that this warming  
 766 could reduce the available potential energy accessible to tropospheric eddy  
 767 activity. Similarly, the stratospheric cooling associated with ozone depletion  
 768 leads to a reduction in downwelling longwave radiation entering the troposphere  
 769 [*Forster and Shine*, 1997]. *Grise et al.* [2009] used a radiative transfer model to  
 770 assess the impact of these radiation changes, finding a significant impact on sur-  
 771 face polar temperatures, although they did not assess the circulation response.  
 772 Indeed, relatively few studies have assessed the impact of radiative processes in  
 773 stratosphere-troposphere coupling in the light of more recent observations. De-  
 774 spite this, it is unlikely that radiative effects play a large role in the observed  
 775 stratosphere-troposphere coupling since relatively realistic coupling can be simu-  
 776 lated in a model lacking interactive ozone or a detailed radiation scheme.
- 777 • **Baroclinic instability:** The growth rate of baroclinic eddies is related to the ver-  
 778 tical shear in zonal wind across the troposphere [*Eady*, 1949]. Some studies  
 779 have suggested that lower stratospheric zonal wind anomalies which penetrate  
 780 into the upper troposphere affect this vertical wind shear, and so the growth of  
 781 baroclinic eddies [*Wittman et al.*, 2007; *Chen and Zurita-Gotor*, 2008]. Hence,

## 2.4. STRATOSPHERE-TROPOSPHERE COUPLING

we may expect reduced tropospheric eddy activity at mid-high latitudes following SSWs, due to weaker lower stratosphere/upper troposphere zonal winds. *Scaife et al.* [2011a] also used this relationship to demonstrate that an increase in European winter storminess and equatorward shift in the North Atlantic storm track projected under climate change are consistent with a strengthening and equatorward shift of the stratospheric polar vortex. It is less clear what effect whether the change in baroclinic eddy activity is sufficient to lead to the annular mode signals of the kind shown in Figure 2.7, although tropospheric eddies have been demonstrated to be important in driving annular mode variability [*Limpasuvan and Hartmann*, 1999].

- **Downward control:** Under steady-state or time-mean conditions, the ‘downward control’ principle of *Haynes et al.* [1991] allows the streamfunction,  $\psi$ , of the TEM residual circulation is given by

$$\psi(\phi, z) = \int_z^{\infty} \left( \frac{\rho_0 a \bar{\mathcal{F}} \cos^2 \phi}{\partial \bar{m} / \partial \phi} \right)_{\phi=\phi(z')} dz', \quad (2.13)$$

where  $\bar{\mathcal{F}}$  is the total wave driving term from Equation 2.10, and  $\bar{m} = a \cos \phi (\bar{u} + a\Omega \cos \phi)$  is the angular momentum per unit mass. Strictly, the integration is along a line of constant angular momentum, but this is approximated as vertical (an approximation which breaks down near the equator). Hence, it can be seen that under these conditions the residual circulation at a given altitude depends only on the wave drag above that altitude.

This relation therefore shows that circulation induced by stratospheric wave drag extends to the Earth’s surface, although it should be noted above assumptions (particularly steady-state) do not strictly hold in the real atmosphere. *Thompson et al.* [2006] suggested that this induced residual circulation (or ‘balanced response’) is sufficient to explain the observed stratosphere-troposphere coupling. Others, however, have argued that the observed annular mode-like tropospheric

804 response cannot be generated in the zonal-mean framework of downward con-  
 805 trol, necessitating feedbacks involving tropospheric eddies [*Kushner and Polvani,*  
 806 *2004; Song and Robinson, 2004*].

- 807 • **Planetary wave reflection:** The critical surface formed in the stratosphere dur-  
 808 ing SSW events acts to reflect upwards-propagating planetary waves, as described  
 809 in Section 2.1.2.1. *Perlitz and Harnik [2003]* argued that these reflected plane-  
 810 tary waves re-enter the troposphere and affect the tropospheric wave structures,  
 811 leading to the observed tropospheric response. *Shaw et al. [2010]* have further  
 812 suggested that strong two-way coupling exists in the presence of both a verti-  
 813 cal reflecting surface and a strong meridional PV gradient, which act to create a  
 814 ‘wave guide’.
- 815 • **Local adjustment to PV anomalies:** Under the QG approximation, PV anomalies  
 816 ,  $q'$ , can be related to geopotential height anomalies,  $Z'$ , through

$$q' = \mathcal{L}(Z'), \quad (2.14)$$

815 where  $\mathcal{L}$  is a linear Laplacian-like operator [*Charney and Stern, 1962*]. It follows  
 816 that the geopotential anomalies (and with QG approximations, other dynamical  
 817 fields) associated with a given PV anomaly can be derived by inverting this op-  
 818 erator. The geopotential height anomalies associated with a PV anomaly can be  
 819 thought to be localised in that they decay with a typical vertical scale,  $H$ , and hor-  
 820 izontal scale,  $L$ . In the case of lower-stratospheric PV anomalies, their influence  
 821 may therefore extend to the troposphere. *Hartley et al. [1998]* and *Black [2002]*  
 822 performed such PV-inversions to calculate the tropospheric effect of stratospheric  
 823 PV anomalies. They found stratospheric PV anomalies to contribute significantly  
 824 to anomalies at the tropopause, which extend to the Earth’s surface.

825 It can be argued that PV-inversion does not constitute a ‘mechanism’ since it is not  
 826 a time-dependent relationship and does not imply a direction of causality. How-  
 827 ever, *Ambaum and Hoskins [2002]* developed a physical mechanism analogous to

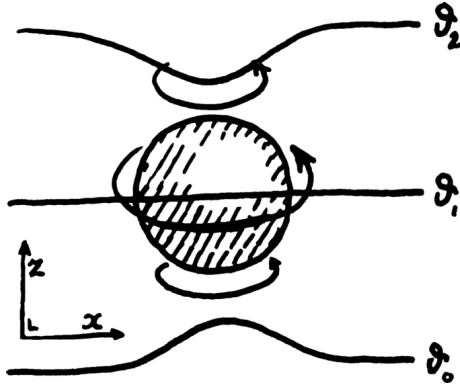


**Figure 2.10:** Schematic of the bending of isentropic surfaces (labelled  $\theta_0$ ,  $\theta_1$ , and  $\theta_2$ ) toward a positive potential vorticity anomaly. The arrows represent winds associated with the potential vorticity anomaly, becoming weaker away from the anomaly. Figure from *Ambaum and Hoskins [2002]*.

PV-inversion, as follows. Anomalies of PV act to bend isentropic surfaces [*Hoskins et al., 1985*], as illustrated in Figure 2.10. At high latitudes, the tropopause lies approximately on a potential vorticity surface, also the potential temperature of the tropopause will be conserved for adiabatic changes (Section 2.1.2.1). Hence, the tropopause will also bend in the presence of stratospheric potential vorticity anomaly; moving upwards for a positive anomaly, and downwards for a negative anomaly. This deformation of the tropopause will then lead to hydrostatic and geostrophic adjustment of the tropospheric column below, which can be thought of in terms of the conservation of angular momentum, with a stretched tropospheric column leading to an increase of vorticity and lower pressure. It is therefore be expected that a strengthening of the stratospheric polar vortex would be associated with negative sea-level pressure anomalies over the pole, and a weakening with positive pressure anomalies, which is consistent with the observed annular mode relationships (Section 2.4.1).

Importantly, *Ambaum and Hoskins [2002]* noted a stratosphere-leading time-lagged relationship between the strength of the stratospheric polar vortex, the tropopause height and the NAO, with the stratosphere acting to integrate the NAO. This therefore represents a time-dependent and causal mechanism for stratosphere-troposphere coupling.

847      The above list is not exhaustive but represents the most prominent proposed mech-  
848      anisms. It is clear that several of these mechanisms are not mutually exclusive and so it  
849      is likely that more than one is at work in the real atmosphere. Furthermore, a difficulty  
850      in distinguishing the relative importance of the different mechanisms is that they are  
851      largely consistent with observations, particularly the zonal mean response to strato-  
852      spheric variability. It is therefore important to identify situations in which mechanisms  
853      make different predictions and test these against reality and numerical simulations.

854      One such situation is in the response to zonally asymmetric stratospheric anomalies.  
855      For instance, the planetary wave reflection and downward control mechanisms are  
856      largely sensitive only to zonal-mean quantities. Hence, it might be expected that under  
857      these mechanisms the tropospheric response to two equal zonal-mean stratospheric  
858      anomalies would be the same, even if the anomalies have different zonal asymmetries.  
859      On the other hand, the tropospheric response via adjustment to PV anomalies would  
860      be expected to be local to the stratospheric anomalies.

861      It is the aim of Chapters 3 and 4 to diagnose zonally asymmetric stratospheric  
862      variability, specifically split and displaced vortex events, in observations and model  
863      simulations. Part of the motivation for this analysis is then to study the tropospheric  
864      response in order to test the relative importance of the above mechanisms.

---

## A geometrical description of vortex variability

---

Much of the work contained in this chapter is based upon *Seviour et al. [2013]*, published in *Geophysical Research Letters*, although the analysis presented here has been significantly extended.

### 3.1 Introduction

A quantitative description of stratospheric polar vortex variability is desirable for a number of reasons; it allows for the comparison of different studies, observational data sets, and model simulations, as well as permitting robust definitions of extreme events. Traditional methods to quantify vortex variability have been based on zonal-mean diagnostics, such as the zonal-mean zonal wind [e.g., *Andrews et al., 1987*]. This was motivated both by the simplicity of these diagnostics and the physical reasoning that the strength of the zonal flow controls the propagation of planetary waves [*Charney and Drazin, 1961*, Section 2.1.2]. *McInturff [1978]* provided the first quantitative definition of SSWs<sup>1</sup> (referred to in that text as “major stratospheric warmings”) using zonal mean quantities as below.

---

<sup>1</sup>In the literature, this is often called “the WMO definition”.

883        “A stratospheric warming can be said to be major if at 10 mb or below  
 884        the latitudinal mean temperature increases poleward from 60 degrees lati-  
 885        tude and an associated circulation reversal is observed (i.e., mean westerly  
 886        winds poleward of 60° latitude are succeeded by mean easterlies in the  
 887        same area).”

888        A number of variations of this definition have since appeared in the literature. Most  
 889        commonly, the temperature gradient criterion has been neglected and/or zonal wind  
 890        reversals at a particular latitude (usually 60°N) used instead of the stricter criterion of a  
 891        reversal everywhere poleward of 60°N [e.g., *Labitzke and Naujokat, 2000; Christiansen,*  
 892        *Reichler et al., 2012*].

893        Although the reversal of zonal-mean zonal wind is physically relevant for the prop-  
 894        agation of planetary waves, the choice of 60°N and 10 hPa in the definition of SSWs  
 895        is less physically significant. Indeed, different numbers of SSWs are identified if these  
 896        locations are varied. *Butler et al. [2014]* found that a greater number of events are iden-  
 897        tified if the threshold is located either equatorward or poleward of 60°N. Some studies  
 898        have aimed to avoid this sensitivity to spatial location by quantifying vortex variability  
 899        through empirical orthogonal function (EOF) analysis, using fields over a larger area.  
 900        This includes the Northern Annular Mode (NAM) (calculated either from the three-  
 901        dimensional geopotential height field [*Baldwin and Dunkerton, 2001*] or zonal-mean  
 902        geopotential height [*Baldwin and Thompson, 2009*]), EOFs of zonal wind [*Limpasuvan*  
 903        *et al., 2004*], and vertical profiles of polar cap-averaged temperature [*Kuroda, 2004*].  
 904        SSW events are then defined by a threshold in the principal component of the relevant  
 905        EOF.

906        As it has become increasingly recognised that SSWs generally occur as either split or  
 907        displaced vortex events, studies have aimed to objectively distinguish these two types  
 908        of event. Commonly this has been achieved through Fourier decomposition of the zonal  
 909        wave structure. For instance, *Nakagawa and Yamazaki [2006]* defined SSWs through  
 910        a polar temperature criterion and then split these events into two groups depending  
 911        on whether the 150 hPa Eliassen-Palm (EP) flux prior to the events was dominated by

### 3.1. INTRODUCTION

912 zonal wavenumber one or two. *Charlton and Polvani [2007]* (hereafter CP07) intro-  
913 duced a new classification method, which does not rely on Fourier decomposition; first  
914 they identified events using the traditional wind reversal at 60°N, 10 hPa criterion, then  
915 they calculated the circulation around the two largest contours of relative vorticity on  
916 the vortex edge. If these two contours have a circulation ratio of 2:1 or lower the event  
917 is classified as a split, and all other events are automatically classed as displacements.

918 Both Fourier decomposition of the zonal wave structure and the method of CP07  
919 rely on an Eulerian framework, with fields analysed at a fixed spatial location. *Waugh*  
920 [*1997*] first applied two-dimensional moment diagnostics (otherwise known as el-  
921 liptical diagnostics) to the stratospheric polar vortex to provide an alternative semi-  
922 Lagrangian (or vortex-oriented) framework. These diagnostics are calculated by fitting  
923 an ellipse to a contour and then determining its properties such as the centre, ori-  
924 entation, aspect ratio, and area (a further diagnostic, excess kurtosis—a measure of the  
925 ‘peakedness’ of the distribution—was introduced by *Matthewman et al. [2009]*). This al-  
926 lows the movement and elongation of the vortex to be quantified. *Waugh [1997]* also  
927 compared these diagnostics to the traditional Fourier decomposition. He showed that  
928 wave-1 and 2 amplitudes relate most strongly to the displacement and elongation of  
929 the vortex respectively, however, these relationships were not found to be strong, with  
930 correlations of daily values less than 0.5. These weak relationships were attributed  
931 to the fact that planetary wave propagation can be affected by changes in the merid-  
932 ional PV gradient, even if the vortex shape and location are fixed. Furthermore, the  
933 wave-1 amplitude depends to some extent on the elongation of the vortex as well as  
934 the location of the centre (and similarly for the wave-2 amplitude). He concluded that  
935 it is difficult to extract quantitative information about the shape and location of the  
936 vortex based on wave amplitudes alone, highlighting the advantages of the moment  
937 diagnostics.

938 *Hannachi et al. [2010]* then applied a hierarchical clustering algorithm to daily  
939 values of the area, centroid latitude, and aspect ratio diagnostics and found that the  
940 vortex falls preferably into three clusters corresponding to undisturbed, split, and dis-  
941 placed states. These groupings were used by *Mitchell et al. [2013]* (hereafter M13)

942 to identify split and displaced vortex events; if the vortex remained in the split or dis-  
 943 placed cluster for at least five consecutive days it was classified as the corresponding  
 944 event. Significantly, as discussed in Section 2.4.1, M13 demonstrated that split vortex  
 945 events penetrated deep into the troposphere and resulted in significant surface anom-  
 946 a lies, while anomalies associated with displaced vortex events do not descend far below  
 947 the tropopause. This is in agreement with *Nakagawa and Yamazaki [2006]* who found  
 948 tropospheric anomalies to be larger following SSWs with dominant wave 2 amplitude,  
 949 however, it contrasts with *Charlton and Polvani [2007]*, who found little difference in  
 950 the tropospheric impact of split and displaced vortex events. This highlights the poten-  
 951 tial importance of the method of classification of split and displaced vortex events in  
 952 any study.

953 In this chapter we wish to develop a method for the classification of split and dis-  
 954 placed vortex events with the following properties:

- 955     1. Based on vortex moment diagnostics.
- 956     2. Can be easily applied to a range of data sets, including climate model simulations.
- 957     3. Computationally inexpensive.

958 The motivation for the use of moment diagnostics includes their advantages in quanti-  
 959 fying the shape and location of the vortex, as noted above. This, in turn, is desirable  
 960 because the location of the vortex near the tropopause may be important for under-  
 961 standing the regional tropospheric effect of stratospheric anomalies [e.g., *Ambaum and*  
 962 *Hoskins, 2002*, Section 2.4.3]. Previous calculations of vortex moment diagnostics have  
 963 been based on the distributions of quasi-conservative tracers such as PV on isentropic  
 964 surfaces [*Mitchell et al., 2011*] or long-lived tracer (e.g., N<sub>2</sub>O) concentrations [*Waugh,*  
 965 *1997*]. These quantities have strong meridional gradients allowing for clear determi-  
 966 nation of the vortex edge [*Nash et al., 1996*]. Unfortunately, many climate models do  
 967 not output PV or tracer concentrations, and these are often computationally expensive  
 968 or impractical to calculate. As such, we wish to develop a method which uses geopo-  
 969 tential height, a variable which is output by all contemporary climate models. This

### 3.2. VORTEX MOMENT DIAGNOSTICS

effort will also allow us to test the robustness of the result of M13 regarding the different surface impacts of split and displaced vortex events using a semi-independent classification method and extended data set.

The remainder of this chapter is structured as follows. The next section introduces the necessary theoretical background for the calculation of moment diagnostics. Section 3.3 describes the methods used for the classification of split and displaced vortex events, and compares these events with those determined by M13 and CP07. Section 3.4 contrasts the surface impacts of split and displaced vortex events calculated using the new method and discusses potential mechanisms behind any differences.

## 3.2 Vortex moment diagnostics

The moments,  $M_n$ , of a one-dimensional distribution can be classified by their order,  $n$ , and provide familiar parameters. These are the area under the distribution (0th order), mean (1st order), variance (2nd order), skewness (3rd order), and kurtosis (4th order), given by

$$M_n = \int_S x^n f(x) dx, \quad (3.1)$$

where  $S$  represents the extent of the distribution,  $f(x)$ , to be integrated over. The extension of this for a two-dimensional distribution is straightforwardly

$$M_{nm} = \iint_S x^n y^m f(x, y) dx dy, \quad (3.2)$$

where the order of the moment is now defined as  $m + n$ , meaning it is possible to have different diagnostics with the same order (e.g.,  $M_{01}$ ,  $M_{10}$ ). Although these diagnostics can be further extended to three dimensions, this has been demonstrated to be highly computationally expensive [Li and Ma, 1994], and would require assumptions about the lower and upper bounds of the vortex region. We therefore calculate two-dimensional moment diagnostics for the stratospheric polar vortex on quasi-horizontal surfaces. We use two variables; geopotential height ( $f(x, y) = Z(x, y)$ ) on the 10 hPa pressure level, and potential vorticity ( $f(x, y) = q(x, y)$ ) on the 850 K potential temperature (isentropic) surface, which lies close to 10 hPa. Following Waugh [1997],

the calculation of moment diagnostics is simplified by transforming the spherical data  $q(\phi, \lambda)$  and  $Z(\phi, \lambda)$ , where  $\phi$  is latitude and  $\lambda$  longitude, to Cartesian coordinates using the polar stereographic projection

$$x = \frac{\cos \lambda \cos \phi}{1 \pm \sin \phi}, \quad y = \frac{\pm \sin \lambda \cos \phi}{1 \pm \sin \phi}, \quad (3.3)$$

where the positive sign is used in the Northern Hemisphere and negative in the Southern Hemisphere.

In order to calculate moment diagnostics for the stratospheric polar vortex we must first isolate the vortex region by defining the vortex edge. Different methods have previously been used for this calculation; *Waugh and Randel* [1999] used the mean PV at the maximum of the mean meridional PV gradient, while *Matthewman et al.* [2009] defined the vortex edge on a daily basis, using the average value of PV poleward of 45°N nine days before the onset of a SSW (their SSWs were defined by zonal-mean zonal wind reversal, as in CP07). A more complex method due to *Nash et al.* [1996], starts by transforming PV to ‘equivalent latitude’ [*Butchart and Remsberg*, 1986] coordinates, before defining the vortex edge as the position of the largest gradient in a plot of PV against equivalent latitude. This method was applied in *Mitchell et al.* [2011] to calculate the vortex edge.

None of the three methods outlined above are found to be appropriate for the present study. We wish to directly compare the PV and geopotential height-derived moments, but the methods of *Waugh and Randel* [1999] and *Nash et al.* [1996] rely on meridional gradients in PV and so may not be transferable to geopotential height. Furthermore, the method of *Matthewman et al.* [2009] is impractical because we wish to define the events from the moment diagnostics, so will not know their dates before calculation. Instead, we pick a simple definition; PV ( $q_b$ ) or geopotential height ( $Z_b$ ) on the vortex edge is defined as the value of the December-March (DJFM) mean at 60°N for the Northern Hemisphere and the June-September (JJAS) mean at 60°S for the Southern Hemisphere. This is seen to lie close to contours defined by the above methods, and results are insensitive to small changes in the latitude chosen.

Having defined the vortex edge, we extend the method [Matthewman et al. \[2009\]](#) to isolate the vortex region by introducing a transformed PV field,  $\hat{q}$ , given by

$$\hat{q}(x, y) = \begin{cases} q(x, y) - q_b & \text{if } q(x, y) > q_b, \\ 0 & \text{if } q(x, y) \leq q_b, \end{cases} \quad (3.4)$$

and similarly for geopotential height

$$\hat{Z}(x, y) = \begin{cases} Z(x, y) - Z_b & \text{if } Z(x, y) < Z_b, \\ 0 & \text{if } Z(x, y) \geq Z_b. \end{cases} \quad (3.5)$$

By substituting  $f(x, y) = \hat{q}(x, y)$  or  $f(x, y) = \hat{Z}(x, y)$  in equation 3.2 it is then possible to calculate the moment diagnostics. The zeroth order moment diagnostic,  $M_{00}$  can be used to define the ‘equivalent area’,  $A_{\text{eq}}$  [[Matthewman et al., 2009](#)], as

$$A_{\text{eq}} = \frac{M_{00}}{q_b} \quad \text{or} \quad A_{\text{eq}} = \frac{M_{00}}{Z_b}, \quad (3.6)$$

depending on whether PV or geopotential height based diagnostics are calculated. Because  $M_{00} \approx Aq$ , where  $A$  is the vortex area, the equivalent area can be considered a measure of both vortex strength and area. The first order moment diagnostic can be used to calculate the vortex centroid,

$$(\bar{x}, \bar{y}) = \left( \frac{M_{10}}{M_{00}}, \frac{M_{01}}{M_{00}} \right). \quad (3.7)$$

In order for higher order moment diagnostics to be useful, the moment equation (3.2), must be transformed to the *centralised moment* form [[Hall, 2005](#)]. This calculates moments relative to the vortex centroid, and is given by

$$J_{mn} = \iint_S f(x, y)(x - \bar{x})^n(y - \bar{y})^m dx dy. \quad (3.8)$$

Two useful parameters can be derived from the second-order centralised moment diagnostics, the vortex orientation,  $\psi$  (defined as the angle between the major axis of the ellipse and the  $x$ -axis) and the aspect ratio,  $r$  (defined as the ratio of the lengths of the major to minor axes), given by

$$\psi = \frac{1}{2} \tan^{-1} \left( \frac{2J_{11}}{J_{20} - J_{02}} \right), \quad (3.9)$$

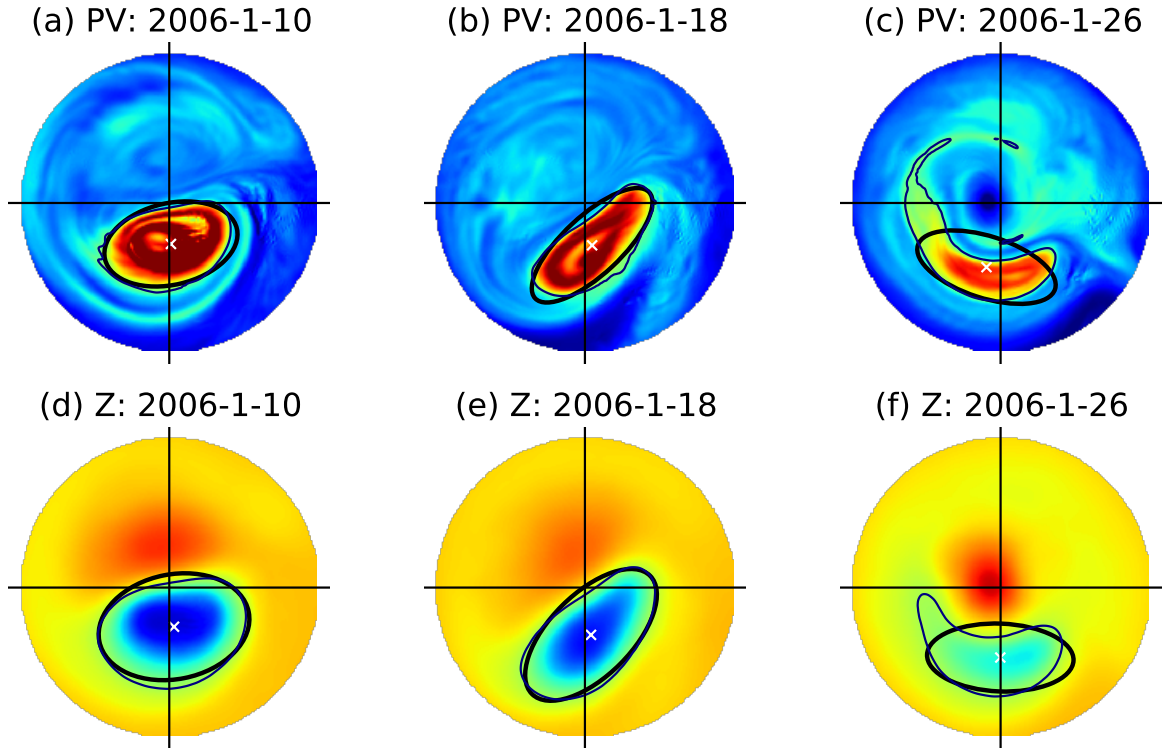


**Figure 3.1:** PV on the 850 K  $\theta$  surface (a,b,c) and geopotential height at 10 hPa (d,e,f) 8 days before (a,d), at onset (b,e), and 8 days following the onset (c,f) of a displaced vortex event. Contours of  $q_b$  and  $Z_b$  are shown in thin black lines, the equivalent ellipse in a thick dark line, and its centroid with a white cross. Data are transformed to Cartesian coordinates with a polar stereographic projection.

$$r = \left| \frac{(J_{20} + J_{02}) + \sqrt{4J_{11}^2 + (J_{20} - J_{02})^2}}{(J_{20} + J_{02}) - \sqrt{4J_{11}^2 + (J_{20} - J_{02})^2}} \right|^{1/2}. \quad (3.10)$$

Using the area, centroid, orientation, and aspect ratio, the *equivalent ellipse* can be uniquely defined. Figure 3.1 shows the equivalent ellipse calculated from both PV and geopotential height fields over a 16-day period centred on a displaced vortex event (classified using the method in Section 3.3). It can be seen that the equivalent ellipse provides a qualitatively good fit to the vortex, although this is less good in Figures 3.1(c,f) when the vortex becomes less elliptical and filamentation occurs. Greater fine-scale structure and filamentation is visible in the PV field due to its quasi-conservative properties, however reasonable agreement can be seen between the PV and geopotential height ellipses.

### 3.3. DATA AND METHODS

Equivalent ellipses for an example of a split vortex event are shown in Figure 3.2. It can be seen that after the vortex has separated the equivalent ellipse becomes less physically significant, as it spans the two vortices. *Matthewman et al.* [2009] introduced the 4th order moment diagnostic, “excess kurtosis”, in order to identify splits of the polar vortex; it is given by

$$\kappa_4 = M_{00} \frac{J_{40} + 2J_{22} + J_{04}}{(J_{20} + J_{02})^2} - \frac{2}{3} \left[ \frac{3r^4 + 2r^2 + 3}{(r^2 + 1)^2} \right]. \quad (3.11)$$

This has the property of being negative for a vortex with a “pinched” shape, zero for a perfectly elliptical vortex, and positive for a vortex with a strong central core. When negative kurtosis was detected *Matthewman et al.* [2009] split the PV field into two regions along the minor axis of the equivalent ellipse and re-calculated moment diagnostics for the vortices in these regions separately.

In this study we do not make use of the excess kurtosis or calculate separate diagnostics for split vortices for two reasons. First, as a 4th order diagnostic it is a highly skewed variable, making its use in event classification problematic (this was also found by *Hannachi et al.* [2010]). Second, this procedure is more computationally expensive, requiring about three times the number of calculations during split vortex events. Hence, we calculate single moment diagnostics even when the vortex has split, but bear in mind that these may not represent the properties of any real vortex.

Code for the calculation of moment diagnostics using the method described in this section is available from <https://github.com/wseviour/vortex-moments>. Additionally, a comparison of aspect ratio and centroid latitude with zonal wavenumber amplitudes is given in Appendix 3.A.

## 3.3 Data and methods

### 3.3.1 Reanalysis data

For the analysis in this chapter Northern Hemisphere winter daily-mean data for December–March (DJFM) are employed from the European Centre for Medium-Range Weather Forecasts (ECMWF) reanalyses. The ERA-40 data set [*Uppala et al.*, 2005] is used from

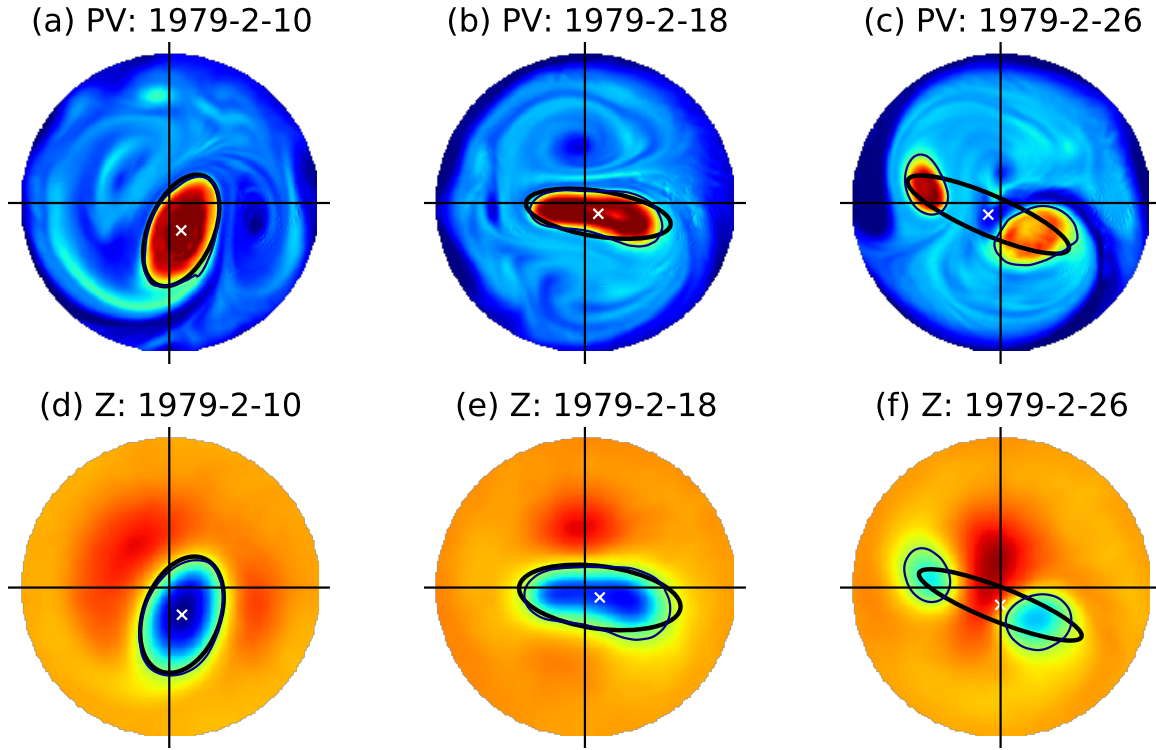


**Figure 3.2:** As Figure 3.1 but for a split vortex event.

1958-1978 and ERA-Interim [Dee et al., 2011] from 1979-2009. The combination of  
 these two data sets is chosen in order to maximise the total number of years entering  
 the analysis (ERA-40 runs only to 2002), as well as to compare results from the  
 more recent ERA-Interim with previous studies using only ERA-40, such as Charlton  
 and Polvani [2007] and Mitchell et al. [2013].

ERA-Interim is similar to ERA-40 but uses ECMWF's operational four-dimensional  
 variational data assimilation system (4D-Var) as opposed to the 3D-Var system used  
 in ERA-40. It also has higher horizontal and vertical resolution, improved humidity  
 analysis, model physics, data quality control, bias handling and other improvements  
 as noted in Simmons [2007]. The majority of observational data for the stratosphere  
 entering both reanalyses is from radiosonde and satellite measurements. It is important  
 to note that in the pre-satellite era (1958-1971) observations in the stratosphere were  
 much more sparse, leading to greater errors in reanalyses during this time [Uppala  
 et al., 2005].

### 3.3. DATA AND METHODS

A number of studies have evaluated the stratospheric circulation in ERA-40 and ERA-Interim against other observations or reanalyses. *Randel et al.* [2004] found ERA-40 to closely match measurements of the zonal stratospheric circulation derived from radiosonde, rocketsonde and lidar measurements. *Karpetchko et al.* [2005] found that the representation of the polar vortices in ERA-40 agrees well with the NCEP/NCAR reanalysis, and CP07 demonstrated that this also holds for the occurrence of SSWs. *Seviour et al.* [2012] showed that the strength of the stratospheric meridional mean stratospheric circulation in ERA-Interim agrees well with previous reanalysis, but that the residual vertical velocity is more smoothly represented.

In order to perform a consistent analysis across the two data sets, ERA-Interim data is linearly interpolated to the lower resolution ERA-40 ( $1.125^\circ \times 1.125^\circ$ ) Gaussian grid. PV is also interpolated from pressure levels to the 850 K isentropic surface (which lies close to 10 hPa), as this quantity has the property of being conserved under adiabatic flow. In the calculation of the vortex edge. Both in the calculation of the vortex edge (climatological mean  $q$  or  $Z$  at  $60^\circ\text{N/S}$ ) and the moment diagnostics themselves, no clear jumps were seen between ERA-40 and ERA-Interim data sets. As such, the two are considered together with no bias corrections. For the remainder of this thesis, this combined ERA-40 and ERA-Interim data set is referred to as ‘ERA’.

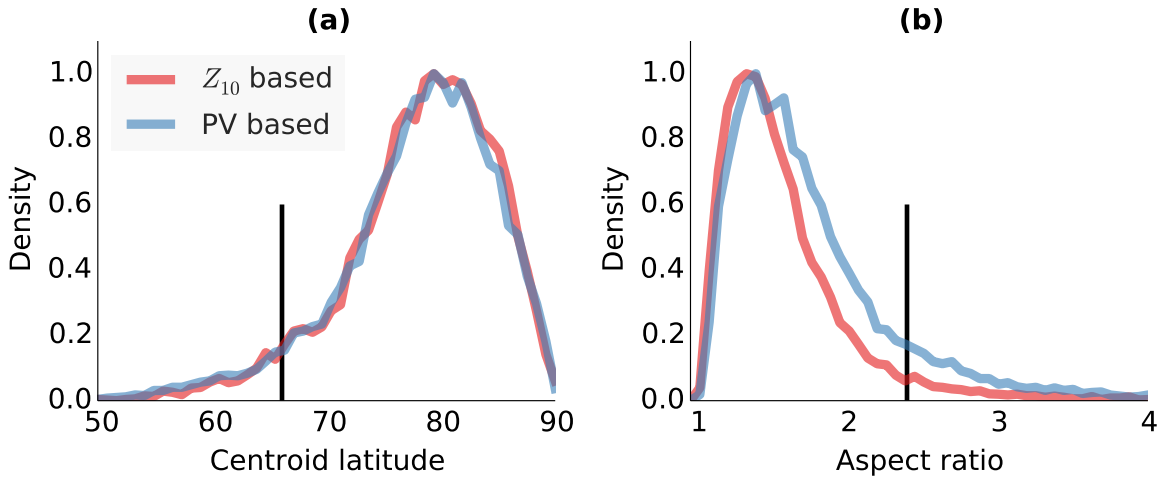
#### 3.3.2 Moment diagnostic calculation

In order to calculate the moment diagnostics, the values of PV and geopotential height on the vortex edge ( $q_b$  and  $Z_b$ ) must first be determined. These are the  $60^\circ\text{N}$  DJFM/ $60^\circ\text{S}$  JJAS mean values of PV at 850 K ( $q_{850}$ ) and 10 hPa geopotential height ( $Z_{10}$ ) respectively. They are found to be  $q_b = 460$  PVU (1 PVU =  $10^{-6}\text{Km}^2\text{kg}^{-1}\text{s}^{-1}$ ) and  $Z_b = 30.2$  km for the Northern Hemisphere, and  $q_b = 618$  PVU and  $Z_b = 29.0$  km for the Southern Hemisphere. Using these values the moment diagnostics are calculated from ERA data for 1958–2009 using the method described in Section 3.2.

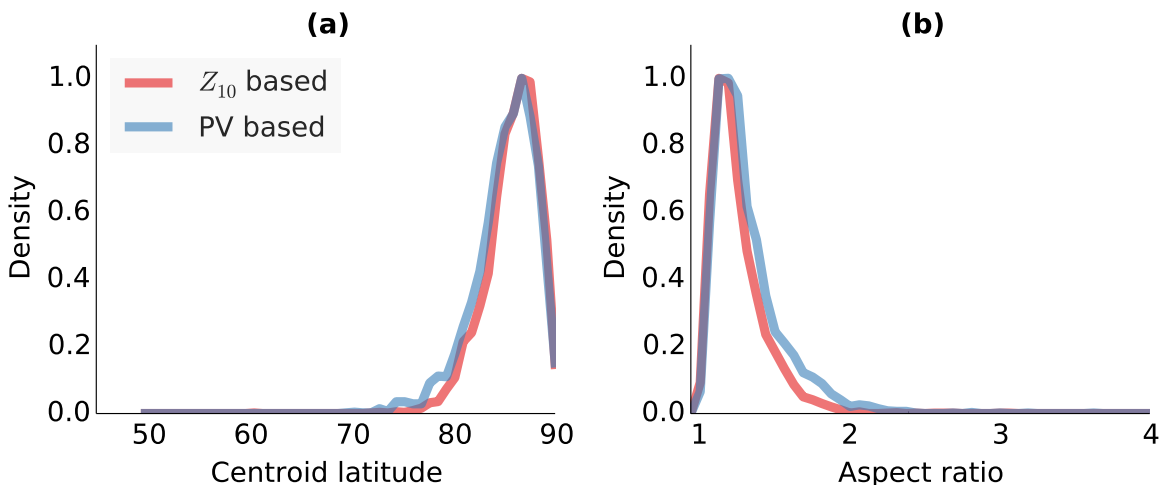
As discussed in Section 3.2 the excess kurtosis diagnostic is not used in the present analysis. In the interests of simplicity, only the aspect ratio and centroid latitude diagnostics are used to identify events, and the centroid longitude, orientation and equivalent area are not used. The aspect ratio and centroid latitude are the most intuitive diagnostics for this purpose, with a high aspect ratio and poleward centroid latitude expected during split vortex events, and a low aspect ratio and equatorward centroid latitude expected during displaced vortex events.

Figure 3.3 shows the distributions of these two quantities calculated from  $q_{850}$  and  $Z_{10}$  for the Northern Hemisphere vortex. The centroid latitude distributions are almost identical, with a peak near  $80^{\circ}\text{N}$  which is in agreement with previous studies [Waugh and Randel, 1999; Mitchell et al., 2011]. The aspect ratio distributions have a similar shape, with a peak at about 1.3, but the PV based diagnostic has a larger tail. This is because the PV field contains more small-scale filamentary structures than geopotential height (e.g. Figures 3.1 and 3.2), making high aspect ratios more likely. As well as having similar distributions, the time series of the PV and geopotential height derived diagnostics (not shown) are significantly correlated, with correlation coefficients of 0.9 for daily centroid latitude and 0.6 for aspect ratio. Overall, these results suggest that geopotential height-derived moment diagnostics are appropriate for the identification of split and displaced vortex events.

Figure 3.4 shows the same distribution as Figure 3.3, but for the Southern Hemisphere vortex aspect ratio and centroid latitude. As in the case of the Northern Hemisphere, the geopotential height and PV-based distributions have very similar shapes, with the PV-based aspect ratio having a slightly larger tail. Comparing the Northern and Southern Hemisphere distributions it can be seen that there is much less variability in both aspect ratio and centroid latitude in the Southern Hemisphere. This is because of the reduced planetary wave propagation into the Southern Hemisphere stratosphere, in turn a result of lesser forcing from orography and land-sea temperature contrasts. The peak in the Southern Hemisphere centroid latitude is at about  $86^{\circ}\text{S}$ ; the same as that found by Waugh and Randel [1999].



**Figure 3.3:** Distributions of the December-March centroid latitude (a) and aspect ratio (b), of the Northern Hemisphere stratospheric polar vortex over 1958-2009. Diagnostics are calculated from geopotential height at 10 hPa ( $Z_{10}$ ) and potential vorticity at 850 K (PV). Thresholds of 66°N in centroid latitude and 2.4 in aspect ratio are used to define events, and are indicated by the black vertical lines.



**Figure 3.4:** As Figure 3.3 but for moment diagnostics calculated for the Southern Hemisphere stratospheric polar vortex over June-September.

1103 A result of this reduced Southern Hemisphere vortex variability is that only one  
 1104 SSW has been observed in the Southern Hemisphere (discussed further in Chapter 5).  
 1105 The rest of this chapter relates to the classification and impacts of split and displaced  
 1106 vortex events and so focuses only on the Northern Hemisphere. However, it should be  
 1107 noted that all the methods below can also be applied to the Southern Hemisphere.

### 1108 3.3.3 Event identification

1109 Previous attempts to identify SSW events have used a clustering method [*Coughlin*  
 1110 *and Gray, 2009; Hannachi et al., 2010*]. These methods attempt to classify the vortex  
 1111 state for each day into a number of groups, which may be specified beforehand or  
 1112 determined by the clustering algorithm. Individual days within the same cluster should  
 1113 be physically similar, while those in different clusters distinct. More precisely, clustering  
 1114 aims to maximise the between-cluster variance while minimising the within-cluster  
 1115 variance. In the case of the stratospheric polar vortex, clusters may represent, for  
 1116 instance, stable, split, and displaced states. Events are then typically defined by the  
 1117 vortex persisting in a particular cluster for a number of days.

1118 A large number of clustering algorithms exist, and some may be more appropriate  
 1119 than others for certain uses. Here, three different algorithms are applied to the moment  
 1120 diagnostics in centroid latitude-aspect ratio space, and their outcomes shown in Figure  
 1121 3.5(a,b,c). Details of the three algorithms are given below:

1122 (a) **K-means** clustering requires the number of clusters,  $K$ , to be specified beforehand  
 1123 (in Figure 3.5,  $K = 3$ ). The algorithm begins by randomly selecting  $K$  data points  
 1124 to be the centroids of the initial clusters, all other data points are assigned to the  
 1125 cluster with the nearest centroid. Having assigned the initial cluster membership,  
 1126 the algorithm proceeds as follows:

- 1127 1. Compute the centroids (the vector means),  $\bar{\mathbf{x}}_k$  of each cluster.
- 1128 2. Calculate the distance between the current data point,  $\mathbf{x}_i$ , and each of the  $K$   
   1129  $\bar{\mathbf{x}}_k$ s. (Various distance measures can be used; in Figure 3.5(a), the Euclidean  
   1130 distance is used).

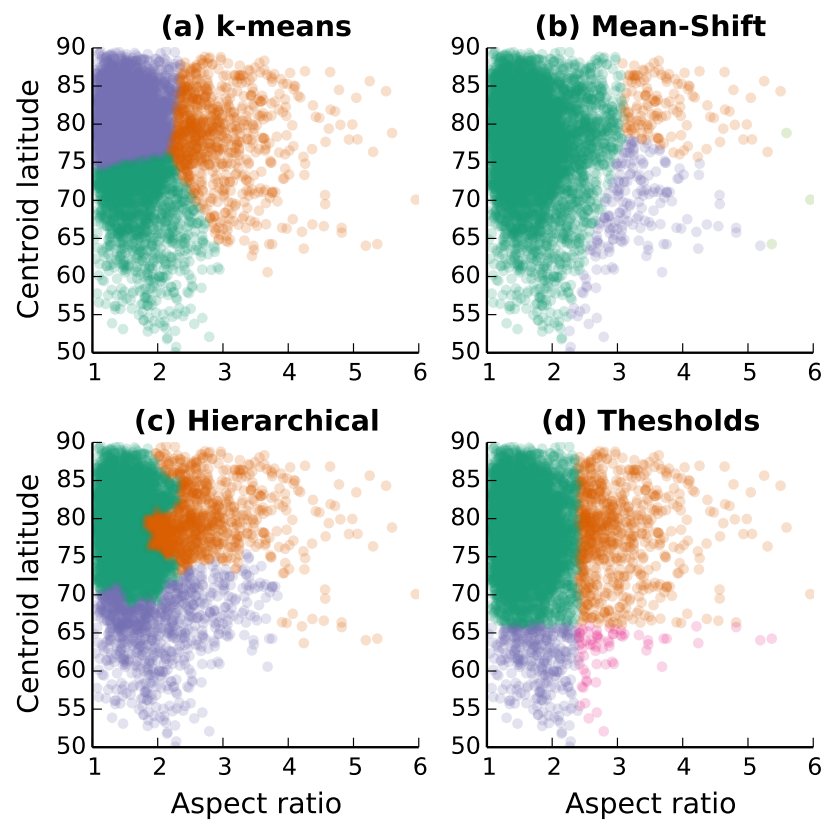


**Figure 3.5:** Three clustering algorithms and a threshold division applied to the moment diagnostics in centroid latitude-aspect ratio space. For the *k*-means and hierarchical algorithms three clusters were specified. The mean-shift algorithm determined the number of clusters to be 4.

- 1131     3. If  $\mathbf{x}_i$  is not in the group with the closest mean then reassign it to that group,  
 1132       otherwise repeat step 2 for  $\mathbf{x}_{i+1}$ .

1133     This is repeated until a full cycle through each  $\mathbf{x}_i$  produces no reassessments. An  
 1134       advantage of this method is that it is computationally efficient, but the major dis-  
 1135       advantage is that the number of clusters must be pre-determined. Several meth-  
 1136       ods exist to estimate the ideal number of clusters, which generally have the aim  
 1137       of finding the best compromise between minimising within-cluster variance and  
 1138       maximising between-cluster variance. *Coughlin and Gray [2009]* applied  $K$ -means  
 1139       clustering to several variables representing the stratospheric polar vortex. They  
 1140       used a method known as silhouette values [?] and determined the ideal number  
 1141       of clusters to be two (representing stable and disturbed vortex states).

- (b) **Mean-shift** clustering aims to discover ‘blobs’ in a data set. It works by updating candidates for centroids to be the mean of the points within a given region. That is, given a candidate centroid  $\mathbf{x}_i$  for iteration  $t$ , the candidate is updated according to

$$\mathbf{x}_i^{t+1} = \mathbf{x}_i^t + \mathbf{m}(\mathbf{x}_i^t), \quad (3.12)$$

where  $\mathbf{m}$  is the mean shift vector. This is calculated as

$$\mathbf{m}(\mathbf{x}_i) = \frac{\sum_{\mathbf{x}_j \in N(\mathbf{x}_i)} K(\mathbf{x}_j - \mathbf{x}_i) \mathbf{x}_j}{\sum_{\mathbf{x}_j \in N(\mathbf{x}_i)} K(\mathbf{x}_j - \mathbf{x}_i)}, \quad (3.13)$$

1142     where  $K(\mathbf{x}_j - \mathbf{x}_i)$  is a kernel function which determines the weight of nearby points.  
 1143       Typically, and in Figure 3.5(b), a Gaussian kernel is used,  $K(\mathbf{x}_j - \mathbf{x}_i) = e^{-c \|\mathbf{x}_j - \mathbf{x}_i\|^2}$ .  
 1144        $N(\mathbf{x}_i)$  represents the set of points for which  $K(\mathbf{x}_i) \neq 0$ . This shifting is repeated  
 1145       until  $\mathbf{m}$  converges. Following this calculation, the candidates are then filtered to  
 1146       remove near duplicates. The greatest advantage of this method is that it automati-  
 1147       cally sets the number of clusters, so no prior assumptions about the data set are  
 1148       required. A disadvantage is that it requires multiple nearest neighbour searches  
 1149       during each iteration, and so may not be scalable to large data sets. In Figure  
 1150       3.5(b) the number of clusters was determined to be four.

### 3.3. DATA AND METHODS

(c) **Hierarchical** clustering proceeds by calculating a series of nested clusters. To begin with, all data points are considered each as a separate cluster and then at each iteration the nearest two clusters are merged. There are a number of methods to identify the distance between clusters when those clusters consist of more than one member. Following *Hannachi et al.* [2010] the *complete-linkage* method; defining the distance as the largest distance between members in the two groups. As with the *K*-means clustering, the number of clusters desired must be pre-determined, otherwise the algorithm will run to completion with a single cluster consisting of all data points. Again, many methods exist to determine the optimum number of clusters. *Hannachi et al.* [2010] used the gap statistic method [*Tibshirani et al.*, 2001] with vortex area, centroid latitude, and aspect ratio moment diagnostics, and found a slight preference for three clusters. As such, three clusters are used in Figure 3.5(c).

Figure 3.5 demonstrates that the three clustering methods produce very different results. As well as the size and extent of the clusters, there is also disagreement between this and past studies on the optimum number of clusters; *Coughlin and Gray* [2009] found two clusters using a silhouette values method, *Hannachi et al.* [2010] found three clusters using the gap statistic, while the mean-shift algorithm applied here produces four clusters. Further sensitivity tests were performed by randomly removing 1% of the data and re-calculating the clustering. It was found that very different clusters were calculated with this small alteration to the data, suggesting that these clusterings may not be robust if applied to different data sets, such as climate model simulations. The likely reason for this sensitivity is that the data itself is not highly clustered; as can be seen in Figure 3.3 no clear bi-modality is present. Rather, it is more appropriate to view the split and displaced vortex states as the tails of a distribution rather than distinct clusters or regimes.

For the reasons above, clustering methods are deemed inappropriate for the present study, and a simpler, more robust, thresholds-based method is introduced. Days with an aspect ratio  $> 2.4$  (11% of all days) or a centroid latitude  $< 66^\circ\text{N}$  (5% of all days) are

classified as split and displaced states respectively. A small number of days lie beyond both thresholds, and these are classified as a mixed state (1% of all days). The vast majority of days (83%) lie in the stable state, where neither threshold is exceeded. The choice of thresholds is somewhat subjective but the results presented below are not sensitive to the exact choice of threshold. They were chosen to give a similar frequency of split and displaced vortex events (identified using the method below) as CP07 and M13.

*Mitchell et al. [2011]* found that the aspect ratio and centroid latitude follow an extreme value distribution [*Coles, 2001*] and it is noted that both thresholds chosen here lie beyond the extreme value thresholds of their respective distributions (these were found to be 2.3 for aspect ratio and 72°N for centroid latitude). Some theoretical motivation for the aspect ratio threshold can also be provided by the theoretical stability of an idealised elliptical vortex. *Love [1893]* found that the Kirchoff ellipse (an elliptical patch of uniform vorticity in a quiescent fluid) is linearly unstable if the aspect ratio exceeds 3. The aspect ratio threshold of 2.4 used here lies below this limit, and so under this idealised model it might expect that some split vortex events do not display a full separation into two vortices.

Having classified each day into these four groups, a persistence criterion is introduced in order to identify split and displaced vortex events. A displaced vortex event requires the centroid latitude to remain equatorward of 66°N for 7 days or more, while a split vortex event requires the aspect ratio to remain higher than 2.4 for 7 days or more. The onset date is defined as the day that the appropriate threshold is first exceeded, and to ensure that no events are counted twice, these onset dates are required to be spaced at least 30 days apart, chosen to reflect radiative timescales in the lower stratosphere [*Newman and Rosenfield, 1997*]. Using this method, 17 displaced and 18 split vortex events (listed in Table ??) are identified over the 52 winters, an average of 7 per decade. This frequency lies between the values of CP07 (6 per decade) and M13 (8 per decade). Although data is restricted to DJFM in this analysis, no measures are taken to exclude early final warmings which may occur in late March. This is motivated by the fact that these are highly dynamically driven events which may have significant

No.	Event onset	Event type	$\Delta T_{10}$ (K)	$\bar{U}_{10}$ (m s <sup>-1</sup> )
1*	1961-3-9	D	10.2	2.7
2*	1962-1-30	S	1.9	38.9
3*	1962-3-7	S	-1.0	16.9
4*	1964-3-15	D	11.9	1.3
5†	1966-2-26	D	2.5	-5.9
6	1967-12-29	S	13.0	19.4
7†	1970-1-5	S	8.5	-4.0
8	1971-1-15	S	10.8	-1.7
9*	1972-2-4	S	-1.6	33.6
10†	1973-2-4	S	7.3	-6.6
11*	1974-3-12	D	5.3	-4.8
12*	1975-3-16	D	7.6	-8.0
13*	1976-3-31	D	8.2	-13.3
14†	1977-1-7	S	7.6	-5.5
15*†	1978-3-25	D	2.5	-9.3
16	1979-2-18	S	5.6	-0.4
17	1984-2-25	D	11.6	-4.4
18	1984-12-25	S	15.0	-1.7
19*	1986-1-7	S	3.4	29.9
20*	1986-3-21	D	9.1	-12.2
21	1987-1-20	D	8.3	-7.7
22	1987-12-10	S	9.8	-3.0
23*	1992-3-22	D	7.6	-4.4
24*†	1995-2-2	D	5.6	7.7
25	1998-12-15	D	8.2	8.1
26	1999-2-24	S	6.6	-12.7
27	2001-2-7	S	5.2	-7.2
28*	2001-3-15	S	-6.8	12.1
29*	2002-3-21	S	-1.5	5.1
30	2003-1-17	S	6.1	16.8
31	2004-1-2	D	5.8	-4.8
32*	2005-3-11	D	3.1	-5.0
33	2006-1-17	D	4.2	-14.3
34	2008-2-18	D	4.6	2.3
35	2009-1-18	S	13.2	16.9

**Table 3.1:** A summary table of displaced (D) and split (S) vortex events, identified from 10 hPa geopotential height data from 1958-2009.  $\Delta T_{10}$  represents the mean area-weighted 50°-90°N cap temperature anomaly at 10 hPa calculated 5 days either side of the event onset date.  $\bar{U}_{10}$  represents  $\bar{U}$  at 60°N and 10 hPa averaged over the same period. Asterisks (\*) represent those numbers that do not coincide (i.e. within 10 days and of the same type) with events defined by CP07 and daggers (†) events which do not coincide with events of M13.

1210 impacts on the troposphere [Hardiman *et al.*, 2011]. The events defined here may  
 1211 therefore include some which would traditionally be classed as final warmings (i.e. the  
 1212 zonal-mean zonal wind does not return to westerly). For this reason, there events are  
 1213 not referred to as SSWs, but simply as split and displaced vortex events.

1214 Figures 3.6 and 3.7 show geopotential height at the peak of each of the split and  
 1215 displaced vortex events. The peak is defined as the day with the maximum aspect ratio  
 1216 or minimum centroid latitude in the two weeks following the onset date of split and  
 1217 displaced vortex events respectively. Almost all of the split vortex events show two  
 1218 clearly separated vortices or a pinched vortex shape, which is approximately symmet-  
 1219 rical about the North Pole. Two exceptions are Figures 3.6(a) and (k), in which the  
 1220 vortex is highly elliptical but not clearly split. Figure 3.6(n) shows an event with a  
 1221 highly elliptical vortex that is also somewhat displaced from the pole, indicating that it  
 1222 has some displaced nature. The majority of split vortex events are seen to occur along  
 1223 the 90°E-90°W axis, in line with the climatological wave-2 pattern [Andrews *et al.*,  
 1224 1987]. Figure 3.6(h) shows an exception to this, with an orientation orthogonal to the  
 1225 majority of events.

1226 The displacement events mostly show a smaller and weaker vortex, owing to the  
 1227 fact that they are more common later in winter (see Figure 3.8). Some events, par-  
 1228 ticularly those occurring in late March, are also likely to be events which would tradi-  
 1229 tionally be defined as final warmings. It can be seem that the majority of displacement  
 1230 events occur in the direction of the 0-90°E quadrant, again in line with the climatolog-  
 1231 ical wave-1 pattern. However, there are some exceptions to this, for instance Figures  
 1232 3.7 (c) and (i), which show a westward-displaced vortex.

### 1233 3.3.4 Comparison with CP07 and M13

1234 The split and displaced vortex events identified using the above method are now com-  
 1235 pared with those of the CP07 and M13 methods. Table 3.1 identifies those events which  
 1236 do not coincide with the events of CP07 and M13, where ‘coincide’ is taken to mean  
 1237 events within 10 days and of the same type. Of the 35 events identified, 16 were found  
 1238 not to coincide with events of CP07 (10 displacement and 6 split). Six events were

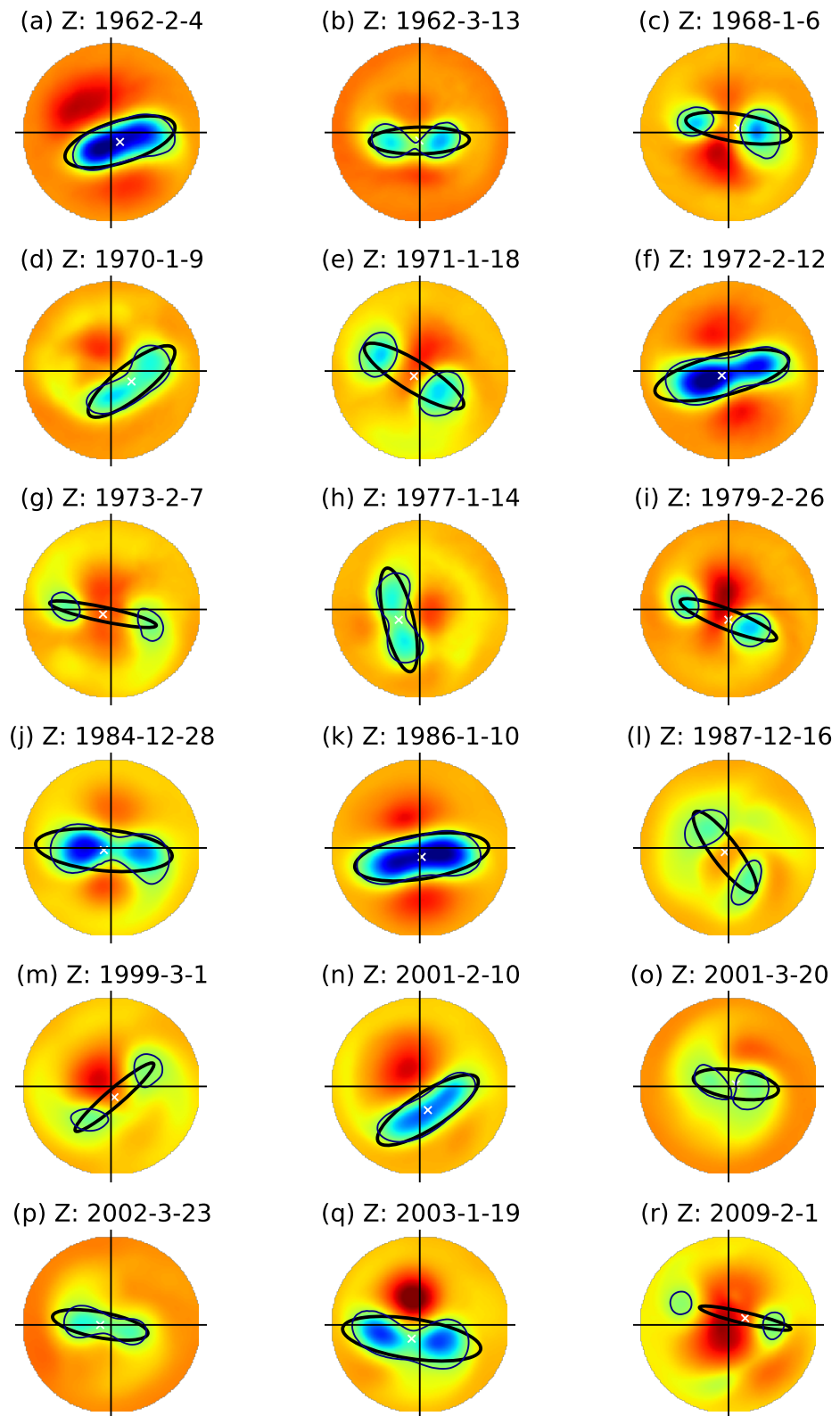


**Figure 3.6:** 10 hPa geopotential height at the peak of each of the 18 split vortex events identified in ERA. The peak is defined as the day with the largest aspect ratio during the two weeks following the onset date. The vortex edge is shown as a thin black contour, the equivalent ellipse the thick black contour and its centroid as a white cross. Data are transformed to cartesian coordinates with a polar stereographic projection.

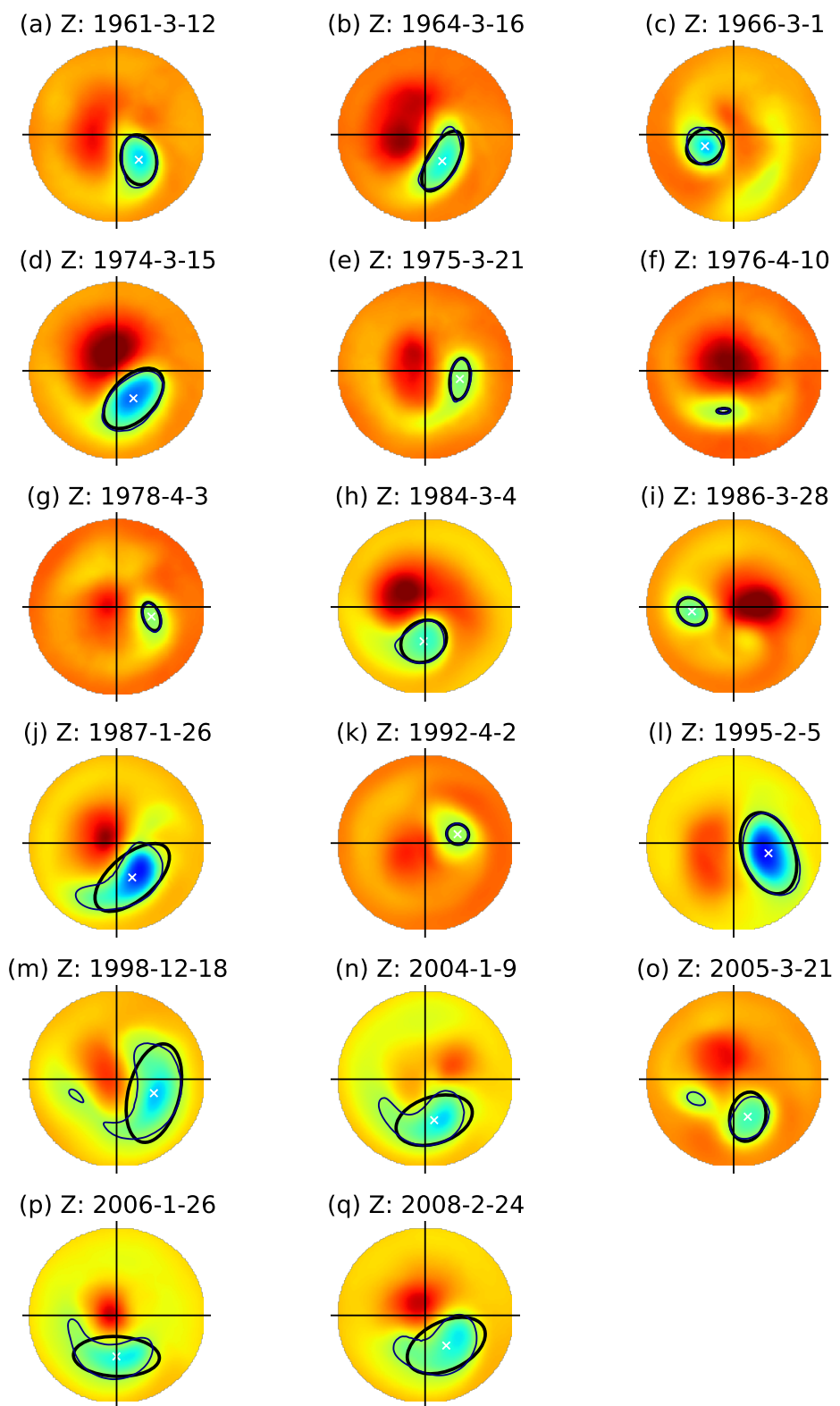


**Figure 3.7:** As Figure 3.6 but for the 17 displaced vortex events identified in ERA.

### 3.3. DATA AND METHODS

1239 found not to coincide with those of M13 (3 displacement and 3 split), although this  
1240 comparison only covers the 28 events from 1958-2002, as it was not possible to repro-  
1241 duce the M13 method over the longer period studied here because of the difficulties  
1242 with hierarchical clustering discussed in Section 3.3.3. Just two completely new events  
1243 were identified (i.e. not coinciding with either CP07 or M13); these are the displaced  
1244 vortex events with onset dates 1978-3-25 and 1995-2-2.

1245 Table 3.1 also shows polar cap averaged 10 hPa temperature anomalies ( $\Delta T_{10}$ ),  
1246 averaged 5 days either side of the event to give a measure of the event magnitude.  
1247 The events of CP07 show a larger average anomaly than events identified with the  
1248 current method, although the two are not statistically significantly different: CP07 av-  
1249 erage 8.6 K [6.1, 10.9] split and 7.8 K [5.5, 9.9] for displaced vortex events, while the  
1250 current method averages 5.7 K [3.0, 8.3] for split and 6.8 K [5.5, 8.2] for displaced  
1251 vortex events (numbers in square brackets represent the 95% uncertainty range, calcu-  
1252 lated using a bootstrap test). It can be seen that while the vast majority of events show  
1253 positive values of  $\Delta T_{10}$  (i.e. warming), four events show negative values. All of these  
1254 events are also identified by M13, and they attributed the negative values to the pres-  
1255 ence of a strong, cold vortex prior to the event. Zonal-mean zonal wind at 60°N and  
1256 10 hPa ( $\bar{U}_{10}$ ), averaged over the same period is also shown in Table 3.1. The major-  
1257 ity of events show negative values, in line with the traditional wind reversal criterion,  
1258 although some show positive values. This again may result from a strong vortex prior  
1259 to these events, as well as the fact that the current method may detect events with a  
1260 distorted but strong vortex.

1261 The seasonal distribution of split and displaced vortex events identified by the cur-  
1262 rent method ( $Z_{10}$ ), M13, and CP07, is shown in Figure 3.8. In all three methods split  
1263 vortex events are more frequent in early-mid winter, with a peak in January. For dis-  
1264 placed vortex events, both the current method and M13 show a skew towards events  
1265 occurring later in winter. However, there is less similarity with the CP07 distribution of  
1266 displaced vortex events. CP07 indicates an approximately flat distribution throughout  
1267 winter, and many fewer displaced vortex events overall. It should be noted that the sea-  
1268 sonal distribution of split vortex events from the moment based methods does not arise

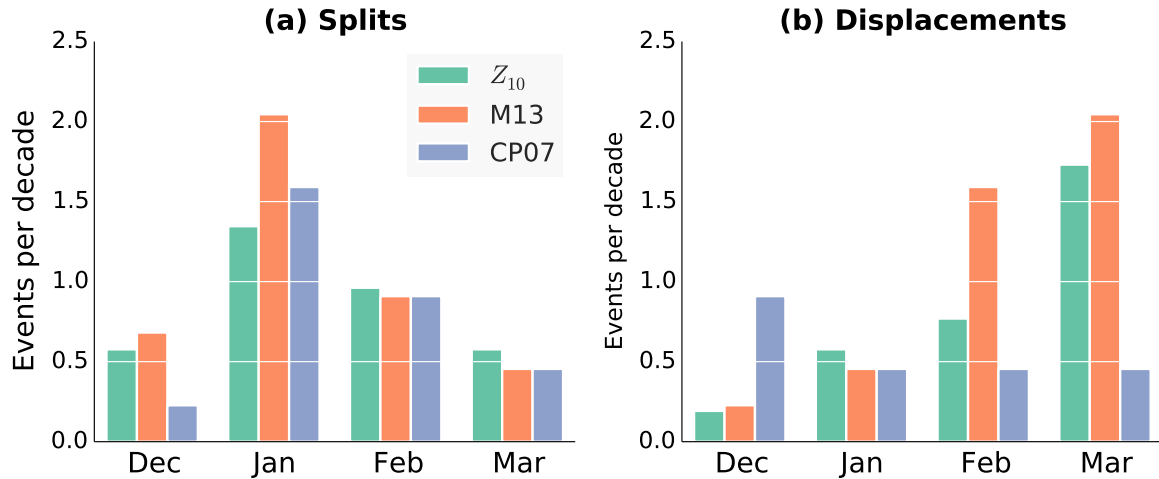
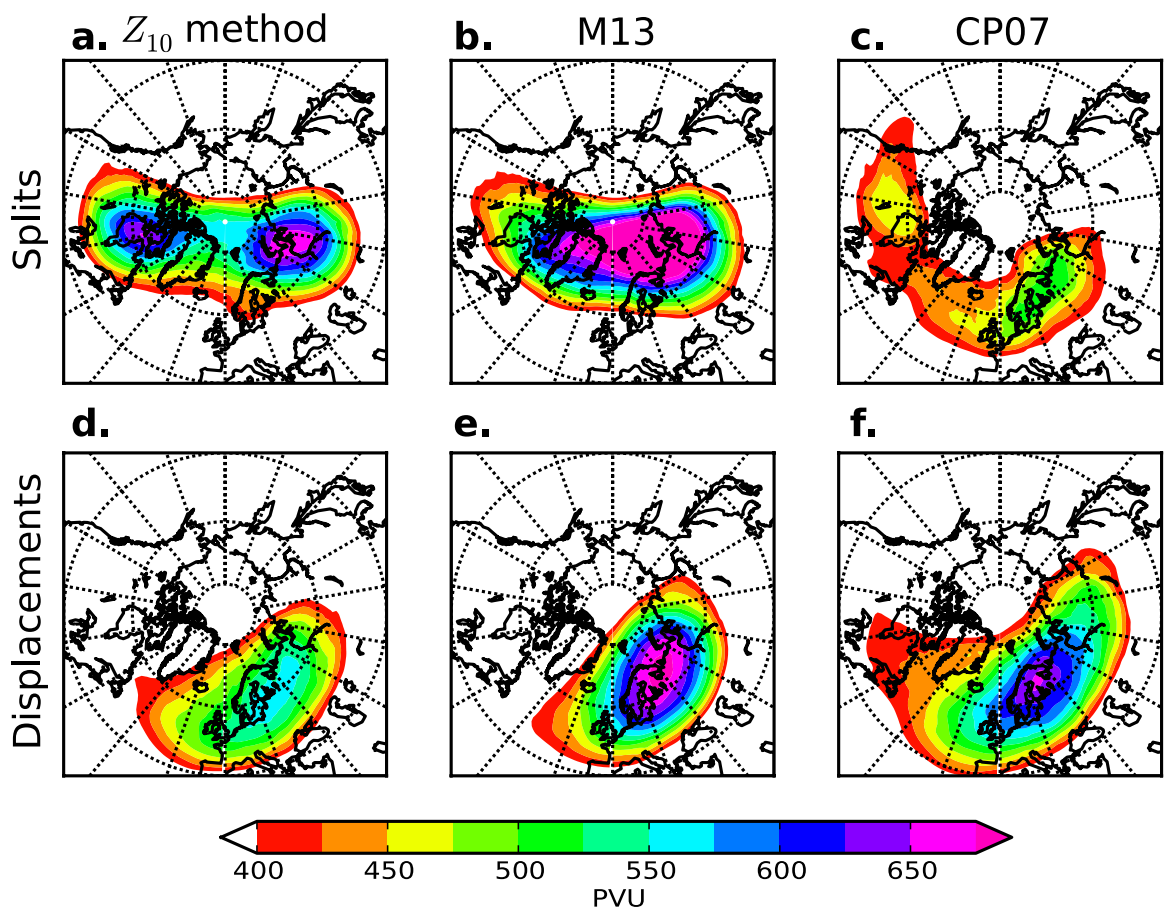


**Figure 3.8:** Histogram of the seasonal distribution of displaced and split vortex events, form the current ( $Z_{10}$ ) method, M13 and CP07.

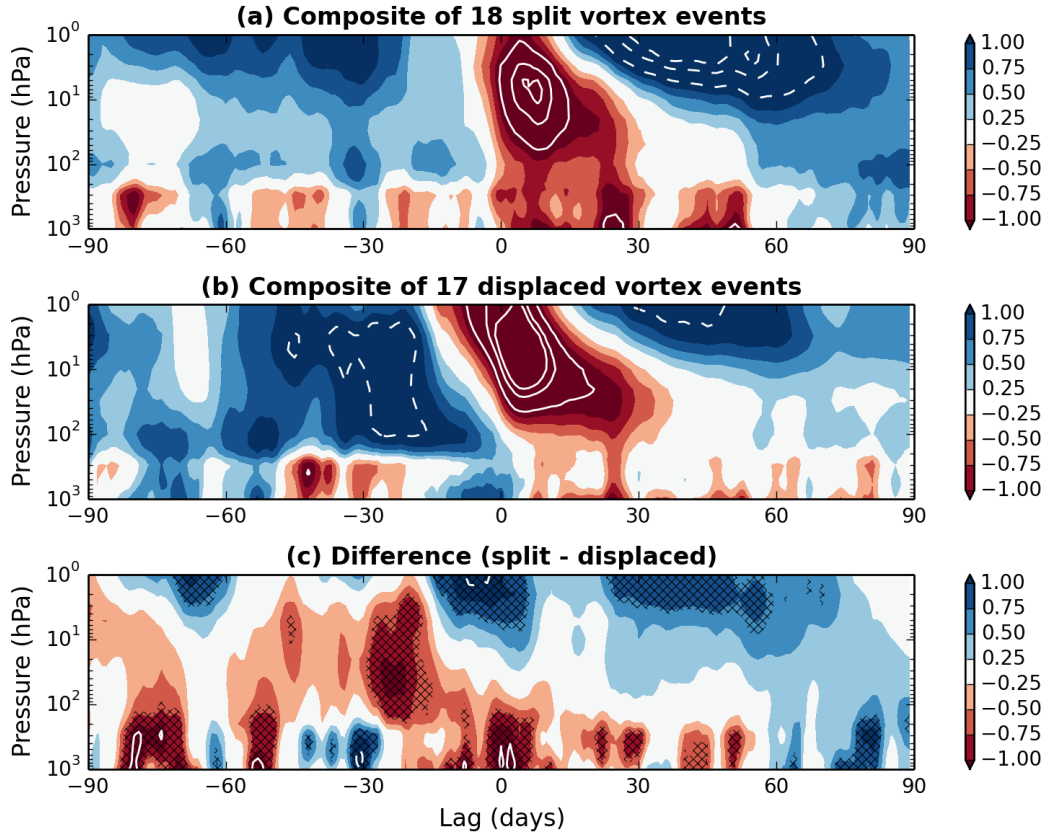
from the underlying climatology of aspect ratio, which remains approximately constant throughout winter (e.g., Figure 4.2). The centroid latitude does however, show a small equatorwards trend throughout winter, which may to some extent account for the seasonal distribution of displaced vortex events [Mitchell *et al.*, 2011].

Figure 3.9 compares the average shape of the stratospheric polar vortex following the split and displaced vortex events identified by the three methods. Composites of PV in the mid-stratosphere (850 K) are shown averaged 5 days following each event. For the split vortex events, the current method ( $Z_{10}$ ) method clearly shows two separated vortices, one centred over Canada and the other over Siberia. For the M13 events the split vortex composite shows the vortex stretched across the same 90°W-90°E line, although not as clearly split, while the composite for the CP07 events looks very different. This has a weak vortex centred over Canada, with the other over Northern Europe in a similar location to the composite for displaced events. All three composites for displaced events show a vortex centred over Northern Europe, but this extends most westward in the CP07 composite, suggesting that there may be some contamination from misdiagnosed split vortex events.

Overall, Figure 3.9 demonstrates that the current method succeeds (in a composite sense) in identifying displaced and split vortex events at least as well as the methods of M13 or CP07. When comparing the three methods, CP07 is the clear outlier. This is



**Figure 3.9:** Composites of potential vorticity at the 850 K isentropic surface from the ERA reanalysis over 1958-2009. Composites are taken over the 5 days following the onset date of split vortex events (a,b,c) and displaced vortex events (d,e,f). The current ( $Z_{10}$ ) method (a,b) is compared with that of M13 (b,e) and CP07 (c,f).



**Figure 3.10:** Composites of the time-height evolution of the NAM during (a) 17 vortex displacement events and (b) 18 splitting events. (c) shows the difference in these composites, and hashed regions represent those that are 95% significant according to a two-tailed bootstrap test. Lag 0 is at the onset of an event as measured at 10 hPa. Contour intervals are 0.25 and the region between -0.25 and 0.25 is unshaded. Data is from the ECMWF Reanalyses 1958-2009.

most likely because the CP07 approach employs a zonal-mean threshold which cannot accurately capture some extreme events (as discussed in M13).

## 3.4 Influence on the troposphere

Having verified that this new method identifies split and displaced vortex events as skillfully as previous methods, it is now possible to study their influence on the troposphere. This is motivated by the result of M13 who, as discussed in Section 2.4.1, found tropospheric anomalies to be larger following split vortex events than displaced vortex events. Figure 3.10(a,b) shows time-height composites of the NAM over the 90 days following split and displaced vortex events. Here the method of *Baldwin and Thompson*

### 3.4. INFLUENCE ON THE TROPOSPHERE

[2009] is used to define the NAM as the leading empirical orthogonal function (EOF) of daily wintertime (November-April) zonal mean geopotential height anomalies poleward of 20°N. The anomalies are calculated by subtracting the seasonal cycle which has been smoothed with a 90-day low-pass filter. The daily NAM anomalies are then determined by projecting daily geopotential anomalies onto the leading EOF patterns. Finally, the NAM is normalised at each level so that the entire time series has unit variance.

In agreement with M13, it can be seen that the tropospheric NAM is more negative during the 60 days following split vortex events than displaced vortex events. Also similar to M13 is the fact the vertical evolution for the two events greatly differs, with split vortex events occurring almost instantaneously throughout the depth of the atmosphere and displaced vortex taking almost two weeks to propagate through the stratosphere. The near-barotropic nature of split vortex events suggests that resonant excitation of the barotropic normal mode [*Esler and Scott, 2005*] is an important influence in this case.

The difference in the NAM composites (split minus displaced) is shown in Figure 3.10(c). Statistical significance in this difference is calculated with the null hypothesis that there is no difference between the NAM response to split and displaced vortex events, and assessed using a two tailed bootstrap test with the following procedure:

- i. The labels ‘split’ and ‘displacement’ are randomly re-assigned to the 35 events.
- ii. NAM composites and the composite difference of these randomly assigned events are calculated.
- iii. The above steps are repeated 10 000 times, to form a distribution of random composite differences. If the true composite difference lies < 2.5% or > 97.5% within this distribution, then it can be said to be 95% significant.

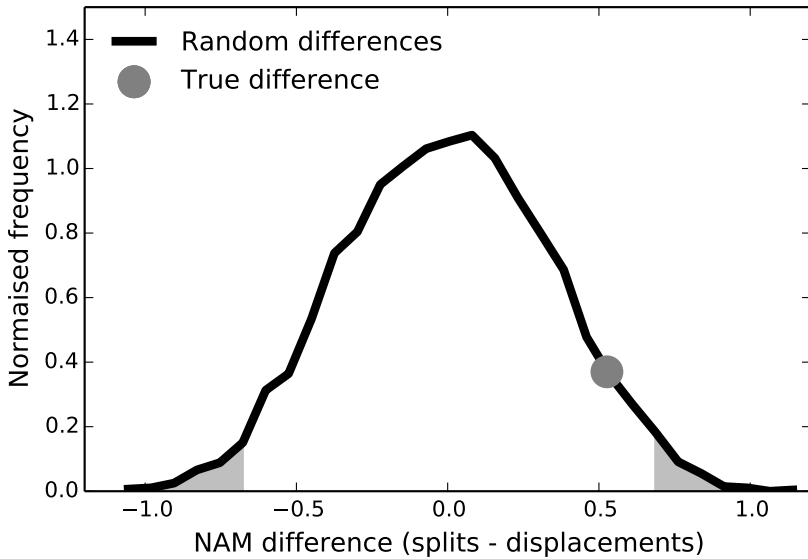


**Figure 3.11:** Distribution of 0-30 day mean NAM composite differences between split and displaced vortex events, formed by randomly shuffling the labels ‘split’ and ‘displacement’ between events. The 95% significant region (according to a two-tailed test; i.e. < 2.5% and > 97.5%) is shaded and the true composite difference is at the 94th percentile.

1322 Some significant differences are seen between the split and displaced vortex compos-  
 1323 ites. For instance, a more negative stratospheric NAM is seen to precede displaced  
 1324 vortex events, while the dipole in the upper stratospheric and tropospheric NAM near  
 1325 lag 0 represents the difference in baroclinicity of the two types of event. Some regions  
 1326 of significant differences are seen in the tropospheric NAM from 0-60 days, but there  
 1327 are also some regions that are not significant. Care must be taken when interpret-  
 1328 ing the importance of small significant regions these may arise by chance, even if no  
 1329 physical relationship exists.

1330 The difference in the tropospheric anomalies following split and displaced vortex  
 1331 events is tested more robustly by examining surface anomalies averaged over the 30  
 1332 days following onset. This difference is again tested using the bootstrap procedure out-  
 1333 lined above. The distribution of randomly calculated composite differences along with  
 1334 the true composite difference is shown in Figure 3.11. It can be seen that the true NAM  
 1335 difference does not lie in the 95% significant region, so the null hypothesis that there  
 1336 is no difference between anomalies following split and displaced vortex events cannot  
 1337 be rejected. It should be noted that the statistical test here is different to that carried

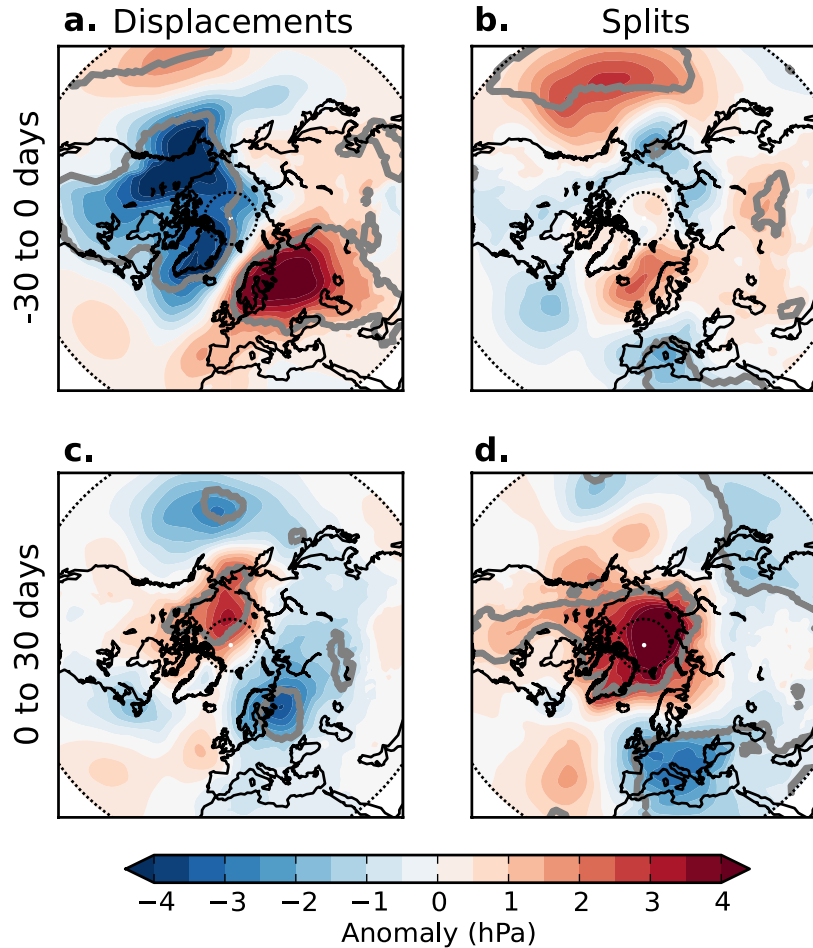


**Figure 3.12:** Composites of mean sea-level pressure anomalies in the 30 days before (a,b) and 30 days after (c,d) the onset dates of displaced (a,c) and split (b,d) vortex events from the  $Z_{10}$  method. Data is from the ECMWF reanalyses (1958-2009). Anomalies are calculated for each day and gridpoint from the climatology for that day of the year and gridpoint. Grey contours indicate regions of greater than 95% statistical significance according to a bootstrap significance test.

out by M13. They tested whether the surface NAM following split and displaced vortex events were different from randomly selected winter dates, finding that anomalies following splits are, but those following displacements are not. They did not, however, test the *difference* between split and displaced vortex events.

The NAM does not provide the full description of surface variability, and so in Figure 3.12 composites of MSLP 30 days before and 30 days following the onset dates of displaced and split vortex events are presented. Statistical significance is calculated against the null hypothesis that anomalies before and after split and displaced vortex

1346 events are indistinguishable from other winter dates. This is again estimated from a  
 1347 two-tailed bootstrap test, in which 10 000 composites of equal size are formed from  
 1348 randomly selected winter dates, and the percentile of the true composite calculated  
 1349 from this distribution.

1350 The strongest precursor is found for displaced vortex events, with a wave-1 pattern  
 1351 that is similar to the climatological stationary wave pattern [e.g. *Garfinkel and Hart-*  
 1352 *mann, 2008*], suggesting increased wave-1 propagation into the stratosphere. How-  
 1353 ever, the strongest anomalies following events occur after split vortex events, with a  
 1354 pattern resembling the negative phase of the NAM, though with a southern centre of  
 1355 action shifted towards Europe. A further difference between the split and displaced  
 1356 vortex composites is that their is a more negative MSLP anomaly over Scandinavia and  
 1357 Siberia following displaced vortex event. Overall, the main features of Figure 3.12  
 1358 compare very well with the corresponding diagnostics from M13.

1359 The mechanism of the stratosphere's influence on the troposphere proposed by *Am-*  
 1360 *baum and Hoskins [2002]* states that changes in the PV near the tropopause affect the  
 1361 tropopause height and induce tropospheric anomalies below (more details are given  
 1362 in Section 2.4.3). In order to investigate this mechanism, composites of tropopause  
 1363 height over the 10 days before, 10 days after, and 10-20 days after split and displaced  
 1364 vortex events are shown in Figure 3.13. The measure of tropopause height used is that  
 1365 of *Wilcox et al. [2012a]*, who construct a blended thermal and dynamical tropopause.  
 1366 Significance is again calculated using a two-tailed bootstrap test.

1367 In line with the MSLP anomalies shown in Figure 3.12, tropopause height anom-  
 1368 lies are seen to be larger prior to displaced vortex events, with a wave-1-like struc-  
 1369 ture. Following events, tropopause height anomalies are seen to approximately mirror  
 1370 stratospheric PV anomalies (Figure 3.9). That is, following displaced vortex events an  
 1371 elevated tropopause is seen over Europe and Scandinavia, with a lowered tropopause  
 1372 over Canada, and following split vortex events two regions of elevated tropopause are  
 1373 present over Canada and Siberia with a depression between.

It is possible to quantitatively examine (although only approximately) whether these tropopause anomalies are consistent with changes in stratospheric PV above.

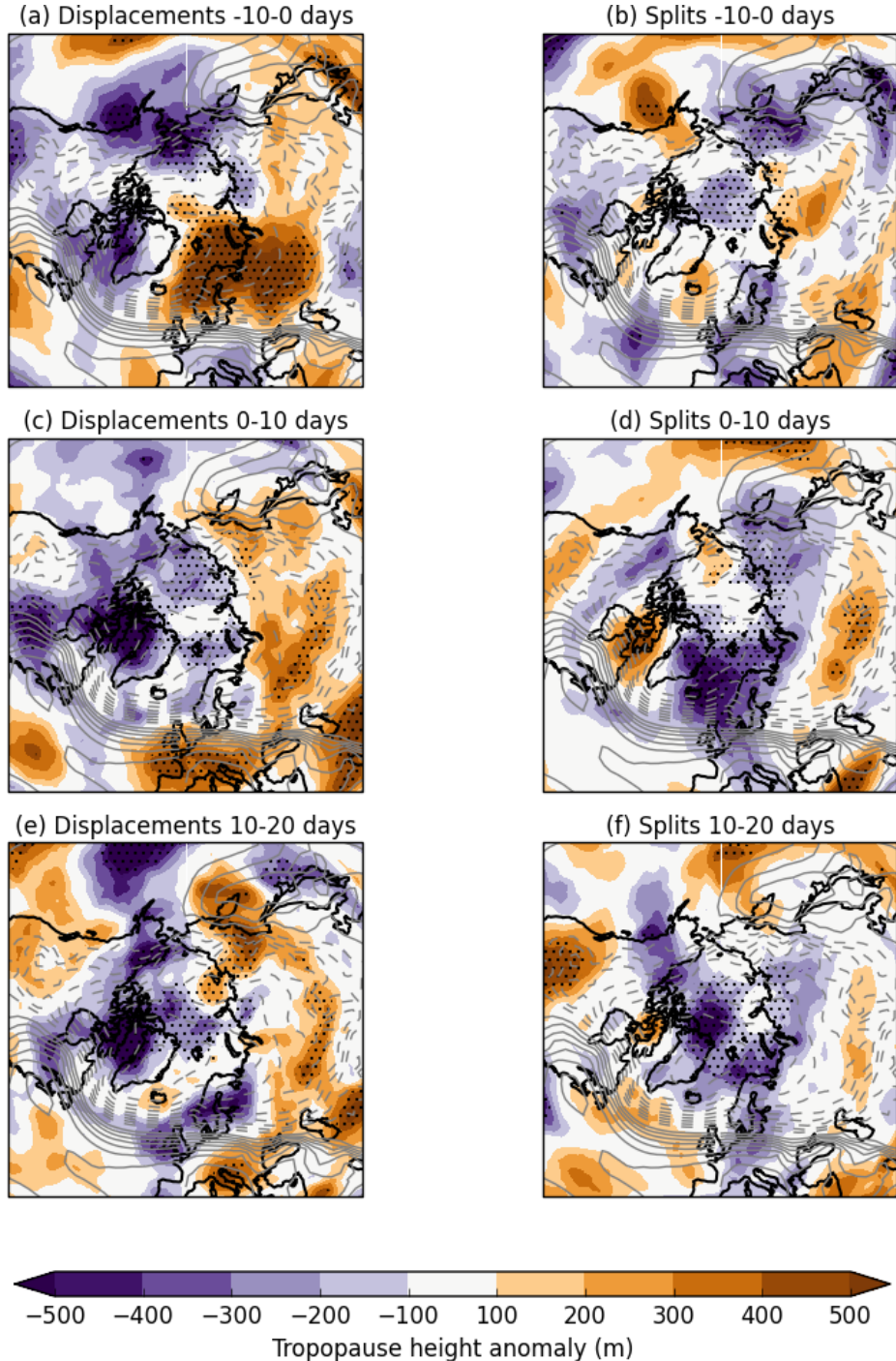


**Figure 3.13:** Composites of tropopause height anomalies averaged 10 days before (a,b), 10 days after (c,d) and 10-20 days after displaced and split vortex events. Anomalies are calculated for each day and gridpoint from the climatology for that day of the year and gridpoint. Stippling indicates regions of greater than 95% statistical significance according to a Monte-Carlo significance test. Grey contours indicate the first EOF of NH mean sea-level pressure, which explains 33% of the variance (dashes represent negative values).

Changes in tropopause pressure,  $\Delta p_{\text{trop}}$ , are related to changes in stratospheric PV,  $\Delta q$ , through

$$\Delta q \approx -q(1 + \text{Bu}) \frac{\Delta p_{\text{trop}}}{p_{\text{trop}}}, \quad (3.14)$$

where Bu is the Burger number, which is approximately equal to one for any PV anomaly [Amabaum and Hoskins, 2002]. The change in tropopause height,  $\Delta h_{\text{trop}}$  can be calculated using the hydrostatic relation

$$\Delta h_{\text{trop}} = -\frac{\Delta p_{\text{trop}}}{p_{\text{trop}}} \frac{RT_{\text{trop}}}{g}, \quad (3.15)$$

where  $T_{\text{trop}}$  is the tropopause temperature. Hence

$$\Delta h_{\text{trop}} = \frac{\Delta q}{q} \frac{RT_{\text{trop}}}{g(1 + \text{Bu})}. \quad (3.16)$$

Using a typical value of the PV change as  $\sim 10\%$  (e.g., see Figure 3.9), along with  $T_{\text{trop}} = 210\text{K}$ , gives a change of tropopause height of  $\Delta h_{\text{trop}} \approx 300\text{m}$ , which is indeed approximately in line with the tropopause height anomalies seen in Figure 3.13. This, along with the fact that the pattern in tropopause height anomalies approximately mirrors that of stratospheric PV anomalies, suggests that these tropopause height anomalies are induced by changes in stratospheric PV above.

Also shown in Figure 3.13 is the surface NAM pattern (the leading EOF of DJFM daily MSLP). It can be seen that following split vortex events more than displaced (especially days 0-10), the negative tropopause height north of Iceland aligns more closely with the minimum in the NAM (this region is also a node of the NAO). This may be significant if it is expected that the fluctuation-dissipation theorem (FDT) holds in the tropospheric response to stratospheric forcing. For systems in which the FDT holds, the response of a system projected on a mode of variability should linearly scale with the projection of the forcing on that mode [Ring and Plumb, 2008]. Under the assumption that the tropopause height perturbation represents the “forcing”, this may project more strongly on the NAM/NAO following split vortex events, consistent with a greater surface response to these events. Overall, however, the pattern correlations between the split and displaced vortex tropopause height anomalies and the NAM are

### 3.5. CONCLUSIONS

1392 not statistically significantly different because the tropopause height field is very noisy.  
1393 In order to give a more detailed analysis a greater number of events would be needed.

## 1394 3.5 Conclusions

1395 Recent research has demonstrated the need to distinguish between split and displaced  
1396 stratospheric polar vortex events because of their different dynamics and impacts on  
1397 the troposphere. However, previous methods to identify these events are impractical  
1398 for application to climate model or seasonal prediction simulations because they are  
1399 highly sensitive to model climatology or rely on non-standard variables. Motivated by  
1400 this, we have developed a new method to identify displaced and split vortex events  
1401 which requires only geopotential height at 10 hPa. The method is summarised as  
1402 follows:

1403 i. To identify the vortex region, a single contour of 10 hPa geopotential height is  
1404 selected. This is the value of the DJFM mean zonal-mean at 60°N.

1405 ii. Using this contour the centroid latitude and aspect ratio moment diagnostics can  
1406 be calculated.

1407 iii. Events are identified using a threshold criterion: Displaced events occur if the  
1408 centroid latitude remains equatorward 66°N for 7 days or more. Split events occur  
1409 if the aspect ratio remains above 2.4 for 7 days or more. In order to ensure events  
1410 are not counted twice, no two events may occur within 30 days.

1411 Vortex moment diagnostics derived from geopotential height are highly correlated with  
1412 those derived from PV although fewer high aspect ratio values are seen. The use of  
1413 geopotential height here is motivated by the fact that it is commonly output by climate  
1414 models, whereas PV is not. However, in cases where PV is available (such as in reanal-  
1415 yses) its use is preferable because of its quasi-conservative properties and smaller-scale  
1416 features. The above method can be easily adapted to be used with PV-based vortex  
1417 moments.

1418 Analysis of the stratosphere following events identified by this method demon-  
1419 strates that it is able to accurately identify split and displaced vortex events. Most  
1420 of the events identified coincide with those of M13, and about half with events identi-  
1421 fied by CP07. Composite analysis indicates that the position of the stratospheric polar  
1422 vortex following these events is at least as extreme as that from the previous methods.

1423 Having identified these events, their impact on the troposphere is investigated.  
1424 Composites of the NAM indicate a more negative surface NAM over the month fol-  
1425 lowing split vortex events than following displaced vortex events. This supports the  
1426 finding of M13, using a different event identification method and extended data set.  
1427 However, using a bootstrap test the composite *difference* of the surface NAM is not  
1428 found to be statistically significant.

1429 Anomalies of tropopause height following split and displaced vortex events are  
1430 found to be co-located with stratospheric PV anomalies. They are also of a magnitude  
1431 consistent with being induced by changes in the stratospheric polar vortex. Surface  
1432 anomalies induced by changes in tropopause height may explain therefore explain the  
1433 different surface anomalies following split and displaced vortex events. However, it is  
1434 not possible to draw firm conclusions on this because of the relatively small number of  
1435 events and the noise of the MSLP and tropopause height fields.

1436 Overall, statistically significant results about the difference in the tropospheric re-  
1437 sponse to split and displaced vortex events will require a larger number of events. This  
1438 is achieved through the analysis of climate model simulations in the next chapter.

### 1439 3.A Comparison with zonal wave amplitudes

1440 Many studies have characterised stratospheric polar variability by its zonal wave struc-  
 1441 ture [e.g, *Randel*, 1988; *Yoden et al.*, 1999; *Nakagawa and Yamazaki*, 2006; *Coughlin*  
 1442 and *Gray*, 2009]. It is therefore instructive to compare this wave analysis with the mo-  
 1443 ment diagnostics developed in this chapter. Here this is carried out for the displaced  
 1444 and split vortex events shown in Figures 3.1 and 3.2 respectively. A similar comparison  
 1445 was shown by *Waugh* [1997] and *Waugh and Randel* [1999], and the results here are  
 1446 consistent with their findings.

1447 Zonal wavenumber decomposition is carried out by taking the Fourier transform  
 1448 of the 60°N, 10 hPa geopotential height field over all longitudes. The amplitude of  
 1449 wave- $n$  on a given day is then given by the modulus of the  $n$ th Fourier component on  
 1450 that day. In ERA data, the amplitude of DJFM wave-2 is, on average, about 30% that  
 1451 of wave-1, and wave-3 13% of wave-1, indicating a Charney-Drazin filtering of zonal  
 1452 wavenumbers, as discussed in Section 2.1.2.1.

1453 The correlation of geopotential height-derived daily aspect ratio and the wave-  
 1454 2 amplitude over DJFM is 0.30 and that of centroid latitude and wave-1 amplitude  
 1455 -0.22, both of which are statistically significant. These relationships are illustrated in  
 1456 the examples of split and displaced vortex events in Figure 3.14. In the case of the  
 1457 1979 split vortex event the wave-2 amplitude peaks approximately 5 days before the  
 1458 peak of the aspect ratio. Wave-2 amplitude is also more variable than aspect ratio in  
 1459 early winter, although the two are correlated at this time. In the case of the 2006 dis-  
 1460 placed vortex event, the difference is even greater. The wave-1 amplitude peaks about  
 1461 three weeks before the centroid latitude, and is actually anomalously small at the peak  
 1462 of centroid latitude. Before and after the event, the wave-1 amplitude and centroid  
 1463 latitude are highly correlated.

1464 The physical reasons for these differences of wave and moment diagnostics are  
 1465 investigated in Figure 3.15. This compares the vortex structure at the peak wave am-  
 1466 plitude and peak aspect ratio/centroid latitude for the two events. For the 1979 split  
 1467 vortex event, the vortex appears split at both times but there is a greater separation

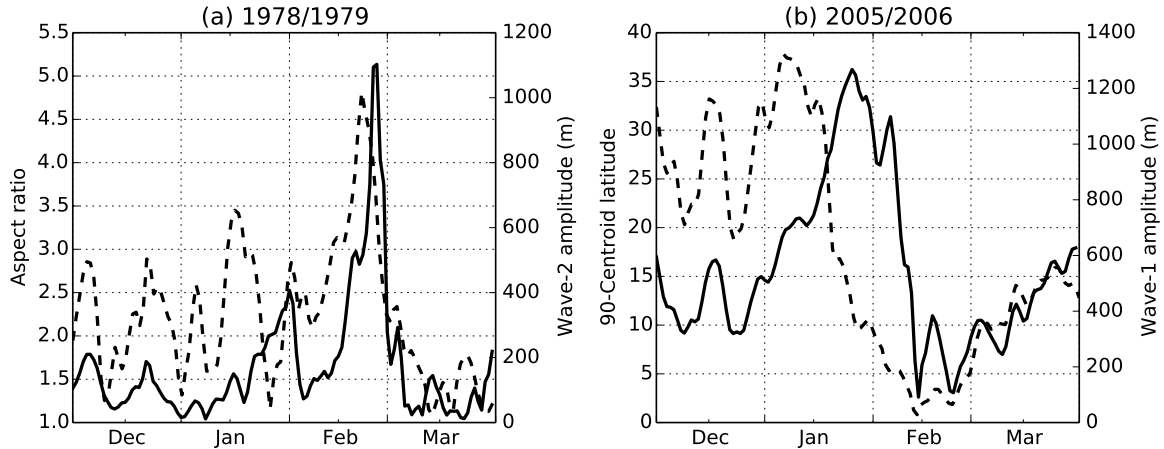


**Figure 3.14:** (a) Aspect ratio (solid line) and wave-2 amplitude (dashed line) over the winter 1978-1979. (b) Centroid latitude (solid line) and wave-1 amplitude (dashed line) over the winter 2005-2006. Centroid latitude is expressed as its deviation from the North Pole.

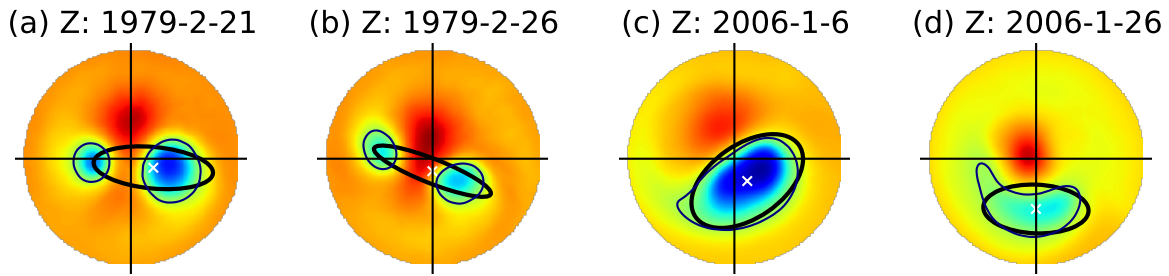


**Figure 3.15:** 10 hPa geopotential height on the day of maximum wave-2 amplitude (a) and maximum aspect ratio (b) for the 1979 split vortex event; and maximum wave-1 amplitude (c) and minimum centroid latitude (d) for the 2006 displaced vortex event. The vortex edge contour, equivalent ellipse, and centroid latitude are shown as Figure 3.1.

1468 between the vortices at the time of maximum aspect ratio. The wave-2 amplitude is  
1469 greatest at the earlier time, however, because the vortices (particularly the eastern vor-  
1470 tex) are stronger. Similarly for the 2006 event, at the time of maximum wave-1 ampli-  
1471 tude the vortex is not displaced far from its average position but its strength means that  
1472 the wave-1 amplitude is greater than the much more displaced vortex found later. Gen-  
1473 erally, the sensitivity of wave amplitudes to vortex strength means that wave amplitdes  
1474 may actually decline during periods of intense wave breaking due to the weakening of  
1475 the vortex, even if that vortex is significantly distorted.

1476 Overall, these results show that as the vortex departs from zonal symmetry linear  
1477 wave theory breaks down and changes in the wave-1 and wave-2 amplitudes cannot be  
1478 simply interpreted as changes in the position and elongation of the vortex respectively.

1479

## CHAPTER 4

1480

---

1481

### Representation of vortex variability in climate models

1482

---

1483

## 4.1 Introduction

1484 Over the past decade an increasing number of climate models have included a well-  
1485 resolved stratosphere, with model lids above the stratopause. For example, the fifth  
1486 Coupled Model Intercomparison Project (CMIP5) [*Taylor et al., 2012*] includes 15 mod-  
1487 els with an uppermost level above the stratopause, whereas the previous intercompar-  
1488 ison project, CMIP3, includes only five [*Cordero and Forster, 2006*]. The CMIP5 model  
1489 simulations are significant in that they are evaluated in the the Intergovernmental Panel  
1490 on Climate Change (IPCC) Fifth Assessment Report (AR5) [*Stocker et al., 2013*]. This  
1491 change in model stratospheric resolution has been largely motivated by an increased  
1492 understanding of the stratosphere’s influence on tropospheric climate (discussed in  
1493 *Gerber et al. [2012]* and Chapters 2 and 3).

1494 The effect of this greater stratospheric resolution was studied by *Charlton-Perez*  
1495 *et al. [2013]*, who compared stratospheric variability between high-top and low-top  
1496 models within the CMIP5 ensemble (they defined “high-top” as a model lid above 1 hPa,  
1497 and “low-top” below). They found that the low-top models have a weaker and less  
1498 realistic representation of daily to interannual polar stratospheric variability than high-  
1499 top models, and attributed this to the fact that the low-top models simulate fewer

1500 SSW events than high-top. This is combined with a slightly weaker tropospheric NAM  
 1501 response in the two months following SSW events in the low-top compared to high-top  
 1502 models.

1503 These results are supported by similar studies which compared natural variability  
 1504 in high and low-top versions of the same model. *Cagnazzo and Manzini* [2009] found  
 1505 that a high-top model gave a more realistic representation of the influence of ENSO  
 1506 on the NH extratropical stratosphere. Similarly, *Hardiman et al.* [2012b] showed the  
 1507 influence of the QBO on the extratropics as well as decadal trends in the NAO were  
 1508 more realistically simulated by the high-top than the low-top model. These differences  
 1509 have again been linked to the different simulation of SSW events in high- and low-top  
 1510 models [*Sassi et al.*, 2010].

1511 Other studies have compared simulations of climate change with high- and low-top  
 1512 models. *Huebener et al.* [2007] linked a increased weakening of the stratospheric polar  
 1513 vortex in high-top simulations to a more southward shift of the NH winter storm track,  
 1514 which in turn affects trends in North Atlantic temperatures and precipitation. *Manzini*  
 1515 *et al.* [2014] investigated climate change simulations of high- and low-top models in  
 1516 the CMIP5 ensemble. They found that the inter-model spread in the simulation of  
 1517 changes of stratospheric polar vortex winds accounts for a significant fraction of the  
 1518 inter-model spread of trends in the surface NAM under climate change. Interestingly,  
 1519 *Manzini et al.* [2014] also show that global surface temperature trends under climate  
 1520 change (and so climate sensitivity) are larger for high-top compared to low-top models.  
 1521 However, when comparing pairs of high- and low-top versions of the same (or similar)  
 1522 models, little climate sensitivity difference is detected, and they conclude that this  
 1523 difference is unlikely to have a physical basis.

1524 Despite these findings about the differences between high- and low-top models, it  
 1525 is important to note that a model lid above the stratopause is not a sufficient condition  
 1526 for the accurate representation of stratospheric processes or stratosphere-troposphere  
 1527 coupling. Indeed, *Charlton-Perez et al.* [2013] found that the frequency of SSWs in  
 1528 high-top CMIP5 models varies widely, from about 2.5 to 8 events per decade.

#### 4.1. INTRODUCTION

In this chapter we apply the methods developed in Chapter 3 to evaluate the representation of stratospheric polar vortex variability in the CMIP5 climate models. Motivated by these results which demonstrate a more realistic representation of tropospheric and stratospheric climate in high-top models, we select only models with a lid height above the stratopause. In doing this we extend the work of *Charlton-Perez et al. [2013]* to consider the two-dimensional structure of the polar vortex using moment diagnostics, including the identification of split and displaced vortex events.

The only previous study to apply vortex moment diagnostics to climate model simulations is that of *Mitchell et al. [2012]*. They studied models from the second Chemistry-Climate Model Validation (CCMVal-2) project, although their analysis was limited because only three models of the 18 in CCMVal-2 provided the daily PV which was necessary for the calculation of moment diagnostics. They also did not classify split and displaced vortex events in their analysis, instead focussing on the mean state of the vortex. Using the new methods developed in Chapter 3, we are now able to calculate moment diagnostics and classify split and displaced vortex events using geopotential height from a much larger number of models.

There are three main objectives to this investigation. First, we wish to evaluate the current state of models' representation of the stratospheric polar vortex and stratosphere-troposphere coupling, including whether there are any consistent biases among models. Second, we aim to determine if there is a relationship between model parameters (such as horizontal and vertical resolution) and biases in their representation of vortex variability. This may motivate future model improvements to reduce these biases. Third, we will investigate whether the increased sample size of the CMIP5 ensemble can be used to better understand the mechanism behind the different tropospheric response to split and displaced vortex events, which was described in Chapter 3.

### 1555 4.1.1 CMIP5 model simulations

1556 For this analysis only climate models with a lid height above the stratopause are se-  
 1557 lected from the CMIP5 ensemble. In total, 13 such models were available from 8 dif-  
 1558 ferent modelling centres. Although another two (CESM1-WACCM and MIROC-ESM)  
 1559 are listed in the CMIP5 ensemble, appropriate data was not found to be available  
 1560 for these models in the CMIP5 archive (<http://pcmdi3.llnl.gov/esgcet/home.htm>). These models are listed in Table 4.1. It can be seen that 12 of the 13 models  
 1561 have an uppermost level which is in the upper mesosphere (70-80 km), but CanESM2  
 1562 has a significantly lower lid which is very close to the stratopause.  
 1563

1564 Historical simulations have been used throughout this analysis. These include ob-  
 1565 served climate forcings, such as from greenhouse gasses, ozone depletion, land-use  
 1566 change, tropospheric and stratospheric aerosols and solar variability. The simulation  
 1567 period considered is limited to 1958-2005, so that it coincides with the ERA-40/ERA-  
 1568 Interim reanalysis period (CMIP5 historical simulations end at 2005). Limiting the  
 1569 model simulation analysis to the same period as reanalysis may be important because  
 1570 several studies have suggested that external forcing, such as volcanic eruptions and so-  
 1571 lar variability, has a significant impact on stratospheric variability [e.g., Robock, 2000;  
 1572 Gray *et al.*, 2010]. In order to achieve the largest possible ensemble size, all available  
 1573 ensemble members have been used for each model, which leads to different numbers  
 1574 of years entering the ensemble from different models. This does, however, necessitate  
 1575 that any results appearing in the ensemble mean should also be checked against the  
 1576 results from each individual model to ensure that it is not biased by a particular model.

## 1577 4.2 Vortex mean state and variability

### 1578 4.2.1 Moment diagnostics

1579 The centroid latitude and aspect ratio moment diagnostics are calculated for each of the  
 1580 CMIP5 models over DJFM from the 10 hPa geopotential height field, using the method  
 1581 described in Section 3.3.2. For each model the value of the DJFM mean geopotential

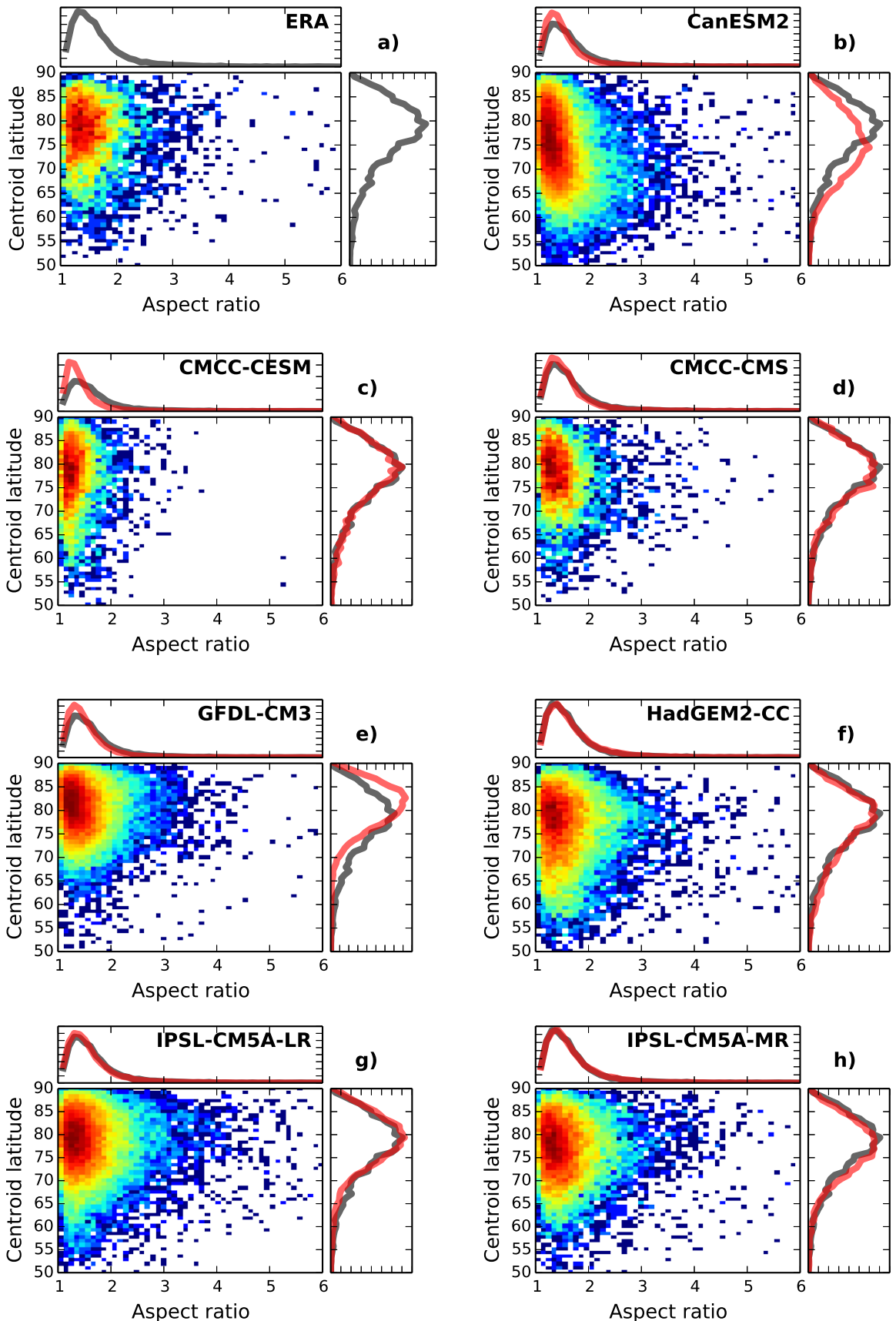


**Figure 4.1:** Distributions of centroid latitude and aspect ratio for the ERA (grey lines) (a) and the CMIP5 models (red lines). Joint distributions are shown with a logarithmic scale such that red squares represent the densest regions.

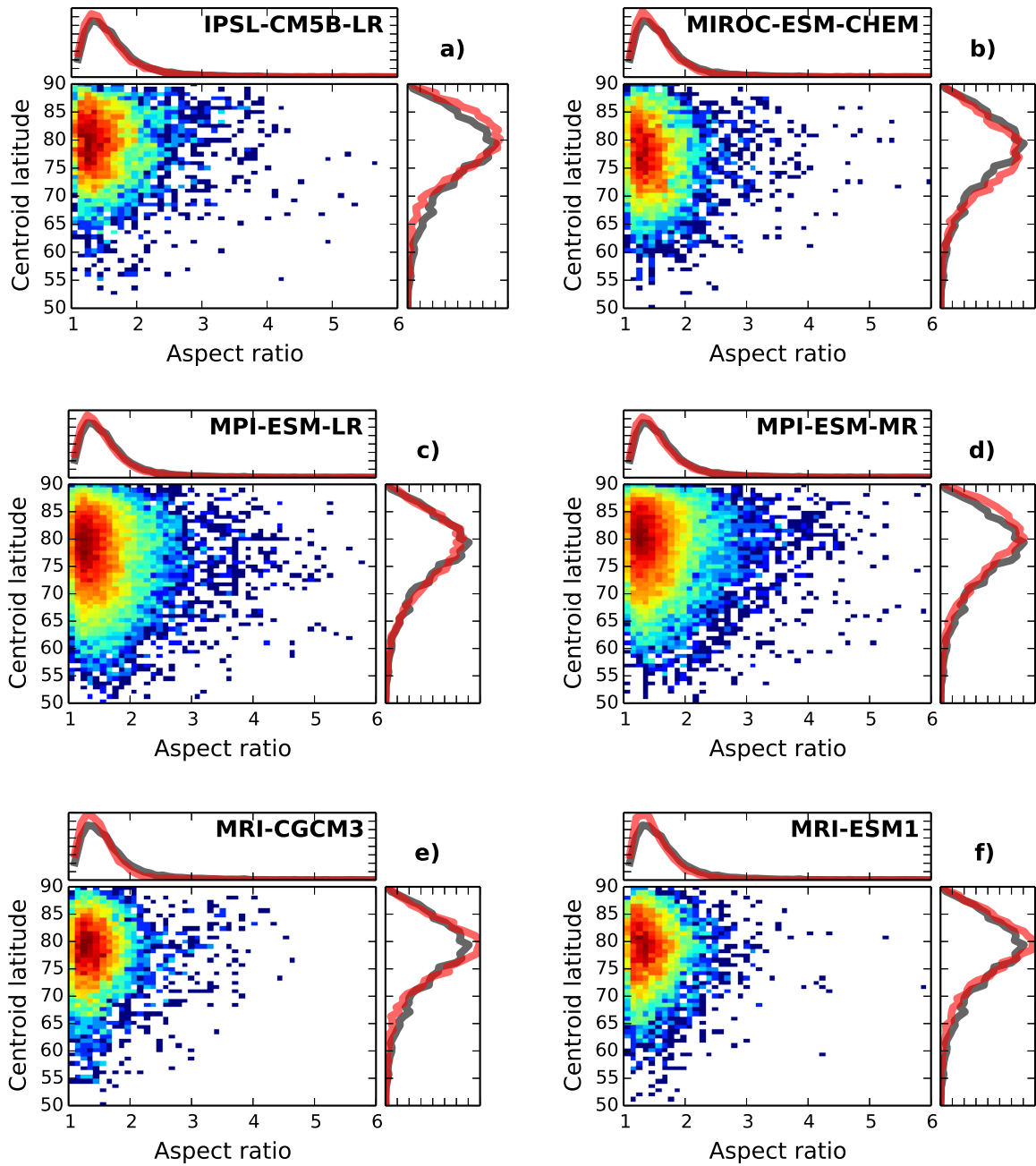


**Figure 4.1:** (Continued)

#### 4.2. VORTEX MEAN STATE AND VARIABILITY

Model	Ensemble size	Lid/ km	Levels	dh/km	dz <sub>1</sub> /km	dz <sub>2</sub> /km
CanESM2	5	48.1	35	268	1.48	2.30
CMCC-CESM	1	80.6	39	536	1.49	1.89
CMCC-CMS	1	80.6	95	268	0.65	0.68
GFDL-CM3	5	76.3	48	191	1.32	1.75
HadGEM2-CC	3	84.1	60	144	0.82	1.18
IPSL-CM5A-LR	5	70.4	39	254	1.21	1.75
IPSL-CM5A-MR	3	70.4	39	169	1.21	1.75
IPSL-CM5B-LR	1	70.4	39	254	1.21	1.75
MIROC-ESM-CHEM	1	87.8	80	399	0.77	0.73
MPI-ESM-LR	3	80.6	47	268	0.87	1.70
MPI-ESM-MR	3	80.6	95	268	0.65	0.68
MRI-CGCM3	1	80.6	48	107	0.88	1.87
MRI-ESM1	1	80.6	48	107	0.88	1.87

**Table 4.1:** Parameters of the CMIP5 models studied in this chapter. Where the model lid is defined in terms of a pressure, its height was estimated using  $z = -H \ln(p/p_0)$  with  $H = 7$  km and  $p_0 = 1000$  hPa. Following [Anstey et al. \[2013\]](#), horizontal resolution, dh, is estimated at 45°N and vertical resolution is shown averaged over two regions; 5-15 km (dz<sub>1</sub>) and 15-30 km (dz<sub>2</sub>).

height at 60°N and 10 hPa is used to define the appropriate contour for the calculation of the moment diagnostics. This accounts for biases in the mean geopotential height between different models.

The resulting joint distributions of daily centroid latitude and aspect ratio from each of the models are shown in Figure 4.1, along with that from the ERA-40/ERA-Interim reanalysis (hereafter ERA) calculated in Chapter 3. For each model the joint distribution histogram is plotted with a logarithmic colour scale which is normalised according to the number of days entering each box. As discussed in Chapter 3, it can be seen that the joint distribution for ERA has an approximately triangular distribution with high aspect ratio/poleward centroid latitude, and low aspect ratio/equatorward centroid latitude being relatively more common than high aspect ratio/equatorward centroid latitude. This shape of distribution is well replicated by most of the models, although CanESM2 has a significantly different shape, with the high aspect ratio/equatorward centroid latitude being more common.

No clear consistent biases among models emerge from this analysis. CanESM2 has a modal centroid latitude which is about 5° too far equatorward compared to ERA.

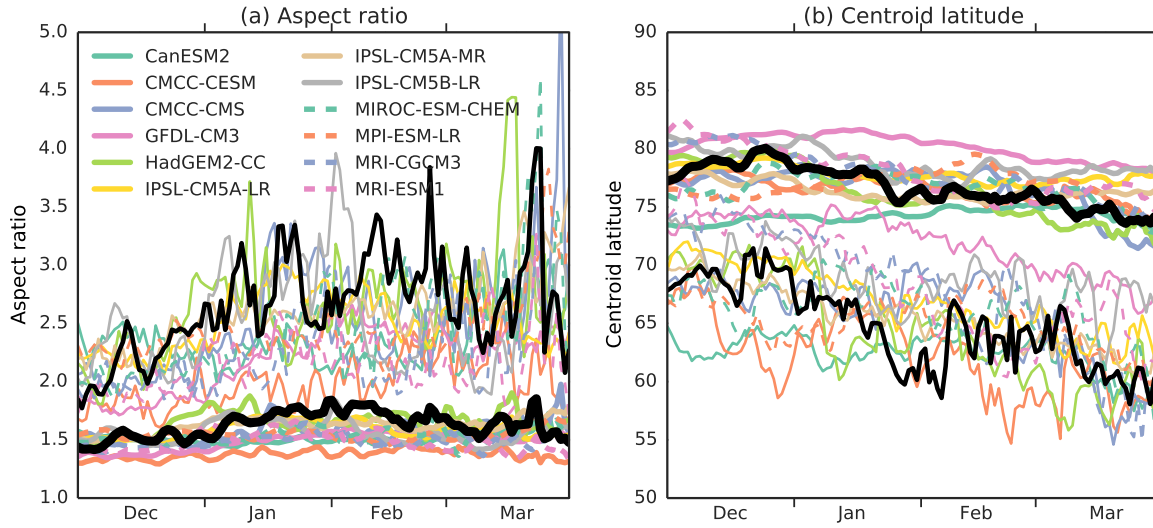


**Figure 4.2:** Seasonal cycle of aspect ratio and centroid latitude in ERA (black) and the CMIP5 models (colours). Thick lines represent the mean and thin lines the 95th or 5th percentile for aspect ratio and centroid latitude respectively.

1598 Contrastingly, GFDL-CM3 has a modal centroid latitude about  $2.5^{\circ}$  more poleward than  
 1599 observed. CMCC-CESM displays a clear bias in the aspect ratio, with a distribution  
 1600 much less skewed towards high values than in reanalysis.

1601 The winter seasonal cycle of aspect ratio and centroid a latitude in the CMIP5 mod-  
 1602 els is shown in Figure 4.2. For the mean aspect ratio and centroid latitude, the majority  
 1603 of models agree well with reanalysis. CMCC-CESM has a consistently too low mean as-  
 1604 pect ratio, while GFDL-CM3 has a consistently too poleward mean centroid latitude,  
 1605 indicating that these biases are not strongly seasonally dependent. On the other hand,  
 1606 the large equatorward bias in the CanESM2 mean centroid latitude is much larger in  
 1607 December and early January than later in winter. The 95th percentile of aspect ratio is  
 1608 lower than reanalysis for the majority of models throughout the season, indicating that  
 1609 models have, on average, too little variability in aspect ratio

## 1610 4.2.2 Displaced and split vortex events

1611 Displaced and split vortex events are identified within the CMIP5 ensemble using the  
 1612 threshold-based method developed in Section 3.3.3. The same thresholds as used for  
 1613 ERA ( $66^{\circ}\text{N}$  for centroid latitude and 2.4 for aspect ratio) are used for the models in

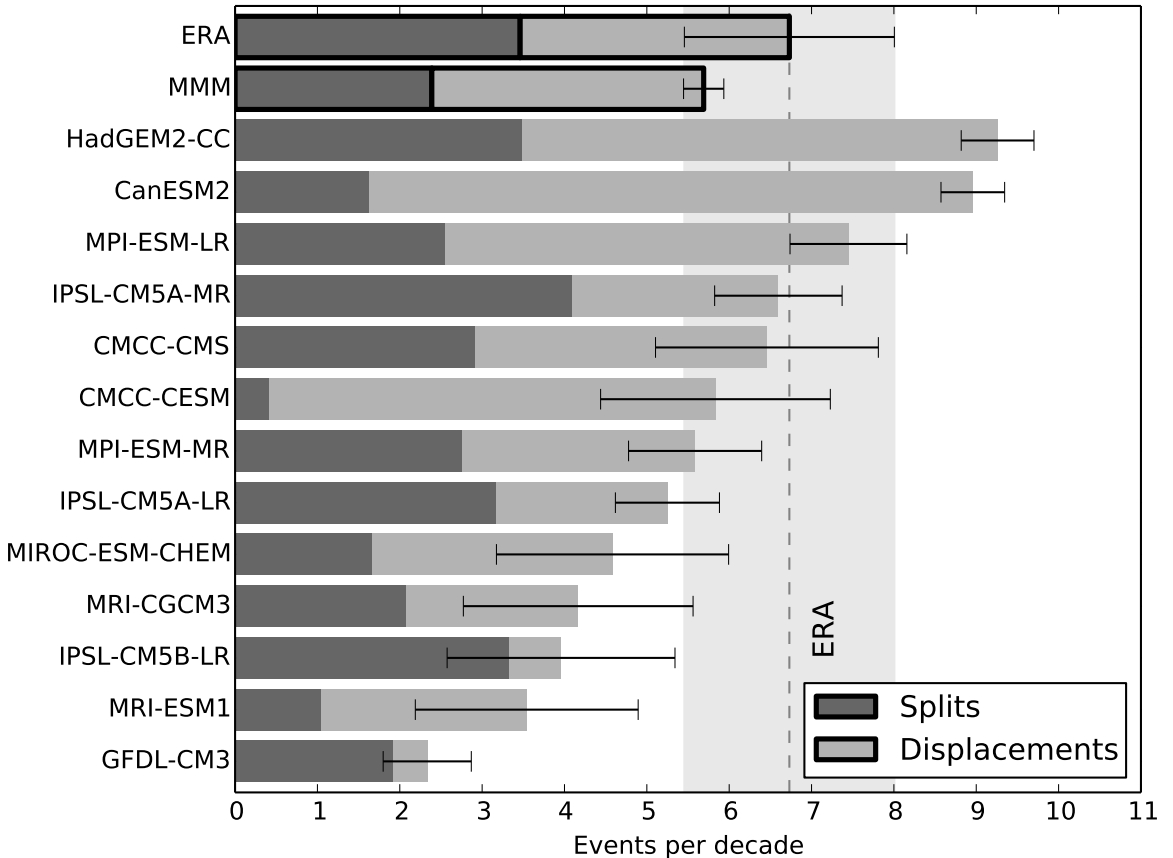


**Figure 4.3:** Frequency of split and displaced vortex events in the CMIP5 models, ERA, and the multi-model mean (MMM). Error bars are for the frequency of all events, and represent one  $\sigma$  range, assuming a binomial distribution of events. The grey shaded region represents the one  $\sigma$  range for ERA, along with the mean (dashed line.)

order to identify, as much as possible, geometrically equivalent events. The same persistence of 7 days was also used. The frequency of displaced and split vortex events for each model is shown in Figure 4.3.

The total frequency of displaced and split vortex events for each of the CMIP5 models agrees well with the equivalent SSW frequency calculated by *Charlton-Perez et al. [2013]*, who identified events based on the reversal of zonal-mean zonal wind at 60°N and 10 hPa. They also found HadGEM2-CC to have the highest frequency of events within the CMIP5 ensemble, while MRI-CGCM3 is the model with the lowest frequency of SSWs in their study (excluding GFDL-CM3 and MRI-ESM1 which *Charlton-Perez et al. [2013]* did not analyse, MRI-CGCM3 is the second-lowest frequency in the present

study). This similarity between *Charlton-Perez et al.* [2013] and the present study indicates that the close relationship between moment diagnostics-defined events and SSWs defined by zonal-mean zonal wind, as described in Chapter 3, also holds for climate models (although this is not explicitly studied here).

As well as the large differences in the total frequency of displaced and split vortex events, it can be seen in Figure 4.3 that the ratio of frequencies of these events varies significantly between models. For instance CanESM2 and CMCC-CESM simulate almost entirely displaced vortex events, while IPSL-CM5B-LR and GFDL-CM3 simulate almost entirely split vortex events. In the multi-model mean (MMM) these biases largely cancel, to give a approximately equal ratio of displaced to split vortex events, which is in agreement with reanalysis.

The seasonal distribution of these displaced and split vortex events is illustrated in Figure 4.4. Some models (CMCC-CMS, HadGEM2-CC and IPSL-CM5A-LR) replicate the observed distribution, with split vortex events being more likely in early winter, and displaced vortex events in late winter. Other models, however, have a very different distribution of events. CanESM2, CMCC-CESM and MPI-ESM-LR all show little seasonal variability in the frequency of events.

It is now considered how model biases in the climatology of the stratospheric polar vortex, discussed in Section 4.2.1, affect the frequency of split and displaced vortex events. The climatological average state of the vortex is defined by the mode – the peak of the probability distribution function – of the aspect ratio and centroid latitude. Unlike the mean, this quantity is not affected by extreme values and it represents the most likely state of the vortex. The peak can be estimated by the maximum value of a histogram, however this introduces significant random errors and is sensitive to the selection of bin size. A more accurate estimation of the mode can be made by fitting the aspect ratio and centroid latitude with a theoretical distribution and then finding the peak of that distribution. Following *Mitchell et al.* [2011], we fit the aspect ratio with a generalised extreme value (GEV) distribution of the form

$$f(x; \mu, \sigma, \xi) = \frac{a^{(-1/\xi)-1}}{\sigma} e^{-a^{-1/\xi}}, \quad (4.1)$$

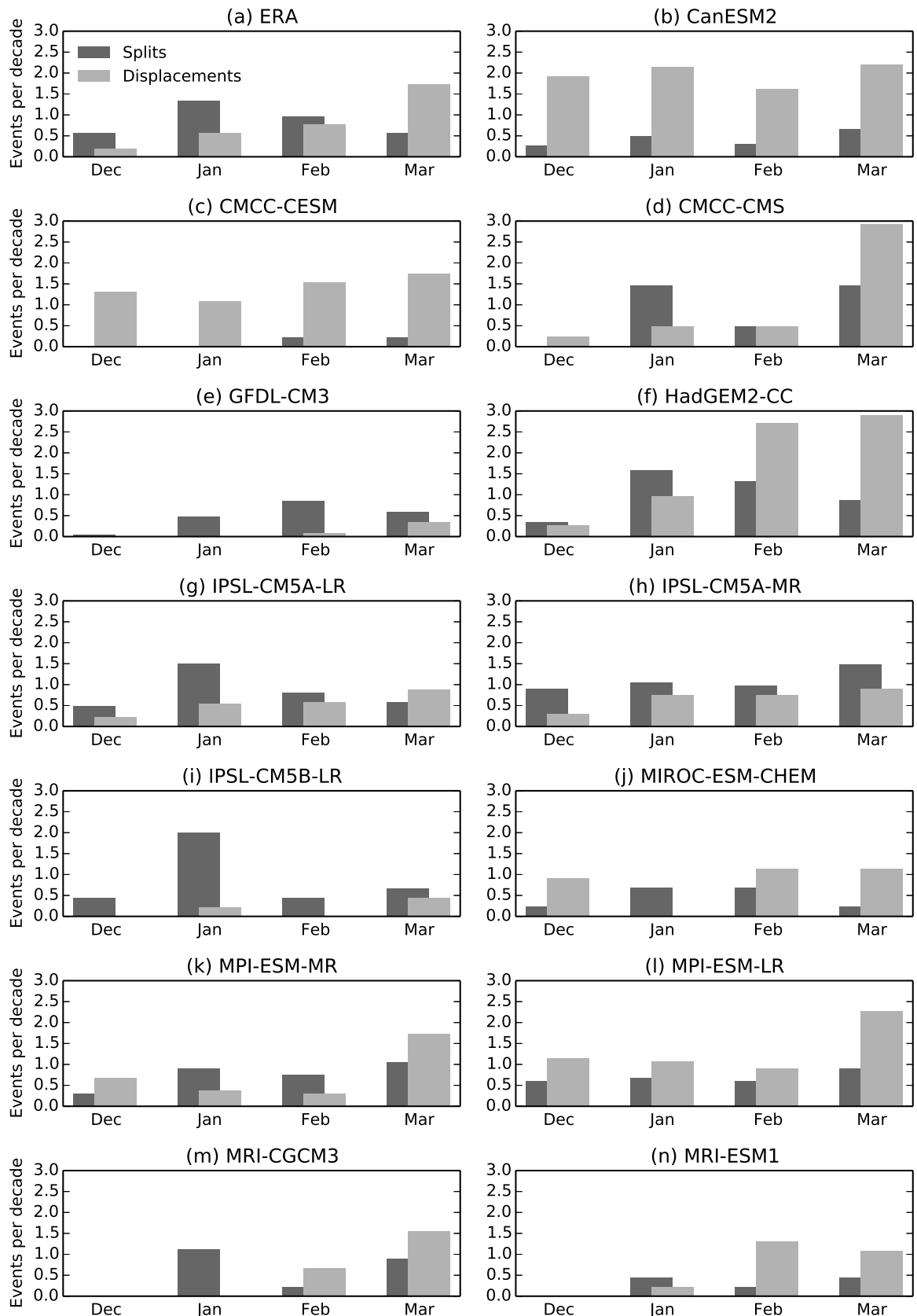


**Figure 4.4:** Seasonal distribution of the occurrence of split and displaced vortex events in ERA (a) and the CMIP5 models.

with

$$a = 1 + \xi \frac{x - \mu}{\sigma}, \quad (4.2)$$

where  $\mu$  determines the position of the peak along the  $x$ -axis,  $\sigma$  determines the variance of the distribution and  $\xi$  the skewness. These parameters are determined using the method of maximum-likelihood estimation [Wilks, 2006]. This method is also used to fit a Gaussian distribution of the form

$$f(x; \mu, \sigma) = \frac{1}{\sigma \sqrt{2\pi}} \left( -\frac{(x - \mu)^2}{2\sigma^2} \right), \quad (4.3)$$

1641 where  $\mu$  determines the position of the peak along the  $x$ -axis and  $\sigma$  is the standard  
 1642 deviation, to the cube of the centroid latitude, and then the cube root taken to return  
 1643 the original distribution (this is carried out because an analytic distribution does not fit  
 1644 the unscaled centroid latitude). Mitchell *et al.* [2011] found that these distributions ac-  
 1645 curately fit the histograms of centroid latitude and aspect ratio in reanalysis data, apart  
 1646 from the extreme tails of the distribution. Qualitative inspection of the distribution for  
 1647 each model confirms that they also provide a similarly good fit to each of the model's  
 1648 histograms.

1649 Figure 4.5 shows the relationship between the modal aspect ratio and centroid  
 1650 latitude and frequency of split and displaced vortex events. It can be seen that strong  
 1651 linear relationships exist; the modal aspect ratio accounts for 79% of the variance in  
 1652 the frequency of split vortex events and the modal centroid latitude accounts for 76%  
 1653 of the variance in the frequency of displaced vortex events. This demonstrates that  
 1654 biases in the most likely state of the vortex account for the vast majority of inter-model  
 1655 spread in the representation of extremes. An implication of this is that the models are  
 1656 consistent in their representation of the variability of aspect ratio and centroid latitude,  
 1657 relative to the model climatology.

1658 It can also be seen in Figure 4.5 that the values for ERA lie very close to the best fit  
 1659 lines of the CMIP5 models. This implies that the accuracy of a model's representation  
 1660 of the frequency of displaced and split vortex events can be significantly improved by  
 1661 a more accurate average vortex state. Furthermore, while the ERA value for modal

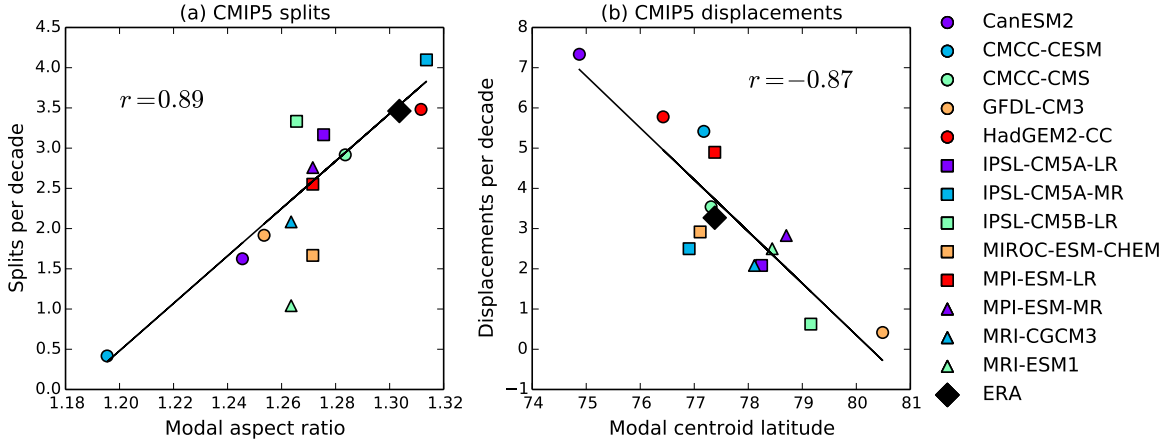


**Figure 4.5:** Comparison of the DJFM mean aspect ratio with frequency of split vortex events (a) and DJFM mean centroid latitude with frequency of displaced vortex events (b) in the CMIP5 ensemble and ERA. Linear best fits and the correlation coefficients for all the models are also shown.

1662 centroid latitude lies approximately in the middle of that for the CMIP5 models, only  
 1663 two models have a larger modal aspect ratio than ERA, indicating that a too circularly-  
 1664 symmetric vortex is a common bias among models.

1665 The structure of the stratospheric polar vortex during split and displaced vortex  
 1666 events in the CMIP5 ensemble is shown in Figure 4.6. This displays composites of  
 1667 10 hPa geopotential height at the onset date of the events for each model. It can  
 1668 be seen that the majority of models accurately reproduce splitting events as occurring  
 1669 along the 90°W-90°E axis, and displacement events with a vortex shifted towards Scan-  
 1670 dinavia and Siberia. CanESM2 is an exception to this, with split vortex events which  
 1671 are elliptical but centred quite far from the pole. The IPSL-CM5B-LR model shows  
 1672 a composite for displaced vortex events which actually appears as an uneven split,  
 1673 although this composite only consists of three events so is not statistically significant.  
 1674 There is also significant inter-model spread in the relative strengths of the Aleutian and  
 1675 Azores highs during split vortex events. Several models (GFDL-CM3, IPSL-CM5A-LR,  
 1676 IPSL-CM5B-LR, MRI-ESM1) show an approximately equal strength Aleutian and Azores  
 1677 highs, while others (CMCC-CMS, HadGEM2-CC, IPSL-CM5A-MR, MPI-ESM-LR, MPI-  
 1678 ESM-MR, MRI-CGCM2) show a weaker Azores high, which is in closer agreement with

reanalysis. The more symmetrical Aleutian and Azores highs indicate a greater dominance of wave-2 activity in split vortex events than is found in observations, where not all split vortex events are dominated by wave-2 activity [Waugh, 1997; Mitchell *et al.*, 2013].

### 4.2.3 Wave diagnostics

Given the common bias among the CMIP5 models towards low aspect ratios, it might be suspected that the models have too little wave-2 activity. The relative magnitudes of wave-1 and wave-2 planetary waves are diagnosed using the same method described in Appendix 3.A. In order to determine the climatological wave activity for each model, the resulting distributions of daily wave amplitudes were fitted with a GEV distribution using maximum-likelihood estimation, and the peak of that distribution determined, as in the previous section. A GEV distribution was found to be a good fit for the distributions of each model. As previously, this method has the advantage of determining the ‘most-likely’ wave amplitude, and unlike the mean it is not affected by large extreme values.

The resulting ratios of wave-2 to wave-1 amplitude for each of the CMIP5 models and ERA are shown in Figure 4.7(a). ERA is seen to lie approximately in the middle of the models; 7 models have a greater ratio, and 6 models lesser. The same ratio of wave amplitude was calculated by Butchart *et al.* [2011] for the CCMVal-2 models. They found a bias towards a relative lack of wave-2 activity, with 13 of 17 models having a lower ratio than reanalysis. The current results show that this bias is not present among the high-top CMIP5 ensemble, and so the bias towards low aspect ratio cannot be attributed to a relative lack of wave-2 activity (this is also true of the absolute value of wave-2 amplitude, in which 5 of 13 models have a lower value than ERA).

Comparing Figures 4.7(a) and 4.5(a), it can be seen that the model with the lowest ratio of wave amplitudes (CMCC-CESM) also has the lowest aspect ratio, while the model with the highest ratio (IPSL-CM5B-LR) has the highest aspect ratio. However, across all models the amplitudes of the individual wavenumbers are not significantly correlated with either the modal aspect ratio or the centroid latitude. This suggests

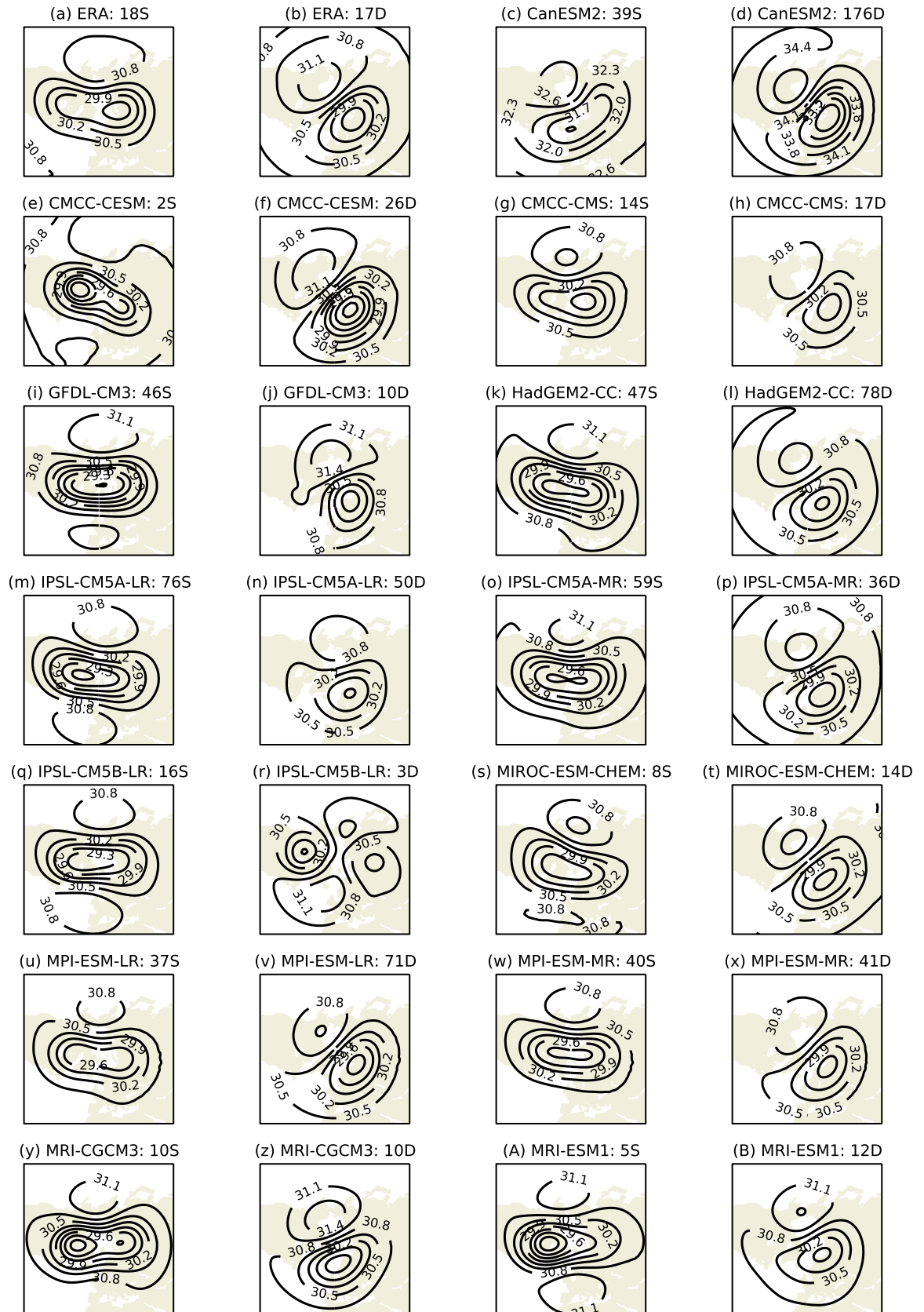


**Figure 4.6:** Composites of 10 hPa Z at the onset date of split (S) and displaced (D) vortex events in ERA (a,b) and the CMIP5 models. The number of events entering the composite and their type are shown in the title of each plot. The contour interval is 0.3 km.

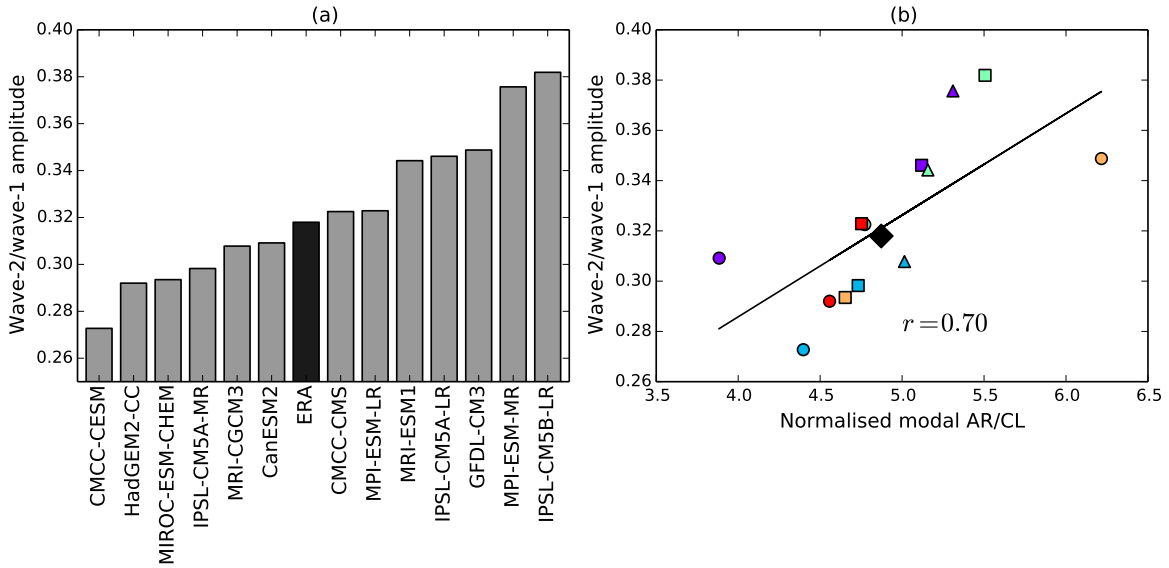


**Figure 4.7:** (a) Ratio of zonal wavenumber-2 to wave-1 amplitude, calculated from the DJFM daily geopotential height field at  $60^{\circ}\text{N}$ , 10 hPa. Amplitudes are calculated from the peak of a GEV distribution fitted to the relevant histogram. (b) Ratio of wave amplitudes against the normalised ratio of modal aspect ratio to modal centroid latitude. Normalisation scales the aspect ratio and centroid latitude by their respective standard deviations. Additionally, the centroid latitude is expressed as the deviation from the pole. Points are coloured as Figure 4.5.

that wave-1 activity does not exclusively affect centroid latitude, nor wave-2 exclusively affect aspect ratio, as was found by [Waugh \[1997\]](#) and discussed in Appendix 3.A. Rather, it is the relative wave amplitudes that affect the relative aspect ratio and centroid latitude climatologies. This is demonstrated in Figure 4.7(b), which shows the ratio of wave amplitudes against the ratio of aspect ratio to centroid latitude. In order that the ratio of moment diagnostics is not biased towards a particular quantity, it is normalised by dividing each of aspect ratio and centroid latitude by their respective standard deviations. The centroid latitude is also expressed as the deviation from the pole (this makes the correlation positive, but does not affect its magnitude). The correlation between the ratio of wave amplitudes to moment diagnostics is 0.70, which is statistically significant at the 95% level. Moreover, if the two outliers (CanESM2 and GFDL-CM3, which were shown to have an unrealistic polar vortex climatology [Figure 4.1]) are removed the correlation becomes much greater ( $r = 0.95$ ). Hence, although there is no one-to-one mapping between individual wave amplitudes and moment di-

agnostics, the ratio of wave amplitudes strongly determines the relative climatology of the moment diagnostics.

## 4.3 Stratosphere-troposphere coupling

### 4.3.1 Zonal-mean response to displaced and split vortex events

The time-height evolution of the atmosphere around split and displaced vortex events in each of the CMIP5 models is displayed in Figure 4.8. This shows composites of polar cap ( $60^{\circ}$ - $90^{\circ}$ N) geopotential height ( $Z$ ) anomalies from 90 days before to 90 days following events. The anomalies are calculated from the climatology of each day for each model. The figures extend downwards only to 500 hPa (rather than 1000 hPa). This is because models differ in their representation of geopotential height which is below ground level; some allow negative values, while others set this as an undefined value. This introduces significant errors in the calculation of a climatology and anomalies at levels where the geopotential height is occasionally below ground level. Polar cap  $Z$  is highly correlated with the NAM (calculated from zonal mean  $Z$  according to the method of *Baldwin and Thompson [2009]*) over the levels shown in Figure 4.8. *Kushner [2010]* also demonstrated composites of the NAM and polar cap  $Z$  following SSWs to be very similar. Indeed, comparing Figures 4.8 (a) and (b) with Figure 3.10 shows that the ERA composites for polar cap  $Z$  and the NAM are very similar. In Figure 4.8 the number of events entering each composite is shown in the upper right-hand corner, and it should be noted that composites of a small number of events are likely to be subject to significant statistical uncertainty.

It can be seen that there are large inter-model differences in the evolution of polar cap  $Z$  following split and displaced vortex events. For some models (e.g. CanESM2, CMCC-CMS) lower stratospheric anomalies persist for about 45 days, similar to reanalysis, while for others (e.g. IPSL-CM5A-LR, GFDL-CM3) these persist for much longer, beyond 60 days. There are also differences in the stratospheric precursors to events;

1748 while some models (e.g. CanESM2, GFDL-CM3, MRI-CGCM3) simulate a stronger neg-  
 1749 ative anomaly prior to displacement events, similar to reanalysis, others (HadGEM2-  
 1750 CC, IPSL-CM5A-MR, MRI-ESM1), show more negative anomalies prior to split vortex  
 1751 events.

1752 Most significantly, there is a large spread in the tropospheric anomalies over the  
 1753 10-90 days following split and displaced vortex events. Several models (e.g. IPSL-  
 1754 CM5A-LR, IPSL-CM5A-MR, MPI-ESM-LR) show only very weak anomalies below ap-  
 1755 proximately 200 hPa, while others (e.g., CMCC-CESM, GFDL-CM3, MRI-ESM1) show  
 1756 stronger anomalies. Among those models which do show stronger tropospheric anom-  
 1757 alies, there are also differences in the relative magnitude following split and displaced  
 1758 vortex events. For instance, for GFDL-CM3, and MRI-ESM1 tropospheric anomalies  
 1759 following displaced vortex events are stronger, while for MIROC-ESM-CHEM and MPI-  
 1760 ESM-MR anomalies following split vortex events are stronger, in closer agreement with  
 1761 reanalysis.

1762 As well as these large inter-model differences, there are also some consistent fea-  
 1763 tures among models. Almost all models show a barotropic onset to split vortex events,  
 1764 with anomalies occurring at the same time throughout the depth of the atmosphere.  
 1765 In contrast, displaced vortex events appear more baroclinic, with onset occurring first  
 1766 near the uppermost level. This is consistent with the difference found in reanalysis,  
 1767 indicating that this is likely to be a robust difference between the response to split and  
 1768 displaced vortex events. These features are also apparent in the multi-model mean  
 1769 (MMM) (Figures 4.8 C and D). This mean is calculated so as to give each event an  
 1770 equal weight (rather than each model), and so does not give undue weight to models  
 1771 with only a small number of events. On the other hand this does mean that greater  
 1772 weight is given to models with more ensemble members and more events (almost one  
 1773 third of all displaced vortex events come from CanESM2), but the difference in baro-  
 1774 clinicity of split and displaced vortex events is observed to be very consistent among  
 1775 models.

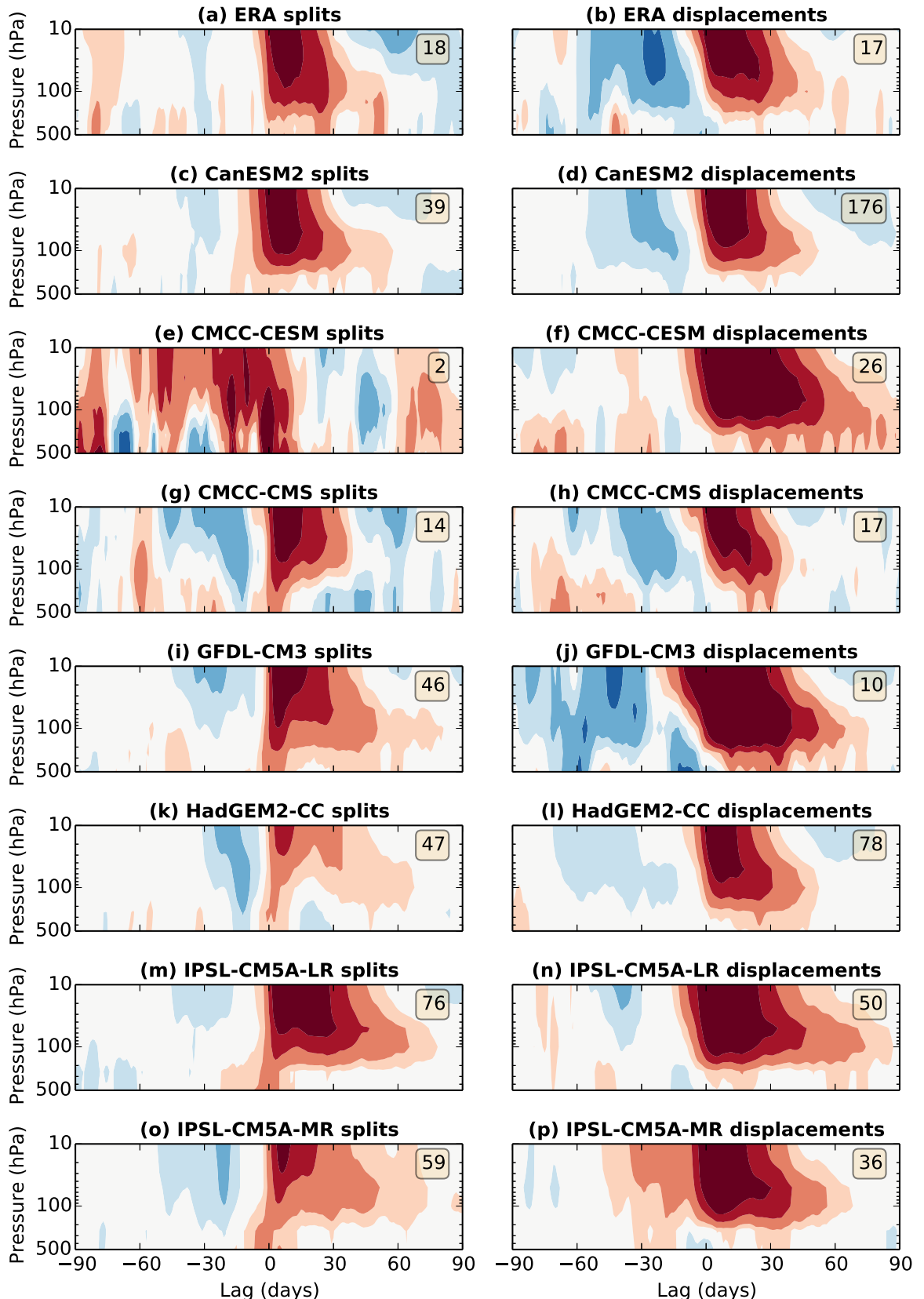


**Figure 4.8:** Composites of normalised polar cap averaged  $Z$  anomalies following split and displaced vortex events in ERA (a,b), the CMIP5 models, and the multi-model mean (C,D). Numbers in the upper right of each plot represent the number of events entering the composite.

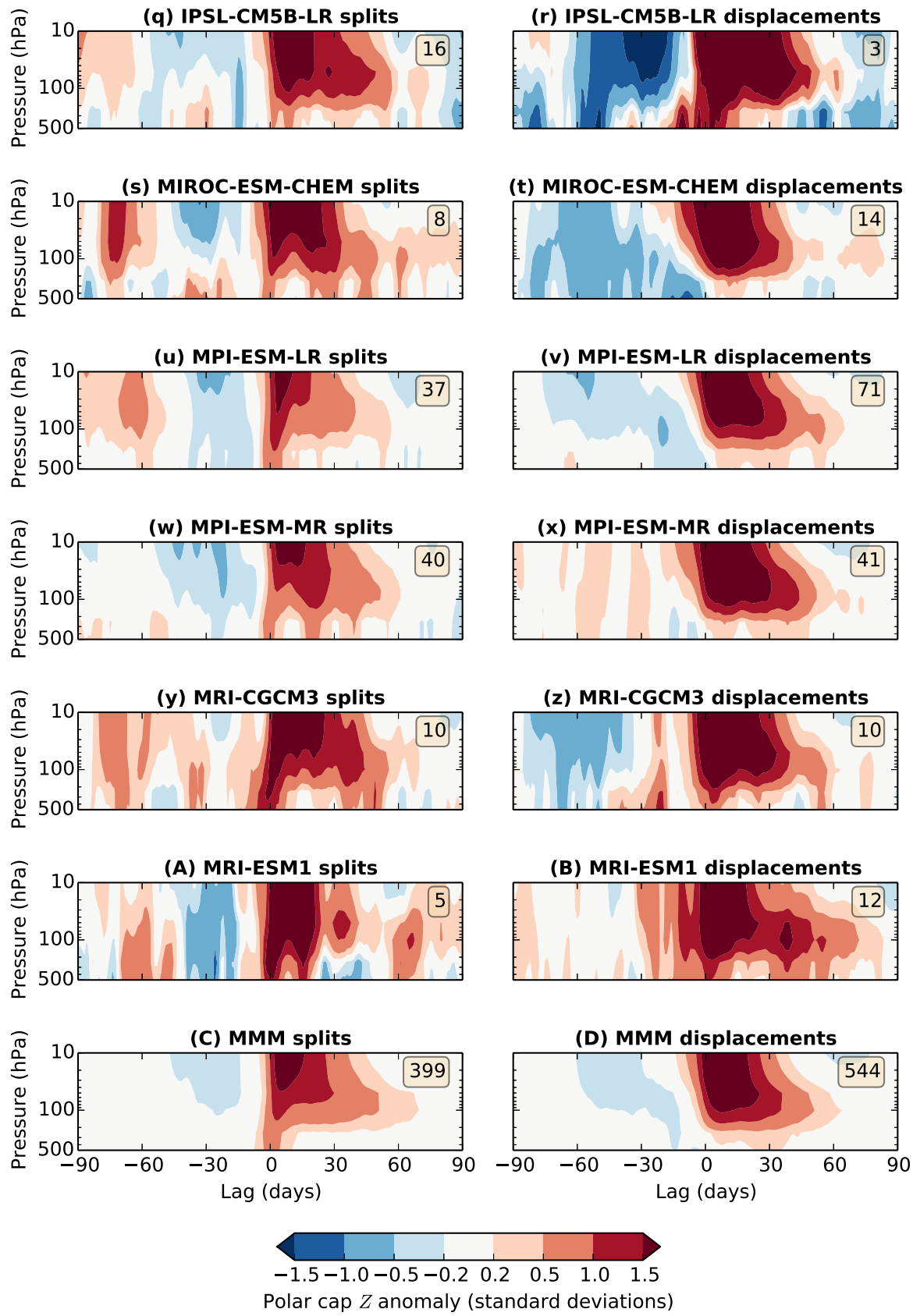


Figure 4.8: (Continued)

### 1776 4.3.2 Spatial response to displaced and split vortex events

1777 Mean sea-level pressure (MSLP) anomalies averaged over the 30 days following split  
 1778 and displaced vortex events for each of the CMIP5 models are displayed in Figure 4.9.  
 1779 Also shown are the anomalies for ERA (a,b) (the same as Figure 3.12) as well as the  
 1780 multi-model mean (c,d), again calculated so as to give each event an equal weight. The  
 1781 climatology from which anomalies are calculated is determined by a 10-day running  
 1782 mean of the average for each day of the year at each spatial location. The number of  
 1783 events entering each composite is shown, and again, care must be taken interpreting  
 1784 composites of a small number of events due to statistical uncertainty.

1785 Following both split and displaced vortex events, all models show a positive MSLP  
 1786 anomaly near the North Pole, and a negative anomaly centred over Western Europe  
 1787 and the North Atlantic. This pattern is consistent with a negative projection onto the  
 1788 North Atlantic Oscillation. Less consistent among models are anomalies over the North  
 1789 Pacific; many models (e.g. MRI-CGCM3, IPSL-CM5A-LR) show positive anomalies,  
 1790 while MPI-ESM-LR and MPI-ESM-MR have negative anomalies following both split and  
 1791 displaced vortex events. MIROC-ESM-CHEM has different sign anomalies in the North  
 1792 Pacific following split (negative) and displaced (positive) vortex events. In the multi-  
 1793 model mean, a weakly positive North Pacific anomaly is seen.

1794 This inconsistency in the Pacific anomalies has important consequences for the in-  
 1795 terpretation of zonal mean anomalies following split and displaced vortex events. For  
 1796 instance, the IPSL-CM5A-LR model shows weak tropospheric anomalies (relative to  
 1797 other models) of polar cap averaged  $Z$  following split and displaced vortex events  
 1798 (Figure 4.8 (m,n)), but a relatively strong NAO signal (Figure 4.9 (m,n)), particularly  
 1799 following split vortex events. The reason for this difference is that the model also shows  
 1800 relatively strong positive North Pacific anomalies, that to some extent cancel the North  
 1801 Atlantic anomalies in the polar cap average. Such an effect would also be seen in the  
 1802 NAM, even if calculated from non zonally-averaged  $Z$ , since the surface NAM pattern  
 1803 (the leading EOF of MSLP) has centres of action of the same sign in the North Atlantic  
 1804 and North Pacific [e.g., *Amblard et al., 2001*].

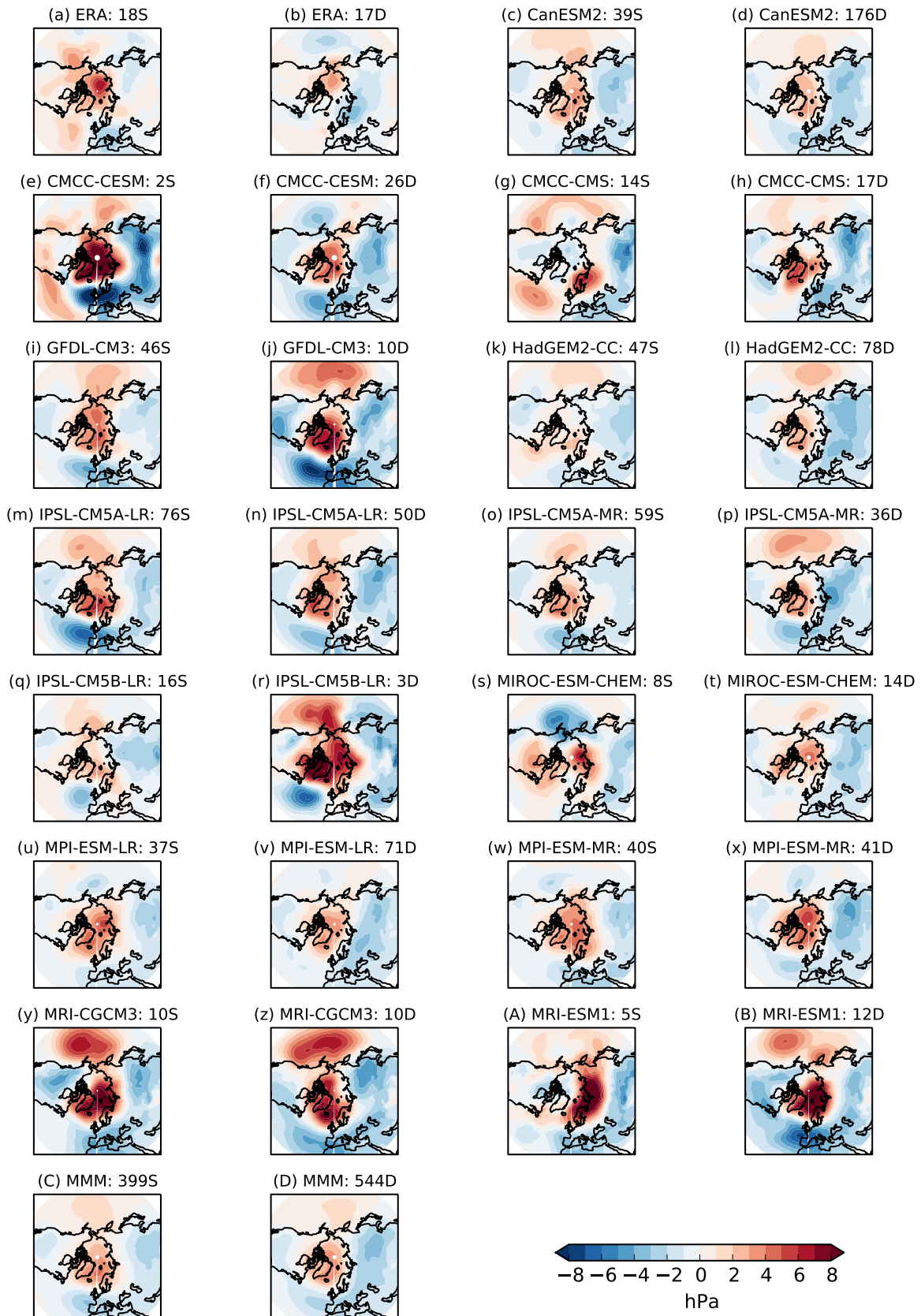


**Figure 4.9:** Composites of mean sea-level pressure anomalies averaged 0-30 days following split (S) and displaced (D) vortex events in the CMIP5 ensemble. Also shown are the ERA composite (a,b) and the multi-model mean (C,D). The multi-model mean is calculated as to give each event an equal weighting.

#### 4.3. STRATOSPHERE-TROPOSPHERE COUPLING

A robust difference found between MSLP anomalies following split and displaced vortex events in almost all models and the multi-model mean is that anomalies over Russia and Eastern Europe are more strongly negative following displaced vortex events. Indeed, the only two models which do not show this difference are CMCC-CESM and MRI-ESM1, but these models simulate only 2 and 5 split vortex events respectively, so the difference is unlikely to be statistically significant. In the multi-model mean, this difference has a magnitude of about 2-3 hPa across most of Russia. In order to understand the possible stratospheric influence on this difference, lower stratospheric anomalies are studied. Figure 4.10 shows composites of 100 hPa Z averaged over the 10 days following the onset of split and displaced vortex events. This shorter time period (rather than the 30 days used for the MSLP composites) is chosen to represent the typical time scale of a split or displacement of the vortex, which is shorter than the time scale taken for the re-formation of the vortex and return towards the climatological mean. However, it should be noted that composites taken over the 30 days show similar structure, but with reduced magnitude (not shown).

As well as the composite for each model, and the split minus displaced vortex difference, a multi-model mean is also shown in Figure 4.10 (Q,R,S). Because this is a mean of model absolute values, and models have different climatologies, the MMMs for split and displaced vortices are scaled to have the same hemispheric mean magnitude. This avoids introducing a bias in the climatology of any particular model into the MMM difference.

For all models with the exception of CanESM2, the 100 hPa Z split vortex composite shows an elliptical vortex with the major axis aligned along the 90°W-90°E line which is similar to the composite at 10 hPa (Figure 4.6). For the displaced vortex composite the 100 hPa vortex is centred over Siberia for almost all models, eastward of the 10 hPa composite which is centred over Scandinavia. This again highlights the more barotropic nature of split vortex events compared to baroclinic displaced vortex events, in which the vortex shows a westward tilt with height (as also demonstrated by *Matthewman et al. [2009]*).

1834 In the split minus displaced vortex difference, the majority of models show a large  
 1835 positive region over Russia and Eastern Europe and a negative region centred over  
 1836 northern Canada. The positive region over Siberia has a minimum, which is negative  
 1837 in some cases, located near 90°E, which is consistent with the position of minimum  
 1838 in the split vortex composite. It can be seen that the multi-model mean difference  
 1839 (Figure 4.10 (S)) is remarkably similar to the reanalysis difference (Figure 4.10), both  
 1840 in terms of the location and magnitude of anomalies. This suggests that the CMIP5  
 1841 models, on average, realistically represent the evolution of split and displaced vortex  
 1842 events through the depth of the stratosphere. Again, this result is consistent among  
 1843 the majority of models, and so not highly sensitive to the exclusion or inclusion of any  
 1844 particular model.

1845 Figure 4.11 shows the split minus displaced vortex composite difference for MSLP  
 1846 averaged 0-30 days following onset and the 100 hPa Z composite difference averaged  
 1847 0-10 days following onset, for both ERA and the CMIP5 MMM. Statistical significance in  
 1848 the MSLP difference is calculated by a two-tailed bootstrap test with the null hypothesis  
 1849 that the anomalies following split and displaced vortex events are populations from the  
 1850 same probability distribution. The following procedure is used:

- 1851 1. All events are grouped together and selected from them, with replacement, are  
 1852 two random subsets which are equal in size to the total number of split and  
 1853 displaced vortex events respectively.
- 1854 2. The difference of the averages of these two subsets is taken.
- 1855 3. The above is repeated 5000 times to form a distribution of random composite  
 1856 differences.
- 1857 4. If the actual composite difference lies lower than the 2.5% or higher than the  
 1858 97.5% levels of this distribution then it can be said there is a less than 95% chance  
 1859 that an anomaly at least this large would arise if anomalies following split and  
 1860 displaced vortex events are populations from the same distribution. Hence the  
 1861 null hypothesis can be rejected.

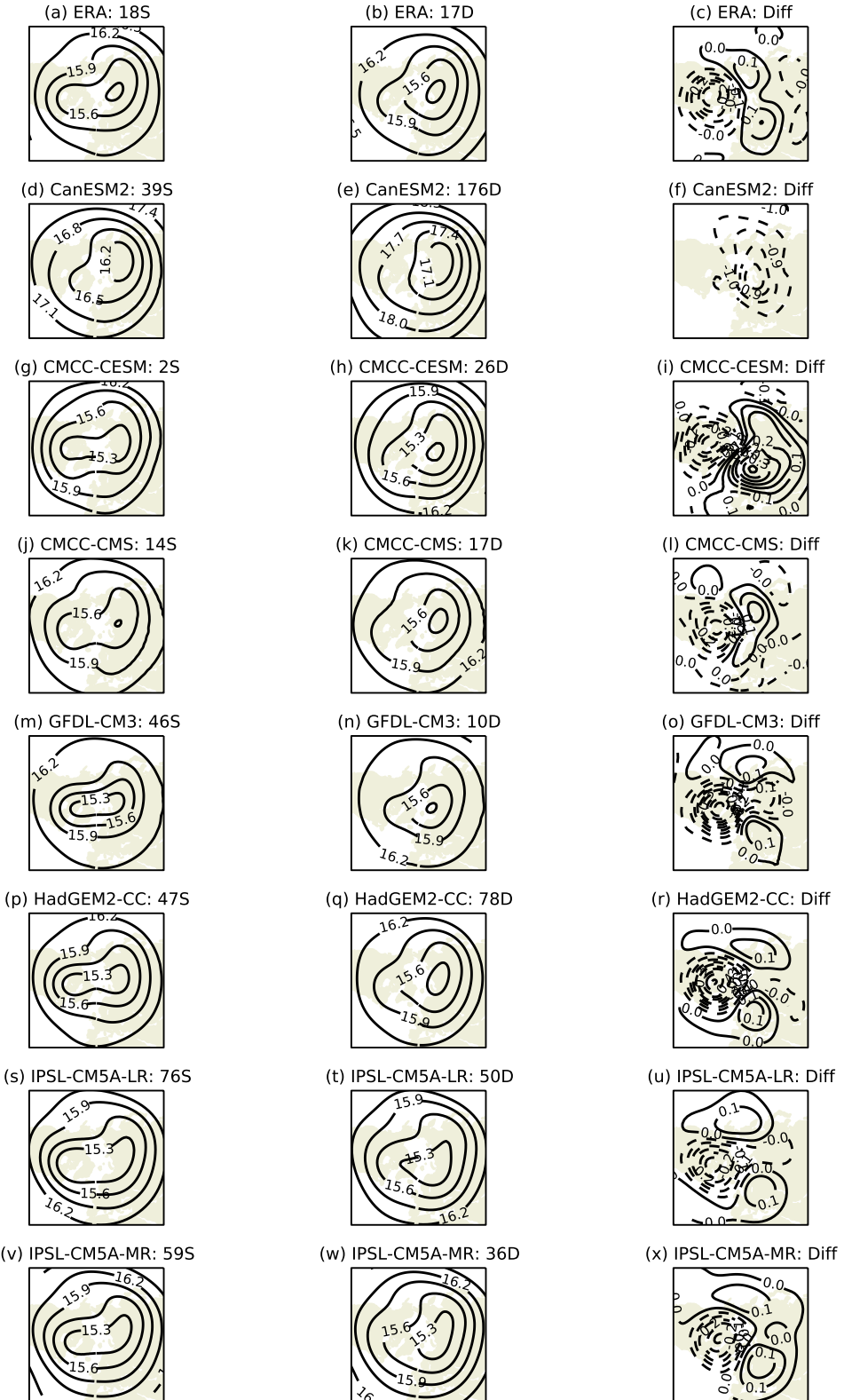


**Figure 4.10:** Composites of 100 hPa geopotential height (km) averaged in the 10 days following the onset of split (S) and displaced (D) vortex events in ERA, each of the CMIP5 models, and the multi-model mean (MMM). The right hand column displays the difference of splits minus displacements. The multi-model mean is calculated so as to give each event an equal weighting.

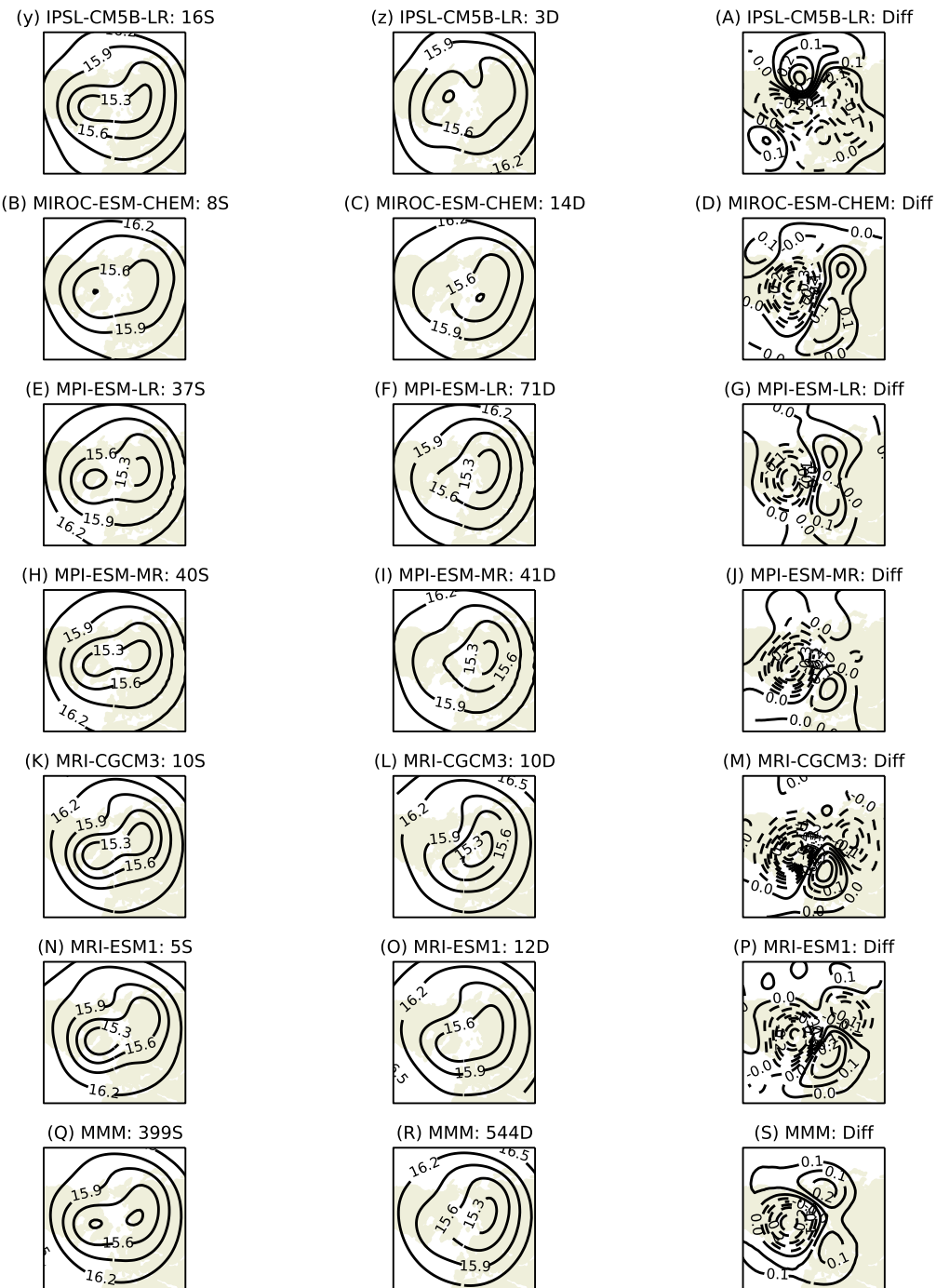


**Figure 4.10:** (Continued)

#### 4.4. DISCUSSION

1862 For the case of ERA, very little statistical significance in the composite difference is  
1863 seen, while in the CMIP5 MMM there are large statistically significant regions. This is  
1864 due to the greatly increased sample size in CMIP5; a total of 943 events compared to  
1865 just 35 in ERA.

1866 In the CMIP5 MMM difference the most significant feature is the large positive  
1867 anomaly (a result of a more negative anomaly following displaced vortex events) over  
1868 Scandinavia, Eastern Europe and Russia. There is also a significant negative anomaly  
1869 over northern Canada and a positive anomaly in the western Atlantic. This pattern  
1870 is zonally asymmetric and so does not project strongly onto the polar cap average,  
1871 therefore explaining the small difference in polar cap averaged  $Z$  (Figure 4.8 (C,D)).  
1872 The CMIP5 difference pattern also does not strongly project onto the NAO as there  
1873 is a similarly negative NAO following both split and displaced vortex events (Figure  
1874 4.9 (C,D)). For the ERA MSLP difference there are stronger negative anomalies over  
1875 Europe (although not statistically significant) and positive anomalies over the North  
1876 Pole, which does project more strongly onto the NAO, as discussed in Section 3.4.

1877 The CMIP5 difference of Figure 4.11(b) shows the positive 100 hPa  $Z$  anomalies  
1878 over Siberia over-lie the positive MSLP anomalies, while the negative 100 hPa  $Z$  over  
1879 northern Canada over-lies negative MSLP anomalies. A somewhat similar, but not sta-  
1880 tistically significant pattern is seen in ERA, although the Siberian anomaly is more pole-  
1881 wards and the negative anomaly over Canada is much weaker. Importantly, the 100 hPa  
1882 pressure surface lies close to the tropopause, and 100 hPa  $Z$  can therefore give an indi-  
1883 cation of tropopause height. Indeed, comparing the 100 hPa  $Z$  and tropopause height  
1884 anomalies for ERA (Figures 4.10 (a,b) and 3.13 (c,d)) shows that anomalous nega-  
1885 tive  $Z$  is approximately co-located with an anomalously high tropopause, although the  
1886 tropopause height field is much noisier. The implications of this result for mechanisms  
1887 of stratosphere-troposphere coupling are discussed in Section 4.4.2.

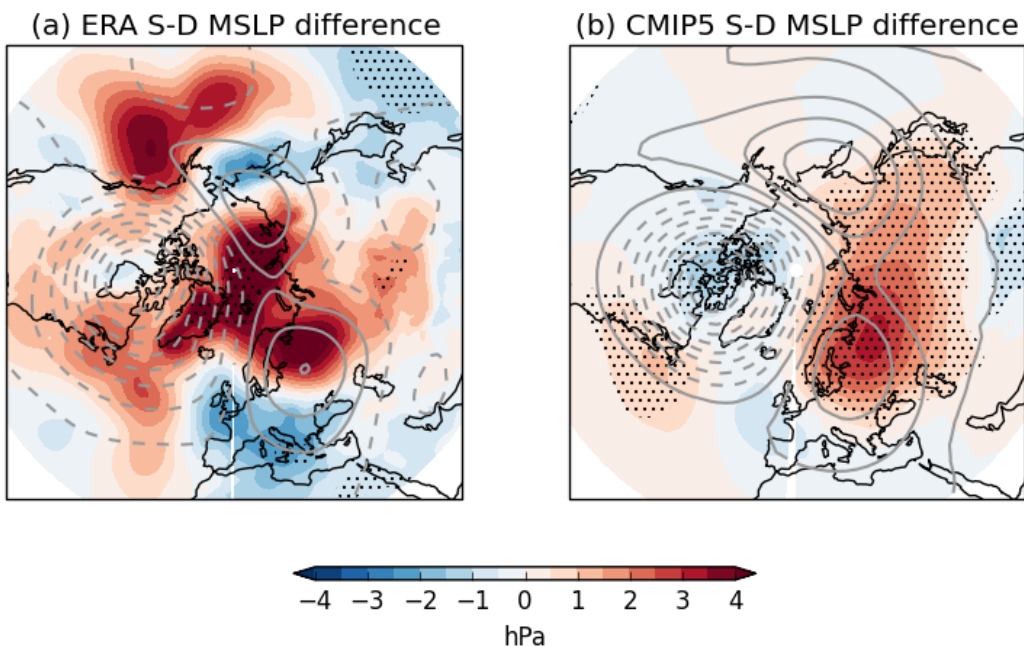


**Figure 4.11:** Difference (S-D) of composites of mean sea-level pressure averaged 0-30 days following split (S) and displaced (D) vortex events in ERA and the CMIP5 ensemble. Stippling indicates regions that are >95% significant according to a two-tailed bootstrap test. Grey contours represent the difference in 100 hPa geopotential height averaged 0-10 days following events the contour interval is 40 m, dashed contours represent negative values and the lowest magnitude contours are  $\pm 20$  m.

## 1888 4.4 Discussion

### 1889 4.4.1 Effect of model resolution

1890 We have demonstrated that there are large differences in the representation of the  
 1891 average state of the stratospheric polar vortex among high-top CMIP5 models. This  
 1892 amounts to an inter-model range in the modal centroid latitude of more than  $5^{\circ}$  and  
 1893 in the aspect ratio of 0.12, which corresponds to (77% and 22% of the ERA standard  
 1894 deviation respectively). Because a similar number of models have a poleward as an  
 1895 equatorward centroid latitude bias, the multi-model mean is approximately accurate.  
 1896 In contrast, only two of 14 models have higher modal aspect ratio than reanalysis.

1897 Importantly, we have shown that these biases in the undisturbed state of the vortex  
 1898 are closely related to biases in the frequency of split and displaced vortex events. An  
 1899 implication of this is that these models have a realistic representation of variability  
 1900 relative to the average state. In order to understand the origin of these biases we now  
 1901 consider whether any of the model horizontal and vertical resolution properties listed  
 1902 in Table 4.1 are related to models' polar vortex climatology.

1903 There are no statistically significant correlations between the modal aspect ratio or  
 1904 centroid latitude and horizontal resolution or between the centroid latitude and ver-  
 1905 tical resolution. However, a stronger relationship is found between vertical resolution  
 1906 and the modal aspect ratio and this is shown in Figure 4.12. Even so, the relatively  
 1907 wide scatter of points as well as the small correlation coefficient values indicate that  
 1908 vertical resolution fails to account for a substantial fraction of inter-model variability in  
 1909 the modal aspect ratio. Indeed, the  $p$ -values of these correlations are 93.8% and 81.2%  
 1910 for the 5-15 km and 15-30 km vertical resolutions respectively (calculated using a two-  
 1911 tailed  $t$ -test). However, these relationships appear quite nonlinear, with aspect ratio  
 1912 being relatively more sensitive to changes in resolution when the resolution is coarse  
 1913 (high  $dz$ ) and less sensitive when the resolution is finer (low  $dz$ ). This can be addressed  
 1914 by instead calculating the Spearman's rank correlations, which test the monotonicity  
 1915 of the relationships. These are  $-0.60$  ( $p = 96.9\%$ ) and  $-0.75$  ( $p = 99.7\%$ ) for ver-  
 1916 tical resolutions over 5-15 km and 15-30 km respectively, therefore indicating more

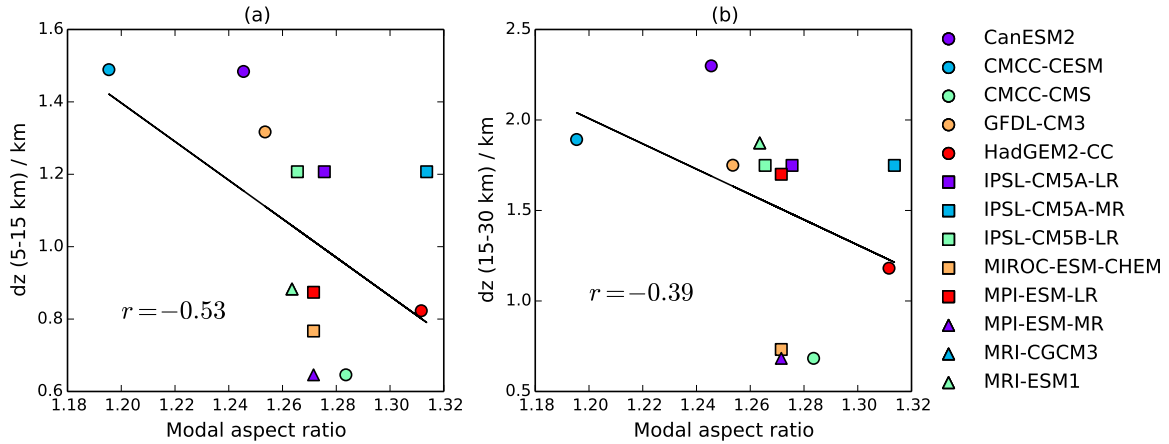


**Figure 4.12:** Correlation between modal aspect ratio and model vertical resolution over two regions (5-15 km and 15-30 km). Correlations,  $r$ , are shown along with the  $p$ -value calculated by a bootstrap test with null hypothesis  $r = 0$ .

1917 statistically significant relationships. However, because the two measures of vertical  
 1918 resolution are themselves correlated ( $r = 0.79$ ), it is difficult to interpret which of the  
 1919 two regions (if any) has the largest impact on the modal aspect ratio.

1920 Two important caveats should be noted in interpreting these correlations. First,  
 1921 comparing pairs of models from the same family but with different resolutions does not  
 1922 show a correlation between vertical resolution and modal aspect ratio. In the present  
 1923 ensemble this comparison is limited to IPSL-CM5A-LR/IPSL-CM5A-MR and MPI-ESM-  
 1924 LR/MPI-ESM-MR. It can be seen from Figure 4.12(a) that the IPSL models have the  
 1925 same vertical resolution but different modal aspect ratios and the MPI models have  
 1926 different vertical resolutions but very similar modal aspect ratios. While this is a very  
 1927 limited comparison of only two pairs of models, it may suggest that it is in fact other  
 1928 model differences which may give rise to the correlations shown in Figure 4.12.

1929 A second caveat is that interpreting this significance, it should be noted that six  
 1930 different relationships between model resolution parameters and moment diagnostics  
 1931 have been tested using the parameters in Table 4.1 (treating the measures of vertical  
 1932 resolution as a single parameter since they are highly correlated). Assuming these  
 1933 parameters to be independent, there is an approximately 26% chance of finding at  
 1934 least one 95% significant correlation among those tested.

#### 4.4. DISCUSSION

1935 It is interesting to note, however, that *Anstey et al.* [2013] found vertical res-  
1936 olution among CMIP5 models to correlate with increased NH winter blocking fre-  
1937 quency (although, as with this study, the relationship did not hold in comparing mod-  
1938 els from the same family). They found the strongest relationship to be with upper-  
1939 troposphere/lower-stratosphere (UTLS) vertical resolution (i.e. over the 5-15 km re-  
1940 gion). Since blocking events are known to be closely linked to stratospheric variability  
1941 (as discussed in Sections 2.4.1 and 2.4.2, the combination of the present study with  
1942 *Anstey et al.* [2013] may suggest that UTLS vertical resolution is an important factor in  
1943 the representation of stratosphere-troposphere coupling.

1944 There is also some physical motivation for the importance of UTLS vertical reso-  
1945 lution in the representation of stratosphere-troposphere coupling because of the sen-  
1946 sitivity of planetary wave propagation to vertical gradients in this region. This sensi-  
1947 tivity can be measured by the quasi-geostrophic refractive index,  $n_s$  [*Matsuno*, 1970],  
1948 with planetary waves tending to propagate towards regions of high  $n_s$  and becoming  
1949 evanescent in regions where  $n_s < 0$ .  $n_s$  depends both on the the vertical gradient in  
1950 static stability ( $\partial N^2 / \partial z$ ) and the vertical shear of zonal wind ( $\partial \bar{u} / \partial z$ ). Using a linear  
1951 primitive equation numerical model, *Chen and Robinson* [1992] found a large vertical  
1952 gradient in static stability near the tropopause as well as a strong vertical shear of the  
1953 zonal flow. They found that small changes in these quantities have a large effect on  
1954  $n_s$ , and therefore that the tropopause acts as a “valve” for the propagation of plane-  
1955 tary waves between the troposphere and stratosphere. In a more recent observational  
1956 study, *Grise et al.* [2010] have confirmed the existence of fine-scale structure in static  
1957 stability near the tropopause. It therefore may be the case that a higher model vertical  
1958 resolution near the tropopause is necessary to capture this structure and hence more  
1959 accurately represent planetary wave propagation from troposphere to stratosphere.

1960 The fact that there is not a significant relationship between the modal centroid lat-  
1961 itude and vertical resolution may suggest that wave-2 propagation is more sensitive to  
1962 vertical resolution than wave-1. Indeed, it might be expected that wave-2 propagation  
1963 is more sensitive to near-tropopause resolution because the ‘window’ for permissible  
1964 wave-2 propagation is narrower (*Charney and Drazin* [1961]; Equation 2.7), meaning

1965 smaller differences in vertical gradients are required to exclude wave-2 propagation  
 1966 than wave-1 propagation. However, no significant correlations are found among the  
 1967 CMIP5 models between vertical resolution and wave amplitudes (using the measures  
 1968 shown in Figure 4.7).

1969 Overall, a more systematic study is necessary to understand the importance of UTLS  
 1970 vertical resolution in the representation of stratosphere-troposphere coupling by cli-  
 1971 mate models. This should consist of a ‘clean comparison’ of models in which only  
 1972 vertical resolution is varied, and which therefore avoids the difficulty of interpreting  
 1973 results when many parameters are varied at once as in the CMIP5 ensemble.

#### 1974 4.4.2 Measures of stratosphere-troposphere coupling

1975 We have shown that zonally-averaged quantities such as polar cap  $Z$  (which is highly  
 1976 correlated with the NAM [Kushner, 2010]) following split and displaced vortex events  
 1977 are much less consistent among models than the NAO. This inconsistency is dominated  
 1978 by differences in the North Pacific, with some models showing positive MSLP anom-  
 1979 lies and others negative. Interestingly, a similar result was found in the recent study  
 1980 of Davini *et al.* [2014], who found the blocking pattern associated with SSWs to be  
 1981 consistent with that associated with the NAM over the North Atlantic, but not over the  
 1982 North Pacific.

1983 As discussed in Section 2.4 many studies of stratosphere-troposphere coupling have  
 1984 focused on the lag-height behaviour the NAM. For instance the comparison of stratosphere-  
 1985 troposphere coupling in high-top and low-top CMIP5 models by Charlton-Perez *et al.*  
 1986 [2013]. This and several other studies make further approximations as to the zonal na-  
 1987 ture of the coupling by calculating the NAM based on zonal-mean geopotential height,  
 1988 according to the method of Baldwin and Thompson [2009]. Our results suggest that  
 1989 because of the difference in model consistency over the two ocean basins, zonal-mean  
 1990 diagnostics or the NAM alone are not good descriptors of inter-model variability. There-  
 1991 fore, we suggest that the NAO index or the full two-dimensional surface fields should  
 1992 be shown alongside the NAM when making inter-model comparisons.

This difference between the NAM and NAO signals in CMIP5 models may also give some insight into the physical relevance of these two modes of variability. Some studies have suggested that the NAO is in fact a regional manifestation of the planetary-scale annular structure of the NAM [e.g., *Thompson and Wallace*, 1998; *Wallace and Thompson*, 2002]. Furthermore, many observational studies have asserted that tropospheric anomalies following SSWs represent the NAM [e.g., *Baldwin and Dunkerton*, 1999, 2001; *Thompson et al.*, 2000].

On the other hand, *Amбаум et al.* [2001] suggested that the NAO paradigm is a more physically relevant measure of NH variability than the NAM. They found that MSLP anomalies over the North Atlantic and Pacific are not significantly correlated (also shown by *Deser* [2000]) and argued that the annular NAM pattern is a statistical artifact. *Huth* [2006] also showed that principal component analysis favours the NAO as the more physically relevant mode of variability. Furthermore, *Amбаум and Hoskins* [2002] found that changes in North Pacific tropospheric subtropical and polar jets are much less correlated with the strength of the stratospheric polar vortex than are the North Atlantic jets.

Under the significant assumption that the CMIP5 models can accurately represent the physics underlying these modes of variability (the investigation of which is beyond the scope of this chapter), our results tend to favour the NAO rather than the NAM as the more physically relevant mode, at least in terms of stratosphere-troposphere coupling.

#### 4.4.3 Difference between split and displaced vortex events

As well as the consistent NAO signal following split and displaced vortex events, we have found that there are also some consistent differences in anomalies following the two types of event. In particular, MSLP anomalies following displaced vortex events are more negative over Scandinavia and Siberia than following split vortex events. From the fact that these MSLP differences are co-located with 100 hPa Z (Figure 4.11), which is in turn related to tropopause height, it may be possible to gain some understanding

2021 of the mechanism behind the difference in the surface response to split and displaced  
 2022 vortex events.

2023 This co-location of surface anomalies and tropopause height is consistent with a  
 2024 localised spinup/spindown caused by stretching/compression of the tropospheric col-  
 2025 umn. Changes in tropopause height are, in turn, caused by the bending of isentropic  
 2026 surfaces towards PV anomalies resulting from the movement of the stratospheric po-  
 2027 lar vortex. Such a mechanism was discussed by *Ambaum and Hoskins [2002]* and in  
 2028 Section 2.4.3.

2029 Other mechanisms that have been proposed for stratosphere-troposphere coupling  
 2030 fail to account for these regional differences. For instance, the amplification of intrin-  
 2031 sic modes of variability [*Robinson, 1991*] can only explain differences which project  
 2032 onto these modes such as the NAO or NAM, unlike observed difference. Stratosphere-  
 2033 troposphere coupling by the reflection of planetary waves [*Perlitz and Harnik, 2003;*  
 2034 *Shaw et al., 2010*] also cannot explain the observed difference since it does not project  
 2035 onto the dominant tropospheric planetary wave modes.

2036 This argument relates only to the mechanism underlying the *difference* between the  
 2037 surface responses to split and displaced vortex events, and not to the overall responses.  
 2038 It is important to note that there are many similarities in the responses, especially in  
 2039 the NAO region. All the mechanisms discussed in Section 2.4.3 can be used to explain a  
 2040 stratospheric influence on the NAO, and since they are not physically inconsistent with  
 2041 one another, it is possible that a number may operate at the same time.

2042 Unfortunately, the small number of observed split and displaced vortex events com-  
 2043 bined with large tropospheric noise means there is very little statistical significance  
 2044 in the observed difference of MSLP anomalies (see Figure 4.11(a)). Hence it is not  
 2045 possible to compare our model and observational results for this difference, and there  
 2046 remains the possibility that CMIP5 models do not realistically represent the surface re-  
 2047 sponds to split and displaced vortex events. Therefore, it is possible that stratosphere-  
 2048 troposphere coupling mechanisms in models are different to those in the real world.

## 2049 4.5 Conclusions

2050 Applying the method developed in Chapter 3, the climatology of the stratospheric po-  
 2051 lar vortex and its coupling with the troposphere has been analysed in stratosphere-  
 2052 resolving CMIP5 simulations. The main conclusions of this investigation are as follows:

2053 **Models representation of the stratospheric polar vortex and stratosphere-troposphere  
 2054 coupling.** A wide range of biases among CMIP5 models has been found in the average  
 2055 state of the stratospheric polar vortex. Some models have a vortex which is too equa-  
 2056 torward, while others too poleward. The majority of models have a vortex which is too  
 2057 circularly symmetric. The relative magnitudes of wave-1 and wave-2 activity to a large  
 2058 extent determine these biases, although there is no one-to-one relationship between  
 2059 wavenumbers and the aspect ratio or centroid latitude of the vortex.

2060 There is also a wide spread in the frequency of split and displaced vortex events,  
 2061 although in the multi-model mean the frequency of these events is in agreement with  
 2062 observations. Importantly, biases in the average state of the vortex have been shown to  
 2063 relate closely to biases in the frequency of split and displaced vortex events. Hence an  
 2064 improvement in the average state of the vortex is likely to lead to an improvement in the  
 2065 representation of extremes.

2066 Almost all models accurately simulate the more barotropic nature of split vortex  
 2067 events compared to displaced vortex events. MSLP anomalies following these events  
 2068 consistently show a negative NAO in line with observations, but are much less con-  
 2069 sistent in the North Pacific, leading to a large spread when zonal mean quantities are  
 2070 investigated.

2071 **Mechanisms for stratosphere-troposphere coupling.** Consistent differences in the  
 2072 MSLP anomalies following split and displaced vortex events in the CMIP5 models have  
 2073 been found to be co-located with the difference in near-tropopause Z anomalies. This  
 2074 is consistent with a localised tropospheric response to stratospheric PV anomalies (as  
 2075 discussed in Section 2.4.3) being the mechanism behind the different responses to the  
 2076 two events. It also excludes mechanisms which rely on projections onto major modes of

variability such as the NAO or NAM. This result only applies to the *difference* between responses to split and displaced vortex events, not the overall responses, which also have some similarities.



stratosphere itself can act as a source of enhanced predictability [Baldwin *et al.*, 2003; Charlton *et al.*, 2003; Christiansen, 2005; Hardiman *et al.*, 2011]. Because the effect of the stratosphere on the troposphere is especially pronounced following SSW events, past work has focused on the influence of these events on forecast skill. For instance, both Kuroda [2008] and Sigmund *et al.* [2013] found that enhanced tropospheric predictability can be obtained if forecasts are initialised at the onset of SSW events. However, SSWs are highly nonlinear events which previous studies have not found predictable beyond about two weeks in advance [Marshall and Scaife, 2010; Taguchi, 2014]. This may therefore limit their usefulness in seasonal prediction. SSWs also occur almost exclusively in the NH, with only one event in the approximately 60 year record having been observed in the SH, in September 2002 [Roscoe *et al.*, 2005].

As discussed in Section 2.1.3, the rarity of SSWs in the SH is a result of less dynamical forcing from vertically propagating planetary waves in the SH relative to the NH stratosphere. This reduced dynamical forcing also means that anomalies in the Antarctic stratosphere persist for longer than those in the Arctic [Simpson *et al.*, 2011]. Hence, the SH stratospheric circulation may be predictable on longer time scales, and thus more useful for seasonal forecasts despite the lack of SSWs. Indeed, Thompson *et al.* [2005] and Son *et al.* [2013] have found that smaller-amplitude variations in the Antarctic stratospheric polar vortex are followed by coherent temperature and pressure anomalies at the Earth's surface which resemble the Southern Annular Mode (SAM) pattern. These observations led Roff *et al.* [2011] to find that improved forecasts of the SAM up to 30 days ahead may be achieved with a stratosphere-resolving model. As the dominant mode of variability in the extratropical SH, the SAM affects the position of storm tracks, rainfall, surface air temperature, and ocean temperatures across the extratropics [e.g., Silvestri and Vera, 2003; Reason and Rouault, 2005; Hendon *et al.*, 2007]. As such, there are considerable societal benefits and interests in its prediction [Lim *et al.*, 2013].

Another reason for interest in the prediction of the Antarctic stratosphere is the interannual variability in springtime ozone depletion, which can significantly affect the

## 5.1. INTRODUCTION

amount of harmful ultraviolet radiation reaching the Earth’s surface over the Southern Hemisphere. The magnitude of this interannual variability is a significant fraction of the magnitude of long-term depletion caused by emission of chlorofluorocarbons (CFCs) and other ozone-depleting substances. While ozone-depleted air is confined over the polar region by the stratospheric polar vortex during winter and spring (resulting in the ozone hole), this air is released to mid-latitudes following the ultimate breakdown of the vortex (final warming) in late spring/early summer. The extent of the resulting summertime ozone depletion is largely determined by the total deficit in ozone over the Antarctic during spring [Bodeker *et al.*, 2005].

As discussed in Section 2.2, dynamics play an important role in ozone depletion. Indeed, Salby *et al.* [2012] have shown that interannual variations in Antarctic ozone depletion are highly correlated with changes in planetary wave forcing of the stratosphere. They found that the anomalous vertical EP flux at 70 hPa poleward of 40°S during August-September explains almost all the interannual variance of anomalous ozone depletion during September–November. Using this relationship, they postulate that accurate prediction of planetary wave forcing could allow skillful seasonal forecasts of ozone depletion.

In this chapter, we address directly the predictability of the stratospheric polar vortices using a set of hindcasts (or historical re-forecasts) from a new operational seasonal forecast system with a fully stratosphere-resolving general circulation model. The system accurately simulates the climatology of the NH stratospheric polar vortex including the aspect ratio and centroid latitude. However, we find it does not skilfully predict the winter mean vortex strength, the occurrence of SSWs, or split and displaced vortex events. On the other hand, we find significant skill in the prediction of the Antarctic stratospheric polar vortex up to four months in advance, including for the 2002 SSW. Using the observed relationship between column ozone quantities and the stratospheric circulation, we are then able to infer skillful predictions of springtime ozone depletion, confirming the hypothesis of Salby *et al.* [2012]. This exceeds the lead-time of other contemporary ozone forecasts, which are typically no more than two weeks [Eskes, 2005]. The forecast system also shows significant levels of skill in the prediction of

2160 the surface SAM at seasonal lead times. By studying the variation of hindcast skill with  
 2161 time and height, we demonstrate that this skill is significantly influenced by the descent  
 2162 of predictable stratospheric circulation anomalies.

## 2163 5.2 Seasonal forecast system

2164 The analysis in this chapter is based on results from a set of hindcast predictions pro-  
 2165 duced by the Met Office Global Seasonal Forecast System 5 (GloSea5) [*MacLachlan*  
 2166 *et al.*, 2014]. This system is based upon the HadGEM3 coupled general circulation  
 2167 model [*Hewitt et al.*, 2011], with an atmospheric resolution of  $0.83^\circ$  longitude by  $0.56^\circ$   
 2168 latitude, 85 quasi-horizontal atmospheric levels and an upper boundary at 85 km. The  
 2169 ocean resolution is  $0.25^\circ$  in longitude and latitude, with 75 quasi-horizontal levels.

2170 Initial conditions for the atmosphere and land surface were taken from the ERA-  
 2171 Interim reanalysis [*Dee et al.*, 2011], and initial ocean and sea-ice concentrations from  
 2172 the GloSea5 Ocean and Sea Ice Analysis, based on the FOAM data assimilation system  
 2173 [*Blockley et al.*, 2013]. The ERA-Interim data are linearly interpolated onto model lev-  
 2174 els between the surface and 64.56 km (near 0.1 hPa), and the 64.56 km values are then  
 2175 replicated onto the four subsequent levels up to 85 km. FOAM data are on the same  
 2176 grid as the ocean model. Beyond initialisation the model takes no further observational  
 2177 data, and contains no flux corrections or relaxations to climatology. The model lacks  
 2178 interactive chemistry and ozone concentrations are fixed to observed climatological  
 2179 values averaged over 1994–2005, including a seasonal cycle from the Stratosphere-  
 2180 troposphere Processes and their Role in Climate (SPARC) climatology [*Cionni et al.*,  
 2181 2011]. Climate forcings such as CO<sub>2</sub> and CH<sub>4</sub> concentrations are set to observed val-  
 2182 ues up to 2005 and then follow the IPCC RCP4.5 scenario.

2183 *Scaife et al.* [2014] have shown that this seasonal forecast system produces highly  
 2184 skillful forecasts of the North Atlantic Oscillation (NAO) during the Northern Hemi-  
 2185 sphere winter. They found the correlation of the ensemble mean DJF average NAO  
 2186 with observed values to be  $r = 0.62$ , which is statistically significant from zero at the

2187 99% level. They argue that the combined effects of ENSO, QBO and sea-ice teleconnec-  
 2188 tions, as well as the increased ocean resolution which has improved the representation  
 2189 of Northern Hemisphere blocking events [*Scaife et al.*, 2011b], contribute to this skill.

2190 Hindcast accuracy is verified by comparison to the ERA-Interim reanalysis [*Dee*  
 2191 *et al.*, 2011]. As discussed in Chapter 3, the ERA-Interim data set has been demon-  
 2192 strated to have realistic representation of the stratospheric meridional circulation [*Se-*  
 2193 *viour et al.*, 2012; *Monge-Sanz et al.*, 2013]. It also assimilates observations of ozone  
 2194 concentrations, and this assimilation has been demonstrated to be in close agreement  
 2195 with independent satellite data [*Dragani*, 2011]

2196 In this chapter, hindcasts are analysed for two seasons; December–February (DJF)  
 2197 for prediction of the Northern Hemisphere winter stratospheric polar vortex, and September–  
 2198 November (SON) for the Southern Hemisphere. The SON season is chosen because it  
 2199 represents the time of maximum SH ozone depletion and stratospheric polar vortex  
 2200 variability. For SON a 15-member ensemble of hindcasts was run for each year in the  
 2201 period 1996–2009, while for the DJF analysis a longer 24-member ensemble is avail-  
 2202 able for the winters 1992/1993–2011/2012. The hindcast length is approximately four  
 2203 months from three separate start dates spaced two weeks apart and centered on 1st Au-  
 2204 gust (SON) or 1st November (DJF), with an equal number of members initialised on  
 2205 each start date. Members initialised on the same start date differ only by stochastic  
 2206 parameterisation of model physics, using the Stochastic Kinetic Energy Backscatter v2  
 2207 [SKEB; *Bowler et al.*, 2009] scheme. Details of the hindcast runs for these two seasons  
 2208 are summarised in Table 5.1.

Season	Hindcast period	Initialisation dates	Ensemble size
DJF	92/93–11/12 (20 years)	25/10, 01/11, 09/11	24 (8 on each date)
SON	1996–2009 (14 years)	25/07, 01/08, 09/08	15 (5 on each date)

Table 5.1: Summary table of the two sets of hindcast simulations analysed.

2208

2209 It should be noted that the 20-year, 20-member ensemble hindcasts of DJF were  
 2210 extended from a 14-year, 15-member ensemble, the same as as the SON hindcasts.  
 2211 These extended simulations are, however, slightly shorter than the original ensemble;

2212 ending at the beginning of March rather than the beginning of April. This therefore  
 2213 limits our analysis of the full ensemble so as not to include March. Furthermore, some  
 2214 variables were not produced by the extended DJF ensemble and so the original sorter  
 2215 ensemble must be used in some cases, which is made clear in the text where necessary.

2216 In order to illustrate these hindcast simulations, timeseries of zonal-mean zonal  
 2217 wind ( $\bar{u}$ ) at 10 hPa are shown for 60°N from November–March (Figure 5.1) and 60°S  
 2218 from August–December (Figure 5.2). ERA-Interim values are also shown in both cases  
 2219 (black lines). These are the approximate positions of the centre of the mean position  
 2220 of the stratospheric polar vortex in the mid-stratosphere, and therefore indicate the  
 2221 strength of the stratospheric polar vortex. In order to make the figures comparable,  
 2222 the shorter 14-year, 15-member ensemble is shown for the NH. It can immediately  
 2223 be seen that there is a much greater ensemble spread in the NH, owing to the much  
 2224 greater dynamical variability of the NH stratospheric polar vortex. In both cases it  
 2225 can also be seen that the ensemble spread is initially small and increases rapidly after  
 2226 approximately 15–30 days. This demonstrates the initial constraint to ERA-Interim  
 2227 and the rapid growth of small differences in initial conditions, because of the chaotic  
 2228 nature of the atmosphere. The predictive skill of for the Northern Hemisphere (DJF) is  
 2229 analysed in the next section, and the Southern Hemisphere (SON) in Section 5.4.

### 2230 5.3 Northern Hemisphere results

2231 The climatology of Arctic stratospheric polar vortex winds in the GloSea5 hindcasts is  
 2232 compared to the ERA-Interim reanalysis climatology in Figure 5.9. As in Figure 5.1,  
 2233 the strength of the stratospheric polar vortex is measured by the zonal-mean zonal  
 2234 wind ( $\bar{u}$ ) at 60°N and 10 hPa. The composite for the GloSea5 hindcasts is formed from  
 2235 all the individual ensemble members over the winters 1992/1993–2011/2012 (a total  
 2236 of 480), while that from ERA-Interim is a composite of the same 20 winters. It can  
 2237 be seen that the mean, interquartile range and 95th percentile range of the GloSea5  
 2238 values agree well with the ERA-Interim values, although the ERA-Interim values are  
 2239 noisier as would be expected from a sample size consisting of fewer years.

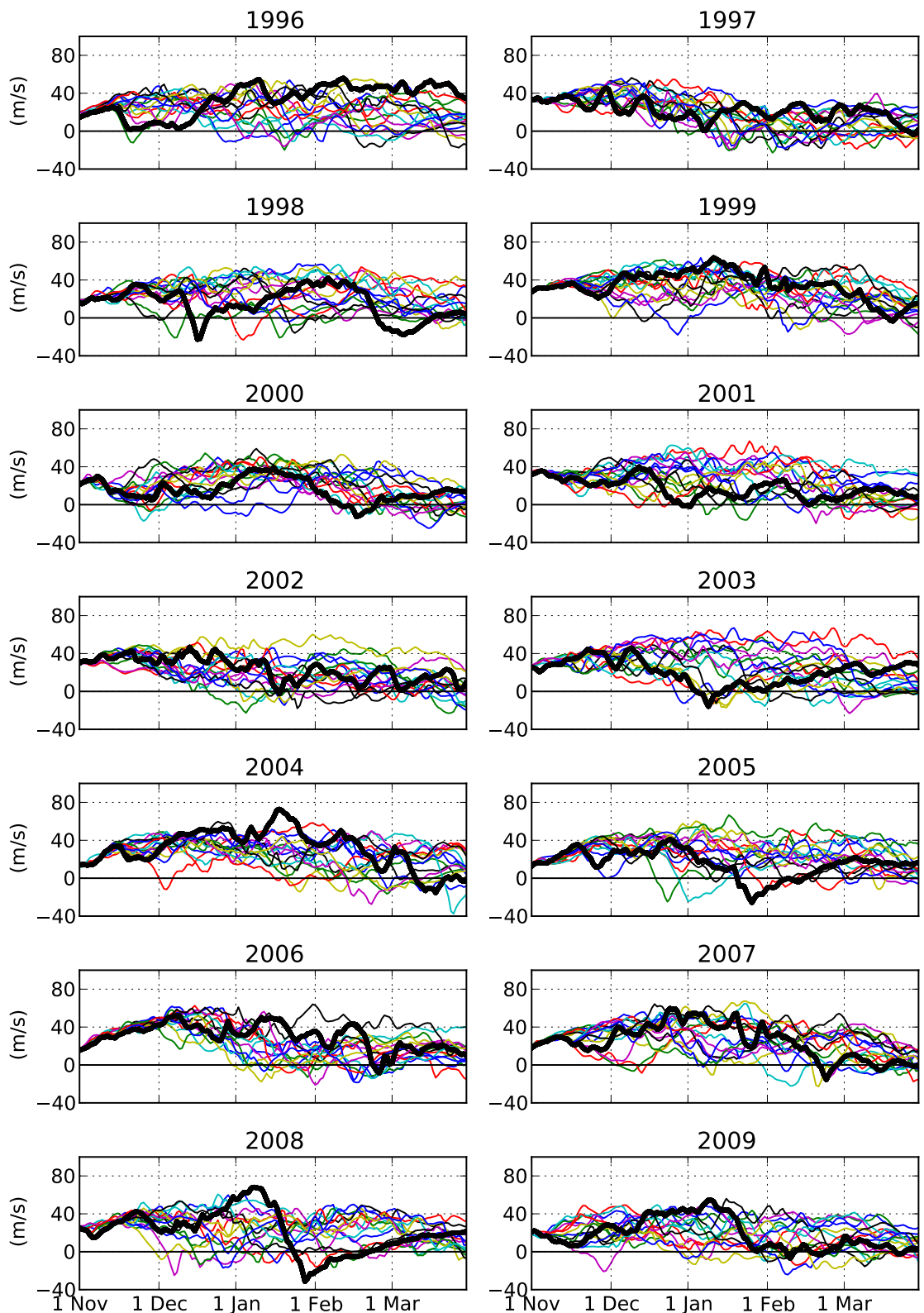


**Figure 5.1:** Timeseries of zonal-mean zonal wind in the Arctic polar vortex ( $60^{\circ}\text{N}$ , 10 hPa) in the ERA-Interim reanalysis (thick black lines) and the GloSea5 ensemble hindcasts (thin coloured lines). Individual ensemble members are initialised from dates centred on November 1st. Years refer to the year of the initialisation date.

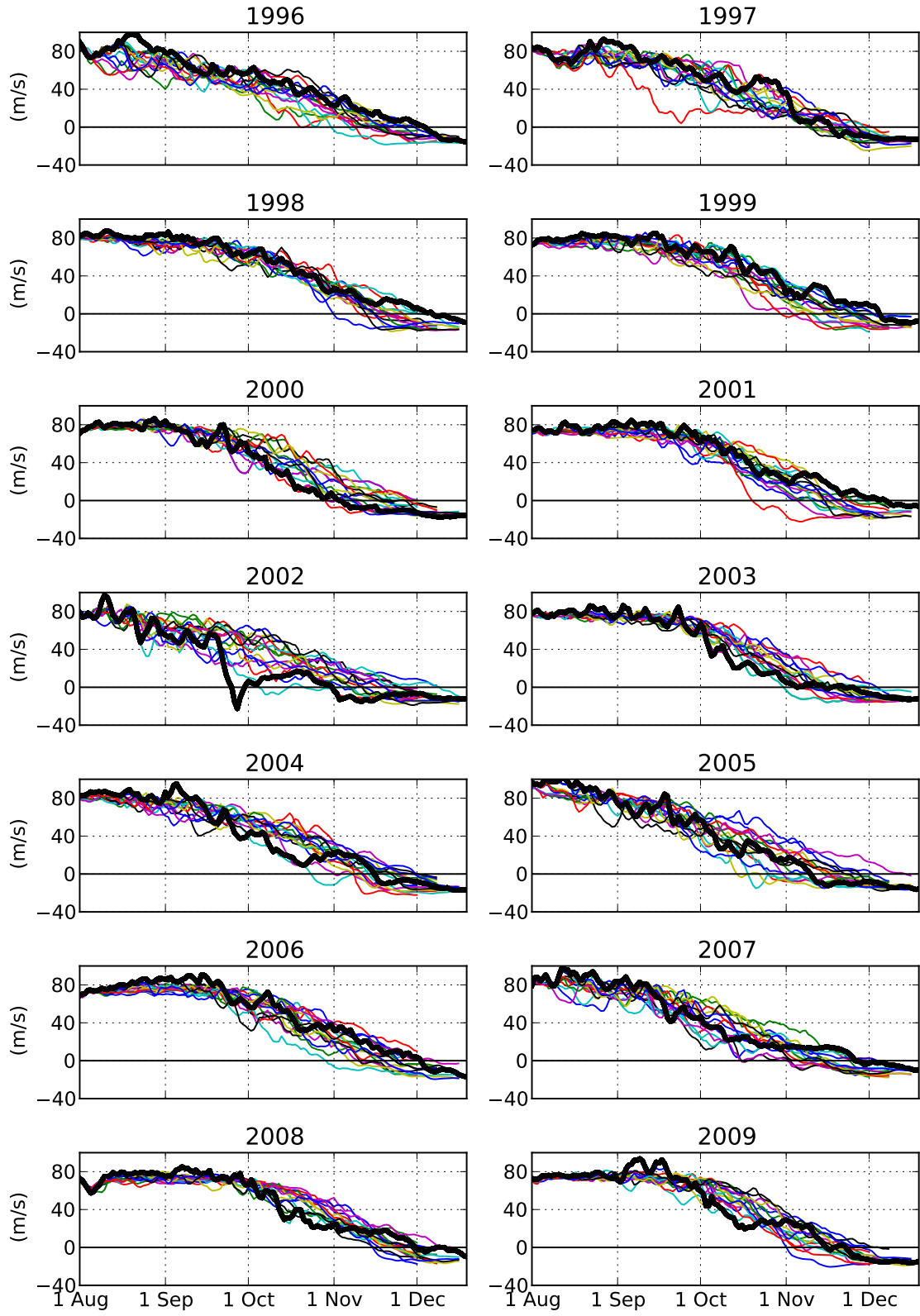


**Figure 5.2:** As figure 5.1 but for the zonal-mean zonal wind in the Antarctic polar vortex ( $60^{\circ}\text{S}$ , 10 hPa), and ensemble members initialised from dates centred on August 1st.

### 5.3. NORTHERN HEMISPHERE RESULTS

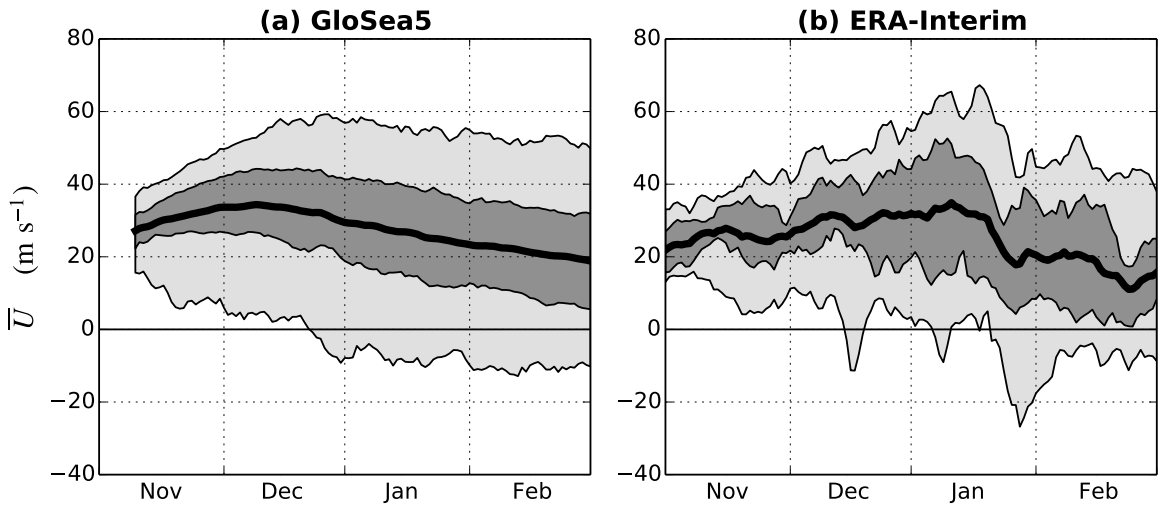


**Figure 5.3:** Time series of daily 10 hPa zonal-mean zonal wind ( $\bar{U}$ ) at  $60^{\circ}\text{N}$  for all GloSea5 ensemble members (a) and ERA-Interim (b) from 1992–2011. The thick black line indicates the mean, dark grey shading the interquartile range and light grey the 95th percentile range.

2240     Figure 5.4 shows the joint distribution of the aspect ratio and centroid latitude mo-  
 2241     ment diagnostics calculated over DJF from the GloSea5 hindcasts, along with the equiv-  
 2242     alent values from ERA-Interim. These diagnostics have been calculated from geopoten-  
 2243     tial height following the method described in Chapter 3. Both aspect ratio and centroid  
 2244     latitude distributions closely match those of ERA-Interim, and the joint distribution  
 2245     shows the characteristic triangular shape which is related to the occurrence of split  
 2246     and displaced vortex events. Together, Figures 5.3 and 5.4 demonstrate that GloSea5  
 2247     accurately simulates the mean state and variability of the stratospheric polar vortex in  
 2248     the mid-stratosphere.

2249     The GloSea5 hindcast predictions of interannual variability of the NH stratospheric  
 2250     polar vortex winds are shown in Figure 5.5. Anomalies are defined from the relevant  
 2251     climatology of either GloSea5 or ERA-Interim. For GloSea5, this climatology is calcu-  
 2252     lated from the mean of each day across all ensemble members in all years, while for  
 2253     ERA-Interim the climatology is the mean of each day, smoothed with a 30-day running  
 2254     mean (in order to account for its increased noise due to the reduced sample size). Re-  
 2255     sults are shown for DJF averages, corresponding to a 1 month average lead time. The  
 2256     correlation between the GloSea5 ensemble mean and ERA-Interim is  $r = 0.24$  which

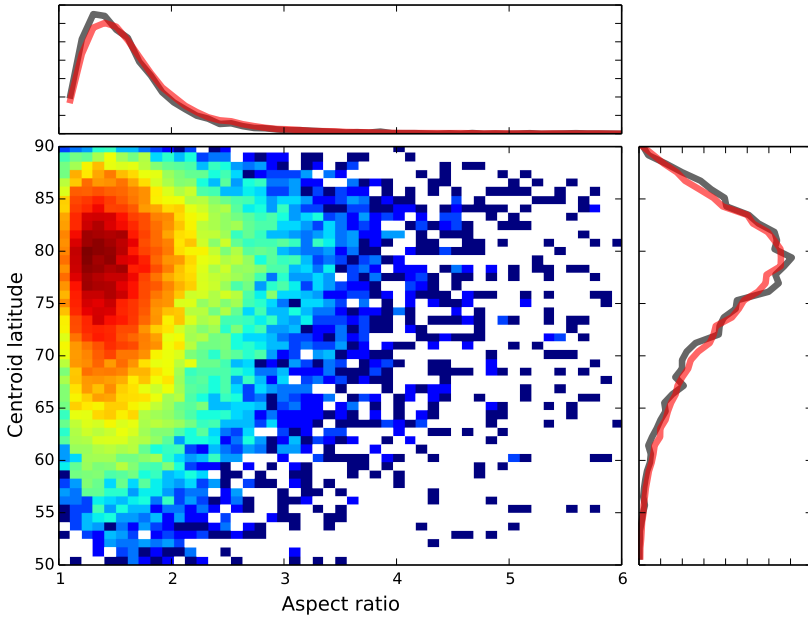


**Figure 5.4:** Distribution (see Figure 4.1) of the centroid latitude and aspect ratio diagnostics derived from geopotential height for all GloSea5 ensemble members (red lines) and ERA-Interim (grey lines) over 1992–2011. The joint distribution is plotted with a logarithmic colour scale such that red represents the densest regions.

is not statistically significant at the 95% level (under the null hypothesis that the two timeseries are uncorrelated). Significance is calculated using a two-tailed bootstrap test, whereby the percentile of the observed correlation is calculated from the distribution of correlations of a large number ( $\sim 10\,000$ ) of pairs of time series formed by re-sampling with replacement from the original time series. As elsewhere in this thesis, these significance tests are used because they make fewer assumptions about the underlying structure of the data than parametric tests [Wilks, 2006].

Although no significant skill is found in the prediction of the seasonal mean strength of the stratospheric polar vortex, it might nonetheless be the case that skilful predictions of SSW events can be made. This is assessed using receiver operating characteristic (ROC) curves, a standard method in forecast evaluation, particularly of binary events [e.g., Wilks, 2006]. In order to calculate the ROC curve, the following procedure is followed:

- 2270 1. For each ensemble member in each year, determine whether an SSW occurs (winters  
2271 with one SSW and two SSWs are treated the same).

### 5.3. NORTHERN HEMISPHERE RESULTS

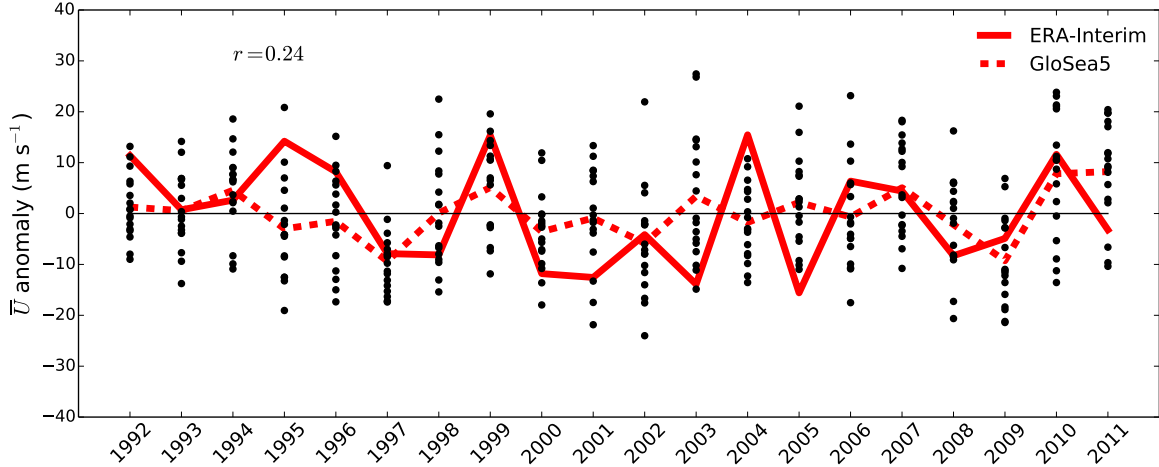


**Figure 5.5:** DJF mean anomalies of  $\bar{U}$  at  $60^{\circ}\text{N}$  and 10 hPa for the GloSea5 ensemble mean and ERA-Interim. Black dots represent individual ensemble members. The correlation between the GloSea5 ensemble mean and ERA-Interim is  $r = 0.24$ , which is not statistically significant from zero. Years refer to the year of the initialisation date.

- 2272 2. Select a threshold for the prediction of an SSW (e.g., 60% of ensemble members
- 2273 forecast an SSW).
- 2274 3. For the given threshold determine the fraction of years for which a SSW was cor-
- 2275 rectly predicted (“hit rate”) and the fraction for which a SSW was predicted but
- 2276 none occurred (“false alarm rate”).
- 2277 4. Repeat the steps 2-3 for a range of thresholds from 0-100%.

2278 In a skilful system the ROC curve should indicate a higher hit rate than false alarm  
 2279 rate, bending towards the upper left corner of the graph, while a random forecast will  
 2280 pass along the 1-1 line.

2281 Figure 5.6 shows the ROC curve for SSWs during DJF, determined by the traditional  
 2282 reversal of  $\bar{U}$  at  $60^{\circ}\text{N}$  10 hPa, with the additional criterion that events must be separated  
 2283 by at least 30 days. It can be seen that the calculated ROC curve lies close to the 1-1  
 2284 line indicating little skill in these predictions. This is despite quite large variations in  
 2285 the fraction of ensemble members predicting SSWs; from 47% (winter 2001/2002) to  
 2286 100% (winter 1997/1998).

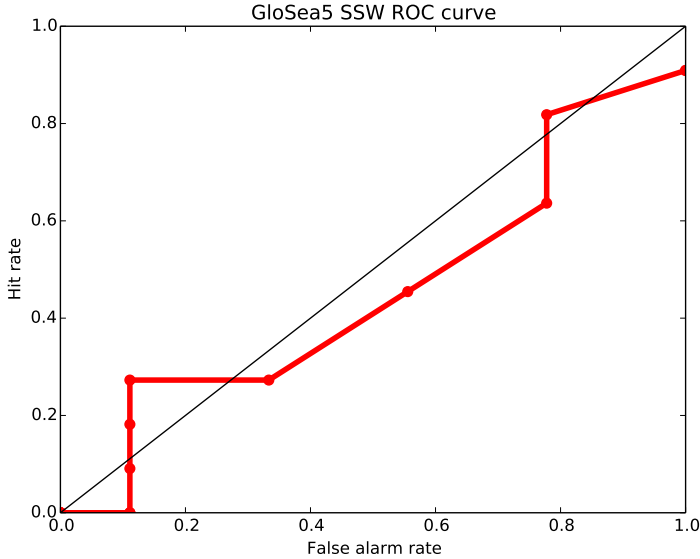


**Figure 5.6:** Receiver operating characteristic (ROC) curve for the prediction of SSW events during DJF for 1992–2011. SSWs are defined as a reversal to easterly  $\bar{u}$  at  $60^{\circ}\text{N}$  10 hPa, and must be separated by at least 30 days.

2287 A similar analysis for the prediction of split and displaced vortex events is shown  
 2288 in Figure 5.7. These events have been calculated from the geopotential height-derived  
 2289 moment diagnostics, using the same procedure as described in Chapter 3. Again, little  
 2290 skill can be seen in the predictions of these events, with both ROC curves lying close  
 2291 to the 1-1 line. It should be noted that GloSea5 predicts a high frequency of split and  
 2292 displaced vortex events (8.5 events/decade; 3.5 split, 5.0 displaced), compared to the  
 2293 observed value of 7 events/decade. This is perhaps not surprising given the HadGEM3  
 2294 model used in GloSea5 is of the same family as HadGEM2-CC, which was found to  
 2295 have the highest frequency of events in Chapter 4.

2296 The evolution of NH hindcast skill as a function of lag and height is evaluated in  
 2297 Figure 5.8. This shows the correlation of ERA-Interim and GloSea5 ensemble mean  
 2298 polar cap ( $60\text{--}90^{\circ}\text{N}$ ) average geopotential height anomalies ( $Z'$ ; which is highly cor-  
 2299 related with the NAM [Kushner, 2010]). Values of  $Z'$  are smoothed with a 30-day  
 2300 running mean before correlations are calculated, and plotted such that values for the  
 2301 15th December represent the correlation of the ERA-Interim and GloSea5 ensemble

### 5.3. NORTHERN HEMISPHERE RESULTS

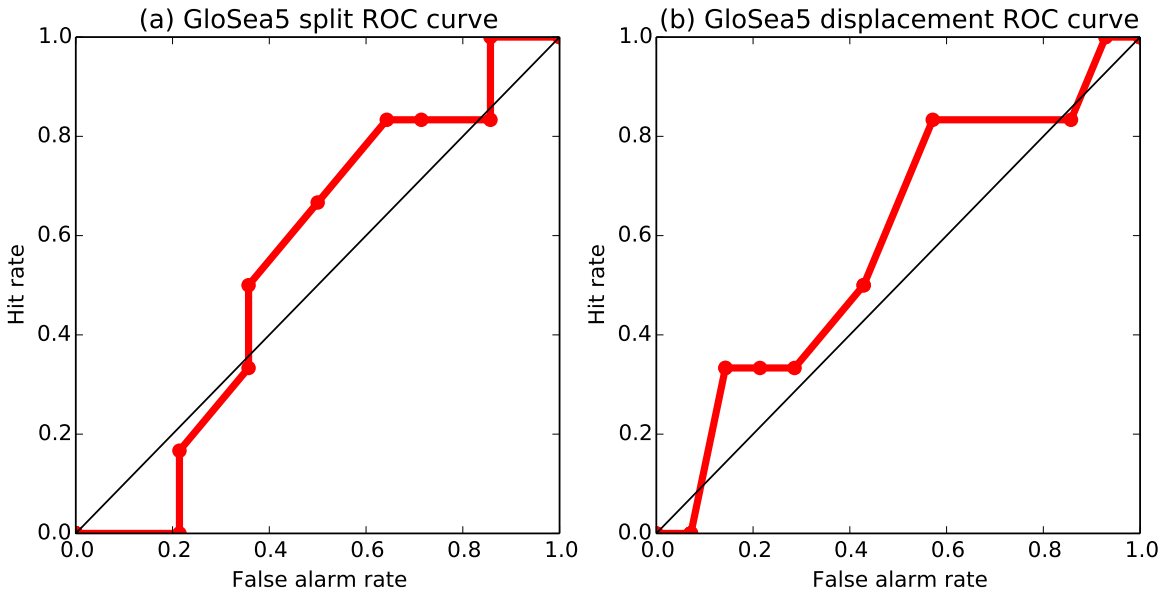


**Figure 5.7:** Receiver operating characteristic (ROC) curves for the prediction of split (a) and displaced (b) vortex events in all GloSea5 ensemble members over 1992–2011. Split and displaced vortex events are identified from geopotential height-derived moment diagnostics using the method described in Chapter 3.

mean December mean values (without this smoothing, a noisier but similar pattern of correlations is seen). Geopotential height data on several levels in the stratosphere is only available in the shorter 14-year, 15-member ensemble, and so the analysis in this figure is limited to these data. Between 1st-9th November the ensemble mean is taken as the average of the 10 initialised ensemble members, and the average of all 15 ensemble members is used after this date.

In mid-November, significant correlations are seen in Figure 5.8 in both the stratosphere and troposphere, as would be expected from the initialisation of the hindcasts from ERA-Interim data (skill is seen to rapidly decay in the tropopause region, however). This skill persists for longer in the stratosphere than the troposphere, owing to the longer timescales of stratospheric variability [e.g., *Simpson et al., 2011*], however, by mid-December no significant correlations are seen in the stratosphere or troposphere.

Significant correlations return in the troposphere in late January/February, and to a lesser extent in the stratosphere. This result is similar to that for the NAO prediction in the same system, which has a greater skill in February than January (Adam Scaife,

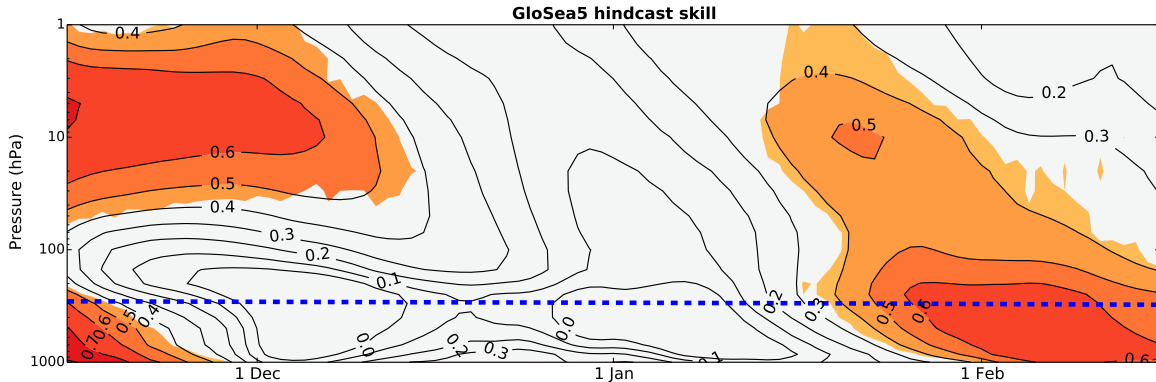


**Figure 5.8:** Correlation of GloSea5 ensemble mean polar cap ( $60\text{--}90^{\circ}\text{N}$ ) geopotential height anomalies ( $Z'$ ) with ERA-Interim values from 1996–2009, as a function of time and height. All values are smoothed with a 30-day running mean before correlations are calculated. The contour interval is 0.1 and all colored regions are greater than zero at the 95% confidence interval, using a bootstrap test at each time at height. The blue dashed line indicates the approximate polar cap mean tropopause level [Wilcox *et al.*, 2012b].

2318 Met Office Hadley Centre, personal communication, 2013). A possible explanation for  
 2319 this behaviour is due to the influence of ENSO, which has been determined to have the  
 2320 greatest effect on the NH extratropics during late January and February [Bell *et al.*,  
 2321 2009]. If indeed the influence of ENSO is important, it is not clear whether this arises  
 2322 from a tropospheric or stratospheric pathway, although the fact that tropospheric skill  
 2323 is greater than stratospheric may suggest the tropospheric pathway is more important.

2324 Detailed analysis of the mechanisms behind the NH surface skill is beyond the scope  
 2325 of this chapter which investigates the role of the stratosphere. Because skill in the  
 2326 prediction of the NH stratosphere has been demonstrated to be low, attention is now  
 2327 turned to the SH. However, the implications of these results are discussed further in  
 2328 Section 5.5.

## 2329 5.4 Southern Hemisphere results

### 2330 5.4.1 Stratospheric polar vortex

2331 The climatology of Antarctic stratospheric polar vortex winds in the GloSea5 hindcasts  
 2332 is compared to the ERA-Interim reanalysis climatology in Figure 5.9. The strength of  
 2333 the stratospheric polar vortex is measured by the zonal-mean zonal wind ( $\bar{u}$ ) at  $60^{\circ}\text{S}$

#### 5.4. SOUTHERN HEMISPHERE RESULTS

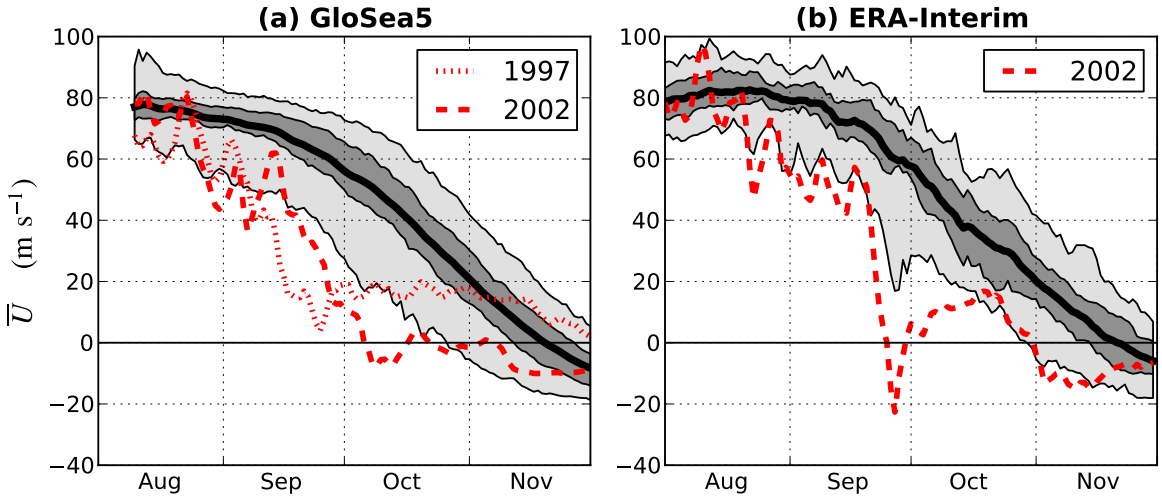


**Figure 5.9:** Time series of daily 10 hPa zonal-mean zonal wind ( $\bar{U}$ ) at  $60^{\circ}\text{S}$  for all GloSea5 ensemble members from 1996–2009 (a) and ERA-Interim from 1979–2010 (b). The thick black line indicates the mean, dark gray shading the interquartile range and light gray the 95th percentile range. Individual time series of the ensemble member of GloSea5 for 2002 which simulated an SSW, and 1997 which simulated a near-SSW, and the year with an observed SSW (2002) are shown in red.

and 10 hPa, which is approximately the center of the mean position of the vortex in the mid-stratosphere. The composite for the GloSea5 hindcasts is formed from all the individual ensemble members over 1996–2009 (a total of 210), while that from ERA-Interim is a composite of all years from 1979–2010 (a total of 32 years). It can be seen that the mean of the GloSea5 hindcasts agrees very closely with ERA-Interim throughout the spring, with only a slight bias towards weaker winds in August and September. The interquartile and 95th percentile ranges of GloSea5 and ERA-Interim also agree well, although the ERA-Interim values are noisier as would be expected from a sample size consisting of fewer years.

The GloSea5 hindcast predictions of interannual variability of the Antarctic stratospheric polar vortex winds are shown in Figure 5.10(a). Anomalies are defined from the relevant climatology of either GloSea5 or ERA-Interim. For GloSea5, this climatology is calculated from the mean of each day across all ensemble members in all years, while for ERA-Interim the climatology is the mean of each day, smoothed with a 30-day running mean (in order to account for its increased noise due to the reduced sample

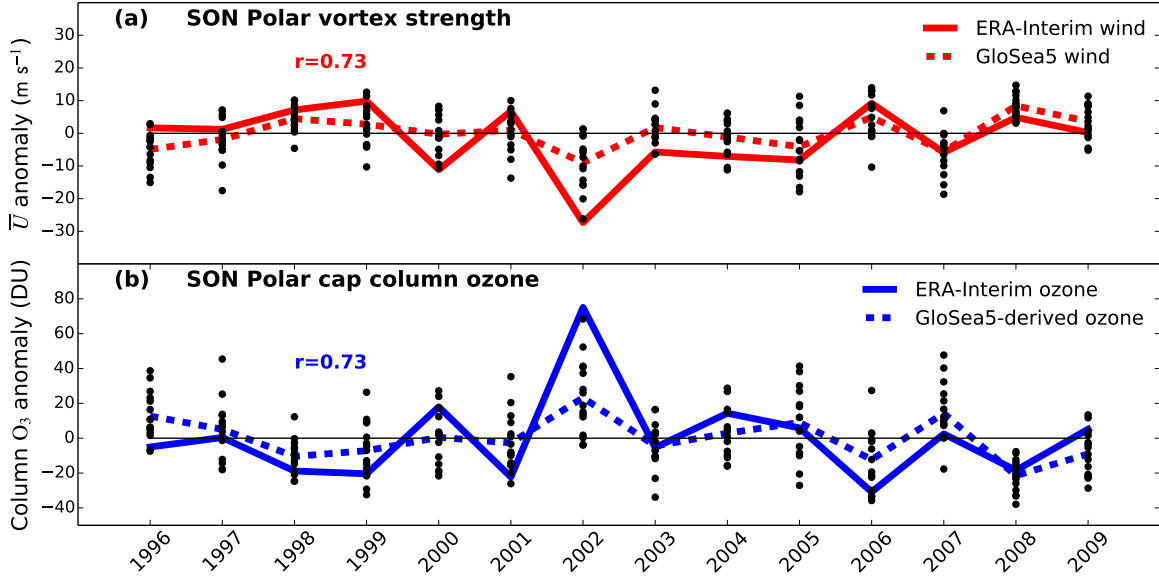


**Figure 5.10:** (a) SON mean anomalies at 10 hPa and 60°S in ERA-Interim and the GloSea5 hindcast ensemble mean. (b) SON mean polar cap averaged (60–90°S) total column ozone anomalies from ERA-Interim and those derived from the GloSea5 anomalies as described in the text. Individual ensemble members are shown as black dots. Hindcasts are initialized near 1st August.

size). Results are shown for September–November (SON) averages, corresponding to a 1 month average lead time. The correlation between the GloSea5 ensemble mean and ERA-Interim is 0.73, which is statistically significant from zero at the 99% confidence level, and has a 95% confidence interval of (0.37,0.90). This correlation does not depend strongly on particular years; the correlation remains significant at the 95% level ( $r = 0.57$ ) if the year 2002 (which has the greatest anomaly) is excluded. Significance is calculated using a two-tailed bootstrap test, whereby the percentile of the observed correlation is calculated from the distribution of correlations of a large number ( $\sim 10,000$ ) of pairs of time series formed by re-sampling with replacement from the original time series. These significance tests make fewer assumptions about the underlying structure of the data than parametric tests [Wilks, 2006], and are used throughout this study.

The skill shown in Figure 5.10(a) cannot be accounted for by persistence of initial anomalies. In fact, there is a negative correlation between  $\bar{u}$  on 9th August, when the last ensemble member is initialised, and the SON mean ( $r = -0.54$ ). Hence, a

#### 5.4. SOUTHERN HEMISPHERE RESULTS

2364 persistence forecast would be negatively correlated with observed values. This rela-  
2365 tionship may be consistent with ideas of a pre-conditioning of the polar vortex [e.g.,  
2366 *McIntyre and Palmer, 1983*]. The standard deviation of all GloSea5 ensemble members  
2367 is  $7.5 \text{ m s}^{-1}$  and that of ERA-Interim is  $9.7 \text{ m s}^{-1}$  indicating that the GloSea5 ensemble  
2368 spread may be too small. However, there are large uncertainties in these values due to  
2369 the short hindcast period and the large 2002 anomaly.

2370 Following *Charlton and Polvani [2007]*, SSWs are defined as a temporary reversal  
2371 of  $\bar{u}$  at  $60^\circ\text{S}$  and 10 hPa, occurring before the final transition to summer easterlies  
2372 (final warming). Under this definition, one SSW event was simulated in the GloSea5  
2373 hindcasts, in 2002. A similar magnitude event (in terms of departure from climatology)  
2374 occurred in a 1997 ensemble member, although  $\bar{u}$  did not quite become easterly. Time  
2375 series of stratospheric polar vortex winds for these two events are shown in Figure  
2376 5.9(a) along with the observed 2002 SSW in Figure 5.9(b). It can also be seen in Figure  
2377 5.9(a) that 2002 has the most anomalous stratospheric polar vortex in the GloSea5  
2378 hindcasts, with 14 of 15 ensemble members simulating negative anomalies, and the  
2379 most negative ensemble mean. It is therefore possible that an increased likelihood the  
2380 2002 event was to some degree detectable about two months in advance, although it  
2381 has not been determined whether this predictability comes from a preconditioning of  
2382 the vortex, as suggested by *Scaife et al. [2005b]*, or the result of external forcing.

2383 Both the SSW events simulated by GloSea5 were vortex displacement events, in  
2384 contrast to the vortex splitting event which occurred in 2002 [*Charlton et al., 2005*].  
2385 This is demonstrated in Figure 5.11, which shows geopotential height in the mid-  
2386 stratosphere at the date of minimum  $\bar{u}$  at  $60^\circ\text{S}$  and 10 hPa, for the two simulated events  
2387 in GloSea5 and the observed event in ERA-Interim. A detailed quantitative analysis us-  
2388 ing moment diagnostics was not found necessary in this case because a qualitative  
2389 inspection is possible with only two events.

2390 The timing of the final warming of the stratospheric polar vortex also has a signif-  
2391 icant effect on stratospheric temperature and ozone concentrations [*Yamazaki, 1987*],  
2392 as well as on the coupling of the stratosphere to the troposphere [*Black and McDaniel,*  
2393 *2007*]. The predictability of these events was investigated in GloSea5, but not found

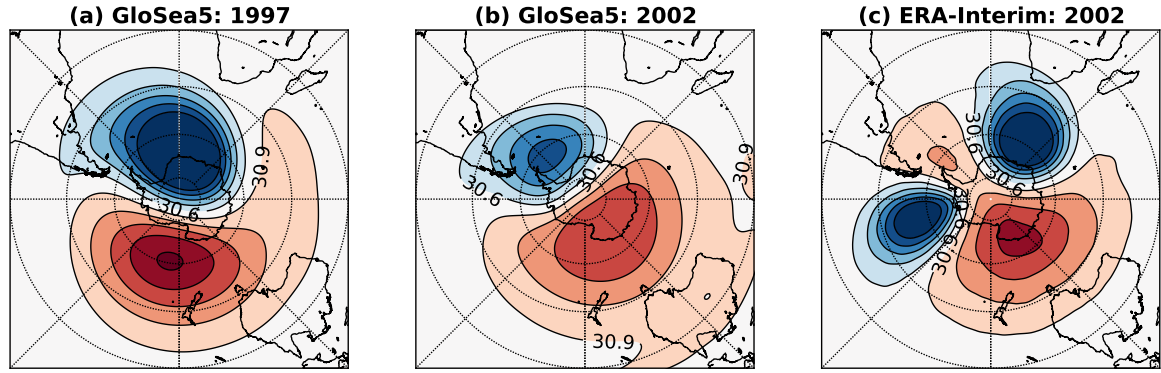


**Figure 5.11:** Geopotential height at 10 hPa on the date at which  $\bar{u}$  at 60°S and 10 hPa is at its minimum value, for the two GloSea5 ensemble members which simulate a SSW (a,b), and for ERA-Interim at the central date of the 2002 SSW (c). Units are km and the contour interval is 0.3 km.

2394 to be highly significant. This is probably because the mean timing of the final warming  
 2395 is towards the end of the four month hindcast simulation (around 20th November at  
 2396 10 hPa), and the final warming does not occur before the end of the hindcast for some  
 2397 ensemble members, thereby introducing a bias in the mean.

#### 2398 5.4.2 Ozone depletion

2399 GloSea5 does not include interactive ozone chemistry, so in order to make ozone fore-  
 2400 casts concentrations must be inferred from other meteorological variables. Total ozone  
 2401 quantities over the Antarctic polar cap have been found to be highly correlated with  
 2402 vertical EP flux poleward of 40°S [Weber *et al.*, 2011; Salby *et al.*, 2012]. EP flux di-  
 2403 agnostics are not routinely produced directly by operational seasonal forecast systems  
 2404 and requires high frequency output at high spatial resolution to calculate. However,  
 2405 vertical EP flux dominates variability of the stratospheric polar vortex, so it may be  
 2406 possible to use the strength of the vortex to infer ozone quantities.

2407 SON mean total column ozone quantities area-weighted averaged over the polar  
 2408 cap (60–90°S) are shown in Figure 5.12(a) for ERA-Interim and the Total Ozone Map-  
 2409 ping Spectrometer (TOMS) satellite instrument [Kroon *et al.*, 2008]. ERA-Interim data  
 2410 are highly correlated with TOMS, verifying the accuracy of ERA-Interim against direct

#### 5.4. SOUTHERN HEMISPHERE RESULTS

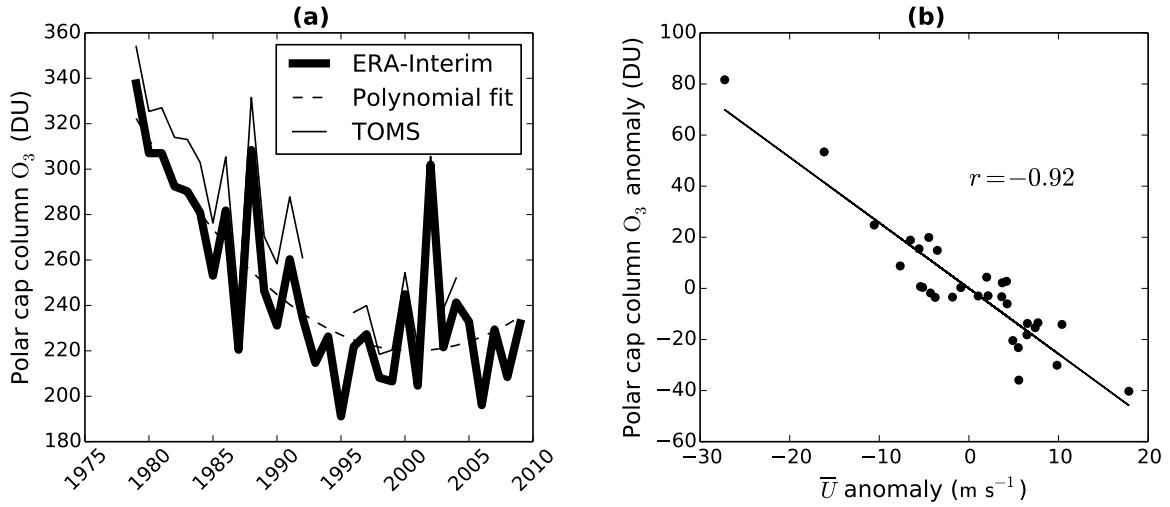


**Figure 5.12:** (a) Time series of SON mean polar cap averaged ( $60\text{--}90^\circ\text{S}$ ) total column ozone in ERA-Interim and the TOMS satellite instrument. The ERA-Interim data are fitted with a 2nd-order polynomial. (b) Anomalies of ERA-Interim column ozone from the polynomial fit plotted against SON mean anomalies at 10 hPa and  $60^\circ\text{S}$  for each year from 1979–2009.

satellite measurements (TOMS values are slightly higher than ERA-Interim; this is probably because TOMS cannot make observations during the polar night). The long-term trend in polar cap total column ozone is calculated by fitting a second-order polynomial to the data. This long-term trend is due to changes in concentrations of CFCs and other ozone-depleting substances, and largely unrelated to dynamical variability. On the other hand, shorter-term interannual changes are strongly related to dynamical variability. In Figure 5.12(b) anomalies of polar cap total column ozone from the long-term trend are plotted against anomalies of the SON mean  $\bar{u}$  at  $60^\circ\text{S}$  and 10 hPa. It can be seen that these two quantities are highly correlated ( $r = -0.92$ ), meaning polar vortex variability explains approximately 85% of the variance of polar cap total column ozone anomalies.

This strong correlation makes it possible to use GloSea5 forecasts of polar vortex winds to produce inferred predictions of polar cap total column ozone quantities. This is carried out by a leave-one-out cross-validation procedure [Wilks, 2006]; the linear regression of ERA-Interim ozone and  $\bar{u}$  anomalies for all years 1979–2009 except the hindcast year is used to produce the hindcast for each ensemble member. Thus no information from the hindcast year enters the hindcast itself. Figure 5.10(b) shows

2428 the GloSea5 ozone hindcasts along with the assimilated values from ERA-Interim. The  
 2429 correlation between the GloSea5 ensemble mean and ERA-Interim is 0.73, which is sta-  
 2430 tistically significant at the 99% level, and has a 95% confidence interval of (0.38, 0.91).  
 2431 Errors from the regression in Figure 5.10(b) for the inferred ozone quantities for each  
 2432 ensemble member are small compared to the spread between ensemble members, and  
 2433 so are not plotted in this figure.

### 2434 5.4.3 Southern Annular Mode

2435 The SAM index in both GloSea5 and ERA-Interim is depicted as the difference between  
 2436 the normalized anomalies of zonally averaged mean sea-level pressure at 40°S and  
 2437 65°S [Gong and Wang, 1999]. These anomalies are calculated from the respective  
 2438 climatologies of GloSea5 and ERA-Interim. The ERA-Interim SAM index calculated in  
 2439 this way is also highly correlated with other measures of the SAM, such as the station-  
 2440 based index of Marshall [2003]. The GloSea5 hindcast skill for the prediction of the  
 2441 seasonal (SON) mean SAM index is shown in Figure 5.13 . The correlation of the  
 2442 GloSea5 ensemble mean and ERA-Interim is 0.64, which is statistically significant at  
 2443 the 95% level, and has a 95% confidence interval of (0.18,0.92) confirming skillful  
 2444 prediction of the SAM at 1 month average lead times. This is similar to the value  
 2445 for the December–February (DJF) NAO correlation skill of 0.62 found by Scaife et al.  
 2446 [2014] in the same seasonal forecast system. The 1-year lag autocorrelation of the  
 2447 SON mean SAM is negative ( $r = -0.36$ ), and accounting for this by sampling pairs  
 2448 of consecutive years in the bootstrap test leads to a narrower confidence interval than  
 2449 presented above. The variability of the SAM simulated by GloSea5 is broadly realistic  
 2450 with a standard deviation of all ensemble members of 0.98 compared to 0.90 in ERA-  
 2451 Interim over the same period.

2452 The SAM is strongly related to surface temperatures over much of the SH extratrop-  
 2453 ics. Figure 5.14(a) shows the correlation of the SON mean SAM from ERA-Interim over  
 2454 1996–2009 with SON mean gridded station-based surface temperature data from the  
 2455 HadCRUT4 data set [Morice et al., 2012]. The HadCRUT4 data set has been chosen to  
 2456 demonstrate the relationship between the SAM and surface temperature because of the

#### 5.4. SOUTHERN HEMISPHERE RESULTS

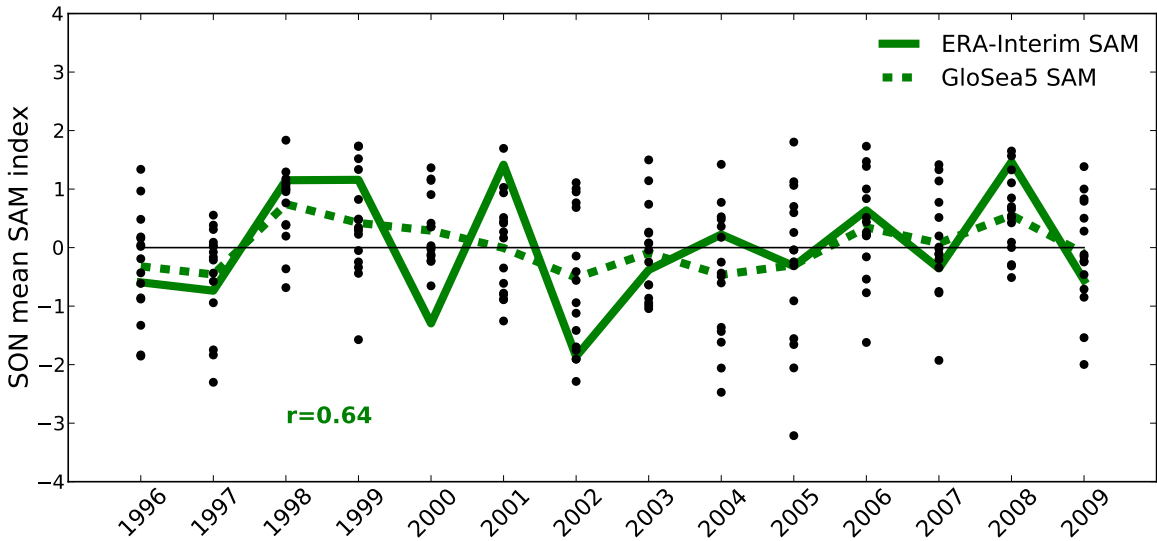


**Figure 5.13:** SON mean Southern Annular Mode (SAM) index in individual GloSea5 hindcast ensemble members (dots), ensemble mean (dashed green curve) and ERA-Interim (solid green curve). The SAM is calculated from mean sea-level pressure data, and hindcasts initialized near 1st August. The correlation of the ensemble mean and ERA-Interim values is 0.64, which is statistically significant at the 95% level.

scarcity of temperature observations in the Southern Hemisphere, meaning reanalysis data is poorly constrained in many regions. The same relationship between surface temperatures and the SAM is shown for the GloSea5 ensemble mean in Figure 5.14(b). Many of the observed correlations are reproduced in the hindcasts, such as the opposite signed correlations over east Antarctica and the Antarctic Peninsula/Patagonia, as well as between eastern Australia and New Zealand. These results are in agreement with Gillett *et al.* [2006] who analysed the temperature patterns associated with the SAM over the longer observational record of 1957–2005.

The GloSea5 ensemble mean SON surface temperature correlation with HadCRUT4 is shown in Figure 5.14(c). Also highlighted (black circles) are the points with the strongest observed correlations with the SAM ( $|r| > 0.5$ ). Regions of significant positive correlations are found over east Antarctica, Patagonia, New Zealand, and eastern Australia. These are regions which also have a strong correlation with the SAM, indicating that the significant surface temperature skill is related to skill in prediction of the SAM. On the other hand, there are also some significant negative correlations

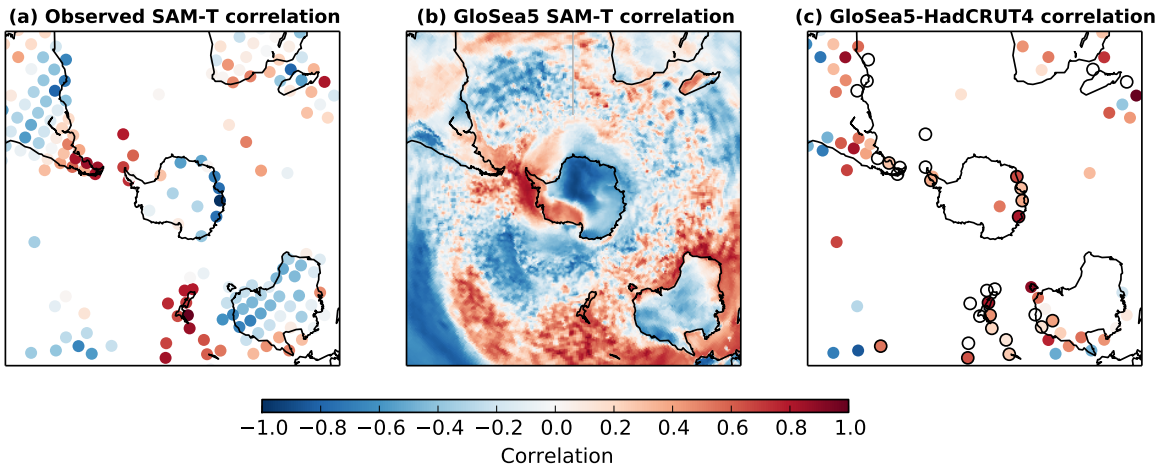


**Figure 5.14:** (a) Correlation of the ERA-Interim SON mean SAM with SON mean HadCRUT4 gridded station-based temperature observations over 1996–2009. (b) Correlation of the SON GloSea5 ensemble mean hindcast SAM with the SON hindcast ensemble mean near-surface temperature. (c) Correlation of observed SON mean HadCRUT4 and hindcast GloSea5 ensemble mean temperature. In (c) only correlations which are significant from zero at the 95% level according to a bootstrap test at each gridpoint are shown. Black circles represent points which have an observed correlation with the SAM with magnitude greater than 0.5.

2472 in subtropical regions, which may indicate a model bias in the temperature pattern  
2473 associated with the SAM in these regions.

#### 2474 5.4.4 Stratosphere-troposphere coupling

2475 It is now investigated whether the statistically significant skill in hindcasts of the strato-  
2476 spheric polar vortex affects that of the surface SAM. Forecast skill as a function of lead-  
2477 time and height is studied for polar cap ( $60\text{--}90^\circ\text{S}$ ) mean geopotential height anomalies  
2478 ( $Z'$ )<sup>1</sup>. Figure 5.15(a) shows the correlation of  $Z'$  in ERA-Interim with the GloSea5 en-  
2479 semble mean hindcast values. Values are smoothed with a 30-day running mean before  
2480 correlations are calculated, and plotted such that values for 15th September represent  
2481 the correlation of the ERA-Interim and GloSea5 ensemble mean September mean val-  
2482 ues (without this smoothing, there are noisier but still significant correlations in a  
2483 similar pattern). Between 1st–9th August the ensemble mean is taken as the average of

<sup>1</sup>At 1000 hPa monthly mean  $Z'$  is highly correlated ( $r = 0.98$ ) with the SAM index

#### 5.4. SOUTHERN HEMISPHERE RESULTS

2484 the 10 initialized ensemble members, and the average of all 15 ensemble members is  
2485 used after this date.

2486 As would be expected from the initialization of GloSea5 from ERA-Interim data,  
2487 correlations are high in both the troposphere and the stratosphere for the August  
2488 mean, due to predictability on weather timescales. However, tropospheric and lower-  
2489 stratospheric skill rapidly decays and becomes statistically insignificant throughout  
2490 September. In contrast, stratospheric correlations remain statistically significant through-  
2491 out the hindcast simulation, and as high as 0.8 through to mid-October (corresponding  
2492 to a 2 month lead time).

2493 Importantly, the region of high levels of stratospheric skill descends with time and is  
2494 present at the tropopause at the same time as a re-emergence of significant tropospheric  
2495 skill in mid-October. This re-emergence cannot be accounted for by the persistence of  
2496 tropospheric anomalies, so must be the result of the effect of another predictable signal  
2497 on the extratropical tropospheric circulation. An obvious candidate for such a signal is  
2498 the polar stratosphere, since this remains predictable throughout the hindcast period.  
2499 The re-emergence of tropospheric skill also occurs at the same time as the strongest  
2500 observed coupling between the stratosphere and troposphere found in other studies  
2501 [e.g., *Thompson et al., 2005; Simpson et al., 2011*].

2502 In order to determine the stratospheric influence on tropospheric skill, a simple  
2503 statistical forecast model is formed, which has as its only input the initial conditions  
2504 of the Antarctic stratosphere. A leave-one-out cross validation (LOOCV) [*Wilks, 2006*]  
2505 procedure is employed as follows:

- 2506 i. Remove the predictand year,  $i$ , from the set of all  $N$  years, leaving  $N - 1$  predictor  
2507 years.
- 2508 ii. Calculate the linear regressions of  $Z'$  at 10 hPa on 1st August with  $Z'$  at all other  
2509 times and heights using the  $N - 1$  predictor years.

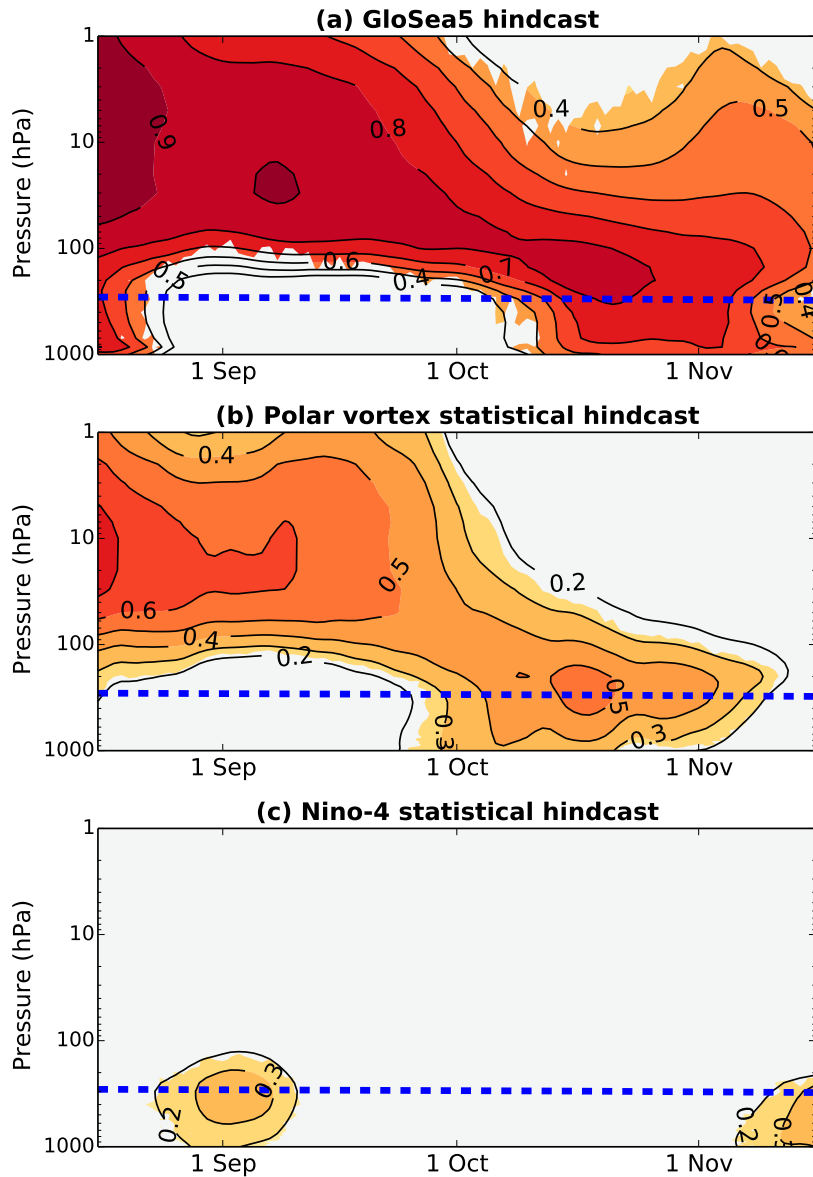


**Figure 5.15:** (a) Correlation of GloSea5 ensemble mean polar cap ( $60\text{--}90^\circ\text{S}$ ) geopotential height anomalies ( $Z'$ ) with ERA-Interim values from 1996–2009, as a function of time and height. (b) Correlation of ERA-Interim from 1979–2010 values with those predicted by a linear statistical model based on  $Z'$  at 10 hPa on 1st August. (c) As (b) but based on the July-mean Niño-4 index. All values are smoothed with a 30-day running mean before correlations are calculated. The contour interval is 0.1 and all colored regions are greater than zero at the 95% confidence interval, using a bootstrap test at each time at height. The blue dashed line indicates the approximate polar cap mean tropopause level [Wilcox et al., 2012b].

#### 5.4. SOUTHERN HEMISPHERE RESULTS

- 2510     iii. Given the value of  $Z'$  at 10 hPa on 1st August for year  $i$  (the predictand year), use  
2511       the linear regressions to produce a forecast for  $Z'$  at all other times and heights for  
2512       this year.
- 2513     iv. Repeat the above steps for  $i = 1, 2, \dots, N$  to produce  $N$  forecasts, each with slightly  
2514       different regression coefficients.

2515     The method ensures that no information from the predictor year enters the regression,  
2516     and provides an estimate of the predictability of an unknown year given the available  
2517     observations. Here, ERA-Interim values are used from 1979–2009; giving  $N = 32$   
2518     years.

2519     Figure 5.15(b) shows the correlation of 30-day running means of these statistical  
2520     hindcasts with ERA-Interim values. As might be expected, skill is initially high in the  
2521     mid-stratosphere but not the troposphere. As with the GloSea5 hindcasts, the region  
2522     of high skill descends with time, and statistically significant correlations re-emerge in  
2523     the troposphere throughout October. This demonstrates that skillful forecasts of the  
2524     Antarctic troposphere during October can be produced based only on knowledge of  $Z'$   
2525     in the mid-stratosphere on 1st August. It also suggests that the re-emergence of tropo-  
2526     spheric skill in the GloSea5 hindcasts in October is likely to be caused by predictable  
2527     stratospheric anomalies which descend with time.

2528     However, it is also possible that a third factor both influences the 1st August strato-  
2529     sphere and the October and November troposphere. ENSO may be such a factor, since  
2530     it has been shown to influence both the surface SAM [Lim et al., 2013] and the polar  
2531     stratosphere [Hurwitz et al., 2011]. The influence of ENSO is therefore assessed using  
2532     the same leave-one-out cross-validation procedure, and shown in Figure 5.15(c). The  
2533     input to the statistical model is the July mean Niño-4 index (sea-surface temperatures  
2534     averaged over 5°S–5°N, 160°–150°W) from the HadISST1 data set [Rayner et al., 2003].  
2535     Similar results are obtained using the July mean Niño-3.4 index or Southern Oscillation  
2536     Index. The Niño-4 index-based statistical hindcasts show some significant tropospheric  
2537     correlations around 1st September and in November, but not during October. Hence,

2538 ENSO cannot account for the October re-emergence of tropospheric skill in the GloSea5  
 2539 hindcasts, at least in this statistical model.

2540 Importantly, the longer 32-year (1979–2010) period of the ERA-Interim reanalysis  
 2541 (rather than the 14-year (1996–2009) period of the GloSea5 hindcasts) is used for the  
 2542 statistical analysis presented in Figures 5.15(b) and (c). The correlation between both  
 2543 the 1st August  $Z'$  at 10 hPa and the July mean Niño-4 index with the SON SAM is  
 2544 not statistically significantly different during 1996–2009 compared with 1979–2010.  
 2545 This was tested using a bootstrap test, which correlates subsets of 14 years from the  
 2546 (detrended) 32 years. Hence correlations found for the shorter period are deemed to  
 2547 be a marginal distribution of those over the longer period, so a more robust measure of  
 2548 sources of predictability can be obtained by studying the longer observational record.  
 2549 A more detailed justification for this choice of analysis period in the statistical hindcasts  
 2550 is given in Appendix 5.A.

2551 Similar features are seen if the statistical hindcasts are repeated using the shorter  
 2552 period, although tropospheric skill from the polar vortex emerges later (in November),  
 2553 and that from Niño-4 earlier (in October). These statistical hindcasts also show lower  
 2554 skill than the GloSea5 hindcasts at almost all times in both the troposphere and strato-  
 2555 sphere, which may indicate the importance of non-linearities or the influence of other  
 2556 external factors which can be captured by the full dynamical model.

## 2557 5.5 Discussion

### 2558 5.5.1 Northern Hemisphere

2559 The fact that hindcasts of the NH stratospheric polar vortex have been shown to be less  
 2560 skilful than those of the SH is not unexpected because of the much greater dynamical  
 2561 variability and chaotic nature of the NH. Indeed, previous studies have not found SSWs  
 2562 to be predictable (in a deterministic sense) beyond about two weeks [*Marshall and*  
 2563 *Scaife, 2010; Taguchi, 2014*]. However, given the fact that the GloSea5 hindcasts have  
 2564 been shown to produce skilful predictions of the DJF NAO [*Scaife et al., 2014*], it is  
 2565 perhaps surprising that somewhat greater skill was not found in Section 5.3. Even if

2566 the vortex was to respond passively to NAO variability, a greater degree of skill might  
 2567 be expected.

2568 A possible explanation for this may be that GloSea5 does not produce skilful fore-  
 2569 casts of the North Pacific, so that the North Pacific and North Atlantic ‘destructively  
 2570 interfere’ in their influence on the stratosphere. However, *MacLachlan et al.* [2014]  
 2571 found GloSea forecasts of DJF surface temperatures to have similar skill in the North  
 2572 Atlantic and North Pacific, as well as the surface NAM to have similar skill as the NAO.  
 2573 Therefore, the reason for the relative lack of skill in hindcasts of the NH stratospheric  
 2574 polar vortex remains unknown. This does, however, suggest that the source of skilful  
 2575 DJF NAO hindcasts in GloSea5 is unlikely to be of tropospheric origin, and other model  
 2576 improvements such as the increased ocean resolution may be more important.

## 2577 5.5.2 Southern Hemisphere

### 2578 5.5.2.1 Model limitations

2579 We have demonstrated that Antarctic total column ozone amounts are predictable up  
 2580 to four months in advance during the austral spring, even with a model which lacks  
 2581 interactive chemistry. While using such a model has the advantage of being less com-  
 2582 putationally expensive than a chemistry-climate model, there are also some drawbacks.  
 2583 Primarily, the model will not be able to simulate zonal asymmetries in ozone concen-  
 2584 trations and their influence on the stratospheric circulation or the feedback between  
 2585 ozone concentrations and stratospheric temperatures. Both these factors have been  
 2586 shown to be important in driving long-term trends in the SAM as a result of ozone  
 2587 depletion [*Thompson and Solomon*, 2002; *Crook et al.*, 2008; *Waugh et al.*, 2009].

2588 Perhaps more relevant for seasonal forecasts is the fact that we have not been able  
 2589 to determine whether the observed strong correlation between the stratospheric cir-  
 2590 culation and Antarctic ozone concentrations is dominated by a chemical or dynamical  
 2591 mechanism. If the relationship is dominated by a chemical mechanism, whereby en-  
 2592 hanced descent over the pole inhibits the activation of ozone-depleting substances, we  
 2593 would expect the correlation to weaken as concentrations of these substances return

2594 to pre-industrial levels. Accurate forecasts of ozone with models lacking interactive  
 2595 chemistry would then not be possible. On the other hand, if the mechanism is largely  
 2596 dynamical, whereby transport of ozone-rich air from the tropics is the important factor,  
 2597 we would not expect the relationship to change in time. Although a study to dis-  
 2598 tinguish these mechanisms has been carried out for chemistry-climate models [*Garny*  
 2599 *et al.*, 2011], it has not been possible to do so in observations. In either case, we do  
 2600 not expect the relationship to break down soon, as concentrations of ozone-depleting  
 2601 substances are not projected to return to 1980 levels until the late 21st century [*WMO*,  
 2602 2011].

### 2603 5.5.2.2 Statistical significance and ensemble size

2604 The correlation skill of 0.64 (95% confidence interval: [0.18,0.92]) for the SON mean  
 2605 SAM in the GloSea5 hindcasts is greater but not inconsistent with that found by *Lim*  
 2606 *et al.* [2013]. They report a correlation of 0.40 for the SON mean SAM from 1st Au-  
 2607 gust initialized forecasts over 1981–2010 using the Predictive Ocean and Atmosphere  
 2608 Model for Australia, version 2 (POAMA2). Over the comparable period of 1996–2009,  
 2609 they find a correlation of 0.54 (Harry Hendon, Australian Bureau of Meteorology, per-  
 2610 sonal communication, 2014). Significantly, POAMA2 has only two model levels in  
 2611 the stratosphere, and so may be unable to simulate the stratosphere-troposphere cou-  
 2612 pling described here. *Lim et al.* [2013] attribute their results to the influence of ENSO  
 2613 through a tropospheric teleconnection. This is not inconsistent with our result shown in  
 2614 Figure 5.15(c), since we find significant tropospheric predictability from ENSO during  
 2615 November, the same time that *Lim et al.* [2013] find the strongest correlation between  
 2616 ENSO and the SAM. The lack of discrepancy between these two systems despite their  
 2617 different stratospheric resolutions may be a result of the ENSO/SAM connection be-  
 2618 ing too weak in GloSea5, or simply that the relatively short hindcast period used here  
 2619 prevents a statistically significant difference being detected.

Despite this significant correlation skill in hindcasts of the SAM, it is clear from Figure 5.13 that the standard deviation of the GloSea5 ensemble mean SAM is much less than that of observations. The signal-to-noise ratio (ratio of the standard deviation

## 5.5. DISCUSSION

of the ensemble mean to that of all ensemble members) is just 0.4. For a ‘perfect’ forecast system (one in which observations are indistinguishable from an ensemble member), the signal-to-noise ratio,  $s$ , and correlation,  $r$ , are directly related by

$$r = \frac{s^2}{\sqrt{(s^2 + 1)(s^2 + n^{-1})}}, \quad (5.1)$$

where  $n$  is the ensemble size [Sardeshmukh *et al.*, 2000; Kumar, 2009]. Hence, given the value of  $s = 0.4$ , the expected correlation would be just 0.3, rather than the 0.64 found. This discrepancy can be explained from the fact that the average correlation between ensemble members and observations (0.27) is much greater than that between pairs of ensemble members (0.13). A similar but smaller difference is also found for the stratospheric polar vortex forecasts, and this is also observed by Scaife *et al.* [2014] for the NAO in the same system. These results mean that individual ensemble members have a smaller predictable signal than observations. This effect was recently discussed by Eade *et al.* [2014], who proposed a rescaling of the ensemble mean to have the same variance as the predictable component of the observed variance (which can be estimated by  $\sigma_{obs}^2 r^2$ , where  $\sigma_{obs}^2$  is the observed variance). However, this procedure is most applicable to forecasts where the scaling can be determined from hindcasts, so that information from the observations does not enter the forecasts themselves. Furthermore, this rescaling does not affect correlation skill scores, and so it is not applied in the current analysis.

Given the above result, it might be expected that more skilful predictions could be obtained with a larger ensemble size. To illustrate the variation of hindcast skill with ensemble size we systematically sample smaller sets of forecasts from the full 15 members for each year, following the method of Scaife *et al.* [2014]. This is repeated many times ( $\sim 10\,000$ ) and an average value for a given sample size calculated. This variation of correlation skill with ensemble size for both the SON mean SAM and stratospheric polar vortex winds is shown in Figure 5.16. These curves closely follow the theoretical relationship of Murphy [1990], which relies only on the mean correlation

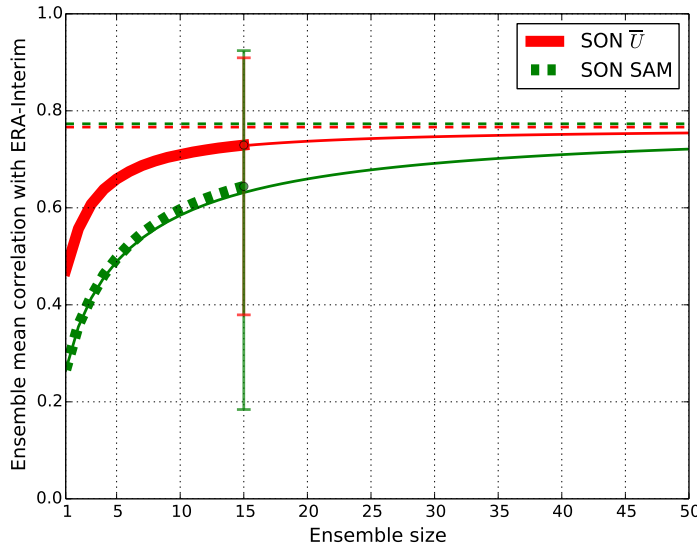


**Figure 5.16:** GloSea5 ensemble mean correlation with ERA-Interim as a function of ensemble size for the SON mean  $\bar{U}$  at 10 hPa and 60°S and SON mean SAM (thick lines). A theoretical estimate of the variation of correlation with ensemble size is shown in each case (thin solid lines), along with its asymptote for an infinite sized ensemble (dashed lines). Error bars represent the 95% uncertainty range for the correlation of the full 15-member ensemble, calculated using a bootstrap test.

between pairs of ensemble members,  $\langle r_{mm} \rangle$ , and the mean correlation between individual ensemble members and observations,  $\langle r_{mo} \rangle$ , given by

$$r = \frac{\langle r_{mo} \rangle \sqrt{n}}{\sqrt{1 + (n - 1)\langle r_{mm} \rangle}}. \quad (5.2)$$

These curves are shown in Figure 5.16, along with their asymptote for an infinite sized ensemble. This shows that the stratospheric forecasts cannot be greatly improved with a larger ensemble size in the current system, but greater correlation scores of the SAM could be achieved with an ensemble size near 30. Although the large uncertainty range does not allow a strong statement about potential predictability, the asymptote near 0.8 is similar to that found by *Scaife et al. [2014]* using a longer hindcast and greater ensemble size for the DJF NAO.

### 5.5.2.3 Application to other seasons

The dynamics of other seasons are different to those of the austral spring, so results presented here for SON do not imply significant skill in prediction of the SAM at other

## 5.5. DISCUSSION

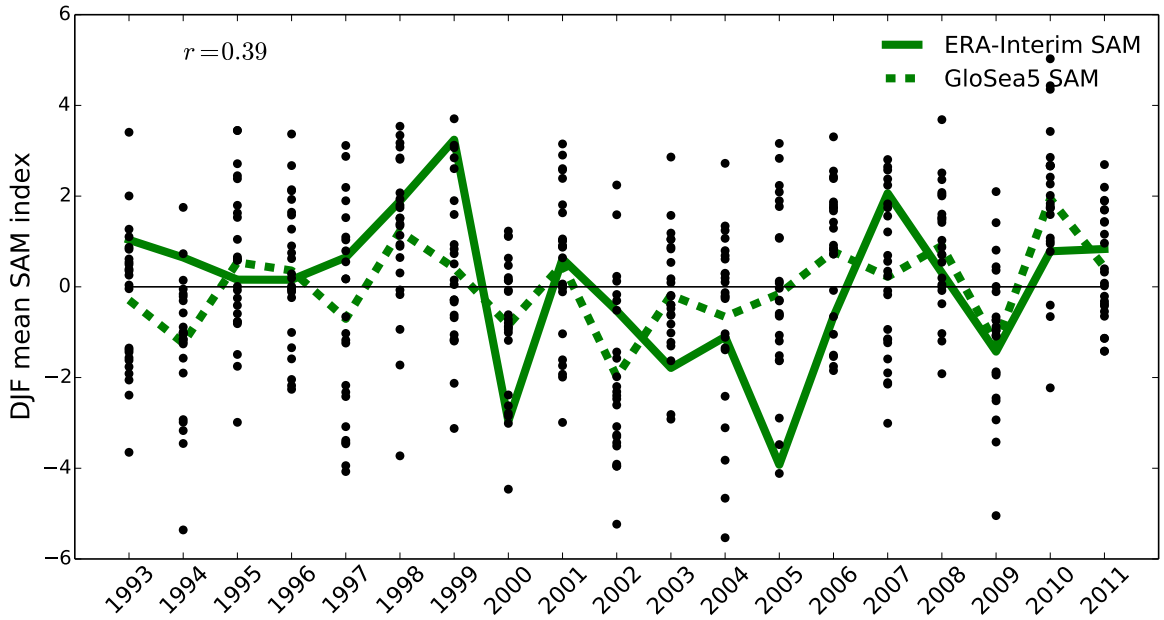


**Figure 5.17:** DJF mean Southern Annular Mode (SAM) index in individual GloSea5 hindcast ensemble members (dots), ensemble mean (dashed green curve) and ERA-Interim (solid green curve). The SAM is calculated from mean sea-level pressure data, and hindcasts initialised near 1st November. The correlation of the ensemble mean and ERA-Interim values is 0.39.

times. Indeed, the 1-month lead time ensemble mean correlation of the DJF SAM with ERA-Interim is lower than that for SON at  $r = 0.39$  (95% confidence interval: [0.15,0.63]), as shown in Figure 5.17. The low signal-to-noise ratio found in Figure 5.13 for SON can also be seen in Figure 5.17.

*Shaw et al. [2010]* found that the strongest downward wave coupling between the stratosphere and troposphere is present during September to December in the SH. They attribute this to the fact that the lower stratospheric vortex is westerly during this time, but the mid-upper stratospheric vortex is easterly (because the final warming occurs first in the upper stratosphere) and acts as a relecting surface for planetary waves. Following the final warming in the lower stratosphere, *Shaw et al. [2010]* find wave coupling to be much weaker. *Shaw et al. [2011]* extended this analysis to also demonstrate that the dynamical influence of stratospheric ozone depletion on the troposphere through wave coupling is greatest during September-December.

On the other hand, separate studies have found that the largest tropospheric signals associated with stratospheric ozone depletion occur later, in DJF [*WMO, 2011*]. This

may seem to contradict the findings of *Shaw et al.* [2010], but the two results can be reconciled if a different mechanism is dominant at this later time. Indeed, as well as an effect on the dynamical coupling between the stratosphere and troposphere, *Grise et al.* [2009] proposed that stratospheric ozone depletion can perturb radiative heating rates in the troposphere which can, in turn, trigger changes in tropospheric dynamics. They used a radiative model to investigate this effect and, importantly, found the largest influence on polar tropospheric temperatures to occur during DJF. A possible physical explanation for this is that it is only after the final warming, when the ozone depleted polar stratospheric air is mixed with lower latitudes, that the radiative effect on the troposphere is significant. While this was only an idealised study which lacked tropospheric dynamics, it may suggest a reconciliation with dynamical coupling being strongest from September–December and radiative from December–February.

The time dependency of SH stratosphere-troposphere coupling is further investigated in Figure 5.18. This shows lag-height correlations of polar cap  $Z'$  in the midstratosphere (10 hPa), lower-stratosphere (70 hPa) and surface (1000 hPa) at the first of each month from August–January using ERA-Interim data (1979–2010). As in Figure 5.15, values are smoothed with a 30-day running mean before correlations are calculated. Midstratosphere-leading significant correlations with the October–November troposphere are seen from 1st August (Figure 5.18(a)), as also shown in Figure 5.15. Furthermore the strongest negative lag correlations of the surface with the stratosphere occur at 1st November (Figure 5.18(l)). This supports the result of *Shaw et al.* [2010] that September–December is the time of strongest stratosphere-troposphere dynamical coupling.

Similar, but weaker lag correlations are seen at 1st January (Figure 5.18(r)). This is unlikely to be due to dynamical coupling since it comes after the stratospheric final warming, and so may be a result of the radiative effect described above. It is important to note that GloSea5 does not contain interactive ozone chemistry, so the radiative effects of ozone variability will not be captured by the model. This may explain, to some extent, the reduced skill in the prediction of DJF SAM compared to the SON SAM, since the predictable effects of the stratosphere on the troposphere are not captured during

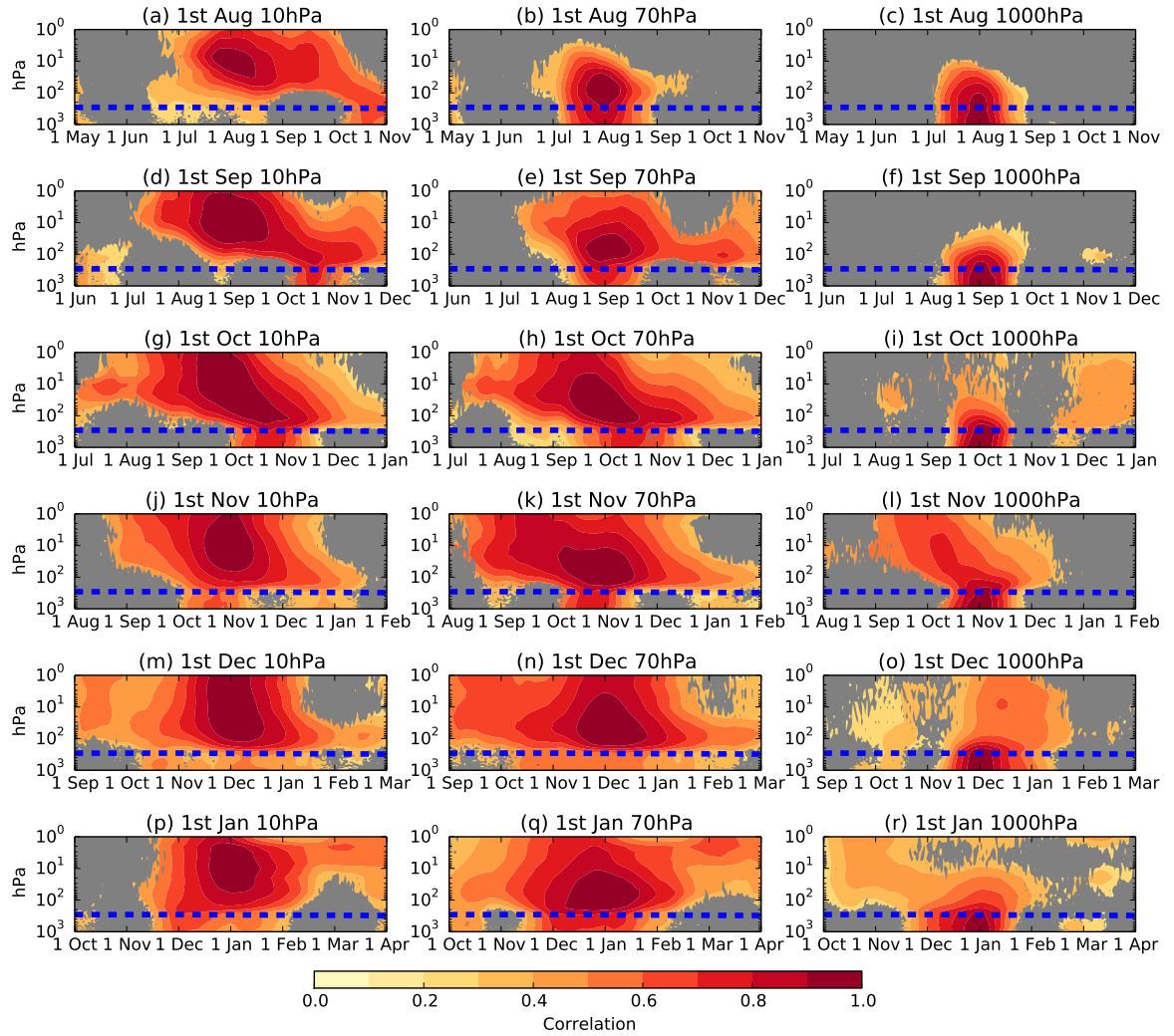


**Figure 5.18:** Correlation of ERA-Interim (1979–2010)  $Z'$  at 10 hPa, 70 hPa, and 1000 hPa with  $Z'$  at other times and lags. Values are smoothed with a 30-day running mean before correlations are calculated, and colours represent correlations that are 95% significant from zero according to a bootstrap test.

2690 DJF. Consequently, more skilful forecasts of the DJF SAM may be possible with a model  
 2691 including interactive ozone chemistry.

## 2692 5.6 Conclusions

2693 Motivated by the results of Chapters 3 and 4, we have analysed the predictability of the  
 2694 polar stratosphere and its influence on the troposphere in a set of hindcasts produced  
 2695 by a stratosphere-resolving seasonal prediction system. Analysis has focussed on the  
 2696 NH for the boreal winter (DJF) and SH for the austral spring (SON), with forecasts  
 2697 initialised at a 1-month lead time.

2698 No statistically significant skill was found in the prediction of the seasonal mean  
 2699 strength of the NH stratospheric polar vortex, or the occurrence of SSWs, split or  
 2700 displaced vortex events. This result may be surprising given that the same system  
 2701 produces skilful hindcasts of the winter NAO, which is known to influence the polar  
 2702 stratosphere. It does, however, suggest that this NAO skill is unlikely to be influenced  
 2703 by the troposphere and may be attributable to other model improvements.

2704 On the other hand, skillful prediction of the interannual variability of the spring  
 2705 Antarctic stratospheric polar vortex at seasonal lead times. This includes capturing an  
 2706 increased likelihood of the 2002 SSW which is the most extreme year in the ensemble  
 2707 mean and has the only ensemble member in 14 years which simulates a SSW (although  
 2708 another is close to simulating a SSW in 1997). Because this variability is observed to  
 2709 be closely correlated with Antarctic column ozone amounts, we are able to perform  
 2710 skillful predictions of interannual variability in Antarctic ozone depletion.

2711 We also find significant skill in hindcasts of the spring mean SAM index. By studying  
 2712 the variation of this skill with time and height, we suggest that this skill is influenced by  
 2713 stratospheric anomalies which descend with time and are coupled with the troposphere  
 2714 in October and November. In fact, the influence of the stratosphere is such that skillful  
 2715 statistical predictions of the October SAM can be made using only information from 1st  
 2716 August in the mid-stratosphere.

## 5.6. CONCLUSIONS

<sup>2717</sup> Assuming that the 14 year period studied here is representative of future years,  
<sup>2718</sup> these results suggest that it may now be possible to make skillful seasonal forecasts of  
<sup>2719</sup> interannual variations in springtime ozone depletion and large scale weather patterns  
<sup>2720</sup> across the Southern Hemisphere.

## 2721 5.A Choice of time period for statistical forecast

2722 The aim of the LOOCV statistical analysis presented in Section 5.4.4 was to estimate  
 2723 the degree of predictability which arises from both the midstratosphere at the start  
 2724 of August and the July-mean Niño-4 index. Importantly, this analysis used the longer  
 2725 ERA-Interim period of 1979-2009 rather than the same 1996-2010 period over which  
 2726 the hindcast simulations were run. A choice of the longer period would be justifiable  
 2727 (and, indeed, preferable) if the relationships between these parameters and the fore-  
 2728 cast parameter ( $Z'$ ) are not physically different over the shorter period. That is, if the  
 2729 shorter period is a marginal distribution of the longer period. This is shown to be the  
 2730 case below.

2731 We use the monthly Southern Oscillation Index (MSLP difference between Darwin  
 2732 and Tahiti, which is highly correlated with the Niño-4 index) data obtained from the  
 2733 Australian Bureau of Meteorology [http://www.bom.gov.au/climate/current/  
 2734 soihtm1.shtml](http://www.bom.gov.au/climate/current/soihtm1.shtml), and a station-based SAM index from the British Antarctic Survey  
 2735 [[Marshall, 2003](#)]. For the 1996-2009 hindcast period we find the correlation of June-  
 2736 July SOI with Oct-Nov SAM to be  $r = 0.63$ . For 1979-2010 (the ERA-Interim period)  
 2737  $r = 0.32$ . In order to justify using the shorter hindcast period (with higher correlation),  
 2738 it would need to be the case that the SAM/SOI correlation is statistically significantly  
 2739 stronger during the hindcast period than the ERA-Interim period, so that these different  
 2740 correlations are not a result of random variability.

2741 To test whether this is the case, we use a bootstrap test which randomly samples  
 2742 (with replacement) 14 years of detrended SAM and SOI from 1979-2013, and calcu-  
 2743 lates the correlation. Figure 5.19 shows a histogram of these correlations along with  
 2744 the 1996-2009 correlation. The 1996-2009 value is not inconsistent with random vari-  
 2745 ability at the 95% level for either a one- or two-tailed test. Therefore we conclude that  
 2746 the SAM/SOI correlation is not statistically significantly greater for 1996-2009. As such  
 2747 the 1996-2009 correlation is a marginal distribution of 1979-2013 so we include the  
 2748 longer ERA-Interim period in our analysis to provide a more robust measure of sources  
 2749 of predictability.

5.A. CHOICE OF TIME PERIOD FOR STATISTICAL FORECAST

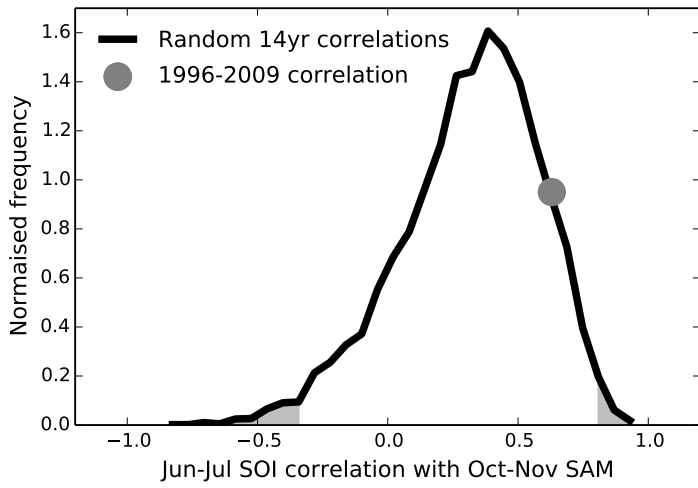


**Figure 5.19:** Histogram of correlations of random 14-year samples of detrended June-July SOI with October-November SAM. Also shown is the correlation over the 1996–2009 hindcast period. Grey shading indicates the < 2.5% and > 97.5% ranges.

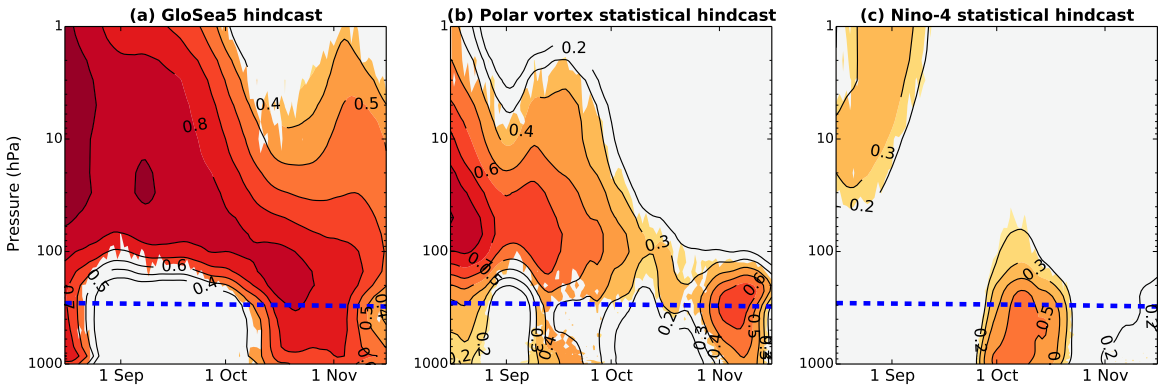


**Figure 5.20:** As Figure 5.15 but all analysis restricted to the 1996–2009 period.

2750        For completeness we include a figure with the same analysis limited to 1996–2009  
 2751        in this appendix (Figure 5.20). Similar features as Figure 5.15 can be seen although  
 2752        tropospheric skill emerges later in Figure 5.20(b) and earlier in Figure 5.20(c).



2753

# CHAPTER 6

2754

---

2755

## Conclusions

2756

---

### 2757 6.1 Summary of results

2758 The main findings of this thesis are summarised as follows:

2759 **Application of moment diagnostics.** It has been demonstrated that vortex moment  
2760 diagnostics can be successfully applied to the geopotential height field, giving similar  
2761 results as when applied to conservative fields such as PV. This therefore provides a  
2762 semi-Lagrangian (or vortex-centric) method which can be readily used to describe the  
2763 geometry of the stratospheric polar vortex in climate model simulations.

2764 It has been further shown that a simple threshold-based method can be applied to  
2765 the vortex moment diagnostics in order to identify split and displaced vortex events.  
2766 The events identified in this way coincide to a large extent with events defined by other  
2767 methods, and capture equally extreme vortex states.

2768 **The stratospheric polar vortex in climate models.** The first multi-model comparison  
2769 of stratospheric polar vortex geometry and split and displaced vortex events has been  
2770 carried out using the stratosphere-resolving CMIP5 models. A wide range of biases  
2771 have been identified in the geometry of the stratospheric polar vortex among models.  
2772 Some models have a vortex which is on average too equatorward, others too poleward,

2773 while the majority of models have a vortex which is too circularly symmetric. Models  
 2774 also vary widely in their frequency of split and displaced vortex events. However,  
 2775 the nature of these events is largely in agreement with observations, in particular the  
 2776 fact that split vortex events appear more barotropic and displaced vortex events baro-  
 2777 clinic. The consistency of this difference in baroclinicity among models lends weight to  
 2778 the idea that split vortex events are caused by a resonant excitation of the barotropic  
 2779 mode, as suggested by *Esler and Scott* [2005]. Significantly, the frequency of split and  
 2780 displaced vortex events has been demonstrated to be highly correlated respectively with  
 2781 the aspect ratio and centroid latitude of the average vortex state. It therefore follows  
 2782 that an improvement in the mean state of the vortex is likely to lead to a more accurate  
 2783 representation of these extremes.

2784 **Stratosphere-troposphere coupling in climate models and observations.** In re-  
 2785 analysis data, using the geopotential height-based vortex moments method, a stronger  
 2786 tropospheric NAM signal is seen following split vortex events than displaced vortex  
 2787 events. This is in agreement with the results of *Mitchell et al.* [2013]. However,  
 2788 a bootstrap significance test of the surface NAM over the month following these events  
 2789 cannot exclude the possibility that this observed difference is due to chance.

2790 In the CMIP5 models, the tropospheric NAM signal following both split and dis-  
 2791 placed vortex events is weak on average. There is no consistent difference between  
 2792 the two apart from close to the onset of events when there is a negative anomaly for  
 2793 split vortex events which extends barotropically through the depth of the atmosphere.  
 2794 However, looking at two-dimensional tropospheric anomalies in mean sea-level pres-  
 2795 sure following split and displaced vortex events shows some consistent features. A  
 2796 negative NAO-like signal is seen which is of similar magnitude following both types  
 2797 of event. The Pacific response is much less robust, with some models simulating neg-  
 2798 ative pressure anomalies, and others positive. The discrepancy between the Atlantic  
 2799 and Pacific responses suggests that the annular mode may not be a good metric for  
 2800 stratosphere-troposphere coupling in the NH.

## 6.1. SUMMARY OF RESULTS

2801 Almost all models show more negative sea-level pressure anomalies over Siberia  
2802 following displaced vortex events than split vortex events. Overall, the differences  
2803 in the surface signals following the two types of events are approximately co-located  
2804 with the difference in lower-stratospheric geopotential height, which in turn follow  
2805 stratospheric PV anomalies. A similar pattern is also seen in tropopause height in  
2806 reanalysis data. This suggests the mechanism behind the different surface responses  
2807 to split and displaced vortex events is one local to lower stratospheric PV anomalies,  
2808 as proposed by *Ambaum and Hoskins [2002]*. However, it should be stressed that  
2809 the similarities in the NAO response suggest that other mechanisms more sensitive to  
2810 zonal-mean anomalies, such as baroclinic instability or planetary wave reflection, also  
2811 play a role.

2812 **Predictability of the polar stratosphere.** Using hindcast simulations produced by a  
2813 stratosphere-resolving seasonal forecast system, no skill has been found in the predic-  
2814 tion of NH SSWs or split or displaced vortex events at lead times beyond one month.  
2815 This suggests that the skillful seasonal prediction of the winter NAO in the same system  
2816 [*Scaife et al., 2014*] is not highly influenced by the stratosphere. It may, however, be  
2817 attributable to other model improvements such as increased atmospheric and oceanic  
2818 horizontal resolution.

2819 On the other hand, skillful prediction of the SH stratospheric polar vortex during  
2820 the austral spring at seasonal lead times has been found. This skill is greater than a per-  
2821 sistence forecast; indeed, a strong late-summer polar vortex is related to a weak spring  
2822 vortex, indicating the importance of preconditioning. Using the observed relationship  
2823 between the strength of the stratospheric polar vortex and polar ozone, it was possible  
2824 to produce skillful forecasts of interannual variations in polar stratospheric ozone de-  
2825 pletion. This prediction is at longer lead times than previous forecasts. Furthermore,  
2826 because interannual variability is significant when compared to the long-term ozone  
2827 depletion trend, such forecasts may be of some interest for populations in the SH.

2828 A further feature of the hindcast simulations is that the year 2002, in which the only  
2829 observed SH SSW occurred, is also the most extreme of the hindcasts with almost all

2830 ensemble members simulating negative stratospheric wind anomalies. It also has one  
 2831 of the two out of 210 ensemble members which simulate SH SSW-like events (although  
 2832 these are displaced vortex events, rather than the split that occurred). This suggests  
 2833 that an increased likelihood of the 2002 event may have been detectable almost two  
 2834 months in advance.

2835 **Stratospheric influence on tropospheric predictability.** The same seasonal forecast  
 2836 system produces forecasts of the austral spring mean surface SAM at one month lead  
 2837 times. It also accurately simulates the surface temperature pattern associated with  
 2838 the SAM, such that the SAM forecast skill leads directly to skilful surface temperature  
 2839 forecasts over much of Antarctica, New Zealand, and eastern Australia. Interestingly,  
 2840 these forecasts were found to be more skilful during October–November (2 month lead  
 2841 time), than September (1 month lead time). The same pattern is replicated in a sta-  
 2842 tistical hindcast which takes as its only input the polar-cap mean geopotential height  
 2843 at 10 hPa on 1st August. The pattern cannot, however, be replicated by a statisti-  
 2844 cal forecast based on the ENSO index. This suggests, therefore, that the tropospheric  
 2845 skill during October–November is largely attributable to the influence of the predictable  
 2846 stratosphere during this time. The October–November stratospheric SAM is, in turn,  
 2847 highly predictable due to a strong negative correlation with the 1st August stratospheric  
 2848 SAM. The fact that the stratospheric influence is greatest in October–November is also  
 2849 backed-up by observational evidence which shows the largest stratosphere-leading cor-  
 2850 relations with the surface during this time. These results highlight the importance of  
 2851 including a well-resolved stratosphere and accurate stratospheric initial conditions in  
 2852 seasonal forecast systems.

## 2853 6.2 Extensions of this work

2854 The work presented in this thesis has raised a number of questions, and motivated  
 2855 future investigations. Some of these ideas are discussed below:

2856 **Systematic variation of model resolution.** It was shown in Figure 4.12 that among  
2857 CMIP5 models there appears to be a relationship between the average aspect ratio  
2858 of the stratospheric polar vortex and vertical resolution, particularly in the upper-  
2859 troposphere/lower-stratosphere. Although this relationship is backed up by the physi-  
2860 cal understanding of the influence fine-scale vertical structure on planetary wave prop-  
2861 agation in this region, it is not highly statistically significant. Furthermore, the rela-  
2862 tionship does not hold when models of the same family but different resolution are  
2863 compared. These issues could be resolved by performing a series of model integrations  
2864 in which only the vertical resolution is changed. The climatology of the stratospheric  
2865 polar vortex would be studied for each integration, and it could be determined if this  
2866 relationship holds. If it does, it could then be found at which point the vertical resolu-  
2867 tion is sufficient for a relatively realistic average vortex state, which would be valuable  
2868 for modelling centres. Such a study need not be highly computationally expensive since  
2869 it involves studying the mean state (rather than extremes such as SSWs), so relatively  
2870 few years need to be simulated.

2871 **The 2002 Southern Hemisphere SSW.** The possibility of an increased likelihood of the  
2872 2002 SH SSW up to two months in advance was suggested in Chapter 5. It is unclear,  
2873 however, what factors influence this predictability. It would therefore be interesting  
2874 to carry out an investigation in which possible influences are systematically changed.  
2875 For instance, the 2002 hindcasts could be re-run with an opposite phase of the QBO,  
2876 different tropical Pacific or Southern Ocean SSTs, or different polar stratospheric initial  
2877 conditions. The change in forecasts of the stratospheric polar vortex could then be  
2878 analysed, indicating which factors are most important. It is likely that there would be  
2879 some difficulty in imposing these different initial conditions consistently. Furthermore,  
2880 such an investigation is likely to be quite computationally expensive as it is likely that  
2881 many ensemble members will be needed in order for a sufficient number of SSWs to be  
2882 simulated.

2883 **Influence of interactive chemistry on seasonal forecast skill.** The seasonal forecast  
 2884 system analysed in Chapter 5 did not include interactive chemistry, with ozone con-  
 2885 centrations set to a climatology. It is therefore unable to capture the feedback between  
 2886 ozone concentrations and the stratospheric circulation, or zonal asymmetries in ozone.  
 2887 *Waugh et al. [2009]* have suggested that such asymmetries could have a significant im-  
 2888 pact on tropospheric climate. This motivates an investigation as to whether improved  
 2889 stratospheric or tropospheric forecasts may be achieved by including interactive chem-  
 2890 istry in a seasonal forecast system. Such a chemistry scheme is likely to be expensive,  
 2891 so the investigation should determine which reactions have the most impact on forecast  
 2892 skill.

2893 **Decadal variability.** Looking by eye at the events detected in Chapter 3, it appears  
 2894 that they cluster in time. For instance, there are 10 events in the 1970s, but only 4 in  
 2895 the 1990s. Figure 6.1 shows an attempt to analyse whether this decadal variability is  
 2896 statistically significant. It shows (solid black line) the frequency of given numbers of  
 2897 split/displaced vortex events within a 10-year moving window (shifting by one year at  
 2898 a time) in the ERA data set. Also shown (dashed black line) is the same calculation  
 2899 applied to randomly shuffled events. Error bars are calculated from the distribution  
 2900 of frequencies of the randomly shuffled events. It can be seen that the frequencies of  
 2901 8/9 events and 3 events per decade are slightly statistically significant from the random  
 2902 variability, so it might be inferred that there is statistically significant decadal variability.

2903 Figure 6.1 also shows the same calculation applied to a 2 ensemble member 1860–  
 2904 2005 historical simulation of the HadGEM2-CC model (a total of 290 years). It can be  
 2905 seen in this case that the simulation is not distinct from random variability. However,  
 2906 *Schimanke et al. [2011]* did find significant decadal variability in a coupled ocean-  
 2907 atmosphere GCM, although their model simulated only 2 events per decade. A future  
 2908 investigation could aim to resolve this issue by studying decadal variability in a greater  
 2909 number of models (such as the CMIP5 ensemble). Longer simulations than those stud-  
 2910 ied in Chapter 4 would be required in order to achieve statistically significant results.

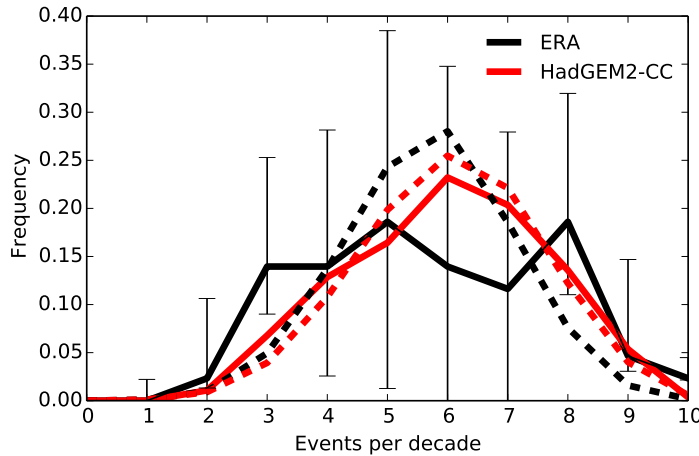


**Figure 6.1:** (solid lines) Normalised frequency of the number of SSWs detected in a 10-year moving window. (dashed lines) Average of 10-year moving window frequency of SSWs whose timing is shuffled randomly 1000 times. Error bars depict the 2.5–97.5% range of the randomly shuffled events.

2911 It would also be interesting to compare historical and control simulations in order to  
 2912 determine if any decadal variability is externally driven or internally generated.

2913 ??**Time scale of stratosphere-troposphere coupling.** In this thesis it has been demon-  
 2914 strated that split vortex events occur barotropically, suggesting an excitation of the  
 2915 barotropic mode. The relative roles of modes of variability can be further investi-  
 2916 gated through a decomposition of temporal modes and then studying coherence be-  
 2917 tween stratospheric and tropospheric modes. This is traditionally carried out through a  
 2918 Fourier spectrum analysis, however, the more modern technique of empirical mode de-  
 2919 composition (EMD) [Huang *et al.*, 1998] may be more suited to this application. EMD  
 2920 has also been used in atmospheric science by Coughlin and Tung [2004]. The method  
 2921 decomposes a given timeseries into a finite number of ‘modes’, each of which have a  
 2922 characteristic frequency. Unlike Fourier analysis, however, this frequency is allowed to  
 2923 vary to some degree, so the modes need not be perfectly periodic. As such, it is more  
 2924 applicable to time series of finite length and with a pronounced seasonal variability,  
 2925 such as the NAM. I have performed a preliminary analysis Figure 6.2 shows an exam-  
 2926 ple of such analysis applied to NH polar-cap average geopotential height. Further  
 2927 investigations can be carried out to analyse the physical relevance of the modes and  
 2928 coherence between the stratosphere and troposphere.

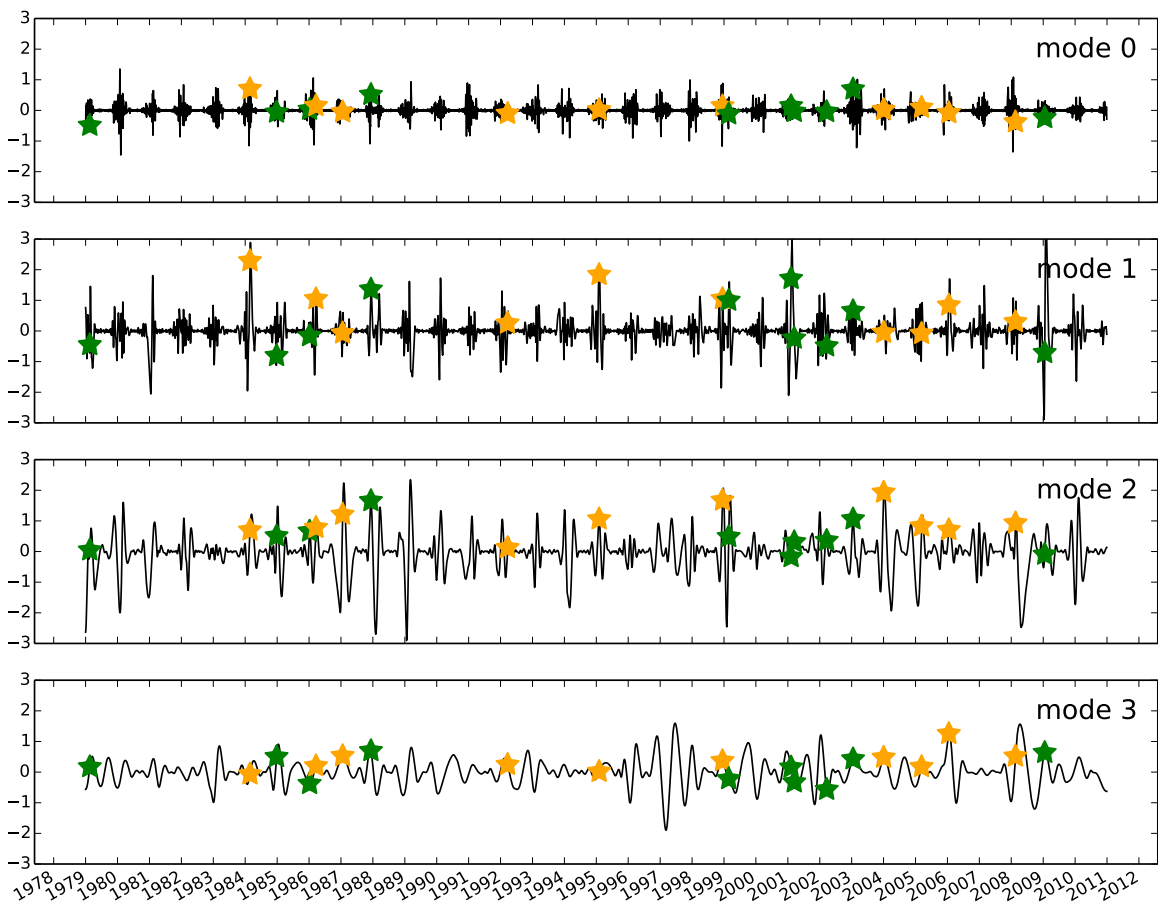


**Figure 6.2:** First four empirical modes of NH ( $60\text{--}90^\circ\text{N}$ ) geopotential height in ERA-Interim data. Yellow and green stars represent displaced and split vortex events respectively.

2929

---

2930

## Bibliography

2931

---

- 2932 Ambaum, M. H. P., and B. J. Hoskins (2002), The NAO troposphere-stratosphere con-  
2933 nection, *J. Climate*, 15, 1969–1978.
- 2934 Ambaum, M. H. P., B. J. Hoskins, and D. B. Stephenson (2001), Arctic Oscillation or  
2935 North Atlantic Oscillation?, *J. Climate*, 14, 3495–3507.
- 2936 Andrews, D., and M. McIntyre (1976), Planetary Waves in Horizontal and Vertical  
2937 Shear: The Generalized Eliassen-Palm Relation and the Mean Zonal Acceleration.,  
2938 *J. Atmos. Sci.*, 33, 2031–2048.
- 2939 Andrews, D., J. R. Holton, and C. Leovy (1987), *Middle Atmosphere Dynamics*, 489 pp.,  
2940 Academic Press, San Diego, Calif.
- 2941 Anstey, J. A., P. Davini, L. J. Gray, T. J. Woollings, N. Butchart, C. Cagnazzo, B. Chris-  
2942 tiansen, S. C. Hardiman, S. M. Osprey, and S. Yang (2013), Multi-model analysis of  
2943 Northern Hemisphere winter blocking: Model biases and the role of resolution, *J.  
2944 Geophys. Res.*, 118, 3956–3971, doi:10.1002/jgrd.50231.
- 2945 Baldwin, M. P., and T. J. Dunkerton (1999), Propagation of the Arctic Oscillation from  
2946 the stratosphere to the troposphere, *J. Geophys. Res.*, 104, 30,937–30,946, doi:10.  
2947 1029/1999JD900445.
- 2948 Baldwin, M. P., and T. J. Dunkerton (2001), Stratospheric harbingers of anomalous  
2949 weather regimes., *Science*, 294, 581–584.
- 2950 Baldwin, M. P., and D. W. J. Thompson (2009), A critical comparison of stratosphere-  
2951 troposphere coupling indices, *Q. J. R. Meteorol. Soc.*, 1672, 1661–1672, doi:10.1002/  
2952 qj.
- 2953 Baldwin, M. P., X. Cheng, and T. J. Dunkerton (1994), Observed correlations be-  
2954 tween winter-mean tropospheric and stratospheric circulation anomalies, *Geophys.  
2955 Res. Lett.*, 21, 1141–1144.

- 2956 Baldwin, M. P., D. B. Stephenson, D. W. J. Thompson, T. J. Dunkerton, A. J. Charlton,  
 2957 and A. O'Neill (2003), Stratospheric memory and skill of extended-range weather  
 2958 forecasts., *Science*, **301**, 636–640, doi:10.1126/science.1087143.
- 2959 Bell, C. J., L. J. Gray, A. J. Charlton-Perez, M. M. Joshi, and A. A. Scaife (2009), Strato-  
 2960 spheric Communication of El Niño Teleconnections to European Winter, *J. Climate*,  
 2961 **22**, 4083–4096, doi:10.1175/2009JCLI2717.1.
- 2962 Black, R. (2002), Stratospheric forcing of surface climate in the Arctic Oscillation, *J.  
 2963 Clim.*, pp. 268–277.
- 2964 Black, R. X., and B. A. McDaniel (2007), Interannual Variability in the Southern Hemi-  
 2965 sphere Circulation Organized by Stratospheric Final Warming Events, *J. Atmos. Sci.*,  
 2966 **64**, 2968–2974, doi:10.1175/JAS3979.1.
- 2967 Blockley, E. W., M. J. Martin, a. J. McLaren, a. G. Ryan, J. Waters, D. J. Lea,  
 2968 I. Mirouze, K. a. Peterson, A. Sellar, and D. Storkey (2013), Recent development  
 2969 of the Met Office operational ocean forecasting system: an overview and assessment  
 2970 of the new Global FOAM forecasts, *Geosci. Model Dev. Discuss.*, **6**, 6219–6278, doi:  
 2971 10.5194/gmdd-6-6219-2013.
- 2972 Bodeker, G., H. Shiona, and H. Eskes (2005), Indicators of Antarctic ozone depletion,  
 2973 *Atmos. Chem. Phys.*, **5**, 2603–2615.
- 2974 Boville, B. A. (1984), The influence of the polar night jet on the tropospheric circulation  
 2975 in a GCM, *J. Atmos. Sci.*, **41**, 1132–1142.
- 2976 Bowler, N., A. Arribas, S. E. Beare, K. R. Mylne, and G. J. Shutts (2009), The local ETKF  
 2977 and SKEB: Upgrades to the MOGREPS short-range ensemble prediction system, *Q. J.  
 2978 R. Meteorol. Soc.*, **776**, 767–776, doi:10.1002/qj.394.
- 2979 Butchart, N., and E. Remsberg (1986), The Area of the Stratospheric Polar Vortex as  
 2980 a Diagnostic for Tracer Transport on an Isentropic Surface, *J. Atmos. Sci.*, **43**, 1319–  
 2981 1339.
- 2982 Butchart, N., A. J. Charlton-Perez, I. Cionni, S. C. Hardiman, P. H. Haynes, K. Krüger,  
 2983 P. J. Kushner, P. A. Newman, S. M. Osprey, J. Perlitz, M. Sigmond, L. Wang,  
 2984 H. Akiyoshi, J. Austin, S. Bekki, A. Baumgaertner, P. Braesicke, C. Brühl, M. Chipper-  
 2985 field, M. Dameris, S. Dhomse, V. Eyring, R. Garcia, H. Garny, P. Jöckel, J.-F. Lamarque,  
 2986 M. Marchand, M. Michou, O. Morgenstern, T. Nakamura, S. Pawson, D. Plummer,  
 2987 J. Pyle, E. Rozanov, J. Scinocca, T. G. Shepherd, K. Shibata, D. Smale, H. Teyssèdre,  
 2988 W. Tian, D. Waugh, and Y. Yamashita (2011), Multimodel climate and variability of  
 2989 the stratosphere, *J. Geophys. Res.*, **116**, D05,102, doi:10.1029/2010JD014995.
- 2990 Butler, A. H., D. J. Seidel, and S. C. Hardiman (2014), Defining sudden stratospheric  
 2991 warmings, *Bull. Amer. Meteor. Soc.*, *in review*.
- 2992 Cagnazzo, C., and E. Manzini (2009), Impact of the Stratosphere on the Winter Tropo-  
 2993 spheric Teleconnections between ENSO and the North Atlantic and European Region,  
 2994 *J. Clim.*, **22**, 1223–1238, doi:10.1175/2008JCLI2549.1.

## BIBLIOGRAPHY

- 2995 Castanheira, J. M., and D. Barriopedro (2010), Dynamical connection between tropo-  
2996 spheric blockings and stratospheric polar vortex, *Geophys. Res. Lett.*, **37**, L13,809,  
2997 doi:10.1029/2010GL043819.
- 2998 Charlton, A. J., and L. M. Polvani (2007), A new look at stratospheric sudden warmings.  
2999 Part I: Climatology and modeling benchmarks, *J. Climate*, **20**, 449–470.
- 3000 Charlton, A. J., A. O'Neill, D. B. Stephenson, W. A. Lahoz, and M. P. Baldwin (2003),  
3001 Can knowledge of the state of the stratosphere be used to improve statistical forecasts  
3002 of the troposphere?, *Q. J. R. Meteorol. Soc.*, **129**, 3205–3224, doi:10.1256/qj.02.232.
- 3003 Charlton, A. J., A. O'Neill, W. A. Lahoz, A. C. Massacand, and P. Berrisford (2005),  
3004 The impact of the stratosphere on the troposphere during the southern hemisphere  
3005 stratospheric sudden warming, September 2002, *Q. J. R. Meteorol. Soc.*, **131**, 2171–  
3006 2188, doi:10.1256/qj.04.43.
- 3007 Charlton-Perez, A. J., M. P. Baldwin, T. Birner, R. X. Black, A. H. Butler, N. Calvo, N. A.  
3008 Davis, E. P. Gerber, N. Gillett, S. Hardiman, J. Kim, K. Krüger, Y.-Y. Lee, E. Manzini,  
3009 B. A. McDaniel, L. Polvani, T. Reichler, T. A. Shaw, M. Sigmond, S.-W. Son, M. Toohey,  
3010 L. Wilcox, S. Yoden, B. Christiansen, F. Lott, D. Shindell, S. Yukimoto, and S. Watan-  
3011 abe (2013), On the lack of stratospheric dynamical variability in low-top versions of  
3012 the CMIP5 models, *J. Geophys. Res.*, **118**, 2494–2505, doi:10.1002/jgrd.50125.
- 3013 Charney, J. G., and P. G. Drazin (1961), Propagation of Planetary-Scale Disturbances  
3014 from the Lower into the Upper Atmosphere, *J. Geophys. Res.*, **66**, 83–109.
- 3015 Charney, J. G., and M. E. Stern (1962), On the stability of internal baroclinic jets in a  
3016 rotating atmosphere, *J. Atmos. Sci.*, **19**, 159–172.
- 3017 Chen, G., and P. Zurita-Gotor (2008), The Tropospheric Jet Response to Prescribed  
3018 Zonal Forcing in an Idealized Atmospheric Model, *J. Atmos. Sci.*, **65**, 2254–2271,  
3019 doi:10.1175/2007JAS2589.1.
- 3020 Chen, P., and W. Robinson (1992), Propagation of planetary waves between the tropo-  
3021 sphere and stratosphere, *J. Atmos. Sci.*, **49**, 2533–2545.
- 3022 Christiansen, B. (2001), Downward propagation of zonal mean zonal wind anomalies  
3023 from the stratosphere to the troposphere: Model and reanalysis, *J. Geophys. Res.*,  
3024 **106**, 27,307–27,322, doi:10.1029/2000JD000214.
- 3025 Christiansen, B. (2005), Downward propagation and statistical forecast of the near-  
3026 surface weather, *J. Geophys. Res.*, **110**(D14104), doi:10.1029/2004JD005431.
- 3027 Cionni, I., V. Eyring, J. F. Lamarque, W. J. Randel, D. S. Stevenson, F. Wu, G. E. Bodeker,  
3028 T. G. Shepherd, D. T. Shindell, and D. W. Waugh (2011), Ozone database in support  
3029 of CMIP5 simulations: results and corresponding radiative forcing, *Atmos. Chem. Phys.*,  
3030 **11**, 11,267–11,292, doi:10.5194/acp-11-11267-2011.
- 3031 Coles, S. (2001), *An Introduction to Statistical Modeling of Extreme Values.*, 209 pp.,  
3032 Springer, London, UK.

- 3033 Cordero, E., and P. Forster (2006), Stratospheric variability and trends in mod-  
 3034 els used for the IPCC AR4, *Atmos. Chem. Phys.*, 6, 5369–5380, doi:10.5194/  
 3035 acp-6-5369-2006.
- 3036 Coughlin, K., and L. J. Gray (2009), A continuum of sudden stratospheric warmings, *J.  
 3037 Atmos. Sci.*, 66, 531–540.
- 3038 Coughlin, K., and K. Tung (2004), 11-Year solar cycle in the stratosphere extracted  
 3039 by the empirical mode decomposition method, *Adv. Sp. Res.*, 34(2), 323–329, doi:  
 3040 10.1016/j.asr.2003.02.045.
- 3041 Crook, J. A., N. P. Gillett, and S. P. E. Keeley (2008), Sensitivity of Southern Hemisphere  
 3042 climate to zonal asymmetry in ozone, *Geophys. Res. Lett.*, 35, L07,806, doi:10.1029/  
 3043 2007GL032698.
- 3044 Davini, P., C. Cagnazzo, and J. A. Anstey (2014), Blocking view of the stratosphere-  
 3045 troposphere coupling, *J. Geophys. Res.*, *in press*, doi:10.1002/2014JD021703.
- 3046 Dee, D. P., S. M. Uppala, A. J. Simmons, P. Berrisford, P. Poli, S. Kobayashi, U. Andrae,  
 3047 M. A. Balmaseda, G. Balsamo, P. Bauer, P. Bechtold, A. C. M. Beljaars, L. van de Berg,  
 3048 J. Bidlot, N. Bormann, C. Delsol, R. Dragani, M. Fuentes, A. J. Geer, L. Haimberger,  
 3049 S. B. Healy, H. Hersbach, E. V. Hólm, L. Isaksen, P. Kållberg, M. Köhler, M. Matricardi,  
 3050 A. P. McNally, B. M. Monge-Sanz, J.-J. Morcrette, B.-K. Park, C. Peubey, P. de Rosnay,  
 3051 C. Tavolato, J.-N. Thépaut, and F. Vitart (2011), The ERA-Interim reanalysis: con-  
 3052 figuration and performance of the data assimilation system, *Q. J. R. Meteorol. Soc.*,  
 3053 137, 553–597, doi:10.1002/qj.828.
- 3054 Deser, C. (2000), On the teleconnectivity of the Arctic Oscillation, *Geophys. Res.  
 3055 Lett.*, 27, 779–782, doi:10.1029/1999GL010945.
- 3056 Dragani, R. (2011), On the quality of the ERA-Interim ozone reanalyses: comparisons  
 3057 with satellite data, *Q. J. R. Meteorol. Soc.*, 137, 1312–1326, doi:10.1002/qj.821.
- 3058 Dunkerton, T. (1978), On the Mean Meridional Mass Motions of the Stratosphere  
 3059 and Mesosphere, *J. Atmos. Sci.*, 35, 2325–2333, doi:10.1175/1520-0469(1978)  
 3060 035<2325:OTMMMM>2.0.CO;2.
- 3061 Eade, R., D. Smith, A. Scaife, E. Wallace, N. Dunstone, L. Hermanson, and N. Robinson  
 3062 (2014), Do seasonal-to-decadal climate predictions underestimate the pre-  
 3063 dictability of the real world?, *Geophys. Res. Lett.*, (41), doi:10.1002/2014GL061146.
- 3064 Eady, E. T. (1949), Long waves and cyclone waves, *Tellus*, 1, 33–52.
- 3065 Eskes, H. (2005), Ozone forecasts of the stratospheric polar vortex-splitting event in  
 3066 September 2002, *J. Atmos. Sci.*, (62), 812–821.
- 3067 Esler, J., and R. Scott (2005), Excitation of transient Rossby waves on the stratospheric  
 3068 polar vortex and the barotropic sudden warming, *J. Atmos. Sci.*, 62, 3661–3682.

## BIBLIOGRAPHY

- 3069 Esler, J. G., L. M. Polvani, and R. K. Scott (2006), The Antarctic stratospheric sudden  
3070 warming of 2002: A self-tuned resonance?, *Geophys. Res. Lett.*, 33, L12,804, doi:  
3071 10.1029/2006GL026034.
- 3072 Farman, J. C., B. G. Gardiner, and J. D. Shanklin (1985), Large losses of total ozone  
3073 in Antarctica reveal seasonal ClO<sub>x</sub>/NO<sub>x</sub> interaction, *Nature*, 315, 207–210, doi:10.  
3074 1038/315207a0.
- 3075 Forster, P. M. d. F., and K. P. Shine (1997), Radiative forcing and temperature trends  
3076 from stratospheric ozone changes, *J. Geophys. Res.*, 102, 10,841–10,855.
- 3077 Garfinkel, C. I., and D. L. Hartmann (2008), Different ENSO teleconnections and their  
3078 effects on the stratospheric polar vortex, *J. Geophys. Res.*, 113, D18,114, doi:10.1029/  
3079 2008JD009920.
- 3080 Garfinkel, C. I., and D. L. Hartmann (2011), The Influence of the Quasi-Biennial Oscil-  
3081 lation on the Troposphere in Winter in a Hierarchy of Models. Part I: Simplified Dry  
3082 GCMs, *J. Atmos. Sci.*, 68, 1273–1289, doi:10.1175/2011JAS3665.1.
- 3083 Garny, H., V. Grewe, M. Dameris, G. E. Bodeker, and A. Stenke (2011), Attribution  
3084 of ozone changes to dynamical and chemical processes in CCMs and CTMs, *Geosci.  
3085 Model Dev.*, 4, 271–286, doi:10.5194/gmd-4-271-2011.
- 3086 Gerber, E. P., S. Voronin, and L. M. Polvani (2008), Testing the Annular Mode Au-  
3087 tocorrelation Time Scale in Simple Atmospheric General Circulation Models, *Mon.  
3088 Weather Rev.*, 136(4), 1523–1536, doi:10.1175/2007MWR2211.1.
- 3089 Gerber, E. P., C. Orbe, and L. M. Polvani (2009), Stratospheric influence on the tro-  
3090 pospheric circulation revealed by idealized ensemble forecasts, *Geophys. Res. Lett.*,  
3091 36(24), 1–5, doi:10.1029/2009GL040913.
- 3092 Gerber, E. P., A. Butler, N. Calvo, A. J. Charlton-Perez, M. Giorgetta, E. Manzini, and  
3093 J. Perlitz (2012), Assessing and Understanding the Impact of Stratospheric Dynam-  
3094 ics and Variability on the Earth System, *Bull. Amer. Meteor. Soc.*, 93, 845–859.
- 3095 Gillett, N. P., T. D. Kell, and P. D. Jones (2006), Regional climate impacts of the Southern  
3096 Annular Mode, *Geophys. Res. Lett.*, 33, L23,704, doi:10.1029/2006GL027721.
- 3097 Gong, D., and S. Wang (1999), Definition of Antarctic Oscillation index, *Geophys. Res.  
3098 Lett.*, 26, 459–462, doi:10.1029/1999GL900003.
- 3099 Gray, L., J. Beer, and M. Geller (2010), Solar influences on climate, *Rev. . . .*, (2009),  
3100 doi:10.1029/2009RG000282.1.INTRODUCTION.
- 3101 Gray, L. J., A. A. Scaife, D. M. Mitchell, S. Osprey, S. Ineson, S. Hardiman, N. Butchart,  
3102 J. Knight, R. Sutton, and K. Kodera (2013), A lagged response to the 11 year solar  
3103 cycle in observed winter Atlantic/European weather patterns, *J. Geophys. Res.*, 118,  
3104 13,405–13,420, doi:10.1002/2013JD020062.

- 3105 Grise, K. M., D. W. J. Thompson, and P. M. Forster (2009), On the Role of Radiative  
 3106 Processes in Stratosphere–Troposphere Coupling, *J. Clim.*, 22(15), 4154–4161,  
 3107 doi:10.1175/2009JCLI2756.1.
- 3108 Grise, K. M., D. W. J. Thompson, and T. Birner (2010), A Global Survey of Static Sta-  
 3109 bility in the Stratosphere and Upper Troposphere, *J. Clim.*, 23(9), 2275–2292, doi:  
 3110 10.1175/2009JCLI3369.1.
- 3111 Haigh, J. D. (2003), The effects of solar variability on the Earth's climate, *Philos. Trans.  
 3112 R. Soc. A*, 361, 95–111.
- 3113 Hall, A. R. (2005), *Generalized Method of Moments (Advanced Texts in Econometrics)*,  
 3114 Oxford University Press, Oxford, UK.
- 3115 Hall, T., and R. Plumb (1994), Age as a diagnostic of stratospheric transport, *J. Geophys.  
 3116 Res.*, 99, 1059–1070, doi:10.1029/93JD03192.
- 3117 Hannachi, A., D. Mitchell, L. Gray, and A. Charlton-Perez (2010), On the use of ge-  
 3118 ometric moments to examine the continuum of sudden stratospheric warmings, *J.  
 3119 Atmos. Sci.*, 68, 657–674.
- 3120 Hardiman, S. C., N. Butchart, A. J. Charlton-Perez, T. a. Shaw, H. Akiyoshi, A. Baum-  
 3121 gaertner, S. Bekki, P. Braesicke, M. Chipperfield, M. Dameris, R. R. Garcia, M. Mi-  
 3122 chou, S. Pawson, E. Rozanov, and K. Shibata (2011), Improved predictability of the  
 3123 troposphere using stratospheric final warmings, *J. Geophys. Res.*, 116, D18,113, doi:  
 3124 10.1029/2011JD015914.
- 3125 Hardiman, S. C., N. Butchart, T. J. Hinton, S. M. Osprey, and L. J. Gray (2012a), Sim-  
 3126 ulations for CMIP5 run with high and low top versions of the Met Office climate  
 3127 model : Effect of adding a well resolved stratosphere on surface climate, *J. Climate*,  
 3128 25, 7083–7099, doi:10.1175/JCLI-D-11-00579.1.
- 3129 Hardiman, S. C., N. Butchart, T. J. Hinton, S. M. Osprey, and L. J. Gray (2012b), The  
 3130 Effect of a Well-Resolved Stratosphere on Surface Climate: Differences between  
 3131 CMIP5 Simulations with High and Low Top Versions of the Met Office Climate Model,  
 3132 *J. Climate*, 25, 7083–7099, doi:10.1175/JCLI-D-11-00579.1.
- 3133 Hartley, D. E., J. T. Villarin, and R. X. Black (1998), A new perspective on the dynamical  
 3134 link between the stratosphere and troposphere, 8311(1996), 1996–1999.
- 3135 Haynes, P., M. McIntyre, T. G. Shepherd, and K. P. Shine (1991), On the "downward  
 3136 control" of extratropical diabatic circulations by eddy- induced mean zonal forces, *J.  
 3137 Atmos. Sci.*, 48, 651–678.
- 3138 Hendon, H. H., D. W. J. Thompson, and M. C. Wheeler (2007), Australian Rainfall and  
 3139 Surface Temperature Variations Associated with the Southern Hemisphere Annular  
 3140 Mode, *J. Clim.*, 20, 2452–2467, doi:10.1175/JCLI4134.1.

## BIBLIOGRAPHY

- 3141 Hewitt, H. T., D. Copsey, I. D. Culverwell, C. M. Harris, R. S. R. Hill, a. B. Keen, A. J.  
3142 McLaren, and E. C. Hunke (2011), Design and implementation of the infrastruc-  
3143 ture of HadGEM3: the next-generation Met Office climate modelling system, *Geosci.*  
3144 *Model Dev.*, 4, 223–253, doi:10.5194/gmd-4-223-2011.
- 3145 Holton, J. (1990), On the global exchange of mass between the stratosphere and tro-  
3146 posphere, *J. Atmos. Sci.*, 47, 392–395.
- 3147 Hoskins, B. J., M. E. McIntyre, and A. W. Robertson (1985), On the use and significance  
3148 of isentropic potential vorticity maps, *Q. J. R. Meteorol. Soc.*, 111(6), 877–946.
- 3149 Huang, N. E., Z. Shen, S. R. Long, M. C. Wu, H. H. Shih, Q. Zheng, N.-C. Yen, C. C.  
3150 Tung, and H. H. Liu (1998), The empirical mode decomposition and the Hilbert  
3151 spectrum for nonlinear and non-stationary time series analysis, *Proc. R. Soc. Lond. A,*  
3152 454(1971).
- 3153 Huebener, H., U. Cubasch, U. Langematz, T. Spangehl, F. Niehörster, I. Fast, and  
3154 M. Kunze (2007), Ensemble climate simulations using a fully coupled ocean-  
3155 troposphere-stratosphere general circulation model., *Philos. Trans. A. Math. Phys.*  
3156 *Eng. Sci.*, 365(1857), 2089–101, doi:10.1098/rsta.2007.2078.
- 3157 Hurwitz, M. M., P. A. Newman, L. D. Oman, and A. M. Molod (2011), Response of the  
3158 Antarctic Stratosphere to Two Types of El Niño Events, *J. Atmos. Sci.*, 68, 812–822,  
3159 doi:10.1175/2011JAS3606.1.
- 3160 Huth, R. (2006), Arctic or North Atlantic Oscillation? Arguments based on the principal  
3161 component analysis methodology, *Theor. Appl. Climatol.*, 89(1-2), 1–8, doi:10.1007/  
3162 s00704-006-0257-1.
- 3163 Ineson, S., and A. A. Scaife (2009), The role of the stratosphere in the European climate  
3164 response to El Niño, *Nat. Geosci.*, 2, 32–36, doi:10.1038/NGEO381.
- 3165 Jacqmin, D., and R. Lindzen (1985), The causation and sensitivity of the northern  
3166 winter planetary waves, *J. Atmos. Sci.*, 42, 724–746.
- 3167 Jung, T., and J. Barkmeijer (2006), Sensitivity of the Tropospheric Circulation to  
3168 Changes in the Strength of the Stratospheric Polar Vortex, *Mon. Weather Rev.*, pp.  
3169 2191–2207.
- 3170 Karpetchko, A., E. Kyrö, and B. M. Knudsen (2005), Arctic and Antarctic polar vor-  
3171 tices 1957–2002 as seen from the ERA-40 reanalyses, *J. Geophys. Res.*, 110(D21),  
3172 D21,109, doi:10.1029/2005JD006113.
- 3173 Kodera, K., and M. Chiba (1995), Tropospheric circulation changes associated with  
3174 stratospheric sudden warmings: A case study, *J. Geophys. Res.*, 100, 11,055–11,068,  
3175 doi:10.1029/95JD00771.
- 3176 Kodera, K., K. Yamazaki, M. Chiba, and K. Shibata (1990), Downward propagation of  
3177 upper stratospheric mean zonal wind perturbation to the troposphere, *Geophys. Res.*  
3178 *Lett.*, 17, 1263–1266.

- 3179 Kolstad, E. W., T. Breiteig, and A. a. Scaife (2010), The association between strato-  
 3180 spheric weak polar vortex events and cold air outbreaks in the Northern Hemisphere,  
 3181 *Q. J. R. Meteorol. Soc.*, 136(649), 886–893, doi:10.1002/qj.620.
- 3182 Kroon, M., J. P. Veefkind, M. Sneep, R. D. McPeters, P. K. Bhartia, and P. F. Levelt (2008),  
 3183 Comparing OMI-TOMS and OMI-DOAS total ozone column data, *J. Geophys. Res.*,  
 3184 113, D16S28, doi:10.1029/2007JD008798.
- 3185 Kumar, A. (2009), Finite Samples and Uncertainty Estimates for Skill Measures for Sea-  
 3186 sonal Prediction, *Mon. Weather Rev.*, 137, 2622–2631, doi:10.1175/2009MWR2814.  
 3187 1.
- 3188 Kuroda, Y. (2004), Role of the Polar-night Jet Oscillation on the formation of the Arctic  
 3189 Oscillation in the Northern Hemisphere winter, *J. Geophys. Res.*, 109(D11), D11,112,  
 3190 doi:10.1029/2003JD004123.
- 3191 Kuroda, Y. (2008), Role of the stratosphere on the predictability of medium-range  
 3192 weather forecast: A case study of winter 2003–2004, *Geophys. Res. Lett.*, 35,  
 3193 L19,701, doi:10.1029/2008GL034902.
- 3194 Kushner, P., and L. Polvani (2004), Stratosphere-troposphere coupling in a relatively  
 3195 simple AGCM: The role of eddies, *J. Climate*, 17, 629–639.
- 3196 Kushner, P. J. (2010), Annular Modes of the Troposphere and Stratosphere, *Stratos.*  
 3197 *Dyn. Transp. Chem. Geophys. Monogr. Ser.*, 190, 59–91.
- 3198 Labitzke, K., and B. Naujokat (2000), The Lower Arctic Stratosphere since 1952, *SPARC*  
 3199 *Newsl.*, (15).
- 3200 Li, B., and S. Ma (1994), Efficient computation of 3D moments, *Pattern Recognition*,  
 3201 1994. Vol. 1 - Conf. A Comput. Vis. Image Process. Proc. 12th IAPR Int. Conf.
- 3202 , 1, 22–26, doi:10.1109/ICPR.1994.576218.
- 3203 Lim, E.-P., H. H. Hendon, and H. Rashid (2013), Seasonal Predictability of the Southern  
 3204 Annular Mode due to its Association with ENSO, *J. Climate*, 26, 8037–8045, doi:  
 3205 10.1175/JCLI-D-13-00006.1.
- 3206 Limpasuvan, V., and D. Hartmann (2000), Wave-Maintained Annular Modes of Climate  
 3207 Variability, *J. Climate*, 13, 4414–4429.
- 3208 Limpasuvan, V., and D. L. Hartmann (1999), Eddies and the annular modes of climate  
 3209 variability, *Geophys. Res. Lett.*, 26, 3133–3136, doi:10.1029/1999GL010478.
- 3210 Limpasuvan, V., D. W. J. Thompson, and D. L. Hartmann (2004), The life cycle of the  
 3211 Northern Hemisphere sudden stratospheric warmings, *J. Climate*, 17, 2584–2596.
- 3212 Love, A. (1893), On the stability of certain vortex motions, *Proc. London Math. Soc.*,  
 3213 (25), 18–43.

BIBLIOGRAPHY

- 3214 MacLachlan, C., A. Arribas, K. A. Peterson, A. Maidens, D. Fereday, A. Scaife, M. Gordon, M. Vellinga, A. Williams, R. E. Comer, J. Camp, P. Xavier, and G. Madec (2014),  
3215 Global Seasonal Forecast System version 5 (GloSea5): a high resolution seasonal  
3216 forecast system, *Q. J. R. Meteorol. Soc.*, submitted.  
3217
- 3218 Manney, G. L., L. Froidevaux, M. L. Santee, R. W. Zurek, and J. W. Waters (1997),  
3219 MLS observations of Arctic ozone loss in 1996–97, *Geophys. Res. Lett.*, 24(22),  
3220 2697–2700.
- 3221 Manzini, E., a. Y. Karpechko, J. Anstey, M. P. Baldwin, R. X. Black, C. Cagnazzo,  
3222 N. Calvo, a. Charlton-Perez, B. Christiansen, P. Davini, E. Gerber, M. Giorgetta,  
3223 L. Gray, S. C. Hardiman, Y.-Y. Lee, D. R. Marsh, B. a. McDaniel, a. Purich, a. a.  
3224 Scaife, D. Shindell, S.-W. Son, S. Watanabe, and G. Zappa (2014), Northern winter  
3225 climate change: Assessment of uncertainty in CMIP5 projections related to  
3226 stratosphere - troposphere coupling, *J. Geophys. Res. Atmos.*, (1), n/a–n/a, doi:  
3227 10.1002/2013JD021403.
- 3228 Marshall, A. G., and A. A. Scaife (2009), Impact of the QBO on surface winter climate,  
3229 *J. Geophys. Res.*, 114, D18,110, doi:10.1029/2009JD011737.
- 3230 Marshall, A. G., and A. A. Scaife (2010), Improved predictability of stratospheric  
3231 sudden warming events in an atmospheric general circulation model with en-  
3232 hanced stratospheric resolution, *J. Geophys. Res.*, 115, D16,114, doi:10.1029/  
3233 2009JD012643.
- 3234 Marshall, G. J. (2003), Trends in the southern annular mode from observations and  
3235 reanalyses., *J. Clim.*, 16, 4134–4143.
- 3236 Martius, O., L. M. Polvani, and H. C. Davies (2009), Blocking precursors to strato-  
3237 spheric sudden warming events, *Geophys. Res. Lett.*, 36, L14,806, doi:10.1029/  
3238 2009GL038776.
- 3239 Matsuno, T. (1970), Vertical Propagation of Stationary Planetary Waves in the Winter  
3240 Northern Hemisphere., *J. Atmos. Sci.*, 27(6), 871–883.
- 3241 Matsuno, T. (1971), A dynamical model of the stratospheric sudden warming., *J. Atmos.*  
3242 *Sci.*, 28(8), 1479–1494.
- 3243 Matthewman, N. J., J. G. Esler, a. J. Charlton-Perez, and L. M. Polvani (2009), A New  
3244 Look at Stratospheric Sudden Warmings. Part III: Polar Vortex Evolution and Vertical  
3245 Structure, *J. Climate*, 22, 1566–1585, doi:10.1175/2008JCLI2365.1.
- 3246 Maycock, A. C., S. P. E. Keeley, A. J. Charlton-Perez, and F. J. Doblas-Reyes (2011),  
3247 Stratospheric circulation in seasonal forecasting models: implications for seasonal  
3248 prediction, *Clim. Dyn.*, 36, 309–321, doi:10.1007/s00382-009-0665-x.
- 3249 McElroy, M. B., R. J. Salawitch, S. C. Wofsy, and J. A. Logan (1986), Reductions of  
3250 Antarctic ozone due to synergistic interactions of chlorine and bromine, *Nature*, 321,  
3251 759–762, doi:10.1038/321759a0.

- 3252 McInturff, R. (1978), Stratospheric warmings: Synoptic, dynamic and general circulation aspects, *NASA Ref. Publ.*, 1017.
- 3253
- 3254 McIntyre, M., and T. Palmer (1983), Breaking planetary waves in the stratosphere, *Nature*, 305(13), 593–600.
- 3255
- 3256 Mitchell, D. M., A. J. Charlton-Perez, and L. J. Gray (2011), Characterizing the Variability and Extremes of the Stratospheric Polar Vortices Using 2D Moment Analysis, *J. Atmos. Sci.*, 68, 1194–1213.
- 3257
- 3258
- 3259 Mitchell, D. M., a. J. Charlton-Perez, L. J. Gray, H. Akiyoshi, N. Butchart, S. C. Hardiman, O. Morgenstern, T. Nakamura, E. Rozanov, K. Shibata, D. Smale, and Y. Yamashita (2012), The nature of Arctic polar vortices in chemistry-climate models, *Q. J. R. Meteorol. Soc.*, 138, 1681–1691, doi:10.1002/qj.1909.
- 3260
- 3261
- 3262
- 3263 Mitchell, D. M., L. J. Gray, J. Anstey, M. P. Baldwin, and A. J. Charlton-Perez (2013), The Influence of Stratospheric Vortex Displacements and Splits on Surface Climate, *J. Climate*, 26, 2668–2682, doi:10.1175/JCLI-D-12-00030.1.
- 3264
- 3265
- 3266 Molina, L., and M. Molina (1987), Production of chlorine oxide ( $\text{Cl}_2\text{O}_2$ ) from the self-reaction of the chlorine oxide ( $\text{ClO}$ ) radical, *J. Phys. Chem.*, 91, 433–436, doi: 10.1021/j100286a035.
- 3267
- 3268
- 3269 Monge-Sanz, B. M., M. P. Chipperfield, D. P. Dee, A. J. Simmons, and S. M. Uppala (2013), Improvements in the stratospheric transport achieved by a chemistry transport model with ECMWF (re)analyses: identifying effects and remaining challenges, *Q. J. R. Meteorol. Soc.*, 139, 654–673, doi:10.1002/qj.1996.
- 3270
- 3271
- 3272
- 3273 Morice, C. P., J. J. Kennedy, N. A. Rayner, and P. D. Jones (2012), Quantifying uncertainties in global and regional temperature change using an ensemble of observational estimates: The HadCRUT4 data set, *J. Geophys. Res.*, 117, D08,101, doi: 10.1029/2011JD017187.
- 3274
- 3275
- 3276
- 3277 Mukougawa, H., T. Hirooka, and Y. Kuroda (2009), Influence of stratospheric circulation on the predictability of the tropospheric Northern Annular Mode, *Geophys. Res. Lett.*, 36(8), 1–5, doi:10.1029/2008GL037127.
- 3278
- 3279
- 3280 Murphy, J. (1990), Assessment of the practical utility of extended range ensemble forecasts, *Q. J. R. Meteorol. Soc.*, 116, 89–125.
- 3281
- 3282 Nakagawa, K. I., and K. Yamazaki (2006), What kind of stratospheric sudden warming propagates to the troposphere?, *Geophys. Res. Lett.*, 33, L04,801, doi:10.1029/2005GL024784.
- 3283
- 3284
- 3285 Nash, E., J. Newman, J. Rosenfield, and M. Schoeberl (1996), An objective determination of the polar vortex using Ertel's potential vorticity, *J. Geophys. Res.*, 101, 9471–9478.
- 3286
- 3287

## BIBLIOGRAPHY

- 3288 Neef, L., S. Walther, K. Matthes, and K. Kodera (2014), Observations of stratospheric  
3289 sudden warmings in Earth rotation variations, *J. Geophys. Res.*, 119, doi:10.1002/  
3290 2014JD021621.
- 3291 Newman, P., and J. Rosenfield (1997), Stratospheric thermal damping times, *Geophys.*  
3292 *Res. Lett.*, 24, 433–436.
- 3293 Newman, P. A. (2010), Chemistry and Dynamics of the Antarctic Ozone Hole, *Stratos.*  
3294 *Dyn. Transp. Chem. Geophys. Monogr. Ser.*, 190, 157–171.
- 3295 Nigam, S. (1990), On the structure of variability of the observed tropospheric and  
3296 stratospheric zonal-mean zonal wind, *J. Atmos. Sci.*, 47, 1799–1813.
- 3297 Norton, W. a. (2003), Sensitivity of northern hemisphere surface climate to simulation  
3298 of the stratospheric polar vortex, *Geophys. Res. Lett.*, 30(12), 1627.
- 3299 O'Neill, A., and V. D. Pope (1988), Simulations of linear and nonlinear disturbances  
3300 in the stratosphere, *Q. J. R. Meteorol. Soc.*, 114, 1063–1110, doi:10.1002/qj.  
3301 49711448210.
- 3302 O'Neill, A., W. L. Grose, V. D. Pope, H. Maclean, and R. Swinbank (1994), Evolution of  
3303 the stratosphere during northern winter 1991/92 as diagnosed from UK Meteorolog-  
3304 ical Office analyses, *J. Atmos. Sci.*, 51, 2800–2817.
- 3305 Perlitz, J., and H.-F Graf (1995), The statistical connection between tropospheric  
3306 and stratospheric circulation of the Northern Hemisphere in winter, *J. Climate*, 8,  
3307 2281–2295.
- 3308 Perlitz, J., and N. Harnik (2003), Observational evidence of a stratospheric influence  
3309 on the troposphere by planetary wave reflection, *J. Climate*, 16(18), 3011–3026.
- 3310 Plumb, R. A. (1981), Instability of the distorted polar night vortex: A theory of strato-  
3311 spheric warmings, *J. Atmos. Sci.*, 38, 2514–2531.
- 3312 Plumb, R. A., and K. Semeniuk (2003), Downward migration of extratropical zonal  
3313 wind anomalies, *J. Geophys. Res.*, 108, 4223, doi:10.1029/2002JD002773.
- 3314 Polvani, L., and P. Kushner (2002), Tropospheric response to stratospheric perturbations  
3315 in a relatively simple general circulation model, *Geophys. Res. Lett.*, 29, 40–43.
- 3316 Quiroz, R. S. (1986), The Association of Stratospheric Warmings With Tropospheric  
3317 Blocking, *J. Geophys. Res.*, 91, 5277–5285.
- 3318 Ramanathan, V. (1977), Troposphere-stratosphere feedback mechanism: stratospheric  
3319 warming and its effect on the polar energy budget and the tropospheric circulation,  
3320 *J. Atmos. Sci.*, 34, 439–447.
- 3321 Randel, W. (1988), The seasonal evolution of planetary waves in the Southern Hemi-  
3322 sphere stratosphere and troposphere, *Q. J. R. Meteorol. Soc.*, 587, 1385–1409.

- 3323 Randel, W., P. Udelhofen, E. Fleming, M. Geller, M. Gelman, K. Hamilton, D. Karoly,  
 3324 D. Ortland, S. Pawson, R. Swinbank, F. Wu, M. Baldwin, M.-L. Chanin, P. Keckhut,  
 3325 K. Labitzke, E. Remsberg, A. Simmons, and D. Wu (2004), The SPARC intercompari-  
 3326 son of middle-atmosphere climatologies, *J. Climate*, (17), 986–1003.
- 3327 Rayner, N. A., D. E. Parker, E. B. Horton, C. K. Folland, L. V. Alexander, D. P. Rowell,  
 3328 E. C. Kent, and A. Kaplan (2003), Global analyses of sea surface temperature, sea  
 3329 ice, and night marine air temperature since the late nineteenth century, *J. Geophys.  
 3330 Res.*, 108(D14), 4407, doi:10.1029/2002JD002670.
- 3331 Reason, C. J. C., and M. Rouault (2005), Links between the Antarctic Oscillation and  
 3332 winter rainfall over western South Africa, *Geophys. Res. Lett.*, 32, L07,705, doi:10.  
 3333 1029/2005GL022419.
- 3334 Reichler, T., J. Kim, E. Manzini, and J. Kröger (2012), A stratospheric connection to  
 3335 Atlantic climate variability, *Nat. Geosci.*, 5(10), 1–5, doi:10.1038/ngeo1586.
- 3336 Rhines, P., and W. Holland (1979), A theoretical discussion of eddy-driven mean flows,  
 3337 *Dyn. Atmos. Ocean.*, 3, 289–325.
- 3338 Ring, M. J., and R. A. Plumb (2008), The Response of a Simplified GCM to Axisymmetric  
 3339 Forcings: Applicability of the Fluctuation–Dissipation Theorem, *J. Atmos. Sci.*,  
 3340 65(12), 3880–3898, doi:10.1175/2008JAS2773.1.
- 3341 Robinson, W. (1991), The dynamics of the zonal index in a simple model of the atmo-  
 3342 sphere, *Tellus A*.
- 3343 Robock, A. (2000), Volcanic eruptions and climate, *Rev. Geophys.*, (1998), 191–219.
- 3344 Roff, G., D. W. J. Thompson, and H. Hendon (2011), Does increasing model strato-  
 3345 spheric resolution improve extended-range forecast skill?, *Geophys. Res. Lett.*, 38,  
 3346 L05,809, doi:10.1029/2010GL046515.
- 3347 Roscoe, H. K., J. D. Shanklin, and S. R. Colwell (2005), Has the Antarctic vortex split  
 3348 before 2002?, *J. Atmos. Sci.*, 62, 581–588, doi:10.1175/JAS-3331.1.
- 3349 Salby, M. L., E. A. Titova, and L. Deschamps (2012), Changes of the Antarctic ozone  
 3350 hole: Controlling mechanisms, seasonal predictability, and evolution, *J. Geophys.  
 3351 Res.*, 117, D10,111, doi:10.1029/2011JD016285.
- 3352 Sardeshmukh, P., G. Compo, and C. Penland (2000), Changes of probability associated  
 3353 with El Niño, *J. Clim.*, 5, 4268–4286.
- 3354 Sassi, F., R. R. Garcia, D. Marsh, and K. W. Hoppel (2010), The Role of the Middle  
 3355 Atmosphere in Simulations of the Troposphere during Northern Hemisphere Winter:  
 3356 Differences between High- and Low-Top Models, *J. Atmos. Sci.*, 67(9), 3048–3064,  
 3357 doi:10.1175/2010JAS3255.1.

## BIBLIOGRAPHY

- 3358 Scaife, A. A., J. R. Knight, G. K. Vallis, and C. K. Folland (2005a), A stratospheric  
3359 influence on the winter NAO and North Atlantic surface climate, *Geophys. Res. Lett.*,  
3360 32(18), 1–5.
- 3361 Scaife, A. A., D. R. Jackson, R. Swinbank, N. Butchart, H. E. Thornton, M. Keil,  
3362 and L. Henderson (2005b), Stratospheric vacillations and the major warming over  
3363 Antarctica in 2002., *J. Atmos. Sci.*, 62, 629–639, doi:10.1175/JAS-3334.1.
- 3364 Scaife, A. a., C. K. Folland, L. V. Alexander, A. Moberg, and J. R. Knight (2008), Euro-  
3365 pean Climate Extremes and the North Atlantic Oscillation, *J. Climate*, 21(1), 72–83,  
3366 doi:10.1175/2007JCLI1631.1.
- 3367 Scaife, A. A., T. Spangehl, D. R. Fereday, U. Cubasch, U. Langematz, H. Akiyoshi,  
3368 S. Bekki, P. Braesicke, N. Butchart, M. P. Chipperfield, A. Gettelman, S. C. Hardi-  
3369 man, M. Michou, E. Rozanov, and T. G. Shepherd (2011a), Climate change pro-  
3370 jections and stratosphere-troposphere interaction, *Clim. Dyn.*, 38, 2089–2097, doi:  
3371 10.1007/s00382-011-1080-7.
- 3372 Scaife, A. A., D. Copsey, C. Gordon, C. Harris, T. Hinton, S. Keeley, A. O'Neill,  
3373 M. Roberts, and K. Williams (2011b), Improved Atlantic winter blocking in a climate  
3374 model, *Geophys. Res. Lett.*, 38(23), doi:10.1029/2011GL049573.
- 3375 Scaife, A. A., A. Arribas, E. Blockley, A. Brookshaw, R. Clark, N. Dunstone, R. Eade,  
3376 D. Fereday, C. Folland, M. Gordon, L. Hermanson, J. Knight, D. Lea, C. MacLachlan,  
3377 A. Maidens, M. Martin, A. Peterson, D. Smith, M. Vellinga, E. Wallace, J. Waters, and  
3378 A. Williams. (2014), Skillful Long Range Prediction of European and North American  
3379 Winters, *Geophys. Res. Lett.*, *in press*.
- 3380 Scherhag, R. (1952), Die explosionsartigen Stratospharenerwärmungen des Spätwin-  
3381 ters 1951/52, *Berichte des Dtsch. Wetterdienstes der US-Zone*, pp. 38–51.
- 3382 Schimanke, S., J. Körper, T. Spangehl, and U. Cubasch (2011), Multi-decadal variability  
3383 of sudden stratospheric warmings in an AOGCM, *Geophys. Res. Lett.*, 38, L01,801,  
3384 doi:10.1029/2010GL045756.
- 3385 Schoeberl, M., and D. Hartmann (1991), The dynamics of the stratospheric polar vortex  
3386 and its relation to springtime ozone depletions, *Science*, 251, 46–52, doi:10.1126/  
3387 science.251.4989.46.
- 3388 Scinocca, J., and P. Haynes (1998), Dynamical forcing of stratospheric planetary waves  
3389 by tropospheric baroclinic eddies, *J. Atmos. Sci.*, 55, 2361–2392.
- 3390 Scott, R. K., and D. G. Dritschel (2006), Vortex–Vortex Interactions in the Winter  
3391 Stratosphere, *J. Atmos. Sci.*, 63, 726–740, doi:10.1175/JAS3632.1.
- 3392 Seviour, W. J. M., N. Butchart, and S. C. Hardiman (2012), The Brewer-Dobson cir-  
3393 culation inferred from ERA-Interim, *Q. J. R. Meteorol. Soc.*, 138, 878–888, doi:  
3394 10.1002/qj.966.

- 3395 Seviour, W. J. M., D. M. Mitchell, and L. J. Gray (2013), A practical method to identify  
 3396 displaced and split stratospheric polar vortex events, *Geophys. Res. Lett.*, **40**, 5268–  
 3397 5273, doi:doi:10.1002/grl.50927.
- 3398 Seviour, W. J. M., S. C. Hardiman, L. J. Gray, N. Butchart, C. MacLachlan, and A. A.  
 3399 Scaife (2014), Skillful seasonal prediction of the Southern Annular Mode and Antarc-  
 3400 tic ozone, *J. Climate*, **27**, 7462–7474, doi:10.1175/JCLI-D-14-00264.1.
- 3401 Shaw, T. a., J. Perlitz, and N. Harnik (2010), Downward Wave Coupling between  
 3402 the Stratosphere and Troposphere: The Importance of Meridional Wave Guiding and  
 3403 Comparison with Zonal-Mean Coupling, *J. Clim.*, **23**(23), 6365–6381, doi:10.1175/  
 3404 2010JCLI3804.1.
- 3405 Shaw, T. a., J. Perlitz, N. Harnik, P. a. Newman, and S. Pawson (2011), The Impact of  
 3406 Stratospheric Ozone Changes on Downward Wave Coupling in the Southern Hemis-  
 3407 phere \*, *J. Clim.*, **24**(16), 4210–4229, doi:10.1175/2011JCLI4170.1.
- 3408 Shepherd, T., R. A. Plumb, and S. C. Wofsy (2005), Preface, *J. Atmos. Sci.*, **62**, 565–566,  
 3409 doi:10.1175/JAS-9999.1.
- 3410 Sigmond, M., J. F. Scinocca, and P. J. Kushner (2008), Impact of the stratosphere  
 3411 on tropospheric climate change, *Geophys. Res. Lett.*, **35**(12), L12,706, doi:10.1029/  
 3412 2008GL033573.
- 3413 Sigmond, M., J. F. Scinocca, V. V. Kharin, and T. G. Shepherd (2013), Enhanced seasonal  
 3414 forecast skill following stratospheric sudden warmings, *Nat. Geosci.*, **6**, 98–102, doi:  
 3415 10.1038/NGEO1698.
- 3416 Silvestri, G. E., and C. Vera (2003), Antarctic Oscillation signal on precipitation  
 3417 anomalies over southeastern South America, *Geophys. Res. Lett.*, **30**, 2115, doi:  
 3418 10.1029/2003GL018277.
- 3419 Simmons, A. (2007), ECMWF Newsletter, *Seminar*, (110).
- 3420 Simpson, I. R., P. Hitchcock, T. G. Shepherd, and J. F. Scinocca (2011), Strato-  
 3421 spheric variability and tropospheric annular-mode timescales, *Geophys. Res. Lett.*,  
 3422 **38**, L20,806, doi:10.1029/2011GL049304.
- 3423 Smith, A. K. (1989), An investigation of resonant waves in a numerical model of an  
 3424 observed sudden stratospheric warming, *J. Atmos. Sci.*, **46**, 3038–3054.
- 3425 Smith, D. M., A. a. Scaife, and B. P. Kirtman (2012), What is the current state of sci-  
 3426 entific knowledge with regard to seasonal and decadal forecasting?, *Environ. Res. Lett.*,  
 3427 **7**, 015,602, doi:10.1088/1748-9326/7/1/015602.
- 3428 Solomon, S., R. R. Garcia, F. S. Rowland, and D. J. Wuebbles (1986), On the depletion  
 3429 of Antarctic ozone, *Nature*, **321**, 755–788, doi:10.1038/321755a0.

## BIBLIOGRAPHY

- 3430 Son, S.-W., A. Purich, H. H. Hendon, B.-M. Kim, and L. M. Polvani (2013), Improved  
3431 seasonal forecast using ozone hole variability?, *Geophys. Res. Lett.*, 40, 6231–6235,  
3432 doi:10.1002/2013GL057731.
- 3433 Song, Y., and W. A. Robinson (2004), Dynamical Mechanisms for Stratospheric  
3434 Influences on the Troposphere, *J. Atmos. Sci.*, 61, 1711–1725, doi:10.1175/  
3435 1520-0469(2004)061.
- 3436 Stewartson, K. (1978), The evolution of the critical layer of a Rossby wave, *Geophys.*  
3437 *Astrophys. Fluid Dyn.*, 9, 185–200, doi:10.1080/03091927708242326.
- 3438 Stocker, T. F., D. Qin, G.-K. Plattner, M. Tignor, S. K. Allen, J. Boschung, A. Nauels,  
3439 Y. Xia, V. Bex, and P. M. Midgley (2013), *IPCC, 2013: Climate Change 2013: The*  
3440 *Physical Science Basis. Contribution of Working Group 1 to the Fifth Assessment Report*  
3441 *of the Intergovernmental Panel on Climate Change*, 1535 pp., Cambridge University  
3442 Press, Cambridge, United Kingdom and New York, NY, USA.
- 3443 Taguchi, M. (2003), Tropospheric Response to Stratospheric Degradation in a  
3444 Simple Global Circulation Model, *J. Atmos. Sci.*, 60, 1835–1846, doi:10.1175/  
3445 1520-0469(2003)060<1835:TRTSDI>2.0.CO;2.
- 3446 Taguchi, M. (2008), Is There a Statistical Connection between Stratospheric Sudden  
3447 Warming and Tropospheric Blocking Events?, *J. Atmos. Sci.*, 65, 1442–1454, doi:  
3448 10.1175/2007JAS2363.1.
- 3449 Taguchi, M. (2014), Predictability of Major Stratospheric Sudden Warmings of the Vor-  
3450 tex Split Type: Case Study of the 2002 Southern Event and the 2009 and 1989  
3451 Northern Events, *J. Atmos. Sci.*, 71(8), 2886–2904, doi:10.1175/JAS-D-13-078.1.
- 3452 Taylor, K. E., R. J. Stouffer, and G. a. Meehl (2012), An Overview of CMIP5 and  
3453 the Experiment Design, *Bull. Amer. Meteor. Soc.*, 93(4), 485–498, doi:10.1175/  
3454 BAMS-D-11-00094.1.
- 3455 Thompson, D., M. Baldwin, and J. Wallace (2002), Stratospheric connection to North-  
3456 ern Hemisphere wintertime weather: Implications for prediction, *J. Climate*, pp.  
3457 1421–1428.
- 3458 Thompson, D. W. J., and S. Solomon (2002), Interpretation of recent Southern Hemis-  
3459 phere climate change., *Science*, 296, 895–899, doi:10.1126/science.1069270.
- 3460 Thompson, D. W. J., and J. M. Wallace (1998), The Arctic Oscillation signature in the  
3461 wintertime geopotential height and temperature fields, *Geophys. Res. Lett.*, 25(9),  
3462 1297–1300.
- 3463 Thompson, D. W. J., and J. M. Wallace (2000), Annular Modes in the Extratropical  
3464 Circulation. Part I: Month-to-Month Variability, *J. Climate*, 13(5), 1000–1016.
- 3465 Thompson, D. W. J., and J. D. Woodworth (2014), Barotropic and Baroclinic Annular  
3466 Variability in the Southern Hemisphere, *J. Atmos. Sci.*, 71, 1480–1493, doi:10.1175/  
3467 JAS-D-13-0185.1.

- 3468 Thompson, D. W. J., J. M. Wallace, and G. C. Hegerl (2000), Annular modes in the  
 3469 extratropical circulation. Part II: Trends, *J. Climate*, (689), 1018–1036.
- 3470 Thompson, D. W. J., M. P. Baldwin, and S. Solomon (2005), Stratosphere-troposphere  
 3471 coupling in the Southern Hemisphere, *J. Atmos. Sci.*, pp. 708–715, doi:10.1175/  
 3472 JAS-3321.1.
- 3473 Thompson, D. W. J., J. C. Furtado, and T. G. Shepherd (2006), On the tropospheric  
 3474 response to anomalous stratospheric wave drag and radiative heating, *J. Atmos. Sci.*,  
 3475 (63), 2616–2629.
- 3476 Tibaldi, S., and F. Molteni (1990), On the operational predictability of blocking, *Tellus*  
 3477 A, 42A, 343–365.
- 3478 Tibshirani, R., G. Walther, and T. Hastie (2001), Estimating the number of clusters in a  
 3479 data set via the gap statistic, *J. R. Stat. Soc.*, 63(Part 2), 411–423.
- 3480 Tomassini, L., E. P. Gerber, M. P. Baldwin, F. Bunzel, and M. Giorgetta (2012), The  
 3481 role of stratosphere-troposphere coupling in the occurrence of extreme winter cold  
 3482 spells over northern Europe, *J. Adv. Model. Earth. Syst.*, 4, M00A03, doi:10.1029/  
 3483 2012MS000177.
- 3484 Toon, O. B., P. Hamill, R. P. Turco, and J. Pinto (1986), Condensation of HNO<sub>3</sub> and HCl  
 3485 in the winter polar stratospheres, *Geophys. Res. Lett.*, 13, 1284–1287.
- 3486 Tung, K. K., and R. S. Lindzen (1979), A Theory of Stationary Long Waves. Part II:  
 3487 Resonant Rossby Waves in the Presence of Realistic Vertical Shears, *Mon. Weather  
 3488 Rev.*, 107, 735–750.
- 3489 Uppala, S. M., Kallberg, P. W., A. J. Simmons, U. Andrae, V. D. C. Bechtold, M. Fiorino,  
 3490 J. K. Gibson, J. Haseler, A. Hernandez, G. A. Kelly, X. Li, K. Onogi, S. Saarinen,  
 3491 N. Sokka, R. P. Allan, E. Andersson, K. Arpe, M. A. Balmaseda, A. C. M. Beljaars,  
 3492 L. V. D. Berg, J. Bidlot, N. Bormann, S. Caires, F. Chevallier, A. Dethof, M. Dragosavac,  
 3493 M. Fisher, M. Fuentes, S. Hagemann, E. Hólm, B. J. Hoskins, L. Isaksen, P. A. E. M.  
 3494 Janssen, R. Jenne, A. P. McNally, J.-F. Mahfouf, J.-J. Morcrette, N. A. Rayner, R. W.  
 3495 Saunders, P. Simon, A. Sterl, K. E. Trenberth, A. Untch, D. Vasiljevic, P. Viterbo, and  
 3496 J. Woollen (2005), The ERA-40 re-analysis, *Q. J. R. Meteorol. Soc.*, 131(612), 2961–  
 3497 3012.
- 3498 Wallace, J., and D. Thompson (2002), The Pacific center of action of the Northern  
 3499 Hemisphere annular mode: Real or artifact?, *J. Clim.*, pp. 1987–1991.
- 3500 Warn, T., and H. Warn (1978), The evolution of a nonlinear critical level, *Stud. Appl.  
 3501 Math.*, 59, 37–71.
- 3502 Waugh, D. (1997), Elliptical diagnostics of stratospheric polar vortices, *Q. J. R. Meteo-  
 3503 rol. Soc.*, 123, 1725–1748.
- 3504 Waugh, D. W., and W. J. Randel (1999), Climatology of Arctic and Antarctic polar  
 3505 vortices using elliptical diagnostics, *J. Atmos. Sci.*, 56, 1594–1613.

## BIBLIOGRAPHY

- 3506 Waugh, D. W., R. A. Plumb, R. J. Atkinson, M. R. Schoeberl, L. R. Lait, P. A. Newman,  
3507 M. Loewenstein, D. W. Toohey, L. M. Avallone, C. R. Webster, and R. D. May (1994),  
3508 Transport out of the lower stratospheric Arctic vortex by Rossby wave breaking, *J.  
3509 Geophys. Res.*, 99, 1071–1088.
- 3510 Waugh, D. W., L. Oman, P. A. Newman, R. S. Stolarski, S. Pawson, J. E. Nielsen, and  
3511 J. Perlitz (2009), Effect of zonal asymmetries in stratospheric ozone on simulated  
3512 Southern Hemisphere climate trends, *Geophys. Res. Lett.*, 36, L18,701, doi:10.1029/  
3513 2009GL040419.
- 3514 Weber, M., S. Dikty, J. P. Burrows, H. Garny, M. Dameris, A. Kubin, J. Abalichin,  
3515 and U. Langematz (2011), The Brewer-Dobson circulation and total ozone from  
3516 seasonal to decadal time scales, *Atmos. Chem. Phys.*, 11, 11,221–11,235, doi:  
3517 10.5194/acp-11-11221-2011.
- 3518 Wilcox, L. J., B. J. Hoskins, and K. P. Shine (2012a), A global blended tropopause  
3519 based on ERA data. Part I: Climatology, *Q. J. R. Meteorol. Soc.*, 138(664), 561–575,  
3520 doi:10.1002/qj.951.
- 3521 Wilcox, L. J., B. J. Hoskins, and K. P. Shine (2012b), A global blended tropopause  
3522 based on ERA data. Part I: Climatology, *Q. J. R. Meteorol. Soc.*, 138, 561–575, doi:  
3523 10.1002/qj.951.
- 3524 Wilks, D. S. (2006), *Statistical Methods in the Atmospheric Sciences*, 2 ed., 627 pp.,  
3525 Academic Press.
- 3526 Wittman, M. a. H., A. J. Charlton, and L. M. Polvani (2007), The Effect of Lower  
3527 Stratospheric Shear on Baroclinic Instability, *J. Atmos. Sci.*, 64(2), 479–496, doi:  
3528 10.1175/JAS3828.1.
- 3529 WMO (2011), Scientific Assessment of Ozone Depletion: 2010, *Tech. rep.*, World Me-  
3530 teorological Organization, Global Ozone Research and Monitoring Project, Report  
3531 52., Geneva.
- 3532 Woollings, T., A. Charlton-Perez, S. Ineson, A. G. Marshall, and G. Masato (2010),  
3533 Associations between stratospheric variability and tropospheric blocking, *J. Geophys.  
3534 Res.*, 115, D06,108, doi:10.1029/2009JD012742.
- 3535 Yamazaki, K. (1987), Observations of the Stratospheric Final Warmings in the Two  
3536 Hemispheres, *J. Meteor. Soc. Japan*, 65, 51–66.
- 3537 Yoden, S., T. Yamaga, P. S, and U. Langematz (1999), A composite analysis of the  
3538 stratospheric sudden warmings simulated in a perpetual January integration of the  
3539 Berlin TSM GCM, *J. Meteor. Soc. Japan*, 77, 431–445.